# Coupled electromagnetic-thermomechanical modeling of electric motors

Nicolas Hanappier

INSTITUT POLYTECHNIQUE DE PARIS

NNT : 2021IPPAX015

Thèse de doctorat

# Coupled electromagnetic-thermomechanical modeling of electric motors

Thèse de doctorat de l'Institut Polytechnique de Paris
préparée à l'Ecole polytechnique

École doctorale n°626
Ecole Doctorale de l'Institut Polytechnique de Paris (ED IP Paris)
Spécialité de doctorat : Mécanique des fluides et des solides, acoustique

Thèse présentée et soutenue à Palaiseau, le 26 Février 2021, par

**NICOLAS HANAPPIER**

Composition du Jury :

| | |
|---|---|
| M. Patrick LE TALLEC<br>Professeur, Ecole polytechnique (Laboratoire de Mécanique des Solides) | Président |
| M. Laurent DANIEL<br>Professeur, Centrale-Supélec (Laboratoire de Génie Électrique de Paris) | Rapporteur |
| M. Krishnaswamy RAVI-CHANDAR<br>Professor, The University of Texas at Austin (Center for Mechanics of Solids and Materials) | Rapporteur |
| Mme Laurence BRASSART<br>Associate Professor, University of Oxford (Department of Engineering Sciences) | Examinateur |
| M. Ryan S. ELIOTT<br>Professor, University of Minnesota (Aerospace Engineering & Mechanics) | Examinateur |
| M. Nicolas TRIANTAFYLLIDIS<br>Professeur, Ecole polytechnique (Laboratoire de Mécanique des Solides) | Directeur de thèse |
| M. Eric CHARKALUK<br>Professeur chargé de cours, Ecole polytechnique (Laboratoire de Mécanique des Solides) | Co-directeur de thèse |
| M. Laurent ROTA<br>Docteur Ingénieur, PSA Group (Direction for Research, Innovation & Advanced Technologies) | Invité |

# COUPLED ELECTROMAGNETIC-THERMOMECHANICAL MODELING OF ELECTRIC MOTORS

NICOLAS HANAPPIER

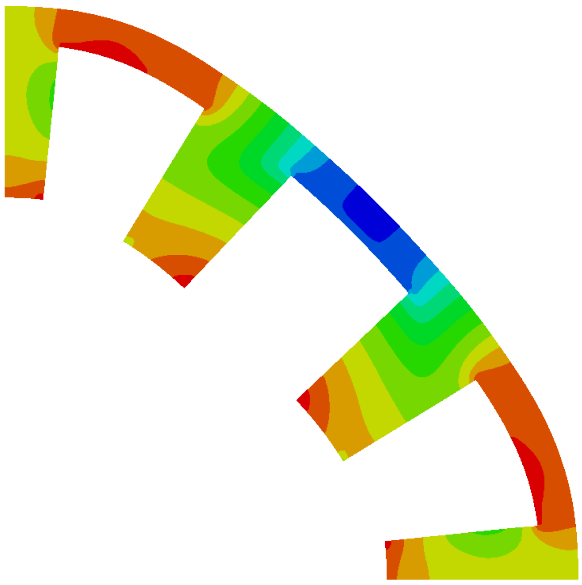

Theory, analytical calculation and numerical models

February 2021

Nicolas Hanappier: *Coupled electromagnetic-thermomechanical modeling of electric motors,* Theory, analytical calculation and numerical models, © February 2021

A ma famille, à mes grands-parents et parents,
A mes enseignants

# FOREWORD

The thesis work presented here was undertaken at the Laboratoire de Mécanique des Solides (LMS) of École polytechnique, France, under the supervision of Professor Eric Charkaluk and Professor Nicolas Triantafyllidis. It was defended on February 26th, 2021.

It is supported by the *André Citroën Research Chair* of Ecole polytechnique.




Some of the results presented here have already been published as:

Hanappier, N., E. Charkaluk, and N. Triantafyllidis (2021). "A coupled electromagnetic–thermomechanical approach for the modeling of electric motors." In: *Journal of the Mechanics and Physics of Solids* 149, p. 104315. DOI: 10.1016/j.jmps.2021.104315.

## ABSTRACT

Future developments of lighter, more compact and powerful motors – driven by environmental and sustainability considerations in the transportation industry – involve higher stresses, currents and electromagnetic fields. For the components used in electric motors – especially for the ferromagnetic ones – strong couplings between mechanical, thermal and electromagnetic effects arise, which are amplified by the higher loads. They affect the machine's performance, thus requiring a consistent multiphysics modeling for the motors' design. Understanding and modeling these couplings has recently become an important subject of research. The work presented here proposes a coupled electromagnetic-thermomechanical continuum theory together with analytical and numerical (finite element) tools for the solutions of boundary value problems arising in electric motors.

In the first part of the work, using the direct approach of continuum mechanics, based on a Eulerian (current configuration) approach, a general modeling framework coupling the electromagnetic, thermal and mechanical fields is derived from the basic principles of thermodynamics using the eddy current approximation. Although the proposed theory is general enough to account for a wide range of material behaviors, particular attention is paid to the derivation of the coupled constitutive equations for isotropic materials under small strain but arbitrary magnetization. As a first application, the theory is employed for the analytical modeling of the rotor and stator of idealized electric motor configurations for which we calculate the electric current, magnetic, stress and temperature fields. At the rotor, the different components of the stress tensor and body force vector are compared to their purely mechanical counterparts due to inertia, quantifying the significant influence of electromagnetic phenomena. At the stator, comparison with coarser models found in the electrical engineering literature is provided, quantifying the influence of the proposed model on the elastic stress and strains' amplitudes.

In the second part of the work, a variational formulation of the problem is presented based on a Lagrangian (reference configuration) approach and shown to be equivalent to the direct approach. The numerical implementation of the proposed model – via a user element in a general purpose finite element code and accounting for non-linear material behavior – is validated by comparison of the results from the analytical models of the simplified stator configuration to the numerical results for small values of the magnetic field (range of linear behavior for the magnetic field). Calculations are then performed on more complex stator configurations with a more intense magnetic field, using a non-linear magnetic response that accounts for magnetic saturation (a Langevin-type model), in order to put forward the capacities of the proposed formulation and obtain results for realistic engineering applications.

## RÉSUMÉ

Le développement de moteurs électriques plus légers, compacts et puissants – entrainé par l'électrification rapide dans le domaine des transports en réponse aux enjeux environnementaux de notre époque – entraine une augmentation des contraintes, des courants et des champs magnétiques dans les composants des moteurs. Ces composants – notamment les composants ferromagnétiques – présentent des couplages forts de leurs propriétés magnéto-thermo-mécaniques, exacerbées dans des moteurs plus fortement sollicités. Les chargements mécaniques et thermiques de la machine influencent ses propriétés magnétiques et la conception de moteurs toujours plus performants nécessite alors d'avoir recours à des modélisations multi-physiques fiables. La compréhension et la modélisation de ces couplages est devenu un sujet de préoccupation important pour les industriels et fait l'objet de nombreux travaux de recherche. Les travaux présentés ici proposent une théorie couplée électromagnétique-thermomécanique du milieu continu et le développement d'outils analytiques et numériques pour la résolution de problèmes aux limites dans les moteurs électriques.

Dans la première partie de ce travail, un cadre de modélisation général couplant les champs électromagnétique, thermique et mécanique est dérivé des principes fondamentaux de la thermodynamique en utilisant l'approche directe de la mécanique des milieux continus en configuration Eulérienne (configuration courante) dans l'approximation des courants de Foucault. Cette formulation est capable de décrire un large panel de comportements couplés et non-linéaires d'origine magnétique, mécanique et thermique. Une attention particulière est portée à la dérivation des équations constitutives couplées pour le cas de matériaux isotropiques en petite déformation mais magnétisation arbitraire. En exemple d'application, la théorie est utilisée pour la modélisation du rotor et du stator de configurations idéalisées de moteurs électriques pour lesquelles nous calculons les courants électriques, le champ magnétique et les champs de contraintes et de température. Au rotor, les différentes composantes du tenseur de contraintes et des forces volumiques sont comparées aux contraintes et aux efforts d'origine uniquement mécanique liés aux forces centrifuges, quantifiant l'influence significative des phénomènes électromagnétiques. Au stator, nous présentons une comparaison avec des modèles plus simples habituellement utilisés pour la modélisation des moteurs électriques, et quantifions l'influence du modèle proposé sur l'amplitude des contraintes élastiques et des déformations.

Dans la seconde partie de ce travail, une formulation variationnelle basée sur une approche Lagrangienne (configuration de référence) est proposée et son équivalence avec la formulation obtenue par l'approche directe est démontrée. L'implémentation numérique du modèle proposé – via la définition d'un « user element » dans un code de calcul aux éléments-finis généraliste et tenant compte de comportements matériaux non-linéaires – est validé par comparaison des résultats numériques aux résultats des modèles analytiques obtenus pour la modélisation du stator en configuration simplifiée, dans le cas de petits champs magnétiques

(domaine de comportement linéaire pour le champ magnétique). Des calculs sont par la suite effectués sur des configurations de stator plus complexes sous champ électromagnétique plus intense, présentant une réponse magnétique non-linéaire avec saturation (modèle de type Langevin), afin de mettre en avant les capacités de la formulation proposée et d'obtenir des résultats plus proches d'applications techniques réalistes.

*Je suis de ceux qui pensent que la science est d'une grande beauté.*
*Un scientifique dans son laboratoire est non seulement un technicien :*
*il est aussi un enfant placé devant des phénomènes naturels*
*qui l'impressionnent comme des contes de fées.*

**— MarieCurie**

## REMERCIEMENTS

Tout au long de cette thèse, j'ai pu approfondir mes connaissances de la mécanique et mon raisonnement scientifique grâce à de nombreux contributeurs que je souhaite vivement remercier. Beaucoup de personnes m'ont également porté, accompagné, inspiré. Je souhaite également les remercier chaleureusement. Ce doctorat est enfin un aboutissement de ma formation - si celle-ci se termine jamais -, et je souhaite remercier certaines personnes m'ayant particulièrement bien accompagné et conseillé le long de ce chemin.

Je remercie en premier lieu, bien évidemment, Eric Charkaluk et Nicolas Triantafyllidis, professeurs et chercheurs au Laboratoire de Mécanique des Solides et directeurs de cette thèse. C'est directement grâce à eux que j'ai pu mener ces travaux qui m'ont passionné pendant trois ans. En plus de leurs grandes connaissances et de tout ce qu'ils m'ont enseigné, j'aimerais souligner leurs formidables qualités humaines, leur engagement au service de leurs étudiants, leur formidable disponibilité, et leur passion pour le métier qu'ils exercent. Je leur dois beaucoup, ce fut un plaisir de travailler avec eux et d'apprendre d'eux durant ces trois ans et je les remercie bien chaleureusement.

Je remercie la chaire André Citroën de l'Ecole polytechnique, et derrière celle-ci le groupe automobile Stellantis, qui a financé ces travaux et permis leur réalisation. Je remercie tout particulièrement Laurent Rota, Stellantis, ainsi que Patrick Le Tallec, directeur du LMS durant mon doctorat, pour les discussions ayant mené au lancement de ce beau projet de thèse. Je remercie Laurent et Olivier Sauvage, Stellantis, ainsi que Raphaël Pile et Jean Le Besnerais, Eomys, pour nos réunions de travail. J'ai beaucoup appris au sujet du moteur électrique et des problématiques du secteur automobile grâce à celles-ci, afin d'orienter au mieux ces travaux vers un résultat qui sera, je l'espère, utile à la recherche comme à l'industrie. Je remercie également Camille Obeid pour ses travaux de stage m'ayant aidé dans l'évaluation de logiciels de calculs.

J'aimerais plus largement remercier l'ensemble du Laboratoire de Mécanique des Solides. J'ai eu la chance de m'épanouir dans un environnement chaleureux, incroyablement talentueux et compétent, entouré de gens particulièrement bienveillants, disponibles et aidants ; cela qu'il s'agisse des chercheurs, des ingénieurs et des doctorants pour la formidable science qui règne au Laboratoire, mais aussi de tous les métiers supports qui nous permettent chaque jour de réaliser notre doctorat dans les meilleures conditions (je pense en particulier à Alexandra Joly, Valérie Jamet, Anna Johnsson, Christiane Periam, Danielle Elizabeth, Abdelfattah Halim, ainsi que Patrick Le Tallec et Andrei Constantinescu successivement directeurs du Laboratoire durant mon doctorat). Je remercie aussi Vincent De Greef,

ingénieur au Laboratoire, pour nos discussions autour de la conception de systèmes expérimentaux dans l'optique de futurs travaux sur l'électromagnétisme au Laboratoire.

Je souhaite remercier particulièrement vigoureusement Ludovic Gil, doctorant au Laboratoire les mêmes années que moi et sur des sujets similaires, pour sa formidable compréhension de la thermodynamique et de la mécanique des solides - je lui dois beaucoup dans la compréhension fine de cette science -, et les échanges fondamentaux que nous avons eu sur ces sujets. J'ai également une pensée particulière pour Laurent Guin, Lucas Benoit-Maréchal et Dipayan Mukerjee, doctorants au Laboratoire également, qui ont participé à travers nos échanges à la construction de mon raisonnement. Je remercie plus généralement l'ensemble des doctorants pour cette bonne ambiance qui règne au Laboratoire et les échanges très riches que nous avons eu.

Je remercie Madame Pizzi, professeur de physique au Lycée Notre Dame du Grandchamp à Versailles, pour ses précieux conseils et l'orientation particulièrement judicieuse suggérée pour ma formation. C'est une grande chance d'avoir eu un professeur si attentif, qui a contribué à me mettre sur cette voie. Je remercie également Alain Erhlacher, directeur du département Génie Mécanique et Matériaux à l'Ecole des Ponts ParisTech, pour ses enseignements, sa vision et ses conseils lors du choix de mon doctorat. Parmi les gens m'ayant encouragé sur la voie du doctorat, merci également à Christine Hottier, Robert Hewson et Christian Mercier.

Enfin, certains soutiens inconditionnels m'ont également accompagné tout au long de ce chemin. Du fond du cœur je remercie Axelle Delorme, bien sûr, toute ma famille, et mes amis.

N. H.
Versailles, 2021

# CONTENTS

# INTRODUCTION

The increasing importance and market share of hybrid and purely electric vehicles – in the urgent quest to reduce the transportation industry's carbon footprint – drives the development of higher performance electric motors in terms of efficiency, power density, reliability, higher rotation velocity, reduced weight and costs. Accurate modeling of both the electromagnetic (i.e. magnetic flux) and thermomechanical (i.e. stresses and temperature fields) is an indispensable part of their design.

## A BRIEF DESCRIPTIONS OF A TYPICAL ELECTRIC MOTOR

To set the stage we start by showing the cross-section of a typical motor, consisting of a turning part, termed "*rotor*" and a fixed part, termed "*stator*" separated by an "*airgap*", as seen in Figure 0.1.

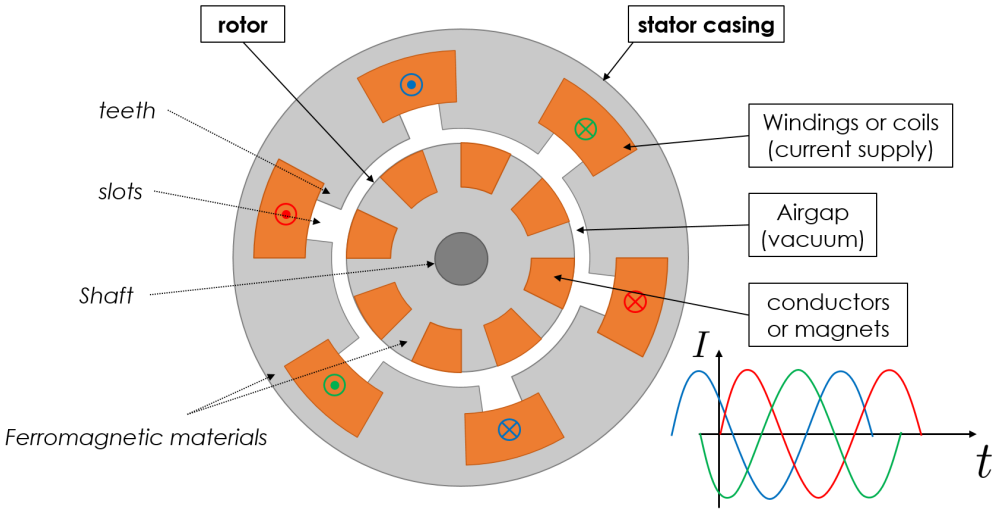


Figure 0.1: Cross-section of a typical motor, showing rotor, airgap and stator, with current supply coil domains.

Stator windings or coils are supplied by multi-phase alternating currents to create a rotating magnetic field. The rotor can have permanent magnets or conducting bars (cage rotor). It can also be made of a plain ferromagnetic material in the case of very high speed machines. In the case of magnets, the motor is called "*synchronous*" given the rotor spins at the same frequency as the stator magnetic field. Motors having rotors with conducting bars or plain ferromagnetic (but without magnets) rely on induction: the rotating stator field induces currents at the rotor, which in turn trigger Lorentz forces creating the rotor motion. An angular velocity differential, called "*slip*", between the rotor and the stator results and the motor is called "*asynchronous*". The dark region at the center of the rotor indicates the motor

shaft, which transmits the mechanical load (torque). The bulk of the rotor and stator are usually made of ferromagnetic materials with high magnetic susceptibility to enhance and channel the magnetic flux.

### MOTIVATION AND SCOPE

Modeling of electric motors has in the past been a topic studied predominantly by the electrical engineering community. The focus has been on the calculation of the magnetic field and resulting torque and iron losses for different motor designs using both analytical and numerical methods.

Since the late 90s, stress calculations in electric motors have appeared as a result of noise and vibrations concerns. Moreover, future developments of lighter, more compact and powerful motors will involve higher stresses, currents and electromagnetic fields. As a result, strong couplings between mechanical, thermal and electromagnetic effects will consequently arise and a consistent multiphysics modeling approach is required for the motors' design. Typical simulations – the bulk of which are presented in the electrical engineering literature – involve a stepwise process, where the resolution of Maxwell's equations provides the Lorentz and magnetic forces which are subsequently used as the external body forces for the resolution of Newton's equations of motion. Existing approximate methods are inadequate to deal with the true multiphysics nature of the electric motor problem, thus requiring a consistent continuum mechanics modeling approach.

In recent years, considerable developments occurred in the field of continuum thermodynamics with the advent of coupled electromagnetic-thermomechanical theories derived using both the direct and variational methods of continuum mechanics. The former, using an Eulerian approach, provides the governing equations and valuable information about the constitutive laws. The latter, using a Lagrangian approach confirms the results of the direct method (a highly nontrivial result in multiphysics problems) and is useful for numerical solutions of the resulting realistic boundary value problems (for a typical example see Figure 0.1).

> The goal of the present work is a thermodynamically consistent continuum formulation of the coupled electromagnetic-thermomechanical problem of electric motors, followed by the analytical and numerical tools required for the solution of the resulting boundary value problem and illustrated by different examples.

### OUTLINE

This thesis is divided into two parts: Part I pertains to the direct approach of continuum mechanics and presents the analytical solution of a simplified motor (rotor and stator part). Part II pertains to the variational formulation of the problem and uses the finite element method to solve a realistic problem (stator part). A detailed literature review is given, as required, at the introduction of each part.

In Chapter 1 of Part we present a very general theory of non-relativistic electrodynamics as the ground to all future developments. In Chapter 2, the general theory is specified to the modeling of electric motors by introducing the eddy current approximation. Attention is paid to the derivation of the coupled constitutive equations for isotropic materials under small strain but arbitrary magnetization. In Chapter 3 the analytical solution of a simplified motor boundary value problem is presented (rotor and stator). For the rotor, we calculate the magnetic field in addition to the temperature field, the magnetic, total and elastic stresses in the rotor and the torque as a function of the applied current and the slip parameter (equivalent to the mechanical torque). The results for three different rotor materials (electric steel, copper and aluminum) using realistic geometric and operational regime values and material parameters are presented. For the stator case, we calculate the magnetic, stresses and displacement fields. The results are compared to the standard model usually used in the electric engineering literature. In Chapter 4, the work of Part I is concluded with a critical review and suggestions for future work

The essential contributions of Part I are:

- Proposing a general framework, based on the direct approach of continuum mechanics using the principles of electromagnetism, mechanics and thermodynamics, suitable for the modeling of coupled thermo-magneto-mechanical problems in electric motors;
- A proper linearization of the constitutive relations in the small strains, arbitrary magnetization regime for materials with coupled magneto-mechanical behaviors;
- Examples of analytical boundary value problems for simplified electric motors to calculate temperature fields and identify different contributions of stress and body forces.

*The developments of Part I up to the rotor boundary value (Section 3.1) have been published in Hanappier, Charkaluk, and Triantafyllidis, 2021a. The complementary stator boundary value problem developments (Section 3.2) have been submitted for publication. The corresponding manuscript is Hanappier, Charkaluk, and Triantafyllidis, 2021b.*

In Chapter 5 of Part II, the variational formulation for the general electrodynamic problem in Chapter 1 is presented in Section 5.1. An eddy current approximation of the variational formulation is presented in Section 5.2, and based of the developments from Chapter 2. In Chapter 6, the numerical implementation of the problem via a user element in a general purpose final element code is presented for the quasi-static case (no induced currents nor acceleration terms). The choice of element types and specific free energy are detailed. In Chapter 7, finite element analysis of stator boundary value problems are performed in the spirit of the analytical problem from Section 3.2. A magnetic material behavior that accounts for magnetic saturation is defined. In Section 7.1, FEM results are validated by comparison with the analytical results from Section 3.2 in the linear range (small magnetic fields). In Section 7.2, the finite element analysis of a more realistic stator geome-

try with teeth and slots at large magnetic fields is performed to put forward the capacities of the numerical code developed. In Chapter 8, we conclude the work of Part II with a critical review and suggestions for future work.

The essential contributions of Part II are:

- Proposing a general variational formulation for the study of coupled magneto-mechanical problems in electric motors, under finite strain and arbitrary magnetic fields and showing its consistency with the direct approach of continuum mechanics in Part I (a non-trivial result for coupled problems);
- A numerical implementation of the variational formulation for finite element analysis of electric motor problems and verification of the code by comparison with the analytical results of Part I;
- Numerical calculation of stresses, strains and magnetic fields in a realistic stator under large magnetic fields accounting for magneto-mechanical couplings.

*The developments of Part II, with improvements on the material behavior, have been submitted for publication. The corresponding manuscript is Hanappier, Charkaluk, and Triantafyllidis, 2021c.*

# Part I

# A MAGNETO-THERMO-MECHANICAL THEORY BASED ON THE DIRECT APPROACH OF CONTINUUM MECHANICS

# 1

# GENERAL ELECTROMAGNETIC THEORY FOR THE CONTINUUM

LITERATURE REVIEW In the late 90s, stress calculations in electric motors have appeared as a result of noise and vibrations concerns (Reyne et al., 1987; Reyne, Sabonnadière, and Imhoff, 1988). At the time already, concerns regarding the intricate coupling between magnetic and mechanical aspects in ferromagnetic materials were raised. These materials with high magnetic permeability constitute the bulk of electric motors. They are used to enhance and channel the magnetic flux within the machine to improve performance. They have intrinsic strongly coupled magnetic and mechanical behavior (Cullity and Graham, 2011; Fonteyn, 2010; Fonteyn et al., 2010b; Fonteyn et al., 2010a). First, they develop important magnetization, which triggers body forces of magnetic origin in addition to the Lorentz force due to currents (e.g. see Reyne et al., 1987). They foremost expand when applied a magnetic field, a phenomenon called *magnetostriction* (Joule, 1847; Lee, 1955; Du Trémolet De Lacheisserie, 1993). More recently, interest in computing stresses in electric motors also arose for questions of motor performance, as the magnetostriction effect is accompanied by it reverse phenomena, referred to as *inverse magnetostriction* or *Villari effect*: stresses in ferromagnetic materials stretch and reorient the magnetic domains within the material. This modifies the material's permeability to the magnetic field and hence its magnetization. In turn the machine's performance that relies on magnetization may be affected. This led to studies of the effect of stresses due to centrifugal forces on magnetization (Rekik, Hubert, and Daniel, 2014), or stresses due to manufacturing and assembling processes (for instance Daikoku et al., 2005; Bernard and Daniel, 2015 for shrink fitting, or Takezawa et al., 2006 for punching of electrical steel sheets). Consequently, important research is now led on the characterization of electrical steel sheets used in electric motors (e.g. see Aydin et al., 2017). For the design of future electric motors with optimized performance, modeling tools are required that can properly account for these fine material characterization and their coupled magneto-mechanical behavior. This is the ground to the current work.

As pointed out by Reyne et al., 1987, the first difficulty in the formulation of magneto-mechanical problems was the evaluation of the distribution of local electromagnetic body forces, for which various expressions were suggested but none achieving general agreement. Since then, continuum mechanics has advanced this problem calling to consistent thermodynamic formulations of continuum electromagnetism[1], specifying material behaviors through the definition of a continuum's specific free energy from which derives combined thermo-magneto-mechanical stresses giving the interface and body forces of electromagnetic origin. The multiplicity of the different formulations, direct as well as variational, is however still today a source of confusion. Different (albeit equivalent) expressions for the Maxwell

1 For an interesting summary of the most important developments in the field the reader is referred to the introduction of Kankanala and Triantafyllidis, 2004

stress and electromagnetic body forces can be obtained and are thus responsible for the difficulty in the correct modeling of stresses in electric motors. For further discussion on this issue, the interested reader is referred to the article by Kankanala and Triantafyllidis, 2004 and book by Hutter, van de Ven, and Ursescu, 2006.

Regarding the direct approach of continuum mechanics, which uses conservation laws to derive the equations of the problem, particularly helpful is the work of Kovetz, 2000 where the body forces due to the electromagnetic field are accounted for through a generalized linear momentum and a generalized Cauchy stress. Their precise form is not postulated but further given as deriving from a specific free energy by application of fundamental principles of mechanics and thermodynamics. The postulate is on the form of the flux of electromagnetic-energy, namely Poynting's vector. The theory developed in this book has been used in many domains (Kankanala and Triantafyllidis, 2004; Thomas and Triantafyllidis, 2009; Dorfmann and Ogden, 2003; Dorfmann and Ogden, 2004; Dorfmann and Ogden, 2005) and Steigmann, 2009 makes the case of its equivalence with other formulations such as those reviewed in Hutter, van de Ven, and Ursescu, 2006. It has been taken to the modeling of electric motors in the recent work by Fonteyn, 2010; Fonteyn et al., 2010b; Fonteyn et al., 2010a. However several approximations are used (e.g. a small strain approximation involving non frame-indifferent invariants and the angular momentum balance principle is not imposed) and may be revisited.

It should be noted that in the following approach, we adopt a macroscopic view of the continua and derive macroscopic constitutive relations. Other recent approaches address the characterization of the magneto-mechanical couplings through multiscale approaches (Daniel, 2018; Daniel, Bernard, and Hubert, 2020). Because these approaches include more physics, their advantage lies in the constitutive laws being described with fewer parameters (Aydin et al., 2017). These methods are very well suited to the understanding of the underlying physics behind magneto-mechanical couplings, and as such offer great insight for the optimization of magnetic behavior. They however have the drawback of much greater computational costs when applied to the modeling of electric motor problems (e.g. see Daniel, Bernard, and Hubert, 2020). Because of this last point, and because recent, they where not included in the scope of the present work.

As a final note, other phenomena of importance in electric motors are: *magnetic hysteresis* that creates losses, and in particular the influence of stress on magnetic hysteresis is studied (e.g. see Daniel, Rekik, and Hubert, 2014; Bernard and Daniel, 2015; Rasilo et al., 2016); *anisotropy*, with grain oriented electrical steel sheets now used to improved machines performance (Lopez et al., 2009; Cassoret et al., 2014; Sugawara and Akatsu, 2013). Moreover, strong currents influence temperature due to ohmic effects, temperature may influence magnetization and electrical conductivity but also stresses through thermal expansion, and so on. Although they are beyond the scope of the present work, the theory exposed is aimed general enough to be able to account for these effect.

OUTLINE To set the stage, and in an effort, for consistency, to start from the most general problem before applying restrictions suitable for electric motor problems in a later Chapter 2, the general formulation for coupled electro-magneto-thermo-mechanical boundary value problems are presented in this chapter. The derivation

is mostly taken from Kovetz, 2000, and presented here for self-sufficiency and clarity of the work exposed in this thesis.

> The method adopted is the current configuration, direct approach of continuum mechanics.

The governing equations and interface conditions are derived from conservation principles of electromagnetism, mechanics and thermodynamics. As in Kovetz, 2000, the conservation principles are written in current configuration (or Eulerian coordinates). The equations in reference configuration (or Lagrangian coordinates) are then derived from the current configuration's equations using kinematic relations.

In Section 1.1, we introduce a few formal conventions as preliminaries. In Section 1.2 the governing equations of the problem are derived based on conservation principles of electromagnetism, mechanics and thermodynamics. In Section 1.3, these governing equations are taken to the reference configuration. In Section 1.4, the constitutive relations are derived based on the restrictions imposed by the second principle of thermodynamics and the angular momentum balance. They are finally taken to the reference configuration in Section 1.5.

## 1.1 CONVENTIONS

OPERATORS Coordinate-free (dyadic) continuum mechanics notation is used with bold scripts referring to tensors, regular scripts to scalars. Let $\boldsymbol{v}(\boldsymbol{x},t)$ and $\boldsymbol{w}(\boldsymbol{x},t)$ two vectors and $\mathbf{t}(\boldsymbol{x},t)$ and $\mathbf{r}(\boldsymbol{x},t)$ two second order tensor. We note,

$$\begin{aligned}
&(\boldsymbol{v}\boldsymbol{w})_{ij} = v_i w_j \,, && (\boldsymbol{v}\cdot\mathbf{t})_j = v_i t_{ij} \,, && \mathbf{t}:\mathbf{r} = t_{ij} r_{ij} \,,\\
&(\boldsymbol{\nabla}\cdot\boldsymbol{v}) = \partial_i v_i \,, && (\boldsymbol{\nabla}\cdot\mathbf{T}) = \partial_i t_{ij} \,, &&\\
&(\boldsymbol{\nabla}\boldsymbol{v})_{ij} = \partial_i v_j \,, && (\boldsymbol{v}\boldsymbol{\nabla})_{ij} = \partial_j v_i \,, &&\\
&(\boldsymbol{\nabla}\times\boldsymbol{v})_i = \epsilon^{ijk}\partial_j v_k \,, &&&&
\end{aligned} \tag{1.1}$$

where $\epsilon^{ijk}$ is the Levi-Civita permutation symbol and with the usual Einstein summation convention on repeated indices.

CURRENT CONFIGURATION AND REFERENCE CONFIGURATION As is usual in continuum mechanics, we introduce the current *deformed* configuration and the reference *initial undeformed* configuration. The position in current configuration is denoted $\boldsymbol{x}$ and mapped to the position in reference configuration $\boldsymbol{X}$ by a one to one mapping: $\boldsymbol{x} = \boldsymbol{x}(\boldsymbol{X},t)$. The displacement $\mathbf{u}$ of a material point between its position in the current configuration and its position in the reference configuration links the position vectors $\boldsymbol{X}$ and $\boldsymbol{x}$, and we introduce the deformation gradient $\mathbf{F}$ and its determinant $J$

$$\boldsymbol{x} = \boldsymbol{X} + \mathbf{u} \,; \qquad \mathbf{F} = \frac{\partial \boldsymbol{x}}{\partial \boldsymbol{X}} \,; \qquad J = \det(\mathbf{F}) \,. \tag{1.2}$$

*Eulerian* (current configuration) fields are written using lowercase letters, while capital letters are used for their *Lagrangian* (reference configuration) counterparts.

Basis vectors of the current configuration are denoted $(\hat{\mathbf{e}}_1, \hat{\mathbf{e}}_2, \hat{\mathbf{e}}_3)$. Those of the reference configuration are denoted $(\hat{\mathbf{E}}_1, \hat{\mathbf{E}}_2, \hat{\mathbf{E}}_3)$.

Should additionally be mentioned that the method adopted in the following tacitly assumes adequate smoothness of the fields involved.

INTERFACES An electric motor comprises different constituents with different physical properties. As a result, our model will encompass multiple material domains, separated by interfaces. These interfaces usually introduce discontinuities, ruled by interface conditions. Only material domains are considered here, i.e. an interface at a point $\mathbf{x}$ propagates with the material velocity $\dot{\mathbf{x}}$.

SPATIAL DERIVATIVES Whenever used in the following, $\partial_i()$ denotes the partial derivative with respect to the position component of the current configuration $\partial()/\partial x_i$. Similarly $\partial_I()$ denotes the partial derivative with respect to the position component $X_i$ of the reference configuration $\partial()/\partial X_I$.

TIME DERIVATIVES For fields $\mathbf{f}(\mathbf{x}, t)$of the current configuration – either scalars or vectors here – , the *partial derivative with respect to time* $\partial\mathbf{f}/\partial t$ is defined as the derivative with respect to time of $\mathbf{f}$ holding $\mathbf{x}$ fixed. We define the *total time derivative* $\frac{d\mathbf{f}}{dt} = \dot{\mathbf{f}}$, as the time derivative holding $\mathbf{X}$ fixed and for the same fields $\mathbf{f}(\mathbf{x}, t)$ of the current configuration, because $\mathbf{x} = \mathbf{x}(\mathbf{X}, t)$ is also a function of time,

$$\dot{\mathbf{f}} = \frac{\partial \mathbf{f}}{\partial t} + \dot{\mathbf{x}} \cdot (\boldsymbol{\nabla} \mathbf{f}) \, . \tag{1.3}$$

Finally, the *flux derivative* $\overset{*}{\mathbf{f}}$ of the vector field $\mathbf{f}(\mathbf{x}, t)$ of the current configuration is defined as

$$\frac{d}{dt} \int_{s(t)} \mathbf{f} \cdot \mathbf{n} \, ds \equiv \int_{s(t)} \overset{*}{\mathbf{f}} \cdot \mathbf{n} \, ds \implies \overset{*}{\mathbf{f}} \equiv \frac{\partial \mathbf{f}}{\partial t} + \dot{\mathbf{x}} (\boldsymbol{\nabla} \cdot \mathbf{f}) - \boldsymbol{\nabla} \times (\dot{\mathbf{x}} \times \mathbf{f}) \, , \tag{1.4}$$

where $s(t)$ is an arbitrary moving surface.

KELVIN-STOKES' THEOREM Kelvin-Stokes' theorem applied to an arbitrary moving surface $s(t)$ with boundary $\partial s(t)$ states

$$\int_{s(t)} (\boldsymbol{\nabla} \times \mathbf{f}) \cdot \mathbf{n} ds = \int_{\partial s(t)} \mathbf{f} \cdot \mathbf{s} dl \, . \tag{1.5}$$

GAUSS' DIVERGENCE THEOREM The divergence theorem applied to an arbitrary volume element $v(t)$ with boundary $\partial v(t)$ and containing a surface of discontinuity $s(t)$ states

$$\int_{\partial v(t)} \mathbf{n} \cdot \mathbf{f} ds = \int_{v(t)} \nabla \cdot \mathbf{f} dv + \int_{s(t) \cap v(t)} \mathbf{n} \cdot [\![\mathbf{f}]\!] ds \, , \tag{1.6}$$

where $\mathbf{f}$ is an arbitrary tensor field.

TRANSPORT THEOREM For time derivatives of volume integrals on the current configuration, Reynold's transport theorem will be used, which states

$$\frac{d}{dt} \int_{v(t)} \mathbf{f} dv = \int_{v(t)} \frac{\partial \mathbf{f}}{\partial t} dv + \int_{\partial v(t)} \mathbf{f} \left( \dot{\mathbf{x}} \cdot \mathbf{n} \right) ds - \int_{s(t) \cap v(t)} [\![\mathbf{f}]\!] \left( \dot{\mathbf{x}} \cdot \mathbf{n} \right) ds \, , \tag{1.7}$$

where $v(t)$ is an arbitrary control volume with boundary $\partial v(t)$ and $s(t)$ is a *material* surface of discontinuity inside the control volume (moving with local velocity $\dot{\mathbf{x}}$). Applying the divergence theorem to the second and third terms of the right hand side of the previous equation then provides

$$\frac{d}{dt}\int_{v(t)} f dv = \int_{v(t)} \left[\frac{\partial f}{\partial t} + \boldsymbol{\nabla}\cdot\left(\dot{\mathbf{x}} f\right)\right] dv \,. \tag{1.8}$$

OTHER USEFUL THEOREM From Kovetz, 2000 (§56.): If $f(\mathbf{a})$ is differentiable, $f(\mathbf{Q}\cdot\mathbf{a}) = f(\mathbf{a})$ for every orthogonal matrix Q if, and only if,

$$a_i \frac{\partial f}{\partial a_j} = a_j \frac{\partial f}{\partial a_i} \,. \tag{1.9}$$

## 1.2 GOVERNING EQUATIONS IN CURRENT CONFIGURATION

As a foreword to the introduction of the electromagnetic equations, we mention here that the governing equations of electromagnetism derive from 3 fondamental principles: the charge conservation principle, the electromagnetic field principle, and the aether frame principle. The charge conservation principle results in Maxwell-Gauss and Maxwell-Ampère's laws, which state the behavior of two electric charge and current potentials: the electric displacement field $\mathbf{d}$ and h-field $\mathbf{h}$. The electromagnetic field principle expresses the behavior of the electromagnetic field $(\mathbf{e}, \mathbf{b})$. The aether frame principle links the charge and current potentials $(\mathbf{d}, \mathbf{h})$ to the electromagnetic field $(\mathbf{e}, \mathbf{b})$ via two material response fields: the polarization $\mathbf{p}$ and magnetization $\mathbf{m}$. The interested reader is referred to Kovetz, 2000 for a more detailed account on electromagnetism.

### 1.2.1 *Charge conservation principle*

As we mentionned above, the conservation of electric charge is usually split into two equations, commonly referred to as Maxwell-Gauss' and Maxwell-Ampère's laws.

MAXWELL-GAUSS'S LAW states that the *volumetric electric charges* $q$ are sources of *electric displacement* $\mathbf{d}$. Applied to an arbitrary moving control volume $v(t)$,

$$\int_{\partial v(t)} \mathbf{d}\cdot\mathbf{n} ds = \int_{v(t)} q dv \,, \tag{1.10}$$

where $\partial v(t)$ is the surface boundary of the control volume $v(t)$ and $\mathbf{n}$ is the outward pointing unit normal to the surface.

From standard arguments involving the arbitrariness of the control volume and Gauss's divergence theorem, one obtains the pointwise form of Gauss's law with its associated interface conditions[2],

$$\boldsymbol{\nabla}\cdot\mathbf{d} = q \,, \qquad \mathbf{n}\cdot[\![\mathbf{d}]\!] = 0 \,, \tag{1.11}$$

2 The present formulation does not consider surface electric charges. Should they be considered, they should be added to the right handside of the interface condition.

$\nabla \equiv \partial()/\partial \mathbf{x}$ is the gradient operator in the current configuration and $\nabla\cdot\mathbf{d}$ thus denotes the divergence of $\mathbf{d}$. $[\![]\!]$ denotes the jump – oriented by the normal $\mathbf{n}$ – in a field quantity across an interface.

AMPÈRE'S LAW states that the circulation of the *magnetomotive intensity*[3] $\boldsymbol{\mathcal{H}} \equiv \mathbf{h} - \dot{\mathbf{x}}\times\mathbf{d}$ about any moving closed contour $\partial s(t)$ is driven by the time variation of the flux of electric displacement $\mathbf{d}$ and by the flux of the *conduction current* $\boldsymbol{\mathcal{j}}$ through the contour,

$$\int_{\partial s(t)} \boldsymbol{\mathcal{H}}\cdot\mathbf{s}\,dl = \frac{d}{dt}\int_{s(t)} \mathbf{d}\cdot\mathbf{n}\,ds + \int_{s(t)} \boldsymbol{\mathcal{j}}\cdot\mathbf{n}\,ds\,, \tag{1.12}$$

where $s(t)$ is any moving surface with boundary $\partial s(t)$, $\mathbf{s}$ is the unit tangent to the contour and $\mathbf{n}$ is the unit surface normal oriented by the contour tangent $\mathbf{s}$.

From standard arguments involving the arbitrariness of the control surface and Stoke's theorem we obtain Ampère's law in local form and the associated interface condition,

$$\nabla\times\boldsymbol{\mathcal{H}} = \overset{*}{\mathbf{d}} + \boldsymbol{\mathcal{j}}\,, \qquad \mathbf{n}\times[\![\boldsymbol{\mathcal{H}}]\!] = \boldsymbol{\kappa}\,, \tag{1.13}$$

where $\boldsymbol{\kappa}$ is a surface conduction current density and $\overset{*}{()}$ is the flux derivative introduced in (1.4).

From the definition of the magnetomotive intensity $\boldsymbol{\mathcal{H}} \equiv \mathbf{h} - \dot{\mathbf{x}}\times\mathbf{d}$ and the expression of the flux derivative (1.4) the pointwise form of Maxwell-Ampère's equation (1.13) is equivalent to the more usual formulation[4],

$$\nabla\times\mathbf{h} = \frac{\partial \mathbf{d}}{\partial t} + \mathbf{j}\,, \qquad \mathbf{n}\times[\![\mathbf{h}]\!] + (\mathbf{n}\cdot\dot{\mathbf{x}})\,[\![\mathbf{d}]\!] = \boldsymbol{\kappa}\,; \qquad \mathbf{j} \equiv \boldsymbol{\mathcal{j}} + q\dot{\mathbf{x}}\,, \tag{1.14}$$

where $\mathbf{j}$ is the total current density, which combines the conduction current density and the convection of electric charges. The interface condition accounts for the continuity of the normal component of $\mathbf{d}$ (1.11).

Finaly, one can verify that the combination of Maxwell-Gauss' and Maxwell-Ampère's laws results in the conservation of electric charges: if we apply Maxwell-Ampère's law on the surface boundary $\partial v(t)$ of an arbitrary control volume $v(t)$, the circulation of $\boldsymbol{\mathcal{H}}$ cancels out (if one cuts the surface boundary $\partial v(t)$ in two parts, they each have opposite circulation of $\boldsymbol{\mathcal{H}}$ on their line boundary). Using Gauss's law, the flux of the electric displacement through $\partial v(t)$ is replaced by the volume integral of electric charges and the charge conservation equation in integral form is obtained,

$$\frac{d}{dt}\int_{v(t)} q\,ds + \int_{s(t)} \boldsymbol{\mathcal{j}}\cdot\mathbf{n}\,ds = 0\,, \tag{1.15}$$

or in local form,

$$\dot{q} + q\nabla\cdot\dot{\mathbf{x}} + \nabla\cdot\boldsymbol{\mathcal{j}} = 0\,, \qquad \text{and equivalently} \qquad \frac{\partial q}{\partial t} + \nabla\cdot\mathbf{j} = 0\,. \tag{1.16}$$

3 It was shown by Minkowski that the magnetomotive intensity $\boldsymbol{\mathcal{H}}$ is the relevant quantity to consider for moving media.

4 Should surface electric charges be considered, they should be added to the right handside of the interface condition.

### 1.2.2 *The electromagnetic field principle*

A second principle of electromagnetism is based on the primitive concept of an electromagnetic field $(\boldsymbol{e}, \mathbf{b})$ behaving according to two laws often referred to as Maxwell-Faraday's law and the no magnetic monopole law.

THE NO-MAGNETIC MONOPOLE LAW – also referred to as Maxwell-Thomson's equation – states the conservation of the flux of the magnetic field $\mathbf{b}$. In other terms, there are no local monopolar sources of magnetic field contained within an arbitrary moving control volume $v(t)$,

$$\int_{\partial v(t)} \mathbf{b}\cdot\mathbf{n}\,ds = 0\,, \tag{1.17}$$

where as introduced before $\partial v(t)$ is the closed surface boundary of $v(t)$ and $\mathbf{n}$ is the outward unit normal to the surface.

Using the standard arguments introduced before, the pointwise form of Maxwell-Thomson's equation then writes

$$\boldsymbol{\nabla}\cdot\mathbf{b} = 0\,, \qquad \mathbf{n}\cdot[\![\mathbf{b}]\!] = 0\,. \tag{1.18}$$

MAXWELL-FARADAY'S LAW states that the circulation of the electromotive intensity $\boldsymbol{\mathcal{e}} \equiv \boldsymbol{e} + \dot{\mathbf{x}}\times\mathbf{b}$[5] on a closed contour $\partial s(t)$ balances the time variations of the flux of the magnetic field $\mathbf{b}$ through the enclosed surface $s(t)$,

$$\int_{\partial s(t)} \boldsymbol{\mathcal{e}}\cdot\mathbf{s}\,dl = -\frac{d}{dt}\int_{s(t)} \mathbf{b}\cdot\mathbf{n}\,ds\,. \tag{1.19}$$

Here again, $\mathbf{n}$ is the outward pointing normal to the surface. $\mathbf{s}$ is the tangent to the contour $\partial s(t)$ oriented according to the right hand rule.

From arguments similar to those used with Maxwell-Gauss' law, Maxwell-Faraday's induction law transforms in pointwise form into

$$\boldsymbol{\nabla}\times\boldsymbol{\mathcal{e}} = -\overset{*}{\mathbf{b}}\,, \qquad \mathbf{n}\times[\![\boldsymbol{\mathcal{e}}]\!] = 0\,, \tag{1.20}$$

where $\overset{*}{()}$ is the flux derivative introduced in (1.4).

From the expression of the electromotive intensity $\boldsymbol{\mathcal{e}}$ and the flux derivative expression (1.4), the pointwise form of Maxwell-Faraday's law can also be expressed in the more usual form,

$$\boldsymbol{\nabla}\times\boldsymbol{e} = -\frac{\partial\mathbf{b}}{\partial t}\,, \qquad \mathbf{n}\times[\![\boldsymbol{e}]\!] - (\mathbf{n}\cdot\dot{\mathbf{x}})\,[\![\mathbf{b}]\!] = 0\,. \tag{1.21}$$

As a final important comment: applying the divergence operator to the second form of Maxwell-Faraday's law (1.21), one gets $\frac{\partial}{\partial t}(\boldsymbol{\nabla}\cdot\mathbf{b}) = 0$. As a consequence, $\boldsymbol{\nabla}\cdot\mathbf{b}$ is a constant in time, function of the space variable $\mathbf{x}$ only. The only element that the no-monopole law adds is the initial condition $\boldsymbol{\nabla}\cdot\mathbf{b} = 0$ everywhere. As a

5 It was shown by Minkowski that the electromotive intensity $\boldsymbol{\mathcal{e}}$ is the relevant quantity to consider for moving media.

result, *the no-monopole law is not to be viewed as an additional governing equation but rather as an initial (or gauge) condition*. For that reason, Kovetz, 2000 (§8.) mentions that Maxwell-Faraday's law and the no-monopole law should be viewed as a single principle of conservation of magnetic flux that includes a governing equation and a gauge.

ELECTROMAGNETIC POTENTIALS An *electric scalar potential* $\phi$ and a *magnetic vector potential* $\mathbf{a}$ can conveniently be defined so that the two previous no monopole and Maxwell-Ampère laws are automatically enforced, setting

$$\begin{aligned} &\boldsymbol{e} \equiv -\boldsymbol{\nabla}\phi - \frac{\partial \mathbf{a}}{\partial t}\,, && [\![\phi]\!] - (\mathbf{n}\cdot\dot{\mathbf{x}})(\mathbf{n}\cdot[\![\mathbf{a}]\!]) = 0\,; \\ &\mathbf{b} \equiv \boldsymbol{\nabla}\times\mathbf{a}\,, && \mathbf{n}\times[\![\mathbf{a}]\!] = \mathbf{0}\,. \end{aligned} \tag{1.22}$$

The potentials $(\phi, \mathbf{a})$ thus defined are not-unique. A *gauge condition* – such as the Coulomb gauge $\boldsymbol{\nabla}\cdot\mathbf{a} = 0$ for instance – needs to be additionally given to ensure uniqueness of the fields. The details leading to the boundary conditions on the potentials $(\phi, \mathbf{a})$ can be found in Kovetz, 2000 (§10.).

### 1.2.3 *Aether frame principle*

The *aether frame principle* postulates the existence of a *Euclidian inertial* frame in which the electromagnetic field $(\boldsymbol{e}, \mathbf{b})$ and the charge and current potentials $(\mathbf{d}, \mathbf{h})$ are linked via the relationship

$$\begin{aligned} &\mathbf{d} = \epsilon_0 \boldsymbol{e} + \mathbf{p}\,, \\ &\mathbf{h} = \frac{1}{\mu_0}\mathbf{b} - \mathbf{m}\,, \end{aligned} \tag{1.23}$$

where $\epsilon_0$ is the electric permittivity of vacuum and $\mu_0$ is the magnetic permeability of vacuum. The *polarization* $\mathbf{p}$ and the *magnetization* $\mathbf{m}$[6] traduce a material response[7] to the electromagnetic field $(\boldsymbol{e}, \mathbf{b})$. In vacuum, $\mathbf{p} = \mathbf{m} = 0$.

### 1.2.4 *Conservation of mass*

A first principle of mechanics is the conservation of mass, which states that the mass contained within a material control volume $v(t)$ is preserved,

$$\frac{d}{dt}\int_{v(t)} \rho\, dv = 0\,. \tag{1.24}$$

Applying the transport theorem yields the pointwise form of the equation,

$$\dot{\rho} + \rho(\boldsymbol{\nabla}\cdot\dot{\mathbf{x}}) = 0\,. \tag{1.25}$$

6 The magnetization $\mathbf{m}$ is also referred to as the *Minkowski magnetization*.

7 The polarization and magnetization create effects similar to electric currents and charges, usually referred to as bound charges and currents – as opposed to the free charges and currents $q$ and $\boldsymbol{\mathcal{j}}$.

From this mass equation, we straightforwardly get an expression for $\dot{\rho}$ that proves very useful in the following: $\dot{\rho} = -\rho \mathbf{I} : (\dot{\mathbf{x}} \boldsymbol{\nabla})$[8]. Because all interfaces considered here are material interfaces – no flow of particles and mass through the interfaces – there is no jump condition associated to the mass conservation principle.

### 1.2.5 *Conservation of linear momentum*

A second mechanical principle is the conservation of linear momentum, which generalized for an electromagnetic-mechanical problem.

> The benefit of the following formulation[a] based on Kovetz, 2000 is that *it makes no postulate on the form of the forces* induced by electromagnetic effects. As a result, it avoids the confusion generated by the multiplicity of electromagnetic force expressions (albeit often equivalent) used in the literature.
>
> *a* Also see Steigmann, 2009 for a detailed account of the formulation by Kovetz, 2000.

The formulation postulates an unknown *generalized electro-magneto-mechanical linear momentum density* $\mathbf{g}$ whose rate of variation depends on known *external body force distributions* $\mathbf{f}$[9] – typically gravity – and on a flux of *generalized traction forces* $\mathbf{t}$ on the boundary of an arbitrary material control volume $v(t)$,

$$\frac{d}{dt}\int_{v(t)} \rho \mathbf{g} dv = \int_{v(t)} \rho \mathbf{f} dv + \int_{\partial v(t)} \mathbf{t} ds \, . \tag{1.26}$$

In doing so, we assume that the electro-magnetic effects are correctly described by surface forces distributed across the entire body. Following Cauchy's theorem[10], the traction $\mathbf{t}$ depends linearly on the normal $\mathbf{n}$ at an interface and we introduce the *generalized Cauchy stress* $\boldsymbol{\sigma}$ defined by

$$\mathbf{t} \equiv \mathbf{n} \cdot \boldsymbol{\sigma} \, . \tag{1.27}$$

As $\mathbf{t}$ may include both mechanical and electromagnetic surface forces, the total Cauchy stress $\boldsymbol{\sigma}$ also mixes both electromagnetic and mechanical stresses.

> Note the *generalized density of momentum* $\rho \mathbf{g}$, which *for an electromagnetic-mechanical system does not reduce to the momentum density of the solid* $\rho \dot{\mathbf{x}}$ *only*. The electro-magnetic fields (photons) also possess momentum to account for. Hence the momentum density $\rho \mathbf{g}$, which is unknown for now but whose *expression will later be derived* in the form of a constitutive relation from thermodynamic arguments; and similarly for the total stress $\boldsymbol{\sigma}$.

Localization of the linear momentum balance principle provides,

$$\rho \dot{\mathbf{g}} = \boldsymbol{\nabla} \cdot \boldsymbol{\sigma} + \rho \mathbf{f} \, , \qquad \mathbf{n} \cdot [\![ \boldsymbol{\sigma} ]\!] = \mathbf{t}_m \, , \tag{1.28}$$

where $\mathbf{t}_m$ in the jump condition models a surface traction applied at the interface.

8 The double tensor contraction ":" introduced is defined as $\mathbf{a} : \mathbf{b} \equiv a_{ij} b_{ij}$.

9 Note that the body force distribution $\mathbf{f}$ is per unit volume.

10 Cauchy's theorem is based on the postulate that the traction $\mathbf{t}$ depends only on the normal $\mathbf{n}$ to the interface, that is only on its orientation (in addition to position and time).

### 1.2.6 *Conservation of angular momentum*

Lastly for mechanical principles, the conservation of angular momentum applied to an arbitrary control material control volume $v(t)$ and generalized to electro-magneto-mechanical systems writes[11]

$$\frac{d}{dt}\int_{v(t)} \mathbf{x}\wedge\rho\mathbf{g}dv = \int_{v(t)} \mathbf{x}\wedge\rho\mathbf{f}dv + \int_{\partial v(t)} \mathbf{x}\wedge\mathbf{t}ds\ , \tag{1.29}$$

where one can notice the contribution $\mathbf{x}\wedge\rho\mathbf{g}$ of the generalized momentum density. Localization provides,

$$\rho\dot{\mathbf{x}}\wedge\mathbf{g} = \boldsymbol{\sigma} - \boldsymbol{\sigma}^{\mathsf{T}}\ . \tag{1.30}$$

Here again there is no associated interface condition because all interface propagate at the speed of the material. Further the model does not account for surface torques.

### 1.2.7 *First principle of thermodynamic*

The first principle of thermodynamics is the conservation of energy,

$$\begin{aligned}\frac{d}{dt}\int_{v(t)} \rho\varepsilon dv = &\int_{v(t)} \rho\mathbf{f}\cdot\dot{\mathbf{x}}dv + \int_{\partial v(t)} \mathbf{t}\cdot\dot{\mathbf{x}}ds\\ &+ \int_{v(t)} \rho r dv + \int_{\partial v(t)} (-\mathbf{q})\cdot\mathbf{n}ds\\ &+ \int_{\partial v(t)} (-\boldsymbol{e}\times\boldsymbol{\mathcal{h}})\cdot\mathbf{n}ds\ .\end{aligned} \tag{1.31}$$

It balances the rate of change of the specific[12] total energy $\varepsilon$ (i.e. of the solid and of the electromagnetic field) contained within the control volume $v(t)$ by the power supplied externally. $r$ is the rate of heating per unit mass[13] – or specific rate of heating – and $\mathbf{q}$[14] is the surface heat flux lost to the surroundings (i.e. pointing outward).

> It is at this level – the energy balance – that the coupling between electromagnetism and thermomechanics is introduced in the formalism of Kovetz, 2000, via the postulate of a flux of electromagnetic energy $\boldsymbol{e}\times\boldsymbol{\mathcal{h}}$, also called Poynting's vector, leaving the control volume through its boundary $\partial v(t)$.[a].
>
> *a* See Kovetz, 2000 (§54.) for the motivations behing this postulate.

Using Cauchy's tetrahedron relation $\mathbf{t} = \mathbf{n}\cdot\boldsymbol{\sigma}$ and the divergence theorem, the pointwise form of the energy balance is obtained, together with an interface condition:

$$\begin{aligned}&\rho\dot{\varepsilon} = \rho(\mathbf{f}\cdot\dot{\mathbf{x}} + r) + \boldsymbol{\nabla}\cdot\left(\boldsymbol{\sigma}\cdot\dot{\mathbf{x}} - \mathbf{q} - \boldsymbol{e}\times\boldsymbol{\mathcal{h}}\right),\\ &\mathbf{n}\cdot\left[\!\left[-\boldsymbol{\sigma}\cdot\dot{\mathbf{x}} + \mathbf{q} + \boldsymbol{e}\times\boldsymbol{\mathcal{h}}\right]\!\right] = 0\ .\end{aligned} \tag{1.32}$$

11 The wedge product of two vectors $\mathbf{a}$ and $\mathbf{b}$ is defined as: $\mathbf{a}\wedge\mathbf{b} \equiv \mathbf{a}\mathbf{b} - \mathbf{b}\mathbf{a}$.
12 By *specific* we mean *per unit mass*.
13 More generally $r$ could be any rate of external supply of energy.
14 The vector heat flux $\mathbf{q}$ is not to be confused with the scalar charge density $q$.

Accounting for the jump conditions on $\boldsymbol{e}$ and $\boldsymbol{h}$, the energy interface condition further becomes,

$$-\mathbf{n}\cdot\left[\!\left[\boldsymbol{\sigma}\cdot\dot{\mathbf{x}}\right]\!\right]+\mathbf{n}\cdot\left[\!\left[\mathbf{q}\right]\!\right]+\boldsymbol{\kappa}\cdot(\mathbf{n}\times\boldsymbol{e})=0\,. \tag{1.33}$$

### 1.2.8 *Second principle of thermodynamic*

The second principle of thermodynamics dictates the sens of evolution of the system stating that the rate of change of the overall entropy of an arbitrary material control volume $v(t)$ exceeds, or at best equals, the entropy supply of thermal origin: the volume and surface heating divided by the local *absolute temperature* $T$,

$$\frac{d}{dt}\int_{v(t)}\rho\vartheta dv\geqslant\int_{v(t)}\frac{\rho r}{T}dv+\int_{\partial v(t)}\mathbf{n}\cdot\left(\frac{-\mathbf{q}}{T}\right)ds\,, \tag{1.34}$$

where $\vartheta$ is the specific entropy distribution.

This expression is known as the Clausius-Duhem inequality and localization provides,

$$\rho\dot{\vartheta}\geqslant\frac{\rho r}{T}-\boldsymbol{\nabla}\cdot\left(\frac{\mathbf{q}}{T}\right)\,,\qquad\mathbf{n}\cdot\left[\!\left[\frac{\mathbf{q}}{T}\right]\!\right]\geqslant 0\,. \tag{1.35}$$

## 1.3 GOVERNING EQUATIONS IN THE REFERENCE CONFIGURATION

In the previous section the governing equations of the general electro-magneto-thermo-mechanical problem where derived in the current (Eulerian) configuration. In the present section, the governing equations are taken to the reference (Lagrangian) configuration, as the reference configuration fields that emerge will be useful in the following. These derivations are standard and can be found in Thomas and Triantafyllidis, 2009; Lax and Nelson, 1976; Kankanala and Triantafyllidis, 2004; Hutter, van de Ven, and Ursescu, 2006; Eringen and Maugin, 1990.

The kinematic relations used to relate volume, oriented line and oriented surface elements of the current configuration to those of the reference configuration are

$$dv=JdV\,,\qquad\mathbf{s}dl=(\mathbf{F}\cdot\mathbf{S})dL\,,\qquad\mathbf{n}ds=(J\mathbf{F}^{-T}\cdot\mathbf{N})dS\,, \tag{1.36}$$

with $\mathbf{F}$ the deformation gradient and $J$ its determinant. The volume and surface control volumes $v(t)$ and $s(t)$ of the current configuration turn into the fixed reference configuration volume $V$ and surface $S$.

### 1.3.1 *Electromagnetic conservation laws*

#### 1.3.1.1 *Maxwell-Gauss' law*

With the above kinematic relations, Maxwell-Gauss' law (1.10) transforms into

$$\int_{\partial V}\mathbf{D}\cdot\mathbf{N}dS=\int_{V}QdV\,, \tag{1.37}$$

where V is an arbitrary control volume of the reference configuration, $\mathbf{D}$ is the *reference configuration electric displacement* and Q is the *reference configuration volume charge density* defined by

$$\mathbf{D} \equiv J\mathbf{F}^{-1}\cdot\mathbf{d}\,, \qquad Q \equiv Jq\,. \tag{1.38}$$

Localization yields,

$$\boldsymbol{\nabla}\cdot\mathbf{D} = Q\,, \qquad \mathbf{N}\cdot[\![\mathbf{D}]\!] = 0\,. \tag{1.39}$$

Note the difference between $\nabla$, the gradient operator in the current configuration, and $\boldsymbol{\nabla}$, the gradient operator in the reference configuration.

#### 1.3.1.2 *Maxwell-Ampere's law*

The integral form of Maxwell-Ampère's law (1.12) becomes in the reference configuration,

$$\int_{\partial S} \mathscr{H}\cdot\mathbf{S}dL = \int_S \dot{\mathbf{D}}\cdot\mathbf{N}dS + \int_S \mathscr{J}\cdot\mathbf{N}dS\,, \tag{1.40}$$

where $\mathscr{H}$, respectively $\mathscr{J}$, is the reference configuration counterpart to the magnetomotive intensity $\mathscr{h}$, respectively electric current $\mathscr{j}$, in the reference configuration, defined as

$$\mathscr{H} \equiv \mathscr{h}\cdot\mathbf{F}\,, \qquad \mathscr{J} \equiv J\mathbf{F}^{-1}\cdot\mathscr{j}\,. \tag{1.41}$$

Localization provides,

$$\boldsymbol{\nabla}\times\mathscr{H} = \dot{\mathbf{D}} + \mathscr{J}, \qquad \mathbf{N}\times[\![\mathscr{H}]\!] = \mathbf{K}\,, \tag{1.42}$$

where $\mathbf{K} = J\mathbf{F}^{-1}\cdot\boldsymbol{\kappa}$ is the reference configuration current sheet .

#### 1.3.1.3 *No magnetic monopole law*

Transposition of the no magnetic monopole law (1.17) in reference configuration provides,

$$\int_{\partial V} \mathbf{B}\cdot\mathbf{N}dS = 0\,, \tag{1.43}$$

where the *reference configuration magnetic field* $\mathbf{B}$ is defined as,

$$\mathbf{B} \equiv J\mathbf{F}^{-1}\cdot\mathbf{b}\,. \tag{1.44}$$

Localization provides,

$$\boldsymbol{\nabla}\cdot\mathbf{B} = 0\,, \qquad \mathbf{N}\cdot[\![\mathbf{B}]\!] = 0\,. \tag{1.45}$$

#### 1.3.1.4 *Maxwell-Faraday's law*

For Maxwell-Faraday's law (1.19), the transposition to the reference configuration leads to,

$$\int_{\partial S} \mathscr{E}\cdot\mathbf{S}\,dL = -\frac{d}{dt}\int_S \mathbf{B}\cdot\mathbf{N}\,dS\,, \tag{1.46}$$

with the reference configuration magnetic field $\mathbf{B}$ introduced in (1.44) and the *reference configuration electromotive intensity* $\mathscr{E}$ defined as

$$\mathscr{E} \equiv \mathscr{e}\cdot\mathbf{F}\,. \tag{1.47}$$

Localization leads to the following pointwise Faraday's equation and associated interface condition in reference configuration

$$\boldsymbol{\nabla}\times\mathscr{E} = -\dot{\mathbf{B}}\,, \qquad \mathbf{N}\times[\![\mathscr{E}]\!] = \mathbf{0}\,. \tag{1.48}$$

#### 1.3.1.5 *Electromagnetic potentials*

The electromagnetic potentials derived in (1.22) can also be taken to the reference configuration and we get[15],

$$\begin{aligned} \mathscr{E} &= -\boldsymbol{\nabla}\Phi - \dot{\mathbf{A}}\,,\\ \mathbf{B} &= \boldsymbol{\nabla}\times\mathbf{A}\,, \end{aligned} \tag{1.49}$$

where the reference configuration electromotive intensity $\mathscr{E}$ and magnetic fields $\mathbf{B}$ were introduced earlier and the *reference configuration electric potential* $\Phi$ and the *reference configuration magnetic vector potential* $\mathbf{A}$ are defined by,

$$\begin{aligned} \Phi &\equiv \phi - \dot{\mathbf{x}}\cdot\mathbf{a}\,,\\ \mathbf{A} &\equiv \mathbf{a}\cdot\mathbf{F}\,. \end{aligned} \tag{1.50}$$

As in the current configuration, the reference configuration potential formulation (1.50) identically satisfies the reference configuration Maxwell-Faraday and No magnetic monopole law (1.48) and (1.45). (1.49) does not uniquely define $\mathbf{A}$ and $\Phi$: the necessity of a gauge condition applies to the reference configuration as well.

### 1.3.2 *Principles of mechanics*

#### 1.3.2.1 *Conservation of mass*

The conservation of mass (1.24) transposed to the reference configuration provides,

$$\frac{d}{dt}\int_V \rho_0\,dV = 0\,, \tag{1.51}$$

15 A derivation is provided in Appendix A.1

where the *mass density in reference configuration* $\rho_0$ is defined as

$$\rho_0 \equiv J\rho \,, \tag{1.52}$$

From the integral law follows the localized equation,

$$\dot{\rho}_0 = 0 \,. \tag{1.53}$$

#### 1.3.2.2 *Conservation of linear momentum*

The linear momentum balance (1.26) transforms into,

$$\frac{d}{dt}\int_V \rho_0 \mathbf{g} dv = \int_V \rho_0 \mathbf{f} dv + \int_{\partial V} \mathbf{T} dS \,, \tag{1.54}$$

where we introduce the *surface traction in the reference configuration* $\mathbf{T}$ and the *generalized first Piola-Kirchhoff stress* $\boldsymbol{\Pi}$ – following from application of Nanson's formula $(1.36)_3$ and the Cauchy stress definition (1.27) –,

$$\mathbf{T} \equiv \mathbf{t}\frac{ds}{dS} = \mathbf{N}\cdot\boldsymbol{\Pi} \,, \quad \boldsymbol{\Pi} \equiv J\mathbf{F}^{-1}\cdot\boldsymbol{\sigma} \,, \tag{1.55}$$

arriving at an analogous of Cauchy's tetrahedron relation in the reference configuration.

From localization the pointwise form of the conservation of linear momentum in reference configuration follows,

$$\rho_0 \dot{\mathbf{g}} = \boldsymbol{\nabla}\cdot\boldsymbol{\Pi} + \rho_0 \mathbf{f} \,, \qquad \mathbf{N}\cdot[\![\boldsymbol{\Pi}]\!] = \mathbf{T}_m \,, \tag{1.56}$$

where $\mathbf{T}_m$ is the external mechanical surface traction in reference configuration.

#### 1.3.2.3 *Conservation of angular momentum*

In the reference configuration, the integral form of the angular momentum balance (1.29) transposes to,

$$\frac{d}{dt}\int_V \mathbf{x} \wedge \rho_0 \mathbf{g} dV = \int_V \mathbf{x} \wedge \rho_0 \mathbf{f} dV + \int_{\partial V} \mathbf{x} \wedge \mathbf{T} dS \,, \tag{1.57}$$

and localization provides,

$$\rho_0 \dot{\mathbf{x}} \wedge \mathbf{g} = \mathbf{F}\cdot\boldsymbol{\Pi} - \boldsymbol{\Pi}^T\cdot\mathbf{F}^T \,. \tag{1.58}$$

### 1.3.3 *Principles of thermodynamics*

#### 1.3.3.1 *First principle of thermodynamic*

The first principle of thermodynamics (1.31) transforms into,

$$\begin{aligned}\frac{d}{dt}\int_V \rho_0 \varepsilon dV = &\int_V \rho_0 \mathbf{f}\cdot\dot{\mathbf{x}} dV + \int_{\partial V} \mathbf{T}\cdot\dot{\mathbf{x}} dS + \int_V \rho_0 r dV \\ &+ \int_{\partial V} (-\mathbf{Q})\cdot\mathbf{N} dS + \int_{\partial V} (-\mathscr{E}\times\mathscr{H})\cdot\mathbf{N} dS \,,\end{aligned} \tag{1.59}$$

which nicely points out the analog of Poynting's vector in the reference configuration $\mathscr{E}\times\mathscr{H}$[16] and introduces the *reference configuration heat flux* $\mathbf{Q}$[17],

$$\mathscr{E}\times\mathscr{H} = J\mathbf{F}^{-1}\cdot(\boldsymbol{e}\times\boldsymbol{h}) \,, \qquad \mathbf{Q} = J\mathbf{F}^{-1}\cdot\mathbf{q} \,. \tag{1.60}$$

Using the relation $\mathbf{T} = \mathbf{N}\cdot\mathbf{\Pi}$ and the divergence theorem, the pointwise form of the energy balance in reference configuration reads,

$$\begin{aligned} &\rho_0\dot{\varepsilon} = \rho_0(\mathbf{f}\cdot\dot{\mathbf{x}} + r) + \boldsymbol{\nabla}\cdot\left(\mathbf{\Pi}\cdot\dot{\mathbf{x}} - \mathbf{Q} - \mathscr{E}\times\mathscr{H}\right) \,, \\ &\mathbf{N}\cdot\left[\!\left[-\mathbf{\Pi}\cdot\dot{\mathbf{x}} + \mathbf{Q} + \mathscr{E}\times\mathscr{H}\right]\!\right] = 0 \,. \end{aligned} \tag{1.61}$$

Accounting for the jump conditions on $\mathscr{E}$ and $\mathscr{H}$, the energy interface condition yields,

$$-\mathbf{N}\cdot\left[\!\left[\mathbf{\Pi}\cdot\dot{\mathbf{x}}\right]\!\right] + \mathbf{N}\cdot\left[\!\left[\mathbf{Q}\right]\!\right] + \mathbf{K}\cdot(\mathbf{N}\times\mathscr{E}) = 0 \,. \tag{1.62}$$

#### 1.3.3.2 *Second principle of thermodynamic*

With the previous development, the second principle of thermodynamics (1.34) becomes in reference configuration

$$\frac{d}{dt}\int_V \rho_0\mathfrak{s}\,dV \geqslant \int_V \frac{\rho_0 r}{T}dV + \int_{\partial V}\mathbf{N}\cdot\left(\frac{-\mathbf{Q}}{T}\right)dS \,, \tag{1.63}$$

and localization provides,

$$\rho_0\dot{\mathfrak{s}} \geqslant \frac{\rho_0 r}{T} - \boldsymbol{\nabla}\cdot\left(\frac{\mathbf{Q}}{T}\right) \,, \qquad \mathbf{N}\cdot\left[\!\left[\frac{\mathbf{Q}}{T}\right]\!\right] \geqslant 0 \,. \tag{1.64}$$

## 1.4 CONSTITUTIVE RELATIONS AND DISSIPATION

### 1.4.1 *Completeness of the system of equations and constitutive relations*

As a summary, the governing equations of the problem are, in the current configuration,

| | | |
|---|---|---|
| Maxwell-Gauss | $\boldsymbol{\nabla}\cdot\mathbf{d} = q$ | (1 equation) |
| Maxwell-Faraday | $\boldsymbol{\nabla}\times\boldsymbol{e} = -\overset{*}{\dot{\mathbf{b}}}$ | (3 equations) |
| Maxwell-Ampère | $\boldsymbol{\nabla}\times\boldsymbol{h} = \boldsymbol{j} + \overset{*}{\dot{\mathbf{d}}}$ | (3 equations) |
| conservation of mass | $\dot{\rho} + \rho(\boldsymbol{\nabla}\cdot\dot{\mathbf{x}}) = 0$ | (1 equation) |
| linear mom. balance | $\rho\dot{\mathbf{g}} = \boldsymbol{\nabla}\cdot\boldsymbol{\sigma} + \rho\mathbf{f}$ | (3 equations) |
| angular mom. balance | $\rho\dot{\mathbf{x}}\wedge\mathbf{g} = \boldsymbol{\sigma} - \boldsymbol{\sigma}^T$ | (3 equations) |
| conservation of energy | $\rho\dot{\varepsilon} = \rho(\mathbf{f}\cdot\dot{\mathbf{x}} + r) + \boldsymbol{\nabla}\cdot\left(\boldsymbol{\sigma}\cdot\dot{\mathbf{x}} - \mathbf{q} - \boldsymbol{e}\times\boldsymbol{h}\right)$ | (1 equation) |

16 Note that despite the same notation "$\times$", the cross product operators acting on fields of the current and reference configuration are not the same (the two configurations have different base vectors). The shift from one operator to the other when changing configuration is detailed in Appendix A.2 (equation A.6).

17 The reference configuration heat flux $\mathbf{Q}$ is not to be confused with the reference configuration charge density $Q$.

The total count gives *15 governing equations*. The no-monopole law does not appear in the count: as explained in the comment accompanying (1.18) it only adds a gauge condition for the magnetic field $\mathbf{b}$ to the information on $\mathbf{b}$ included in Maxwell-Faraday's law. For that reason, it shall not be viewed as a governing equation.

The unknown independent fields of the problem are:

| | | | |
|---|---|---|---|
| $\mathbf{e}$ (3 unknowns), | $\mathbf{b}$ (3 unknowns), | $\mathbf{p}$ (3 unknowns), | $\mathbf{m}$ (3 unknowns), |
| $\boldsymbol{\mathcal{j}}$ (3 unknowns) | $q$ (1 unknown), | | |
| $\mathbf{g}$ (3 unknown), | $\rho$ (1 unknown), | $\mathbf{x}$ (3 unknowns), | $\boldsymbol{\sigma}$ (9 unknowns), |
| $\varepsilon$ (1 unknown), | $\mathcal{s}$ (1 unknown), | $T$ (1 unknown), | $\mathbf{q}$ (3 unknowns). |

The total amounts to *38 unknowns*. The electric displacement $\mathbf{d}$ and the h-field $\mathbf{h}$, and similarly the electromotive and magnetomotive intensities $\boldsymbol{\mathcal{e}}$ and $\boldsymbol{\mathcal{h}}$, are not counted as they are linked to $\mathbf{e}$, $\mathbf{b}$, $\mathbf{p}$ and $\mathbf{m}$ by the aether relations (not accounted for in the equations count here above) and the definitions of $\boldsymbol{\mathcal{e}}$ and $\boldsymbol{\mathcal{h}}$. The body forces $\mathbf{f}$ and the heat source $r$ are out of the count because they are external known quantities.

As a result, *15 governing equations* for *38 unknowns* means that the problem lacks *23 additional equations*. These are to be provided by *23 constitutive relations* that describe the material behavior and the links it imposes between the different variables. These constitutive equations are expected for the following variables,

| | | |
|---|---|---|
| for momentum | $\mathbf{g}$ | (3 equations) |
| for stress | $\boldsymbol{\sigma}$ | (6 equations) |
| for polarization | $\mathbf{p}$ | (3 equations) |
| for magnetization | $\mathbf{m}$ | (3 equations) |
| for heat-flux | $\mathbf{q}$ | (3 equations) |
| for conduction currents | $\boldsymbol{\mathcal{j}}$ | (3 equations) |
| for energy | $\varepsilon$ | (1 equation) |
| for entropy | $\mathcal{s}$ | (1 equation) |

This amounts to the *23 equations* expected. Note that only 6 equations are expected for stress given the angular momentum balance that links three stress components to the others.

The *constitutive relations* are to be given as hypotheses on the material behavior, be them guessed or based on experimental measurements. However they cannot be any: they need to obey *restrictions* set by the physics. These restrictions are applied hereafter. Some arise from the application of the second principle of thermodynamics – these are subsequently derived using the Coleman and Noll, 1963 method, as in Kovetz, 2000 –, others are due to the angular momentum balance.

### 1.4.2 *Restrictions from the second principle of thermodynamics*

In order to derive the restrictions on the constitutive relations set by the second principle of thermodynamics, the Coleman and Noll method first dictates a rearrangement of the Clausius-Duhem inequality. Second, it is convenient to introduce a specific free energy $\psi$ and work with this last constitutive variable instead of the total energy $\varepsilon$. Third, assumptions can be made on the set of thermodynamic state variables of the problem according to the material behavior one wishes to consider. Finally, mathematical arguments yield the restrictions on the constitutive relations in the form of equations linking the different constitutive variables and the state variables of the problem. These steps followed hereafter are all part of the Coleman and Noll, 1963 method.

REARRANGING THE CLAUSIUS-DUHEM INEQUALITY The material behavior – and thus the constitutive equations – should be independent of the external loads to the problem. As a result, in order to find the constitutive restrictions set by the second principle of thermodynamics, one first needs take out the body force and heat supply terms $\rho\mathbf{f}$ and $\rho r$ from (1.64). This is done by expressing $\rho\mathbf{f}$ and $\rho r$ with respect to the other variables of the problem, based on a rearrangement of the linear momentum balance (1.28) and energy balance (1.32). We get for $\rho\mathbf{f}$,

$$\rho\mathbf{f} = \rho\dot{\mathbf{g}} - \boldsymbol{\nabla}\cdot\boldsymbol{\sigma} \,, \tag{1.65}$$

and for $\rho r$,

$$\rho r = \rho\dot{\varepsilon} - \rho\dot{\mathbf{g}}\cdot\dot{\mathbf{x}} + \boldsymbol{\nabla}\cdot\mathbf{q} + \boldsymbol{\nabla}\cdot(\boldsymbol{e}\times\boldsymbol{\mathcal{h}}) - \sigma^{\mathsf{T}} : (\dot{\mathbf{x}}\boldsymbol{\nabla}) \,. \tag{1.66}$$

This last expression accounts for the introduction of the above expression for $\rho\mathbf{f}$ in the energy equation.

The Clausius-Duhem inequality (1.64) is then multiplied by $T > 0$. The term $\boldsymbol{\nabla}\cdot(-\mathbf{q}/T)$ is expanded and $\rho r$ is replaced by its expression (1.66), yielding,

$$\rho\dot{\jmath}T - \rho\dot{\varepsilon} + \rho\dot{\mathbf{g}}\cdot\dot{\mathbf{x}} - \boldsymbol{\nabla}\cdot(\boldsymbol{e}\times\boldsymbol{\mathcal{h}}) + \sigma^{\mathsf{T}} : (\dot{\mathbf{x}}\boldsymbol{\nabla}) - \frac{\mathbf{q}}{T}\cdot(T\boldsymbol{\nabla}) \geqslant 0 \,. \tag{1.67}$$

The computation of the divergence of Poynting's vector, calling to Maxwell's laws in the process, provides (see Kovetz, 2000),

$$\begin{aligned} -\boldsymbol{\nabla}\cdot(\boldsymbol{e}\times\boldsymbol{\mathcal{h}}) = {} & \boldsymbol{\mathcal{j}}\cdot\boldsymbol{e} - \mathbf{p}\cdot\dot{\boldsymbol{e}} - \boldsymbol{m}\cdot\dot{\mathbf{b}} + \epsilon_0(\mathbf{e}\times\mathbf{b})\cdot\ddot{\mathbf{x}} \\ & + \left[\left(\epsilon_0\mathbf{e}\cdot\mathbf{e} + \frac{1}{\mu_0}\mathbf{b}\cdot\mathbf{b} + \boldsymbol{e}\cdot\mathbf{p} - \boldsymbol{m}\cdot\mathbf{b} - \epsilon_0(\mathbf{e}\times\mathbf{b})\cdot\dot{\mathbf{x}}\right)\mathbf{I}\right. \\ & \left. - \epsilon_0\boldsymbol{e}\mathbf{e} - \frac{1}{\mu_0}\mathbf{b}\mathbf{b} - \boldsymbol{e}\mathbf{p} + \boldsymbol{m}\mathbf{b} - \epsilon_0(\mathbf{e}\times\mathbf{b})\dot{\mathbf{x}}\right] : (\dot{\mathbf{x}}\boldsymbol{\nabla}) \\ & + \frac{\mathrm{d}}{\mathrm{d}t}\left[\frac{\epsilon_0}{2}\boldsymbol{e}\cdot\boldsymbol{e} + \frac{1}{2\mu_0}\mathbf{b}\cdot\mathbf{b} + \boldsymbol{e}\cdot\mathbf{p} - \epsilon_0(\mathbf{e}\times\mathbf{b})\cdot\dot{\mathbf{x}}\right] \,, \end{aligned} \tag{1.68}$$

where we introduced the *Lorentz magnetization* defined as,

$$\boldsymbol{m} \equiv \mathbf{m} + \dot{\mathbf{x}}\times\mathbf{p} \,. \tag{1.69}$$

SPECIFIC FREE ENERGY POSTULATE Instead of working with the total specific energy of the continuum $\varepsilon$, we introduce the *specific free energy of the solid* $\psi$ defined in Kovetz, 2000,[18]

$$\psi \equiv \varepsilon - T\mathcal{s} - \mathbf{g}\cdot\dot{\mathbf{x}} + \frac{1}{2}\dot{\mathbf{x}}\cdot\dot{\mathbf{x}} - \frac{1}{\rho}\left[\frac{\epsilon_0}{2}\boldsymbol{e}\cdot\boldsymbol{e} + \frac{1}{2\mu_0}\mathbf{b}\cdot\mathbf{b} + \boldsymbol{\mathcal{e}}\cdot\mathbf{p} - \epsilon_0(\boldsymbol{e}\times\mathbf{b})\cdot\dot{\mathbf{x}}\right] . \tag{1.70}$$

The material time derivative of $\psi$, accounting for the mass conservation equation (1.25) in the computation of $\dot{\rho}$, gives

$$\begin{aligned}\dot{\psi} = {} & \dot{\varepsilon} - \dot{T}\mathcal{s} - T\dot{\mathcal{s}} - \dot{\mathbf{g}}\cdot\dot{\mathbf{x}} - \mathbf{g}\cdot\ddot{\mathbf{x}} + \dot{\mathbf{x}}\cdot\ddot{\mathbf{x}} \\ & - \frac{1}{\rho}\frac{d}{dt}\left[\frac{\epsilon_0}{2}\boldsymbol{e}\cdot\boldsymbol{e} + \frac{1}{2\mu_0}\mathbf{b}\cdot\mathbf{b} + \boldsymbol{\mathcal{e}}\cdot\mathbf{p} - \epsilon_0(\boldsymbol{e}\times\mathbf{b})\cdot\dot{\mathbf{x}}\right] \\ & - \frac{1}{\rho}\mathbf{I} : (\dot{\mathbf{x}}\nabla)\left[\frac{\epsilon_0}{2}\boldsymbol{e}\cdot\boldsymbol{e} + \frac{1}{2\mu_0}\mathbf{b}\cdot\mathbf{b} + \boldsymbol{\mathcal{e}}\cdot\mathbf{p} - \epsilon_0(\boldsymbol{e}\times\mathbf{b})\cdot\dot{\mathbf{x}}\right] .\end{aligned} \tag{1.71}$$

Thus replacing for $\psi$ instead of $\varepsilon$ in the Clausius-Duhem inequality (1.67) now provides,

$$\begin{aligned}-\rho\dot{\psi} - \rho\mathcal{s}\dot{T} - (\rho\mathbf{g} - \rho\dot{\mathbf{x}} - \epsilon_0\boldsymbol{e}\times\mathbf{b})\cdot\ddot{\mathbf{x}} - \mathbf{p}\cdot\dot{\boldsymbol{\mathcal{e}}} - \boldsymbol{\mathcal{m}}\cdot\dot{\mathbf{b}} \\ + (\boldsymbol{\sigma}^T - \boldsymbol{\tau}^T) : (\dot{\mathbf{x}}\nabla) + \dot{\boldsymbol{\mathcal{J}}}\cdot\boldsymbol{\mathcal{e}} - \frac{\mathbf{q}}{T}\cdot(\nabla T) \geqslant 0 .\end{aligned} \tag{1.72}$$

In the computation of expression (1.72), many terms from the expression of $\dot{\psi}$ and $-\nabla\cdot(\boldsymbol{\mathcal{e}}\times\boldsymbol{\mathcal{h}})$ simplify or rearrange. The stress component $\boldsymbol{\tau}$ that we introduced to simplify the expression is defined as,

$$\begin{aligned}\boldsymbol{\tau} \equiv {} & \epsilon_0\left(\boldsymbol{e}\boldsymbol{e} - \frac{1}{2}(\boldsymbol{e}\cdot\boldsymbol{e})\mathbf{I}\right) + \frac{1}{\mu_0}\left(\mathbf{b}\mathbf{b} - \frac{1}{2}(\mathbf{b}\cdot\mathbf{b})\mathbf{I}\right) \\ & - \left(\mathbf{b}\boldsymbol{\mathcal{m}} - (\mathbf{b}\cdot\boldsymbol{\mathcal{m}})\mathbf{I}\right) + \mathbf{p}\boldsymbol{\mathcal{e}} + \dot{\mathbf{x}}\epsilon_0(\boldsymbol{e}\times\mathbf{b}) .\end{aligned} \tag{1.73}$$

THERMODYNAMIC STATE VARIABLES In the following, we limit our scope to material behaviors that are function of the set of *thermodynamic variables*:

$$\mathbf{F},\ \dot{\mathbf{x}},\ \boldsymbol{\mathcal{e}},\ \mathbf{b},\ T,\ \nabla T . \tag{1.74}$$

All constitutive variables $\mathbf{g}$, $\boldsymbol{\sigma}$, $\mathbf{p}$, $\mathbf{m}$, $\mathbf{q}$, $\dot{\boldsymbol{\mathcal{J}}}$, $\psi$ and $\mathcal{s}$ are consequently a priori functions of this set of state variables. These include $\dot{\mathbf{x}}$ because for consistency with classical thermo-mechanics $\mathbf{g}$ is expected to reduce to $\dot{\mathbf{x}}$ in the absence of an electromagnetic field. More advanced material behaviors – not treated here – may be considered by adding higher order gradients or time derivatives in the set of state variables. A set of internal state variables $\xi$ may also be introduced, as is done in Thomas and Triantafyllidis, 2009.

This choice of state variables yields in particular,

$$\psi = \psi(\mathbf{F},\ \dot{\mathbf{x}},\ \boldsymbol{\mathcal{e}},\ \mathbf{b},\ T,\ \nabla T,\ \xi) , \tag{1.75}$$

and using the chain rule, we have

$$\dot{\psi} = \frac{\partial\psi}{\partial\mathbf{F}} : \dot{\mathbf{F}} + \frac{\partial\psi}{\partial\dot{\mathbf{x}}}\cdot\ddot{\mathbf{x}} + \frac{\partial\psi}{\partial\boldsymbol{\mathcal{e}}}\cdot\dot{\boldsymbol{\mathcal{e}}} + \frac{\partial\psi}{\partial\mathbf{b}}\cdot\dot{\mathbf{b}} + \frac{\partial\psi}{\partial T}\dot{T} + \frac{\partial\psi}{\partial\nabla T}\cdot(\dot{\nabla T}) + \frac{\partial\psi}{\partial\xi}\cdot\dot{\xi} . \tag{1.76}$$

18 Note that in the absence of electromagnetic fields, $\mathbf{g}$ reduces to $\dot{\mathbf{x}}$ and $\psi$ to the Helmholtz specific free energy $\psi = u - T\eta$, with $u = \varepsilon - 1/2(\dot{\mathbf{x}}\cdot\dot{\mathbf{x}})$ the internal energy of the system, as expected from classical thermomechanics.

Replacing $\dot{\psi}$ by the above, the entropy inequality (1.72) finally becomes

$$\begin{aligned}\left[\boldsymbol{\sigma}^{\mathsf{T}}-\boldsymbol{\tau}^{\mathsf{T}}-\rho\frac{\partial\psi}{\partial\mathbf{F}}\cdot\mathbf{F}^{\mathsf{T}}\right]:(\dot{\mathbf{x}}\boldsymbol{\nabla})-\left[\rho\frac{\partial\psi}{\partial\dot{\mathbf{x}}}+\rho\mathbf{g}-\rho\dot{\mathbf{x}}-\epsilon_0\boldsymbol{e}\times\mathbf{b}\right]\cdot\ddot{\mathbf{x}}\\-\left[\rho\frac{\partial\psi}{\partial\boldsymbol{e}}+\mathbf{p}\right]\cdot\dot{\boldsymbol{e}}-\left[\rho\frac{\partial\psi}{\partial\mathbf{b}}+\boldsymbol{m}\right]\cdot\dot{\mathbf{b}}-\rho\left[\frac{\partial\psi}{\partial T}+\mathcal{s}\right]\dot{T}\\+\frac{\partial\psi}{\partial\boldsymbol{\nabla}T}:(\dot{\boldsymbol{\nabla}}T)-\rho\frac{\partial\psi}{\partial\xi}\cdot\dot{\xi}+\mathcal{J}\cdot\boldsymbol{e}-\frac{\mathbf{q}}{T}\cdot(\boldsymbol{\nabla}T)\geqslant 0\,.\end{aligned}\tag{1.77}$$

NECESSARY CONSTITUTIVE RELATIONS By the Coleman and Noll, 1963 principle, for any given thermodynamic state of the system $\{\,\mathbf{F},\ \dot{\mathbf{x}},\ \boldsymbol{e},\ \mathbf{b},\ T,\ \boldsymbol{\nabla}T,\ \xi\,\}$, the inequality (1.77) has to hold true for any admissible thermodynamic evolution of the system. The rates of evolution $\dot{\mathbf{x}}\boldsymbol{\nabla}$, $\dot{\boldsymbol{e}}$, $\dot{\mathbf{b}}$, $\dot{T}$, $(\dot{\boldsymbol{\nabla}}T)$ and $\ddot{\mathbf{x}}$ are mathematically unconstrained one to the others by the governing equations exposed earlier thus admissible thermodynamic processes can be designed where they each assume arbitrary values. Consequently, the terms that they multiply should all equal 0. This exhibits the *necessary constitutive equations* of the problem,

$$\begin{aligned}\boldsymbol{\sigma}&=\rho\mathbf{F}\cdot\left(\frac{\partial\psi}{\partial\mathbf{F}}\right)^{\mathsf{T}}+\epsilon_0\left(\boldsymbol{e}\boldsymbol{e}-\frac{1}{2}(\boldsymbol{e}\cdot\boldsymbol{e})\mathbf{I}\right)+\frac{1}{\mu_0}\left(\mathbf{b}\mathbf{b}-\frac{1}{2}(\mathbf{b}\cdot\mathbf{b})\mathbf{I}\right)\\&\quad-\left(\mathbf{b}\boldsymbol{m}-(\mathbf{b}\cdot\boldsymbol{m})\mathbf{I}\right)+\mathbf{p}\boldsymbol{e}+\dot{\mathbf{x}}\epsilon_0(\boldsymbol{e}\times\mathbf{b})\,,\\\mathbf{g}&=-\frac{\partial\psi}{\partial\dot{\mathbf{x}}}+\dot{\mathbf{x}}+\frac{1}{\rho}\epsilon_0(\boldsymbol{e}\times\mathbf{b})\,,\\\mathbf{p}&=-\rho\frac{\partial\psi}{\partial\boldsymbol{e}}\,,\qquad\boldsymbol{m}=-\rho\frac{\partial\psi}{\partial\mathbf{b}}\,,\qquad\mathcal{s}=-\frac{\partial\psi}{\partial T}\,,\qquad\frac{\partial\psi}{\partial\boldsymbol{\nabla}T}=0\,.\end{aligned}\tag{1.78}$$

*A few comments are in order:* First, it immediately arises from the Coleman and Noll method that given the definition (1.70) for $\psi$ and the chosen set of state variables (1.74), by the second principle of thermodynamics the free energy $\psi$ is independent of $\boldsymbol{\nabla}T$.

Second, with the set of state variables considered here, it is a constitutive equation for the Lorentz magnetization $\boldsymbol{m}$ introduced in (1.68) – not the Minkowski magnetization $\mathfrak{m}$ – that naturally arises. This argument is of paramount importance in Kovetz, 2000 in further establishing that $\psi$ is independent of $\dot{\mathbf{x}}$. Indeed, it is shown in Kovetz, 2000 that $\mathbf{p}$ and $\boldsymbol{m}$ are invariant under Galilean transformations and consequently independent of $\dot{\mathbf{x}}$. As a consequence, given the constitutive equations for $\mathbf{p}$ and $\boldsymbol{m}$, $\frac{\partial}{\partial\dot{\mathbf{x}}}\left(\frac{\partial\psi}{\partial\boldsymbol{e}}\right)=\frac{\partial}{\partial\dot{\mathbf{x}}}\left(\frac{\partial\psi}{\partial\mathbf{b}}\right)=0$. Permuting the derivatives implies $\frac{\partial\psi}{\partial\dot{\mathbf{x}}}$ is independent of $\boldsymbol{e}$ and $\mathbf{b}$: $\frac{\partial\psi}{\partial\dot{\mathbf{x}}}=\frac{\partial\psi}{\partial\dot{\mathbf{x}}}(\mathbf{F},\ \dot{\mathbf{x}},\ T,\ \boldsymbol{\nabla}T,\ \xi)$. In the case where $\boldsymbol{e}$ and $\mathbf{b}$ are zero (no electromagnetic field), the linear momentum density $\mathbf{g}$ is expected to reduce to $\dot{\mathbf{x}}$ for consistency with classical thermo-mechanics. By the constitutive relation $(1.78)_2$ for $\mathbf{g}$, this implies $\frac{\partial\psi}{\partial\dot{\mathbf{x}}}=0$ for $\boldsymbol{e}=\mathbf{b}=0$, and because $\frac{\partial\psi}{\partial\dot{\mathbf{x}}}$ is independent of $\boldsymbol{e}$ and $\mathbf{b}$, $\frac{\partial\psi}{\partial\dot{\mathbf{x}}}=0$ *always*. Consequently,

$$\psi=\psi(\mathbf{F},\ \boldsymbol{e},\ \mathbf{b},\ T,\ \xi)\qquad\text{and}\qquad\mathbf{g}=\dot{\mathbf{x}}+\frac{1}{\rho}\epsilon_0(\boldsymbol{e}\times\mathbf{b})\,.\tag{1.79}$$

With this expression for $\mathbf{g}$, we are now in a position to give a more concise than in (1.70) expression for the solid's free energy density

$$\begin{aligned}&\rho\psi(\mathbf{F},\boldsymbol{e},\mathbf{b},T,\xi)=\rho\varepsilon-\rho T\eta-\frac{\rho}{2}\dot{\mathbf{x}}\cdot\dot{\mathbf{x}}-\left[\frac{\epsilon_0}{2}\boldsymbol{e}\cdot\boldsymbol{e}+\frac{1}{2\mu_0}\mathbf{b}\cdot\mathbf{b}+\boldsymbol{e}\cdot\mathbf{p}\right]\;;\\&\textit{alternatively}\quad\rho\varepsilon=\rho\psi+\rho T\eta+\frac{\rho}{2}\dot{\mathbf{x}}\cdot\dot{\mathbf{x}}+\left[\frac{\epsilon_0}{2}\boldsymbol{e}\cdot\boldsymbol{e}+\frac{1}{2\mu_0}\mathbf{b}\cdot\mathbf{b}+\boldsymbol{e}\cdot\mathbf{p}\right]\;.\end{aligned}\tag{1.80}$$

The above expression has a clear physical interpretation: the solid's free energy density (per unit current volume) $\rho\psi$ is obtained from the corresponding total energy density $\rho\varepsilon$ of the continuum by subtracting the thermal contribution, the kinetic energy of the solid and the energy of the electromagnetic field with an additional Legendre transform between fields $\boldsymbol{e}$ and $\mathbf{p}$. Note that in vacuum $T=0$, $\dot{\mathbf{x}}=\mathbf{p}=\mathbf{0}$ and the total energy density per unit volume $\rho\varepsilon=\frac{1}{2}\left[\epsilon_0\boldsymbol{e}\cdot\boldsymbol{e}+\frac{1}{\mu_0}\mathbf{b}\cdot\mathbf{b}\right]$[19] such that $\rho\psi=0$, which motivates calling $\psi$ the specific free energy "of the solid".

Regarding the Cauchy stress expression $(1.78)_1$, one can observe that in the absence of an electromagnetic fields, the stress reduces to $\rho\mathbf{F}\cdot\left(\frac{\partial\psi}{\partial\mathbf{F}}\right)^T$ with $\psi$ reduced to the Helmoltz free energy[20] as is usual for classical thermomechanics. Another important point is that in the presence of an electromagnetic field, the $\rho\mathbf{F}\cdot\left(\frac{\partial\psi}{\partial\mathbf{F}}\right)^T$ term, which is often confusedly termed "mechanical" in the literature, is not necessarily purely mechanical given $\psi$ depends on $\mathbf{F}$ but may also depend on $\boldsymbol{e},\mathbf{b},T$ and $\xi$ as per (1.79) and previous developments.

As mentionned in Kankanala and Triantafyllidis, 2004: "*The contribution to the general stress measure that does not depend on the* $\mathbf{F}$ *derivative of the free energy is termed by some authors (e.g. Tiersten, 1964) as the "Maxwell stress"*". However, Kankanala and Triantafyllidis, 2004 also stress out "*Different choices of arguments of the free energy result in different Maxwell stresses*". For that reason, different authors have different expressions for the Maxwell-stress, which creates confusion. In order to avoid it, the aforementioned definition of the Maxwell-stress is not used in the sequel. The only Maxwell-stress tensor we may refer to is the *Maxwell-stress in vacuum*, given its unambiguous definition (e.g. see Griffiths, 2017):

$$\boldsymbol{\sigma}_{MW}=\epsilon_0\left(\boldsymbol{e}\boldsymbol{e}-\frac{1}{2}(\boldsymbol{e}\cdot\boldsymbol{e})\mathbf{I}\right)+\frac{1}{\mu_0}\left(\mathbf{b}\mathbf{b}-\frac{1}{2}(\mathbf{b}\cdot\mathbf{b})\mathbf{I}\right)\;.\tag{1.81}$$

To conclude with a summary, the *necessary constitutive relations* are:

$$\begin{aligned}&\psi=\psi(\mathbf{F},\boldsymbol{e},\mathbf{b},T,\xi)\;,\qquad\mathbf{g}=\dot{\mathbf{x}}+\frac{1}{\rho}\epsilon_0(\boldsymbol{e}\times\mathbf{b})\;,\\&\mathbf{p}=-\rho\frac{\partial\psi}{\partial\boldsymbol{e}}\;,\qquad\boldsymbol{m}=-\rho\frac{\partial\psi}{\partial\mathbf{b}}\;,\qquad\mathfrak{s}=-\frac{\partial\psi}{\partial T}\;,\\&\boldsymbol{\sigma}=\rho\mathbf{F}\cdot\left(\frac{\partial\psi}{\partial\mathbf{F}}\right)^T+\epsilon_0\left(\boldsymbol{e}\boldsymbol{e}-\frac{1}{2}(\boldsymbol{e}\cdot\boldsymbol{e})\mathbf{I}\right)+\frac{1}{\mu_0}\left(\mathbf{b}\mathbf{b}-\frac{1}{2}(\mathbf{b}\cdot\mathbf{b})\mathbf{I}\right)\\&\qquad\qquad-\left(\mathbf{b}\boldsymbol{m}-(\mathbf{b}\cdot\boldsymbol{m})\mathbf{I}\right)+\mathbf{p}\boldsymbol{e}+\dot{\mathbf{x}}\epsilon_0(\boldsymbol{e}\times\mathbf{b})\;.\end{aligned}\tag{1.82}$$

19 Note that in vacuum, the energy density per unit mass $\varepsilon$ is ill-defined (no mass) and $\rho\varepsilon$ represents an energy per unit volume, non-null despite $\rho=0$ because of the electromagnetic field's energy.

20 See footnote 18 associated to the free energy definition (1.70)

DISSIPATION AND SUFFICIENT CONSTITUTIVE RELATIONS Once the necessary constitutive relations established, from equation 1.72 now only remains the dissipation of the system

$$\mathscr{D} = -\rho\frac{\partial\psi}{\partial\xi}\cdot\dot{\xi} + \boldsymbol{\mathcal{j}}\cdot\boldsymbol{e} - \frac{\mathbf{q}}{T}\cdot(\nabla T) \geqslant 0\,. \tag{1.83}$$

At this point no further details can be given about a generalized *Ohm's law* for the conduction current density $\boldsymbol{\mathcal{j}}$ and a generalized *Fourier's law* for the heat flux $\mathbf{q}$, on how they depend on the thermodynamic state variables, other than (1.83) has to be satisfied by[21]

$$\boldsymbol{\mathcal{j}} = \boldsymbol{\mathcal{j}}(F, \boldsymbol{e}, \mathbf{b}, T, \nabla T, \xi)\,, \quad \mathbf{q} = \mathbf{q}(F, \boldsymbol{e}, \mathbf{b}, T, \nabla T, \xi)\,, \tag{1.84}$$

where it is assumed for simplicity that these vector fields are independent on $\dot{\mathbf{x}}$. The well known forms of these relations require further assumptions about linearity and decoupling between different physical mechanisms and will be discussed in Section 2.2.

### 1.4.3 *New form of the governing equations accounting for the constitutive relations*

With the expressions for $\boldsymbol{\sigma}$ and $\mathbf{g}$ now known from (1.82), the linear momentum and energy balances can be rewritten in more suitable forms.

LINEAR MOMENTUM BALANCE Based on calculation details given in Kovetz, 2000, the divergence of the Cauchy stress tensor $\boldsymbol{\sigma}$ and the time derivative of $\mathbf{g}$, both obtained in (1.82), have expressions

$$\begin{aligned}\nabla\cdot\boldsymbol{\sigma} &= \nabla\cdot\left(\rho F\cdot\left(\frac{\partial\psi}{\partial F}\right)^{T}\right) + \rho\frac{d}{dt}\left(\frac{1}{\rho}\epsilon_0(\boldsymbol{e}\times\mathbf{b})\right) + q\boldsymbol{e} + \boldsymbol{\mathcal{j}}\times\mathbf{b}\\ &\quad + \boldsymbol{m}\times(\nabla\times\mathbf{b}) + \boldsymbol{m}\cdot(\nabla\mathbf{b}) + \mathbf{p}\cdot(\nabla\boldsymbol{e}) + \overset{*}{\mathbf{p}}\times\mathbf{b}\,,\\ \dot{\mathbf{g}} &= \ddot{\mathbf{x}} + \frac{d}{dt}\left(\frac{1}{\rho}\epsilon_0(\boldsymbol{e}\times\mathbf{b})\right)\,.\end{aligned} \tag{1.85}$$

Replacing $\nabla\cdot\boldsymbol{\sigma}$ and $\dot{\mathbf{g}}$ by the above expressions in the linear momentum balance (1.28) provides,

$$\begin{aligned}\rho\ddot{\mathbf{x}} &= \nabla\cdot\left(\rho F\cdot\left(\frac{\partial\psi}{\partial F}\right)^{T}\right) + \rho\mathbf{f} + q\boldsymbol{e} + \boldsymbol{\mathcal{j}}\times\mathbf{b}\\ &\quad + \boldsymbol{m}\times(\nabla\times\mathbf{b}) + \boldsymbol{m}\cdot(\nabla\mathbf{b}) + \mathbf{p}\cdot(\nabla\boldsymbol{e}) + \overset{*}{\mathbf{p}}\times\mathbf{b}\,.\end{aligned} \tag{1.86}$$

21 For more details on the implication of the dissipation inequality on the possible expressions for $\boldsymbol{\mathcal{j}}$ and $\mathbf{q}$, the reader is referred to the very interesting discussion in Kovetz, 2000 (§57.).

The terms $\boldsymbol{\nabla}\cdot\left(\rho\mathbf{F}\cdot\left(\frac{\partial\psi}{\partial\mathbf{F}}\right)^{\mathsf{T}}\right)+\rho\mathbf{f}$ account for the mechanical forces applied to and in the material, but may also include additional electromagnetic contributions to the force given $\psi(\mathbf{F},\boldsymbol{e},\mathbf{b},T,\xi)$ by (1.82). The force term $q\boldsymbol{e}+\boldsymbol{j}\times\mathbf{b}$ is the Lorentz force generalization to continua (e.g. see Steigmann, 2009 or Kovetz, 2000). Finally, the remaining terms denote yet other forces developed due to the magnetization and polarization of a body placed in non uniform and time varying $\boldsymbol{e}$ and $\mathbf{b}$ fields[22]. It should be noted that up to here, no constitutive law has been given for $\psi$ and as such, the precise expression of the body forces that have electromagnetic origin remains unknown. It will likely be different from one material to another as they may have different constitutive behaviors. Only has been enforced up to know that the problem formulation be consistent with thermodynamics, which places constraints from the physics on the possible material behaviors and yields the body forces deriving from $\boldsymbol{\sigma}$ linked to $\psi$ through (1.82) and (1.86).

TEMPERATURE EQUATION Replacing $\rho\mathbf{f}$ using (1.65) in the energy equation (1.32) (as was done with the Clausius-Duhem inequality), one gets

$$\rho\dot{\varepsilon}=\rho r+\rho\dot{\mathbf{g}}\cdot\dot{\mathbf{x}}-\boldsymbol{\nabla}\cdot\mathbf{q}-\boldsymbol{\nabla}\cdot(\boldsymbol{e}\times\boldsymbol{\hbar})+\boldsymbol{\sigma}^{\mathsf{T}}:(\dot{\mathbf{x}}\boldsymbol{\nabla})\,. \tag{1.87}$$

From the definition of the specific free energy given by (1.80),

$$\begin{aligned}\rho\dot{\varepsilon}=\rho\dot{\psi}+\rho\dot{T}\mathfrak{z}+\rho T\dot{\mathfrak{z}}+\rho\dot{\mathbf{x}}\cdot\ddot{\mathbf{x}}+\left[\frac{\epsilon_0}{2}\mathbf{e}^2+\frac{1}{2\mu_0}\mathbf{b}^2+\boldsymbol{e}\cdot\mathbf{p}\right]\mathbf{I}:(\dot{\mathbf{x}}\boldsymbol{\nabla})\\+\frac{d}{dt}\left[\frac{\epsilon_0}{2}\mathbf{e}^2+\frac{1}{2\mu_0}\mathbf{b}^2+\boldsymbol{e}\cdot\mathbf{p}\right]\,.\end{aligned} \tag{1.88}$$

With the expression for $\mathbf{g}$ in (1.82),

$$\rho\dot{\mathbf{g}}\cdot\dot{\mathbf{x}}=\rho\ddot{\mathbf{x}}\cdot\dot{\mathbf{x}}+\frac{d}{dt}\Big[\epsilon_0(\boldsymbol{e}\times\mathbf{b})\cdot\dot{\mathbf{x}}\Big]-\epsilon_0(\boldsymbol{e}\times\mathbf{b})\cdot\ddot{\mathbf{x}}+\big[\epsilon_0(\boldsymbol{e}\times\mathbf{b})\cdot\dot{\mathbf{x}}\big]\mathbf{I}:(\dot{\mathbf{x}}\boldsymbol{\nabla})\,. \tag{1.89}$$

Integrating the above results together with the expression for the divergence of the Poynting vector given by (1.68), and the stress constitutive relation provided by (1.82), the energy equation results in,

$$\rho\dot{\psi}+\rho T\dot{\mathfrak{z}}=\rho r-\boldsymbol{\nabla}\cdot\mathbf{q}-\rho\dot{T}\mathfrak{z}+\boldsymbol{j}\cdot\boldsymbol{e}-\mathbf{p}\cdot\dot{\boldsymbol{e}}-\boldsymbol{m}\cdot\dot{\mathbf{b}}+\rho\frac{\partial\psi}{\partial\mathbf{F}}\cdot\mathbf{F}^{\mathsf{T}}:(\dot{\mathbf{x}}\boldsymbol{\nabla})\,. \tag{1.90}$$

Finally, since by the chain rule and the constitutive relations for $\mathfrak{z}$, $\mathbf{p}$ and $\boldsymbol{m}$,

$$\begin{aligned}\rho\dot{\psi}&=\rho\frac{\partial\psi}{\partial\mathbf{F}}\cdot\mathbf{F}^{\mathsf{T}}:(\dot{\mathbf{x}}\boldsymbol{\nabla})+\rho\frac{\partial\psi}{\partial\boldsymbol{e}}\cdot\dot{\boldsymbol{e}}+\rho\frac{\partial\psi}{\partial\mathbf{b}}\cdot\dot{\mathbf{b}}+\rho\frac{\partial\psi}{\partial T}\dot{T}\\&=\rho\frac{\partial\psi}{\partial\mathbf{F}}\cdot\mathbf{F}^{\mathsf{T}}:(\dot{\mathbf{x}}\boldsymbol{\nabla})-\mathbf{p}\cdot\dot{\boldsymbol{e}}-\boldsymbol{m}\cdot\dot{\mathbf{b}}-\rho\mathfrak{z}\dot{T}\,,\end{aligned} \tag{1.91}$$

the energy equation reduces to,

$$\boxed{\rho T\dot{\mathfrak{z}}=\rho r-\boldsymbol{\nabla}\cdot\mathbf{q}+\boldsymbol{j}\cdot\boldsymbol{e}\,.} \tag{1.92}$$

22 These may or may not balance other forces of electromagnetic origin from the $\psi$-derivative term.

### 1.4.4 *Restrictions from the angular momentum balance*

From the constitutive expression for $\mathbf{g}$ and $\boldsymbol{\sigma}$ in (1.82), application of the angular momentum balance (1.30) provides,

$$\mathbf{F}\cdot\left(\frac{\partial\psi}{\partial\mathbf{F}}\right)^{\mathsf{T}}-\left(\frac{\partial\psi}{\partial\mathbf{F}}\right)\cdot\mathbf{F}^{\mathsf{T}}+\mathbf{b}\frac{\partial\psi}{\partial\mathbf{b}}-\frac{\partial\psi}{\partial\mathbf{b}}\mathbf{b}+\boldsymbol{e}\frac{\partial\psi}{\partial\boldsymbol{e}}-\frac{\partial\psi}{\partial\boldsymbol{e}}\boldsymbol{e}=0\,. \tag{1.93}$$

To obtain this equation, the expressions of $\mathbf{p}$ and $\boldsymbol{m}$ in the stress expression where replaced by their constitutive expressions in (1.82).

From Kovetz, 2000 (§54.-56.), this expression combined to the mathematical theorem (1.9) imposes on the free specific energy functional $\psi(\mathbf{F},\boldsymbol{e},\mathbf{b},\mathsf{T},\xi)$:

$$\psi(\mathbf{F},\ \boldsymbol{e},\ \mathbf{b},\ \mathsf{T},\ \xi)=\psi(\mathbf{Q}\cdot\mathbf{F},\ \mathbf{Q}\cdot\boldsymbol{e},\ \mathbf{Q}\cdot\mathbf{b},\ \mathsf{T},\ \xi)\,, \tag{1.94}$$

for every orthogonal tensor $\mathbf{Q}$. From the polar decomposition theorem, the deformation gradient $\mathbf{F}$ can be expressed as $\mathbf{F}=\mathbf{R}\cdot\mathbf{U}$ (left polar decomposition), where $\mathbf{R}$ is proper orthogonal and $\mathbf{U}$ is symmetric positive definite, yielding for the previous expression:

$$\psi(\mathbf{F},\ \boldsymbol{e},\ \mathbf{b},\ \mathsf{T},\ \xi)=\psi(\mathbf{Q}\cdot\mathbf{R}\cdot\mathbf{U},\ \mathbf{Q}\cdot\boldsymbol{e},\ \mathbf{Q}\cdot\mathbf{b},\ \mathsf{T},\ \xi)\,, \tag{1.95}$$

for any $\mathbf{Q}\in SO(3)$, still. Choosing the particular case $\mathbf{Q}=\mathbf{R}^{\mathsf{T}}$ as $\mathbf{R}\in SO(3)$ and noting that $\mathbf{R}^{\mathsf{T}}\cdot\mathbf{R}=\mathbf{I}$ and $\mathbf{R}^{\mathsf{T}}=\mathbf{U}^{-1}\cdot\mathbf{F}^{\mathsf{T}}$:

$$\psi(\mathbf{F},\ \boldsymbol{e},\ \mathbf{b},\ \mathsf{T},\ \xi)=\psi(\mathbf{U},\ \mathbf{U}^{-1}\cdot\mathbf{F}^{\mathsf{T}}\cdot\boldsymbol{e},\ \mathbf{U}^{-1}\cdot\mathbf{F}^{\mathsf{T}}\cdot\mathbf{b},\ \mathsf{T},\ \xi)\,. \tag{1.96}$$

It follows that the specific free energy is constrained by the material frame indifferent principle to be a functional of the set of arguments $\mathbf{U}$, $\mathbf{U}^{-1}\cdot\mathbf{F}^{\mathsf{T}}\cdot\boldsymbol{e}$, $\mathbf{U}^{-1}\cdot\mathbf{F}^{\mathsf{T}}\cdot\mathbf{b}$, $\mathsf{T}$, $\xi$, or equivalently any combination of these arguments. This provides what Kovetz, 2000 refers to as the specific free energy *in reduced form*, for which two different possible expressions are proposed hereafter.

FIRST POSSIBLE COMBINATION OF ARGUMENTS One first combination is obtained by the left contraction of the first 3 arguments with $\mathbf{U}$ (since $\mathbf{U}$ is positive definite, it is uniquely related to $\mathbf{U}\cdot\mathbf{U}$), leading to

$$\psi=\hat{\psi}(\mathbf{C},\boldsymbol{\mathcal{E}},\tilde{\mathbf{B}},\mathsf{T},\xi)\,;\qquad \mathbf{C}\equiv\mathbf{F}^{\mathsf{T}}\cdot\mathbf{F}=\mathbf{U}\cdot\mathbf{U}\,,\quad \boldsymbol{\mathcal{E}}=\boldsymbol{e}\cdot\mathbf{F},\quad \tilde{\mathbf{B}}\equiv\mathbf{b}\cdot\mathbf{F}\,, \tag{1.97}$$

where we introduced the right Cauchy-Green deformation tensor $\mathbf{C}$ and the Lagrangean field $\tilde{\mathbf{B}}\equiv\mathbf{b}\cdot\mathbf{F}$ and one can recognize the Lagrangean electromotive intensity $\boldsymbol{\mathcal{E}}$. Note that the Lagrangean field $\tilde{\mathbf{B}}$ is not the Lagrangean magnetic field defined in section 1.3. This new functional $\hat{\psi}$ is linked to the original functional $\psi$ brought by the Coleman-Noll method by $\psi(\mathbf{F},\boldsymbol{e},\mathbf{b},\mathsf{T},\xi)=\hat{\psi}(\mathbf{C},\boldsymbol{\mathcal{E}},\mathbf{B},\mathsf{T},\xi)$. Consequently[23],

$$\frac{\partial\psi}{\partial\boldsymbol{e}}=\mathbf{F}\cdot\frac{\partial\hat{\psi}}{\partial\boldsymbol{\mathcal{E}}}\,,\qquad \frac{\partial\psi}{\partial\mathbf{b}}=\mathbf{F}\cdot\frac{\partial\hat{\psi}}{\partial\tilde{\mathbf{B}}}\,,\qquad \frac{\partial\psi}{\partial\mathbf{F}}=2\mathbf{F}\cdot\frac{\partial\hat{\psi}}{\partial\mathbf{C}}+\boldsymbol{e}\frac{\partial\hat{\psi}}{\partial\boldsymbol{\mathcal{E}}}+\mathbf{b}\frac{\partial\hat{\psi}}{\partial\tilde{\mathbf{B}}}\,, \tag{1.98}$$

and the constitutive relations written in terms of $\hat{\psi}$ follow:

23 The partial derivatives of $\psi$ are partial derivatives with respect to the variables $\mathbf{F},\boldsymbol{e},\mathbf{b},\mathsf{T},\xi$ while the partial derivatives for $\hat{\psi}$ are partial derivatives with respect to the variables $\mathbf{C},\boldsymbol{\mathcal{E}},\tilde{\mathbf{B}},\mathsf{T},\xi$.

$$\begin{aligned}
&\mathbf{p} = -\rho\mathbf{F}\cdot\frac{\partial\hat{\psi}}{\partial\boldsymbol{\mathscr{E}}}\,, \qquad \boldsymbol{m} = -\rho\mathbf{F}\cdot\frac{\partial\hat{\psi}}{\partial\tilde{\mathbf{B}}}\,, \qquad \mathscr{s} = -\frac{\partial\hat{\psi}}{\partial T}\,,\\
&\boldsymbol{\sigma} = 2\rho\mathbf{F}\cdot\frac{\partial\hat{\psi}}{\partial\mathbf{C}}\cdot\mathbf{F}^{T} + \epsilon_0\Big(\boldsymbol{e}\boldsymbol{e} - \frac{1}{2}(\boldsymbol{e}\cdot\boldsymbol{e})\mathbf{I}\Big) + \frac{1}{\mu_0}\Big(\mathbf{b}\mathbf{b} - \frac{1}{2}(\mathbf{b}\cdot\mathbf{b})\mathbf{I}\Big)\\
&\qquad\qquad - \Big(\boldsymbol{m}\mathbf{b} + \mathbf{b}\boldsymbol{m} - (\mathbf{b}\cdot\boldsymbol{m})\mathbf{I}\Big) + \dot{\mathbf{x}}\epsilon_0(\boldsymbol{e}\times\mathbf{b})\,.
\end{aligned} \tag{1.99}$$

SECOND POSSIBLE COMBINATION OF ARGUMENTS Another combination provides the set of arguments $\mathbf{C},\ \boldsymbol{e}\cdot\mathbf{F},\ J\mathbf{F}^{-1}\cdot\mathbf{b},\ T,\ \xi$, by multiplying $\tilde{\mathbf{B}}$ in the first formulation by $J \equiv \det(\mathbf{F}) = \det(\mathbf{U})$ and left-contracting with $\mathbf{C}^{-1}$, both uniquely related to $\mathbf{U}$. One recognizes the Lagrangian electromotive intensity $\boldsymbol{\mathscr{E}} = \boldsymbol{e}\cdot\mathbf{F}$ and the Lagrangian magnetic field $\mathbf{B} = J\mathbf{F}^{-1}\cdot\mathbf{b}$ (see Section 1.3). This leads to the functional,

$$\psi = \Psi(\mathbf{C},\ \boldsymbol{\mathscr{E}},\ \mathbf{B},\ T,\ \xi)\,; \qquad \mathbf{C} \equiv \mathbf{F}^{T}\cdot\mathbf{F}\,,\ \ \boldsymbol{\mathscr{E}} = \boldsymbol{e}\cdot\mathbf{F}\,,\ \ \mathbf{B} \equiv J\mathbf{F}^{-1}\cdot\mathbf{b}\,. \tag{1.100}$$

The new functional $\Psi$ is linked to the original functional $\psi$ brought by the Coleman-Noll method by $\psi(\mathbf{F}, \boldsymbol{e}, \mathbf{b}, T, \xi) = \Psi(\mathbf{C}, \boldsymbol{\mathscr{E}}, \mathbf{B}, T, \xi)$. Consequently[24],

$$\begin{aligned}
&\frac{\partial\psi}{\partial\boldsymbol{e}} = \mathbf{F}\cdot\frac{\partial\Psi}{\partial\boldsymbol{\mathscr{E}}}\,, \qquad \frac{\partial\psi}{\partial\mathbf{b}} = J\mathbf{F}^{-T}\cdot\frac{\partial\Psi}{\partial\mathbf{B}}\,,\\
&\frac{\partial\psi}{\partial\mathbf{F}} = 2\mathbf{F}\cdot\frac{\partial\Psi}{\partial\mathbf{C}} + \boldsymbol{e}\frac{\partial\Psi}{\partial\boldsymbol{\mathscr{E}}} + \left(\left(J\mathbf{F}^{-T}\cdot\frac{\partial\Psi}{\partial\mathbf{B}}\right)\cdot\mathbf{b}\right)\mathbf{F}^{-T} - \left(J\mathbf{F}^{-T}\cdot\frac{\partial\Psi}{\partial\mathbf{B}}\right)(\mathbf{F}^{-1}\cdot\mathbf{b})\,,
\end{aligned} \tag{1.101}$$

and the constitutive relations written in terms of $\Psi$ follow:

$$\begin{aligned}
&\mathbf{p} = -\rho\mathbf{F}\cdot\frac{\partial\Psi}{\partial\boldsymbol{\mathscr{E}}}\,, \qquad \boldsymbol{m} = -\rho J\mathbf{F}^{-T}\cdot\frac{\partial\Psi}{\partial\mathbf{B}}\,, \qquad \mathscr{s} = -\frac{\partial\Psi}{\partial T}\,,\\
&\boldsymbol{\sigma} = 2\rho\mathbf{F}\cdot\frac{\partial\Psi}{\partial\mathbf{C}}\cdot\mathbf{F}^{T} + \epsilon_0\Big(\boldsymbol{e}\boldsymbol{e} - \frac{1}{2}(\boldsymbol{e}\cdot\boldsymbol{e})\mathbf{I}\Big) + \frac{1}{\mu_0}\Big(\mathbf{b}\mathbf{b} - \frac{1}{2}(\mathbf{b}\cdot\mathbf{b})\mathbf{I}\Big) + \dot{\mathbf{x}}\epsilon_0(\boldsymbol{e}\times\mathbf{b})\,.
\end{aligned} \tag{1.102}$$

A COMMENT ON MATERIAL FRAME INDIFFERENCE: The principle of material frame indifference (or objectivity) is used in the literature to infer the reduced form of the specific free energy obtained above (e.g. see Dorfmann and Ogden, 2003).

The principle of material frame indifference places restrictions on the constitutive relations by imposing transformation requirements on the constitutive variables. The transformation considered is a Euclidian transformation,

$$\mathbf{x}' = \mathbf{Q}(t)\cdot\mathbf{x} + \mathbf{c}(t)\,, \quad t' = t\,, \tag{1.103}$$

24 The partial derivatives of $\psi$ are partial derivatives with respect to the variables $\mathbf{F}, \boldsymbol{e}, \mathbf{b}, T, \xi$ while the partial derivatives for $\Psi$ are partial derivatives with respect to the variables $\mathbf{C}, \boldsymbol{\mathscr{E}}, \mathbf{B}, T, \xi$.

where $\mathbf{Q}(t)$ is a time dependent orthogonal matrix and $\mathbf{c}(t)$ is an arbitrary time dependent vector. Quoting Tadmor, Miller, and Elliott, 2011 (Section 6.3.3), "*The basic postulate of the principle of material frame-indifference is that all variables for which constitutive relations are required must be objective tensors*". Our understanding is thus that the material frame indifference principle should apply to *all* variables for which constitutive relations are required, and thus that $\mathfrak{z}, \mathbf{p}, \boldsymbol{m}, \boldsymbol{\sigma}$ and $\mathbf{g}$ be objective i.e. transform into $\mathfrak{z}, \mathbf{Q}\cdot\mathbf{p}, \mathbf{Q}\cdot\boldsymbol{m}, \mathbf{Q}\cdot\boldsymbol{\sigma}\cdot\mathbf{Q}^T, \mathbf{Q}\cdot\mathbf{g}$ under any Euclidian transformation (1.103).

From Hutter, van de Ven, and Ursescu, 2006, under a Euclidian transformation, the electromagnetic fields transform according to,

$$\boldsymbol{e}' = \mathbf{Q}\cdot\boldsymbol{e}\ , \qquad \mathbf{b}' = \mathbf{Q}\cdot\mathbf{b}\ , \tag{1.104}$$

for $\mathbf{Q}$ proper orthogonal[25]. The deformation gradient transforms as $\mathbf{F}' = \mathbf{Q}\cdot\mathbf{F}$. Given the transformation law for $\boldsymbol{e}$ and $\boldsymbol{e} = \mathbf{e} + \dot{\mathbf{x}}\times\mathbf{b}$,

$$\mathbf{e}' = \mathbf{Q}\cdot\Big[\mathbf{e} - \big(\mathbf{Q}^T\cdot(\dot{\mathbf{Q}}\cdot\mathbf{x} + \dot{\mathbf{c}})\times\mathbf{b}\big)\Big]\ , \tag{1.105}$$

where we used the relation $(\mathbf{M}\cdot\mathbf{a})\times(\mathbf{M}\cdot\mathbf{b}) = \det(\mathbf{M})(\mathbf{M}^{-1})^T\cdot(\mathbf{a}\times\mathbf{b})$ for any matrix $\mathbf{M}$ and vector fields $\mathbf{a}, \mathbf{b}$. One can observe that as a direct consequence of (1.94) inferred from the angular momentum balance, the constitutive relations obtained for $\psi, \mathfrak{z}, \mathbf{p}$ and $\boldsymbol{m}$ are indeed objective. The constitutive relations for $\boldsymbol{\sigma}$ and $\mathbf{g}$ however are not. Thus objectivity does not apply to *all* the constitutive variables. For that reason, the treatment of Kovetz, 2000 based on the application of the angular momentum balance is here preferred over the application of the principle of material frame indifference. Note that Tadmor, Miller, and Elliott, 2011 (Section 6.3.7) make the case that the material frame indifference principle is a restrictive hypothesis on the macroscopic behavior of a material but does not have to hold true by the laws of physics.

## 1.5 CONSTITUTIVE RELATIONS IN REFERENCE CONFIGURATION

As was done for the governing equations, the constitutive relations can be expressed in the reference configuration. These reference configuration expressions will later be very useful to the derivation of a variational formulation of the problem in Chapter 5. The transforms are here performed for the formulation that has the specific free energy in reduced form $\Psi(\mathbf{C}, \mathscr{E}, \mathbf{B}, T, \xi)$ in (1.100) as it is the one that will be used in the variational formulation.

STRESS EXPRESSION Based on the constitutive relations in (1.102) the expression for the first Piola-Kirchhoff stress $\boldsymbol{\Pi} = J\mathbf{F}^{-1}\cdot\boldsymbol{\sigma}$ expressed with fields of the reference configuration yields,

$$\begin{aligned}\boldsymbol{\Pi} = 2\rho_0\frac{\partial\Psi}{\partial\mathbf{C}}\cdot\mathbf{F}^T + J\epsilon_0\left((\mathbf{C}^{-1}\cdot\mathbf{E})\mathbf{E} - \frac{1}{2}(\mathbf{E}\cdot\mathbf{C}^{-1}\cdot\mathbf{E})\mathbf{I}\right)\cdot\mathbf{F}^{-1}\\ + \frac{1}{\mu_0 J}\left(\mathbf{B}(\mathbf{C}\cdot\mathbf{B}) - \frac{1}{2}(\mathbf{B}\cdot\mathbf{C}\cdot\mathbf{B})\mathbf{I}\right)\cdot\mathbf{F}^{-1} + (\mathbf{F}^{-1}\cdot\dot{\mathbf{x}})\big(J\mathbf{C}^{-1}\cdot\epsilon_0\mathbf{E}\times\mathbf{B}\big)\cdot\mathbf{F}^{-1},\end{aligned} \tag{1.106}$$

25 In the more general case of orthogonal transforms $\mathbf{Q}$, because $\mathbf{b}$ is an axial vector, $\mathbf{b}' = \det(\mathbf{Q})\mathbf{Q}\cdot\mathbf{b}$.

where we account for $\rho_0 = \rho J$ and by analogy with (1.47) we introduced the reference configuration electric field, which we define as,

$$\mathbf{E} \equiv \boldsymbol{e}\cdot\mathbf{F}\,, \tag{1.107}$$

The $\mathbf{E}\times\mathbf{B}$ term in (1.106) is derived using the mathematical relation in Appendix A.2 (equation A.6)[26] and expression (1.106) includes the reference configuration counterpart $\boldsymbol{\Pi}_{MW} = J\mathbf{F}^{-1}\cdot\boldsymbol{\sigma}_{MW}$ of the Maxwell stress in vacuum (1.81),

$$\begin{aligned}\boldsymbol{\Pi}_{MW} = J\epsilon_0 &\left((\mathbf{C}^{-1}\cdot\mathbf{E})\mathbf{E} - \frac{1}{2}(\mathbf{E}\cdot\mathbf{C}^{-1}\cdot\mathbf{E})\mathbf{I}\right)\cdot\mathbf{F}^{-1} \\ &+ \frac{1}{\mu_0 J}\left(\mathbf{B}(\mathbf{C}\cdot\mathbf{B}) - \frac{1}{2}(\mathbf{B}\cdot\mathbf{C}\cdot\mathbf{B})\mathbf{I}\right)\cdot\mathbf{F}^{-1}\,.\end{aligned} \tag{1.108}$$

MOMENTUM DENSITY Transposition of the linear momentum density in (1.82) to the reference configuration is obtained using the field transformations for $\mathbf{E}$ (1.107) and $\mathbf{B}$ (1.44) and the mathematical relation (A.6) for the cross product,

$$\rho_0 \mathbf{g} = \rho_0\dot{\mathbf{x}} + \left((J\mathbf{C}^{-1}\cdot\epsilon_0\mathbf{E})\times\mathbf{B}\right)\cdot\mathbf{F}^{-1}\,. \tag{1.109}$$

AETHER RELATIONS Transposition of the aether relations for $\mathbf{d}$ in (1.23) to the reference configuration, is performed using the field transformations for $\mathbf{D}$ (1.38) and $\mathbf{E}$ (1.107) and the constitutive expression for polarization in (1.102),

$$\begin{aligned}\mathbf{D} &= J\mathbf{F}^{-1}\cdot(\epsilon_0\boldsymbol{e} + \mathbf{p}) \\ &= J\mathbf{C}^{-1}\cdot\epsilon_0\mathbf{E} - \rho_0\frac{\partial\Psi}{\partial\boldsymbol{\mathscr{E}}}\,.\end{aligned} \tag{1.110}$$

For transposition of the aether relations for $\mathbf{h}$ in (1.23) to the reference configuration, we introduce, by analogy with (1.41), a Lagrangian h-field

$$\mathbf{H} \equiv \mathbf{h}\cdot\mathbf{F}\,. \tag{1.111}$$

Using the aether relation for $\mathbf{h}$ in (1.23) then, the Lorentz magnetization expression from (1.69), the field transformation (1.44), and the constitutive expressions for polarization and magnetization in (1.102),

$$\begin{aligned}\mathbf{H} &= \left(\frac{1}{\mu_0}\mathbf{b} - \boldsymbol{m} + \dot{\mathbf{x}}\times\mathbf{p}\right)\cdot\mathbf{F} \\ &= \frac{1}{\mu_0 J}\mathbf{C}\cdot\mathbf{B} + \rho_0\frac{\partial\Psi}{\partial\mathbf{B}} - (\mathbf{F}^{-1}\cdot\dot{\mathbf{x}})\times\rho_0\frac{\partial\Psi}{\partial\boldsymbol{\mathscr{E}}}\,.\end{aligned} \tag{1.112}$$

Similarly for the Lagrangian magnetomotive intensity $\boldsymbol{\mathscr{H}}$, using the field transformation in (1.41), and the definition of the magnetomotive intensity $\boldsymbol{\hbar} = \mathbf{h} - \dot{\mathbf{x}}\times\mathbf{d}$,

$$\begin{aligned}\boldsymbol{\mathscr{H}} &= \frac{1}{\mu_0}\mathbf{b}\cdot\mathbf{F} - \boldsymbol{m}\cdot\mathbf{F} - (\dot{\mathbf{x}}\times\epsilon_0\boldsymbol{e})\cdot\mathbf{F} \\ &= \frac{1}{\mu_0 J}\mathbf{C}\cdot\mathbf{B} + \rho_0\frac{\partial\Psi}{\partial\mathbf{B}} - (\mathbf{F}^{-1}\cdot\dot{\mathbf{x}})\times(J\mathbf{C}^{-1}\cdot\epsilon_0\mathbf{E})\,.\end{aligned} \tag{1.113}$$

Here again, the above derivation uses $\rho_0 = \rho J$ and the identity (A.6).

26 As already mentioned before, despite the same notation "$\times$", the cross product acting on fields of the current configuration is not the same operator as the cross product acting on the fields of the reference configuration. Appendix A.2 (equation A.6) details the shift from one operator to the other when changing configuration.

ENERGY DENSITY Based on the energy density expression from (1.80) and the constitutive equation for polarization from (1.102), the energy density in the reference configuration, expressed as a functional of the Lagrangian fields, is

$$\rho_0 \varepsilon = \rho_0 \left( \Psi(\mathbf{C}, \boldsymbol{\mathscr{E}}, \mathbf{B}, T, \xi) + T\eta + \frac{1}{2}\dot{\mathbf{x}}\cdot\dot{\mathbf{x}} - \boldsymbol{\mathscr{E}}\cdot\frac{\partial \Psi}{\partial \boldsymbol{\mathscr{E}}} \right) + \frac{J\epsilon_0}{2}\mathbf{E}\cdot\mathbf{C}^{-1}\cdot\mathbf{E} + \frac{1}{2\mu_0 J}\mathbf{B}\cdot\mathbf{C}\cdot\mathbf{B} \,. \tag{1.114}$$

# 2

# DIRECT FORMULATION FOR ELECTRIC MOTOR PROBLEMS

In the previous section, a careful derivation of the general equations for a continuum electromagnetic problem, following (Kovetz, 2000), was recalled. Now that the stage is set and all the subtleties of the formulation identified, this chapter provides further approximation of the governing equations and constitutive relations for application to electric motor problems.

A convenient approximation for certain applications of electromagnetism - in particular the modeling of electric machines - is the *eddy current approximation*, which consists of ignoring the electric energy of the problem as compared to its magnetic counterpart (e.g. see Hiptmair and Ostrowski, 2005). The interested reader is referred to Alonso Rodriguez and Valli, 2010 for an extensive review (focused on linear material behaviors), and mathematical justification of the approximation. In the field of coupled magneto-mechanical problems, the eddy current approximation as for example been applied to the modeling of electromagnetic forming processes (Thomas and Triantafyllidis, 2009), or Magnetic Resonance Imaging (MRI) scanners (Ledger et al., 2016). Although not mentioned there, the eddy current approximation is the framework also adopted in the related work of Fonteyn, 2010; Fonteyn et al., 2010b; Fonteyn et al., 2010a. Compared to these later works, the following includes the angular momentum balance in the eddy current approximation. This fundamental principle of mechanics places restrictions on the form of the specific free-energy as highlighted in Section 1.4.4, which should not be neglected. As detailed in the following, it results in a symmetric total stress $\boldsymbol{\sigma}$ in the eddy current approximation, which other related works, despite their significant contribution, do not have (Fonteyn, 2010; Fonteyn et al., 2010b; Fonteyn et al., 2010a).

Electric motors experience only small strains in standard operation. They however operate under large magnetic fields (often up to magnetic saturation levels). The derivation of the constitutive relations for an isotropic magnetoelastic material for small strain $\boldsymbol{\epsilon}$, but arbitrary magnetic field $\mathbf{b}$, although straightforward requires lengthy calculations. Such derivations are not always done consistently in the available literature; a linearized version of the invariants is often considered, thus violating the objective nature of the free energy (equivalently the angular momentum balance) since the small strain tensor $\boldsymbol{\epsilon}$ is not objective. Although the proper calculations have been presented in the literature a long time ago by Pao and Yeh, 1973, following the early works on magnetoelasticity by Brown, 1966, a direct integration in our framework is not possible due to the different formulations adopted (e.g. different independent variables of the free energy densities, different definitions of total stress etc.). A linearization of the constitutive relations can also be found in Eringen and Maugin, 1990 however for small strains $\boldsymbol{\epsilon}$ and small magnetic field $\mathbf{b}$ altogether.

In the following, Section 2.1 presents the eddy current approximation of the problem. Section 2.2 highlights a few material behavior hypothesis one can take,

at least as a first approximation, for electric motor problems. It also highlights how the small strain constitutive relations for magnetization and stresses can be obtained by linearization with respect to the small strain tensor $\boldsymbol{\epsilon}$ of the general constitutive relations that follow from the previous thermodynamically consistent derivation.

## 2.1 EDDY CURRENT APPROXIMATION

### 2.1.1 *Applicability*

In Hiptmair and Ostrowski, 2005, the *eddy current approximation* has been justified for time invariant, local, isotropic, and linear material behavior - i.e. ohmic conductors, with linear magnetization - provided the size of the control volume that is considered is small compared to the wavelength of the electromagnetic waves, which traduces:

$$L\sqrt{\varepsilon\mu}\omega \ll 1 \,, \tag{2.1}$$

where L is the characteristic length of the control volume, $\varepsilon$[1] and $\mu$ are the absolute permittivity and permeablility of the medium and $\omega$ is the angular frequency of the time-harmonic excitation. A second condition needs to be observed: the characteristic time-scale needs to be small compared to the relaxation time of the electric space charges. This traduces:

$$\omega\frac{\varepsilon}{\gamma} \ll 1 \,, \tag{2.2}$$

where $\gamma$ is the electrical conductivity of the medium. Hiptmair and Ostrowski, 2005 also draws attention to the fact that thin or sharp geometries are particular cases of non applicability of the eddy-current formulation[2].

Some works can be found that extend the eddy current approximation to cases of $\gamma$, $\mu$ and $\epsilon$ inhomogeneous in space (e.g; for instance Buffa, Ammari, and Nédélec, 2000) but no formal justification of an extension to the case of non linear magnetization, where the magnetic permeability $\mu$ depends on the magnetic field $\mathbf{b}$, was found in the literature. This case is important to electric motors where magnetization is often subject to saturation or hysteresis. Assumption is taken in the present framework that extension of the eddy current approximation to non linear magnetic materials holds.

For automotive electric motor applications[3], electric polarization can be neglected and the permittivity is that of vacuum: $\epsilon_0 = 8.85\times10^{-12}$ F/m. The characteristic length is at maximum of the order of the rotor diameter, that is around 0.2 m. The typical frequency is on the order of the kHz. The magnetic permeability can typically reach around $5\times10^{-3}\mathrm{N/A^2}$. Thus $L\sqrt{\varepsilon\mu}\omega \approx 2.6\times10^{-4}$ and the first condition (2.1) is satisfied. The electrical conductivity is on the order of $2\times10^{6}$ S/m. Thus $\omega\frac{\varepsilon}{\gamma} \approx 4\times10^{-14}$ and the second condition (2.2) is met.

1 Not to be confused with the energy $\varepsilon$ everywhere else in this document.

2 In their work, Buffa, Ammari, and Nédélec, 2000 further investigate the impact of topology on the eddy current approximation.

3 Emphasis is on typical machines for automotive applications given the support of *Stellantis* through the *André-Citroën Research Chair, Ecole polytechnique*.

### 2.1.2 *Application to the problem*

GOVERNING EQUATIONS The *eddy current approximation* neglects the free electric charges (and hence Gauss' equation (1.11)) and results in ignoring the displacement current $\partial \mathbf{d}/\partial t$ and the convection of electric charges $q\dot{\mathbf{x}}$, and hence $\mathbf{j} = \boldsymbol{\mathcal{j}}$, in Maxwell-Ampère's law (1.13) (e.g. see Hiptmair and Ostrowski, 2005, Alonso Rodriguez and Valli, 2010, Thomas and Triantafyllidis, 2009). The simplified set of electromagnetic equations governing the problem and the associated interface conditions reduce to,

$$\begin{aligned} &\boldsymbol{\nabla}\times\mathbf{h} = \boldsymbol{\mathcal{j}}\,, && \mathbf{n}\times[\![\mathbf{h}]\!] = \boldsymbol{\kappa}\,;\\ &\boldsymbol{\nabla}\times\boldsymbol{e} = -\frac{\partial \mathbf{b}}{\partial t}\,, && \mathbf{n}\times[\![\boldsymbol{e}]\!] - (\mathbf{n}\cdot\dot{\mathbf{x}})\,[\![\mathbf{b}]\!] = \mathbf{0}\,;\\ &\boldsymbol{\nabla}\cdot\mathbf{b} = 0\,, && \mathbf{n}\cdot[\![\mathbf{b}]\!] = 0\,. \end{aligned} \tag{2.3}$$

Note that based on (1.16), the approximate charge conservation with $q$ neglected is now $\boldsymbol{\nabla}\cdot\boldsymbol{\mathcal{j}} = 0$, which is automatically satisfied given $(2.3)_1$. As a consequence of neglecting the electric displacement $\mathbf{d}$, the magnetomotive intensity $\boldsymbol{\mathcal{h}} = \mathbf{h}$ (see equation 1.12), and because neglecting $\mathbf{d}$ implies neglecting $\mathbf{p}$ per (1.23), the Lorentz magnetization $\boldsymbol{\mathcal{m}} = \mathbf{m}$ (see equation 1.69). The electromotive intensity remains $\boldsymbol{\mathcal{e}} = \boldsymbol{e} + \dot{\mathbf{x}}\times\mathbf{b}$, as defined in (1.19).

One more simplification is made possible by the eddy current approximation, consistent with ignoring the electric energy of the system (and Gauss's law), which allows the potential formulation in (1.22) for the electric field $\boldsymbol{e}$ to be expressed only in terms of the magnetic potential vector $\mathbf{a}$ only, such that the electric potential $\phi$ is neglected and the potential formulation becomes,

$$\begin{aligned} &\boldsymbol{e} = \boldsymbol{e}_{\mathrm{app}} - \frac{\partial \mathbf{a}}{\partial t}\,;\\ &\mathbf{b} = \boldsymbol{\nabla}\times\mathbf{a}\,, \end{aligned} \tag{2.4}$$

where $\boldsymbol{e}_{\mathrm{app}}$ is an externally applied electric field (typically to the coil that drives the system, e.g. see Thomas and Triantafyllidis, 2009).

Regarding the other mechanical and thermodynamic governing equations of the problem, the general form of the mass balance, linear momentum balance, angular momentum balance, energy balance and entropy inequality in Chapter 1 remain unaltered in the eddy current approximation. The approximation however results in significant changes to the constitutive relations of the problem, exposed hereafter.

CONSTITUTIVE RELATIONS As a consequence of neglecting the polarization $\mathbf{d}$, and consequently $\mathbf{p}$ linked to $\psi$ through the constitutive relation in (1.82),

$$\frac{\partial \psi}{\partial \boldsymbol{\mathcal{e}}} = \mathbf{0} \implies \psi = \psi(\mathbf{F}, \mathbf{b}, T, \boldsymbol{\xi})\,, \tag{2.5}$$

such that the specific free energy is no longer electro-magneto-thermo-mechanical but only magneto-thermo-mechanical. It justifies saying that the eddy current approximation consists in neglecting the energy associated to the electric field.

For stresses, following in particular Thomas and Triantafyllidis, 2009, the eddy current approximation implies that electric field terms can be ignored compared to their magnetic counterparts in the expression for the stress tensor in $(1.82)_1$. As such, in the eddy current approximation the stress expression reduces to,

$$\boldsymbol{\sigma} = 2\rho \mathbf{F}\cdot\left(\frac{\partial \psi}{\partial \mathbf{F}}\right)^{T} + \frac{1}{\mu_0}\left(\mathbf{b}\mathbf{b} - \frac{1}{2}(\mathbf{b}\cdot\mathbf{b})\mathbf{I}\right) - \left(\mathbf{b}\mathbf{m} - (\mathbf{b}\cdot\mathbf{m})\mathbf{I}\right) . \tag{2.6}$$

Accordingly, expression (1.81) for the Maxwell-stress in vacuum reduces to,

$$\boldsymbol{\sigma}_{MW} = \frac{1}{\mu_0}\left(\mathbf{b}\mathbf{b} - \frac{1}{2}(\mathbf{b}\cdot\mathbf{b})\mathbf{I}\right) . \tag{2.7}$$

The linear momentum density $\mathbf{g}$ and stresses $\boldsymbol{\sigma}$ are linked through the linear momentum balance (1.28). Consequently, because neglected in $\boldsymbol{\sigma}$, electric field terms are neglected in $\mathbf{g}$ as well for consistency, and $\mathbf{g}$ now reduces to the usual linear momentum density,

$$\mathbf{g} = \dot{\mathbf{x}} . \tag{2.8}$$

A similar eddy current approximation for $\mathbf{g}$ and $\boldsymbol{\sigma}$ is performed in Thomas and Triantafyllidis, 2009 (no magnetization) or Ledger et al., 2016 (with magnetization).

To summarize, for the constitutive relations in the eddy current approximation,

$$\begin{aligned} &\psi = \psi(\mathbf{F}, \mathbf{b}, T, \boldsymbol{\xi}) , \qquad \mathbf{g} = \dot{\mathbf{x}} , \qquad \mathbf{m} = -\rho\frac{\partial \psi}{\partial \mathbf{b}} , \qquad \mathcal{s} = -\frac{\partial \psi}{\partial T} \\ &\boldsymbol{\sigma} = \rho \mathbf{F}\cdot\left(\frac{\partial \psi}{\partial \mathbf{F}}\right)^{T} + \frac{1}{\mu_0}\left(\mathbf{b}\mathbf{b} - \frac{1}{2}(\mathbf{b}\cdot\mathbf{b})\mathbf{I}\right) - \left(\mathbf{b}\mathbf{m} - (\mathbf{b}\cdot\mathbf{m})\mathbf{I}\right) . \end{aligned} \tag{2.9}$$

According to the previous developments $\boldsymbol{m}$ was replaced by $\mathbf{m}$ in the expressions. The constitutive law for $\mathbf{p}$ – neglected – was taken out. Save for $\psi$ that now depends on $(\mathbf{F}, \mathbf{b}, T, \boldsymbol{\xi})$ where relevant, the entropy constitutive equality in (1.82) recalled above, together with the dissipation inequality in (1.83) remain unaltered. To conclude, equation (1.80) that links the total energy of the system to the specific free energy becomes, in the eddy current approximation,

$$\rho\varepsilon = \rho\psi(\mathbf{F}, \mathbf{b}, T, \boldsymbol{\xi}) + \rho T\eta + \frac{\rho}{2}\dot{\mathbf{x}}\cdot\dot{\mathbf{x}} + \left[\frac{1}{2\mu_0}\mathbf{b}\cdot\mathbf{b}\right] . \tag{2.10}$$

LINEAR MOMENTUM BALANCE Replacing for the simplified expressions for $\mathbf{g}$ and $\boldsymbol{\sigma}$ in the linear momentum balance (1.28) now provides,

$$\rho\ddot{\mathbf{x}} = \boldsymbol{\nabla}\cdot\left(\rho \mathbf{F}\cdot\left(\frac{\partial \psi}{\partial \mathbf{F}}\right)^{T}\right) + \rho\mathbf{f} + \boldsymbol{\mathcal{j}}\times\mathbf{b} + \mathbf{m}\times(\boldsymbol{\nabla}\times\mathbf{b}) + \mathbf{m}\cdot(\boldsymbol{\nabla}\mathbf{b}) . \tag{2.11}$$

The interface conditions $\mathbf{n}\cdot[\![\boldsymbol{\sigma}]\!] = \mathbf{t}_m$ remains unchanged. The Lorentz forces is now reduced to $\boldsymbol{\mathcal{j}}\times\mathbf{b}$. Other magnetic contribution to forces follow from the remaining terms, *including the* $\psi$*-derivative* given $\psi$ may depend on $\mathbf{b}$. The motion equation obtained differs from that of the general case (1.86) by the terms $q$ and $\mathbf{p}$ now neglected. Consistently, this justifies the approximations made in the expressions (2.9) for the stress and linear momentum density.

TEMPERATURE EQUATION Save for $\psi$ that now depends on $(\mathbf{F}, \mathbf{b}, T, \xi)$, the energy equation in (1.92) remains unaltered. For self sufficiency of this chapter, we recall:

$$\rho T \dot{\mathcal{J}} = \rho r - \boldsymbol{\nabla}\cdot\mathbf{q} + \boldsymbol{\mathcal{J}}\cdot\boldsymbol{\mathcal{E}} \,. \tag{2.12}$$

ANGULAR MOMENTUM BALANCE An important point that this work particularly aims to highlight is the following:

> As a consequence of $\mathbf{g} = \dot{\mathbf{x}}$, the angular momentum balance (1.29) becomes,
>
> $$\boldsymbol{\sigma}^T - \boldsymbol{\sigma} = \mathbf{0} \,, \tag{2.13}$$
>
> now requiring a symmetric total stress $\boldsymbol{\sigma}$ as part of the eddy current approximation.

This requirement of symmetry of the total stress $\boldsymbol{\sigma}$ is not new and generally admitted in the literature on magneto-mechanical problems, in particular related to the modeling of magneto-rheological elastomers (e.g. in Dorfmann and Ogden, 2003 for problems with linear magnetization and negligible polarization, in Kankanala and Triantafyllidis, 2004; Dorfmann, Ogden, and Saccomandi, 2004 for problems with negligible currents and displacement field but arbitrary magnetization). We make the case here that it more generally extends to problems in the eddy current approximation that have currents and arbitrary magnetization altogether.

> Other related works on electric motor modeling that follow the approach adopted here (see Fonteyn, 2010; Fonteyn et al., 2010b; Fonteyn et al., 2010a) do not have this symmetric total stress. They do generally acknowledge it has to be symmetrical (Fonteyn et al., 2010c; Belahcen et al., 2006; Fonteyn, 2010), however the small strain expressions for stresses that they provide violates the stress symmetry [a]. Because the angular momentum is a fundamental principle of mechanics, stress symmetry should be considered. We believe it further helps in establishing the constitutive laws from experimental characterization as it restricts, by the physics, the panel of possible constitutive relations (and thus possibly the number of parameters to fit). We show in the following Section 2.2 how a careful small strain linearization can be performed that preserves the symmetry of the total stress.
>
> [a] In the derivation of their small strain expressions, they replace $\rho\mathbf{F}\cdot\left(\frac{\partial\psi}{\partial\mathbf{F}}\right)^T$ *not* symmetrical in (2.9) – as a consequence of the symmetry on $\boldsymbol{\sigma}$ and asymmetry of the remaining terms in $\boldsymbol{\sigma}$ – by $\rho\frac{\partial\psi}{\partial\boldsymbol{\epsilon}}$ *symmetric by nature* given the symmetry of the small strain tensor $\boldsymbol{\epsilon}$.

The symmetry of $\boldsymbol{\sigma}$ in the eddy current approximation is also verified when working with the stress expressions that have $\hat{\psi}$ or $\Psi$ from (1.99) and (1.102) as derived from enforcement of the angular momentum balance in the general case

in Chapter 1. In these expressions, neglecting the electric field terms with respect to their magnetic counterparts indeed provides the symmetric stress expressions,

$$\begin{aligned}\boldsymbol{\sigma} &= 2\rho\mathbf{F}\cdot\frac{\partial\hat{\psi}}{\partial\mathbf{C}}\cdot\mathbf{F}^{\mathsf{T}} + \frac{1}{\mu_0}\Big(\mathbf{b}\mathbf{b} - \frac{1}{2}(\mathbf{b}\cdot\mathbf{b})\mathbf{I}\Big) - \Big(\mathbf{m}\mathbf{b} + \mathbf{b}\mathbf{m} - (\mathbf{b}\cdot\mathbf{m})\mathbf{I}\Big)\,;\\ \boldsymbol{\sigma} &= 2\rho\mathbf{F}\cdot\frac{\partial\Psi}{\partial\mathbf{C}}\cdot\mathbf{F}^{\mathsf{T}} + \frac{1}{\mu_0}\Big(\mathbf{b}\mathbf{b} - \frac{1}{2}(\mathbf{b}\cdot\mathbf{b})\mathbf{I}\Big)\,.\end{aligned} \tag{2.14}$$

Finally, and consistently with (2.5), regarding the arguments of the specific free energy in reduced form $\hat{\psi}$ and $\Psi$ derived from imposing the angular momentum balance in Section (1.4.4), because of negligible $\mathbf{p}$,

$$\frac{\partial\hat{\psi}}{\partial\mathscr{E}} = \frac{\partial\Psi}{\partial\mathscr{E}} = 0 \implies \psi = \hat{\psi}(\mathbf{C},\tilde{\mathbf{B}},T,\xi) = \Psi(\mathbf{C},\mathbf{B},T,\xi)\,. \tag{2.15}$$

MATERIAL FRAME INDIFFERENCE A comment on material frame indifference is here in order. One can observe that based on the transformation of the fields $\boldsymbol{e}$ and $\mathbf{b}$ under Euclidian transformation in (1.104), all the constitutive variables of the problem, including $\boldsymbol{\sigma}$ are, in the eddy current approximation, now objective[4]. Only the linear momentum density $\mathbf{g} = \dot{\mathbf{x}}$ is not, as in classical mechanics.

### 2.1.3 *In reference configuration*

Following the development in Chapter 1, the governing equations and the constitutive relations of the problem in the eddy current approximation can be transposed to the reference configuration. These reference configuration expressions will later be very useful to the derivation of a variational formulation of the problem in Chapter 5. The transforms are here performed for the formulation of the constitutive relations that has $\psi = \Psi(\mathbf{C},\mathscr{E},\mathbf{B},T,\xi)$ in (1.100) as it is the one that will be used in the variational formulation.

With the fields $\mathscr{H},\mathscr{E},\mathbf{B},\mathbf{K}$ as defined in Chapter 1, the set of Maxwell equations (2.3) transposes to

$$\begin{aligned}&\boldsymbol{\nabla}\times\mathscr{H} = \mathscr{J}\,, \quad \mathbf{N}\times[\![\mathscr{H}]\!] = \mathbf{K}\,;\\ &\boldsymbol{\nabla}\times\mathscr{E} = -\dot{\mathbf{B}}\,, \quad \mathbf{N}\times[\![\mathscr{E}]\!] = 0\,;\\ &\boldsymbol{\nabla}\cdot\mathbf{B} = 0\,, \qquad \mathbf{N}\cdot[\![\mathbf{B}]\!] = 0\,,\end{aligned} \tag{2.16}$$

and as a result of $\mathscr{h} = \mathbf{h}$, $\mathscr{H} = \mathbf{H}$. Further as $\frac{\partial\Psi}{\partial\mathscr{E}} = 0$ in the eddy current approximation, the expression for $\mathscr{H}$ in (1.113) becomes,

$$\mathscr{H} = \frac{1}{\mu_0 J}\mathbf{C}\cdot\mathbf{B} + \rho_0\frac{\partial\Psi}{\partial\mathbf{B}}\,, \tag{2.17}$$

and the same expression is obtained neglecting the electric field in the expression for $\mathbf{H}$ in (1.112), showing consistency with $\mathscr{H} = \mathbf{H}$.

4 At least for Euclidian transformations that exclude symmetries.

The potential formulation from (2.4), with $\mathbf{A}$ defined in Chapter 1, becomes

$$\begin{aligned} \mathscr{E} &= -\dot{\mathbf{A}} \, ; \\ \mathbf{B} &= \boldsymbol{\nabla} \times \mathbf{A} \, . \end{aligned} \tag{2.18}$$

The linear momentum balance, accounting for $\mathbf{g} = \dot{\mathbf{x}}$ yields in reference configuration,

$$\rho_0 \ddot{\mathbf{x}} = \boldsymbol{\nabla} \cdot \boldsymbol{\Pi} \, , \qquad \mathbf{N} \cdot [\![ \boldsymbol{\Pi} ]\!] = \mathbf{T}_m \, . \tag{2.19}$$

Based on the constitutive relations in (2.14) the expression for the first Piola-Kirchhoff stress $\boldsymbol{\Pi} = J\mathbf{F}^{-1} \cdot \boldsymbol{\sigma}$ expressed with fields of the reference configuration yields,

$$\boldsymbol{\Pi} = 2\rho_0 \frac{\partial \Psi}{\partial \mathbf{C}} \cdot \mathbf{F}^T + \frac{1}{\mu_0 J} \left( \mathbf{B}(\mathbf{C} \cdot \mathbf{B}) - \frac{1}{2} (\mathbf{B} \cdot \mathbf{C} \cdot \mathbf{B}) \mathbf{I} \right) \cdot \mathbf{F}^{-1} \, , \tag{2.20}$$

where we account for $\rho_0 = \rho J$. Expression (2.20) includes the reference configuration counterpart $\boldsymbol{\Pi}_{MW} = J\mathbf{F}^{-1} \cdot \boldsymbol{\sigma}_{MW}$ of the Maxwell stress in vacuum (1.81), which becomes in the eddy current approximation,

$$\boldsymbol{\Pi}_{MW} = \frac{1}{\mu_0 J} \left( \mathbf{B}(\mathbf{C} \cdot \mathbf{B}) - \frac{1}{2} (\mathbf{B} \cdot \mathbf{C} \cdot \mathbf{B}) \mathbf{I} \right) \cdot \mathbf{F}^{-1} \, . \tag{2.21}$$

Finally based on (2.10), the eddy current approximation for the Lagrangian total energy density, expressed with fields of the reference configuration provides,

$$\rho_0 \varepsilon = \rho_0 \left( \Psi(\mathbf{C}, \mathbf{B}, T, \boldsymbol{\xi}) + T\eta + \frac{1}{2} \dot{\mathbf{x}} \cdot \dot{\mathbf{x}} \right) + \frac{1}{2\mu_0 J} \mathbf{B} \cdot \mathbf{C} \cdot \mathbf{B} \, . \tag{2.22}$$

## 2.2 CONSTITUTIVE BEHAVIOR

In this section, without loss of generality and for use in electric motor problems we solve in Chapter 3, a few assumptions are made on the material behavior, prior to a discussion on the electromagnetic forces that results.

### 2.2.1 *Assumptions on the materials considered*

The eddy current problem formulated thus far is general, accounting for nonlinear magnetic and mechanical material response, both constitutive and kinematic (finite strains), as well as dissipative phenomena. However certain simplifications can be made; the resulting expressions for the constitutive laws are given progressively below, as more assumptions are introduced from one step to the next. For the remaining of Part I, we work with the specific free energy functional $\hat{\psi}(\mathbf{C}, \tilde{\mathbf{B}}, T, \boldsymbol{\xi})$. The only motivation for this choice was an easier linearization in small strains – compared to expressions with $\Psi(\mathbf{C}, \mathbf{B}, T)$ –, which is displayed hereafter.

ABSENCE OF MECHANICAL AND MAGNETIC DISSIPATION Two main sources of dissipation are possible: plasticity in the metallic parts and magnetic hysteresis of the ferromagnetic ones, requiring the specification of evolution laws for the internal variables $\xi$. A typical electric motor in its steady-state regime experiences only small elastic strains, thus plasticity is neglected. However, it can sustain large magnetization, often up to saturation level. For electric motor applications soft magnetic materials with high permeability and low hysteresis are used. They consist of "*electric steels*" (also termed "*silicon steels, relay steels, transformer steels*"), i.e. iron alloys tailored to produce specific magnetic properties: small hysteresis area resulting in low power loss per cycle, low core loss and high permeability (see Cullity and Graham, 2011). Hence, magnetic hysteresis can be neglected in a first approximation[5]. Consequently internal variables $\xi$ are not required for material description, i.e. $\partial\psi/\partial\xi = 0$, and the specific free energy is a function of strain, magnetic field and temperature: $\hat{\psi}(\mathbf{C}, \tilde{\mathbf{B}}, T)$.

MATERIAL ISOTROPY Isotropy of the material response implies that its specific free energy is a function of six invariants (and temperature), i.e. $\hat{\psi}(\mathbf{C}, \tilde{\mathbf{B}}, T) = \hat{\psi}(I_1, I_2, I_3, \tilde{J}_1, \tilde{J}_2, \tilde{J}_3, T)$, where $I_i$ are the invariants of the right Cauchy-Green tensor $\mathbf{C}$ and $\tilde{J}_i$ are the coupled magneto-mechanical invariants of $\mathbf{C}$ and $\tilde{\mathbf{B}}$ given in (2.23)[6].

DECOUPLING OF PHYSICAL PHENOMENA It is assumed that thermo-mechanical, thermo-magnetic couplings can be neglected, resulting in a separate thermal contribution $\hat{\psi}_{th}$ constructed under the assumption of a constant specific heat coefficient $c_\epsilon$. It is further assumed that, in the absence of magnetic fields, the free energy of the solid is $\hat{\psi}_e(I_1, I_2, I_3)$ and that the magneto-mechanical coupling is described by the magnetic interaction energy $\hat{\psi}_m(\tilde{J}_1, \tilde{J}_2, \tilde{J}_3)$.

$$\begin{aligned} \hat{\psi}(\mathbf{C}, \tilde{\mathbf{B}}, T) &= \hat{\psi}_e(I_1, I_2, I_3) + \hat{\psi}_m(\tilde{J}_1, \tilde{J}_2, \tilde{J}_3) + \hat{\psi}_{th}(T) \,; \\ \hat{\psi}_{th} &= -c_\epsilon T[\ln(T/T_0) - 1] \,, \\ I_1 &= \mathrm{tr}(\mathbf{C}) \,, \quad I_2 = \tfrac{1}{2}(\mathrm{tr}(\mathbf{C})^2 - \mathrm{tr}(\mathbf{C}\cdot\mathbf{C})) \,, \quad I_3 = \det(\mathbf{C}) \,, \\ \tilde{J}_1 &= \tilde{\mathbf{B}}\cdot\mathbf{C}^{-1}\cdot\tilde{\mathbf{B}} \,, \quad \tilde{J}_2 = \tilde{\mathbf{B}}\cdot\tilde{\mathbf{B}} \,, \quad \tilde{J}_3 = \tilde{\mathbf{B}}\cdot\mathbf{C}\cdot\tilde{\mathbf{B}} \,, \end{aligned} \tag{2.23}$$

where $T_0$ is a reference temperature.

The implication of isotropy and decoupling on the generalized Ohm and Fourier laws in (1.84) is discussed next. We assume that the conduction current density $\boldsymbol{\mathcal{j}}$ depends solely on the electromotive force $\boldsymbol{\mathcal{e}}$ and that the heat flux $\mathbf{q}$ is only a function of the temperature gradient $\nabla T$

$$\boldsymbol{\mathcal{j}} = \gamma(\|\boldsymbol{\mathcal{e}}\|)\boldsymbol{\mathcal{e}} \,; \quad \mathbf{q} = -k(\|\nabla T\|)\nabla T \,, \tag{2.24}$$

5 Although not considered here, we point out that the study of hysteresis and in particular its relation to stresses (which further justifies the present work) for evaluation and reduction of losses is part of the hot topics of modern research on electric motors (e.g. see Daniel, Rekik, and Hubert, 2014; Bernard and Daniel, 2015; Rasilo et al., 2016).

6 We note $\tilde{J}_i$ the coupled magneto-mechanical invariants involving $\tilde{\mathbf{B}}$ to allow distinction from the invariants $J_i$ involving $\mathbf{B}$ in Chapter 6.

where the scalar *electrical conductivity* $\gamma(\|\boldsymbol{e}\|) > 0$ and the scalar *thermal conductivity* $k(\|\nabla T\|) > 0$, as dictated by the dissipation inequality (1.83). The norm-dependence of these two scalar quantities is due to material isotropy.

SMALL STRAIN APPROXIMATION For the electric motor applications of interest here, we adopt the small strain approximation, i.e. $\|\boldsymbol{\epsilon}\| \ll 1$, with $\boldsymbol{\epsilon} \equiv (1/2)(\nabla \mathbf{u} + \mathbf{u}\nabla)$ the *small strain tensor*. Using a Taylor series expansions in $\boldsymbol{\epsilon}$ about the reference configuration of the quantities involved up to first order in $\boldsymbol{\epsilon}$ and neglecting terms of order $\boldsymbol{\epsilon}\ \mathbf{b}$[7], we obtain a total stress $\boldsymbol{\sigma}$ as the sum of a purely elastic part $\overset{e}{\boldsymbol{\sigma}}(\boldsymbol{\epsilon})$[8] and a purely magnetic part $\overset{m}{\boldsymbol{\sigma}}(\mathbf{b})$

$$
\begin{aligned}
&\boldsymbol{\sigma} = \overset{e}{\boldsymbol{\sigma}} + \overset{m}{\boldsymbol{\sigma}}\ ; \qquad\qquad \mathbf{m} = \frac{\chi(\|\mathbf{b}\|)}{\mu(\|\mathbf{b}\|)}\mathbf{b}\ ; \\
&\overset{e}{\boldsymbol{\sigma}} \equiv \lambda \mathrm{tr}(\boldsymbol{\epsilon})\mathbf{I} + 2G\boldsymbol{\epsilon}\ , \\
&\overset{m}{\boldsymbol{\sigma}} \equiv \frac{1}{\mu_0}\left[\mathbf{b}\mathbf{b} - \frac{1}{2}(\mathbf{b}\cdot\mathbf{b})\mathbf{I}\right] - \frac{\chi(\|\mathbf{b}\|)}{\mu(\|\mathbf{b}\|)}\left[\mathbf{b}\mathbf{b} - (\mathbf{b}\cdot\mathbf{b})\mathbf{I}\right] + \frac{\Lambda(\|\mathbf{b}\|)}{\mu(\|\mathbf{b}\|)}\mathbf{b}\mathbf{b}\ , \\
&\frac{\chi(\|\mathbf{b}\|)}{\mu(\|\mathbf{b}\|)} = -2\rho_0\left[\frac{\partial\hat{\psi}_m}{\partial\tilde{J}_1} + \frac{\partial\hat{\psi}_m}{\partial\tilde{J}_2} + \frac{\partial\hat{\psi}_m}{\partial\tilde{J}_3}\right]_{\mathbf{C}=\mathbf{I}}\ , \\
&\frac{\Lambda(\|\mathbf{b}\|)}{\mu(\|\mathbf{b}\|)} = 2\rho_0\left[\frac{\partial\hat{\psi}_m}{\partial\tilde{J}_2} + 2\frac{\partial\hat{\psi}_m}{\partial\tilde{J}_3}\right]_{\mathbf{C}=\mathbf{I}}\ ,
\end{aligned}
\tag{2.25}
$$

where $\chi(\|\mathbf{b}\|)$ is the material's *magnetic susceptibility*, $\mu(\|\mathbf{b}\|) = \mu_0[1 + \chi(\|\mathbf{b}\|)]$ its *magnetic permeability* and $\Lambda(\|\mathbf{b}\|)$ a *magneto mechanical coupling* coefficient[9]. It is important to note that at this stage our isotropic material model is valid for small strains but arbitrary magnetization – the typical case of interest in magnetic motors – and that the corresponding magnetic susceptibility, magnetic permeability and magnetomechanical coupling coefficient are functions of the norm of the magnetic field $\mathbf{b}$ (due to isotropy). We should also mention another consequence of small strain: the density equals its reference counterpart, i.e. $\rho = \rho_0$, thus justifying its appearance (2.25). A remark is in order at this point about the expressions presented in (2.25); they differ from similar expressions presented by other authors (e.g. Aydin et al., 2017; Fonteyn, 2010) in view of our use of the objective invariants $\tilde{J}_k$ in our linearization procedure instead of their simplified, non-objective counterparts, together with the decoupling hypothesis we made (significant assumption). The interested reader can find the details of these lengthy derivations in B.1.

We stress that the small strain linearization performed here is the proper way to retrieve the small strain constitutive relations based on the general expres-

7 The small strain constitutive expressions that include terms order $\boldsymbol{\epsilon}\ \mathbf{b}$ and the justification for the omission of these terms in (2.25) are given in B.1. In the completely analogous – $\boldsymbol{e} \to \mathbf{b}$, $\mathbf{p} \to \mathbf{m}$, $\varepsilon_0 \to \mu_0^{-1}$ – electroelastic problems neglecting the coupling terms is justified by assuming the small strain is of the same order as the square of the moderate electric fields, e.g. see Tian et al., 2012; Lefèvre and Lopez-Pamies, 2017.

8 The elastic part of the free energy $\hat{\psi}_e$ is independent of the magnetic field; upon linearization at $\mathbf{C} = \mathbf{I}$ one obtains the classical Lame constants $\lambda$ and $G$ appearing in (2.25).

9 This coefficient gives the curvature of the strain vs magnetic field in a stress-free uniaxial magnetostriction experiment.

sions obtained from the principles of electromagnetism, mechanics and thermodynamics and *preserves the restrictions imposed by these principles*, in particular the symmetry of $\boldsymbol{\sigma}$ in the eddy current approximation. It is of course not in general new (e.g. Pao and Yeh, 1973; Eringen and Maugin, 1990; Tian et al., 2012; Lefèvre and Lopez-Pamies, 2017), however in the field of electric motor modeling, the small strain expressions typically used up to know have not been derived along those lines, which is the cause of the non symmetric total stresses they lead to (Fonteyn et al., 2010c; Belahcen et al., 2006; Fonteyn, 2010). The small strain expressions we derived and propose, in particular their most general version given in Appendix B.1 (no decoupling hypothesis on the specific free energy) give a precise insight on the form of the constitutive relations: they identify clearly the terms in $\epsilon$ that result from magneto-mechanical couplings, and coefficients that depend on $\|\mathbf{b}\|$ only. They may help greatly in fitting experimental data for material characterization (e.g. see Aydin et al., 2017).

LINEAR MAGNETIC BEHAVIOR In further applications in Chapter 3 a linear magnetic behavior is considered such that $\mu$, $\chi$ and $\Lambda$ in (2.25) are constants and the expressions for stresses and magnetization are:

$$\begin{aligned}
&\boldsymbol{\sigma} = \overset{e}{\boldsymbol{\sigma}} + \overset{m}{\boldsymbol{\sigma}} ; \qquad \overset{e}{\boldsymbol{\sigma}} \equiv \lambda \mathrm{tr}(\boldsymbol{\epsilon})\mathbf{I} + 2G\boldsymbol{\epsilon} , \\
&\mathbf{m} = \frac{\chi}{\mu}\mathbf{b} ; \qquad \overset{m}{\boldsymbol{\sigma}} \equiv \frac{1}{\mu_0}\left[\mathbf{b}\mathbf{b} - \frac{1}{2}(\mathbf{b}\cdot\mathbf{b})\mathbf{I}\right] - \frac{\chi}{\mu}\left[\mathbf{b}\mathbf{b} - (\mathbf{b}\cdot\mathbf{b})\mathbf{I}\right] + \frac{\Lambda}{\mu}\mathbf{b}\mathbf{b} , \qquad (2.26) \\
&\chi,\ \Lambda,\ \mu \text{ constants} .
\end{aligned}$$

### 2.2.2 *Resulting body forces of electromagnetic origin*

To gain insight for later applications in Chapter 3, we derive the forces of electromagnetic origin that result from the constitutive behavior derived previously, in the case of a *linear magnetic behavior* ($\chi, \Lambda, \mu$ all constants).

From (2.26), the expression for the electromagnetic part of the stress can be recast into,

$$\overset{m}{\boldsymbol{\sigma}} = \frac{1}{\mu}\left(\mathbf{b}\mathbf{b} - \frac{1}{2}(\mathbf{b}\cdot\mathbf{b})\mathbf{I}\right) + \frac{\chi}{2\mu}(\mathbf{b}\cdot\mathbf{b})\mathbf{I} + \frac{\Lambda}{\mu}\mathbf{b}\mathbf{b} . \qquad (2.27)$$

Accounting for the no-magnetic monopole law (1.18) and Maxwell-ampère's law (1.13) in the derivation, the first term in the stress expression provides the *Lorentz forces*. Accounting for the consitutive magnetization equation in (2.26), the second term provides a *magnetization force* term usually found in the literature (e.g. see Eringen and Maugin, 1990 §3.5 who derive this macroscopic body force term from statistical averaging of a microscopic electromagnetic theory; or Hirsinger and Billardon, 1995, Tiersten, 1990; or Dorfmann and Ogden, 2003 citing Pao, 1978). Accounting for the no magnetic monopole law (1.18) the last term provides a *mag-*

*netostriction force* term. These three contributions are highlighted below, together with the resulting global forces of electromagnetic origin $\overset{\text{m}}{\mathbf{f}}$,

$$\begin{aligned}
&\boldsymbol{\nabla}\cdot\left(\frac{1}{\mu}\left[\mathbf{b}\mathbf{b}-\frac{1}{2}(\mathbf{b}\cdot\mathbf{b})\mathbf{I}\right]\right) &&= \mathbf{j}\times\mathbf{b}\,, && \textit{Lorentz}\,;\\
&\boldsymbol{\nabla}\cdot\left(\frac{\chi}{2\mu}(\mathbf{b}\cdot\mathbf{b})\mathbf{I}\right) &&= \mathbf{m}\cdot(\mathbf{b}\boldsymbol{\nabla})\,, && \textit{magnetization induced}\,;\\
&\boldsymbol{\nabla}\cdot\left(\frac{\Lambda}{\mu}\mathbf{b}\mathbf{b}\right) &&= \frac{\Lambda}{\mu}\mathbf{b}\cdot(\boldsymbol{\nabla}\mathbf{b})\,, && \textit{magnetostrictive}\,;\\
&\overset{\text{m}}{\mathbf{f}} \equiv \boldsymbol{\nabla}\cdot\overset{\text{m}}{\boldsymbol{\sigma}} = \mathbf{j}\times\mathbf{b}+\mathbf{m}\cdot(\mathbf{b}\boldsymbol{\nabla})+\frac{\Lambda}{\mu}\mathbf{b}\cdot(\boldsymbol{\nabla}\mathbf{b})\,; && \quad \mathbf{m}=\frac{\chi}{\mu}\mathbf{b}\,.
\end{aligned} \tag{2.28}$$

For future reference on boundary value problem applications in Chapter 3, it is convenient to reorganize the stress expression and electromagnetic body force terms into,

$$\begin{aligned}
\overset{\text{m}}{\boldsymbol{\sigma}} &= \frac{1+\Lambda}{\mu}\left(\mathbf{b}\mathbf{b}-\frac{1}{2}(\mathbf{b}\cdot\mathbf{b})\mathbf{I}\right)+\frac{\chi+\Lambda}{2\mu}(\mathbf{b}\cdot\mathbf{b})\mathbf{I}\,;\\
\overset{\text{m}}{\mathbf{f}} &= \frac{1+\Lambda}{\mu}\mathbf{j}\times\mathbf{b}+\frac{\chi+\Lambda}{2\mu}\boldsymbol{\nabla}(\mathbf{b}\cdot\mathbf{b})\,,
\end{aligned} \tag{2.29}$$

which interestingly highlights that the magnetostriction body forces can be split into a contribution proportional to the Lorentz force and another proportional to the magnetization force according to (2.28).

### 2.2.3 *Resulting traction at interfaces*

Because of the interface condition for stresses $\mathbf{n}\cdot[\![\boldsymbol{\sigma}]\!]$ from (1.28), surface traction occurs at interfaces between two materials with distinct magnetic properties. In electric motors, these traction occur at interfaces between the ferromagnetic motor components and air (in the airgap region or in the motor surrounding) and are of significant importance given the high magnetic properties of ferromagnetic materials (Fonteyn et al., 2010a). To gain insight and prepare for analytical computation in Chapter 3, the expression of these surface traction at an interface between air and a material that has total stress given by (2.26) are derived below in the 2D, *linear magnetic behavio*r case ($\chi, \Lambda, \mu$ all constants).

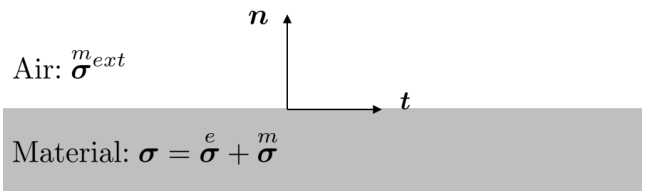


Figure 2.1: An interface between a material domain and air in 2D.

The interface is oriented by a local normal $\mathbf{n}$, and we denote $\mathbf{t}$ the in plane tangent, as pictured in Figure 2.1. Air is assimilated to vacuum[10] with stresses $\overset{\text{m}}{\boldsymbol{\sigma}}^{\text{ext}}$

10 Assimilating air to vacuum is standard hypothesis in the literature.

equal to Maxwell's stresses in vacuum (2.7). The interface is free of any surface currents. In the material the total stress has elastic $\overset{e}{\boldsymbol{\sigma}}$ and magnetic $\overset{m}{\boldsymbol{\sigma}}$ components. The interface condition $\mathbf{n}\cdot[\![\boldsymbol{\sigma}]\!] = \mathbf{0}$ yields an electromagnetic surface traction $\mathbf{n}\cdot\overset{e}{\boldsymbol{\sigma}}$ induced by the jump in magnetic properties, and we have for the normal and tangent components,

$$\mathbf{n}\cdot[\![\boldsymbol{\sigma}]\!] = \mathbf{0} \implies \begin{cases} \overset{e}{\sigma}_{nn} = \overset{m}{\sigma}^{ext}_{nn} - \overset{m}{\sigma}_{nn} = -\dfrac{\Lambda}{\mu} b_n^2 - \dfrac{\chi^2}{2}\mu_0 h_t^2 \ ; \\ \overset{e}{\sigma}_{nt} = \overset{m}{\sigma}^{ext}_{nt} - \overset{m}{\sigma}_{nt} = -\Lambda b_n h_t \ , \end{cases} \tag{2.30}$$

where the continuity of $b_n$ and $h_t$ at interfaces (see interface conditions in (1.18) and (1.13)) are accounted for. As a result of its continuity, $b_n$ – respectively $h_t$ – in (2.30) is unambiguously defined: it has the same value on each side of the interface and there is no necessity of an index referencing to the side, hence the interest for expressions involving $b_r$ and $h_t$ at interfaces free of surface currents. These expressions are used in the stator boundary value problem of Section 3.2, where they are particularly suited. In the rotor boundary value problem of Section 3.1 other (equivalent) form of the expressions are preferred. Finally, in the case where the interface has surface currents $\boldsymbol{\kappa}$, other expressions are involved given the discontinuity in $\mathbf{h}$ ($\mathbf{n}\times[\![\mathbf{h}]\!] = \boldsymbol{\kappa}$).

# 3

# ANALYTICAL MOTOR BOUNDARY VALUE PROBLEMS

This section pertains to analytical steady-state regime solution of idealized electric motor configurations as an application of the theory developed in Chapter 2.

LITERATURE REVIEW A particular class of analytical methods used by the electrical engineering community, termed *"subdomain methods"* (e.g. see: Lubin, Mezani, and Rezzoug, 2011a, Devillers et al., 2016) constitute an approximate but efficient tool used for evaluation of the magnetic field distribution in motor concepts at the preliminary design stage. A wide range of machine technologies, both synchronous or asynchronous, can be addressed, even accounting for non trivial geometries such as idealized rotor and stator teeth and slots (Boughrara, Lubin, and Ibtiouen, 2013; Lubin, Mezani, and Rezzoug, 2011a; Lubin, Mezani, and Rezzoug, 2011b; Lubin, Mezani, and Rezzoug, 2012).

In their recent works motivated by vibroacoustic analysis and design of electric motors, Pile et al., 2019b; Pile et al., 2019a; Pile et al., 2020 investigate analytical expressions for surface forces acting on a stator. They stress out the preference for analytical or semi-analytical methods for fast vibroacoustic design and optimization analyses at low computational cost. Their work however considers a restrictive expression for the magnetic stress tensor resulting in no body forces at the stator (under the hypothesis of negligible stator currents) and a restricted surface traction expressions. These particular works show that electric motor's design would benefit from analytical tools for the fine evaluation of forces, stresses and displacement fields.

OUTLINE To the author's knowledge, complete and detailed analytical computations of stresses in electric motor problems, and in particular based on the theoretical framework exposed earlier, do not exist in the literature. Such computations would greatly help in gaining insight on the coupled magneto-mechanical electric motor problem. They would provide benchmarks for validation of more evolved numerical tools. They could also help in the design of electric motors in the spirit of the pre-design analytical magnetic field computations mentioned in the above literature review.

At first, in Section 3.1, calculation are performed on the rotor of an asynchronous induction electric motor. The solid cylindrical rotor geometry adopted here for the sake of the analytical treatment of the boundary value problem, although uncommon in typical induction motors that have slots for conducting wires, is used for high frequency applications (see Gieras and Saari, 2012). The novelty here lies in the analytical computation of the different body forces, stresses and temperature fields, performed using classical methods of elasticity. The results for three different rotor materials (electric steel, copper and aluminum) using realistic geometric and operational regime values and material parameters are presented.

In a second time in Section 3.2, calculations are performed on a cylindrical stator to provide an extension of the rotor calculation to this thinner component, more likely to deform and a major focus of noise and vibration analyses (Pile et al., 2019b; Pile et al., 2019a; Pile et al., 2020). The analytical treatments highlights slight differences proper to this component compared to the rotor case. The results for the magnetic, stress and displacement fields are provided and later compared with the results obtained for different constitutive laws for stress: (1) neglecting the magnetostriction coefficient $\Lambda$; (2) the stress expression typically used in the vibroacoustic literature (Pile et al., 2019b; Pile et al., 2019a; Pile et al., 2020). This stator case is also meant as a reference for the validation of numerical finite element tools developed in Part II of this work.

Both analytical problems provide simplified strong basis for the understanding of the coupled magneto-mechanical behaviors in electric motors. They show how the analytical magnetic field computations presented by the electrical engineering community (e.g. Lubin, Mezani, and Rezzoug, 2011a; Gieras and Saari, 2012), can be complemented by mechanics. Details for the setting of the corresponding boundary value problems are given below.

FOR BOTH PROBLEMS To allow for analytical solutions, the motor geometries and the material behaviors are simplified using a 2D, plane strain framework and a *isotropic, homogeneous, linearized* material response based on the constitutive equations derived in Section 2.2. In particular, the constitutive laws for stresses and magnetization are as derived in (2.26). The magnetic susceptibility $\chi$ and permeability $\mu$, the magneto-mechanical coupling coefficient $\Lambda$, the electrical conductivity $\gamma$, the thermal conductivity $k$, the Lamé constants $\lambda$, $G$ and the mass density $\rho_0$ are all given constants.

## 3.1 ROTOR BOUNDARY VALUE PROBLEM

### 3.1.1 *Problem description*

The cross-section of the simplified induction motor is shown in Figure 3.1; the motor is considered infinitely long in the normal to the plane and under plane strain conditions. It is composed of a cylindrical ferromagnetic rotor (domain $\mathscr{D}_1$ : $0 \leqslant r \leqslant R_1$), surrounded by a cylindrical tubular stator (domain $\mathscr{D}_3$ : $R_2 \leqslant r \leqslant R_3$), separated by an airgap (domain $\mathscr{D}_2$ : $R_1 \leqslant r \leqslant R_2$). Two different polar coordinate systems are used: the stator's fixed reference frame $\mathscr{S}(r, \theta_s, z)$ and the rotor's moving frame $\mathscr{R}(r, \theta, z)$, where $\theta \equiv \theta_s - \Omega t$, with $\Omega$ the clockwise angular velocity of the rotor, as shown in Figure 3.1.

Following Lubin, Mezani, and Rezzoug, 2011a, the motor is loaded by a current sheet of surface density $\kappa$ perpendicular to the plane located on the internal radius of the stator. This current sheet models typical stator coils or windings supplied by a poly-phased (usually three-phased) alternating electric current of angular fre-

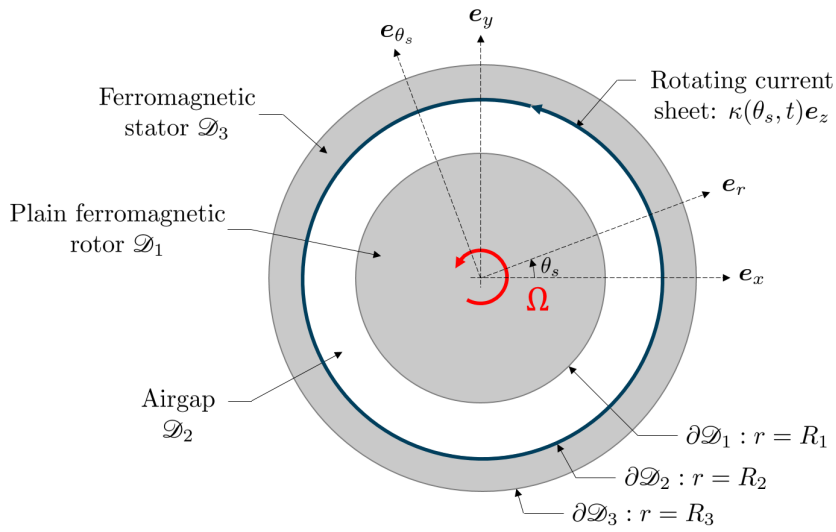


Figure 3.1: Cross-section of the simplified electric motor, indicating rotor, airgap and stator domains and corresponding frames.

quency $\omega$. The coils or windings are organized in $p$ pairs per phase and the applied surface current density is[1]

$$\kappa = \kappa_0 \cos(p\theta_s - \omega t)\hat{e}_z \,, \tag{3.1}$$

with $\kappa_0$ the oscillation's amplitude in A/m. This current sheet rotates around the $z$-axis at the angular frequency $\omega/p$. It creates a rotating magnetic field of the same angular frequency, which triggers induced currents at the rotor. The interaction of the induced currents in the rotor with the magnetic field creates Lorentz forces that result in the rotor spinning at an angular frequency $\Omega$. Given that the phenomenon relies on induction, an angular frequency differential exists between the stator field and the rotor: $\Omega < \omega/p$. We thus define the relative angular frequency $\omega_r$ together with the slip parameter $s$

$$\omega_r = \omega - p\Omega \,; \qquad s \equiv \frac{\omega_r}{\omega} \,, \tag{3.2}$$

where the angular velocities $\omega$ and $\Omega$ are constants, since the steady-state response of the motor is modeled.

Some additional assumptions are necessary to solve the problem.

*i) Infinite permeability, rigid stator* It is assumed that the stator's strains are negligible – thus guaranteeing a constant radius current sheet – and that it has an infinite permeability, i.e. $\mu_3 \longrightarrow \infty$, resulting in a negligible stator h-field

$$r > R_2 : \quad \mathbf{h}_3 = (\nabla \times \mathbf{a}_3)/\mu_3 \approx 0 \,. \tag{3.3}$$

*ii) Constant temperature airgap* The air in the airgap is assumed to be maintained at a constant temperature $T_a$ by forced ventilation. Due to ohmic losses the rotor temperature rises, but a convective heat exchange discharges its excess heat in the airgap. The corresponding radiation condition is

$$r = R_1 : \quad \mathbf{q}\cdot\hat{\mathbf{e}}_r = -k(\nabla T)\cdot\hat{\mathbf{e}}_r = h_c(T(R_1) - T_a) \,, \tag{3.4}$$

1 For simplicity only the fundamental time harmonic of the current supply is considered here.

where $h_c$ is the convection coefficient and $T$ is the rotor temperature field.[2]

*iii) No external mechanical body forces* No purely mechanical body forces, introduced in (1.26) are considered, i.e. $\mathbf{f} = \mathbf{0}$, since gravity effects are assumed negligible compared to inertia and magnetic contributions.

*iv) Constant velocity and acceleration* Assuming a small slip s ($\omega_r \ll \Omega$) and a small vibration amplitude, we can ignore the rates of the displacement $\dot{\mathbf{u}}$ and $\ddot{\mathbf{u}}$ in the velocity and acceleration terms, by keeping only their $\Omega$-dependent contributions, thus considerably simplifying the resulting algebra

$$\dot{\mathbf{x}} \approx r\Omega\hat{\mathbf{e}}_\theta \,, \qquad \ddot{\mathbf{x}} \approx -r\Omega^2\hat{\mathbf{e}}_r \,. \tag{3.5}$$

One consequence is a constant inertia term $-\rho_0 r\Omega^2\hat{\mathbf{e}}_r$ in the linear moment balance (2.11). The other consequence of $(3.5)_1$ are the simpler expressions of the electromotive intensity $\boldsymbol{\mathcal{e}} = \mathbf{e} + \dot{\mathbf{x}}\times\mathbf{b}$ and the material time derivative $\dot{T}$, when expressed in the moving rotor frame (recall $\theta \equiv \theta_s - \Omega t$)

$$\begin{aligned} \boldsymbol{\mathcal{e}} &= \left[-\frac{\partial \mathbf{a}}{\partial t} + \dot{\mathbf{x}}\times\mathbf{b}\right]_{\mathcal{S}} = -\left[\frac{\partial \mathbf{a}}{\partial t} + \Omega\frac{\partial \mathbf{a}}{\partial \theta_s}\right]_{\mathcal{S}} = -\left.\frac{\partial \mathbf{a}}{\partial t}\right|_{\mathscr{R}} , \\ \dot{T} &= \left[\frac{\partial T}{\partial t} + \dot{\mathbf{x}}\cdot(\boldsymbol{\nabla} T)\right]_{\mathcal{S}} = \left[\frac{\partial T}{\partial t} + \Omega\frac{\partial T}{\partial \theta_s}\right]_{\mathcal{S}} = \left.\frac{\partial T}{\partial t}\right|_{\mathscr{R}} . \end{aligned} \tag{3.6}$$

Henceforth all equations are written in the rotor frame $\mathscr{R}$ and all field quantities are functions of $(r, \theta, t)$. These governing equations and boundary conditions for the idealized, 2D motor are summarized below. The variables of the problem are the rotor and airgap vector potential $\mathbf{a} = a_z\hat{\mathbf{e}}_z$, more precisely its unique component $a_z \equiv a$, the rotor temperature $T$ and the rotor elastic stress[3] $\overset{e}{\boldsymbol{\sigma}}$. The parameters of the problem are the rotor electrical conductivity $\gamma$, magnetic permeability $\mu = \mu_0(1+\chi)$, mass density $\rho_0$, specific heat capacity $c_\epsilon$, heat conductivity $k$, rotation angular velocity $\Omega$, the airgap temperature $T_a$, convection coefficient $h_c$, magnetic permeability $\mu_0$, the current angular frequency $\omega_r$ and the number of pole pairs $p$. Specific values of these parameters are later given in Table 3.1 of Section 3.2.3.

$$\mathscr{D}_1 : \begin{cases} \boldsymbol{\nabla}\times\mathbf{b} = \mu\gamma\boldsymbol{\mathcal{e}} \,, \\ \rho_0 c_\epsilon \dfrac{\partial T}{\partial t} - k\boldsymbol{\nabla}^2 T = \gamma\boldsymbol{\mathcal{e}}\cdot\boldsymbol{\mathcal{e}} \,, \\ \boldsymbol{\nabla}\cdot(\overset{e}{\boldsymbol{\sigma}} + \overset{m}{\boldsymbol{\sigma}}) = -\rho_0 r\Omega^2\hat{\mathbf{e}}_r \,, \end{cases}$$

$$\partial\mathscr{D}_1 : \begin{cases} \hat{\mathbf{e}}_r\times[\![\mathbf{h}]\!] = \mathbf{0} \,, \\ \hat{\mathbf{e}}_r\cdot[\![\mathbf{b}]\!] = 0 \,, \\ \hat{\mathbf{e}}_r\cdot(k(\boldsymbol{\nabla} T)) = -h_c(T - T_a) \,, \\ \hat{\mathbf{e}}_r\cdot\left(\overset{e}{\boldsymbol{\sigma}} + \left[\!\left[\overset{m}{\boldsymbol{\sigma}}\right]\!\right]\right) = \mathbf{0} \,, \end{cases} \tag{3.7}$$

2 The temperature field is only defined for the rotor, the $T_1$ notation is not used (the subscript 1 is left out as superfluous).

3 The elastic stress field is only defined in the rotor, the $\overset{e}{\boldsymbol{\sigma}}_1$ notation is not used as unnecessary (the subscript 1 is left out as superfluous).

$$
\begin{aligned}
\mathscr{D}_2 : &\begin{cases} \boldsymbol{\nabla}\times\mathbf{b} = 0 \,, \\ T = T_a \,, \\ \boldsymbol{\sigma} = \overset{m}{\boldsymbol{\sigma}} = \dfrac{1}{\mu_0}\left(\mathbf{b}\mathbf{b} - \dfrac{1}{2}(\mathbf{b}\cdot\mathbf{b})\mathbf{I}\right) \quad \left(\text{with } \boldsymbol{\nabla}\cdot\overset{m}{\boldsymbol{\sigma}} = 0\right) \,, \end{cases} \\
\partial\mathscr{D}_2 : &\begin{cases} \hat{\mathbf{e}}_r\times\mathbf{h} = \kappa_0 \cos(p\theta - \omega_r t)\hat{\mathbf{e}}_z \,, \\ \hat{\mathbf{e}}_r\cdot[\![\mathbf{b}]\!] = 0 \,, \end{cases} \\
\mathscr{D}_1 \cup \mathscr{D}_2 : \mathbf{a} = a(r,\theta,t)\hat{\mathbf{e}}_z \,,\ \boldsymbol{e} &= -\frac{\partial \mathbf{a}}{\partial t} \,,\ \mathbf{b} = \boldsymbol{\nabla}\times\mathbf{a} = \frac{1}{r}\frac{\partial a}{\partial\theta}\hat{\mathbf{e}}_r - \frac{\partial a}{\partial r}\hat{\mathbf{e}}_\theta \,.
\end{aligned}
\tag{3.8}
$$

In the stress boundary condition on $\partial\mathscr{D}_1$ there is no elastic stress field in the airgap, i.e. $\overset{e}{\boldsymbol{\sigma}}_2 = 0$; in contrast to the magnetic stress field $\overset{m}{\boldsymbol{\sigma}}$ that exists in both the rotor and the airgap (where it equals Maxwell-stress in vacuum). The boundary condition on the radial component of the magnetic field on $\partial\mathscr{D}_2$ simply provides the leak of magnetic field to the stator domain $\mathscr{D}_3$. The boundary condition on the tangent component of the airgap h-field accounts for the negligible stator h-field based on (3.3) and without ambiguity the index referring to the airgap side on $\mathbf{h}$ is dropped.

*v*) External torque applied at rotor's center To balance the moment produced by the shear stresses, it is assumed that an external mechanical torque is applied at the center line of the rotor ($r = 0$) along the $z$-axis. The resulting torque per unit rotor length $\mathscr{T}\hat{\mathbf{e}}_z$ is

$$
\mathscr{T} = r^2 \int_0^{2\pi} \sigma_{r\theta}(r,\theta)\mathrm{d}\theta \,, \tag{3.9}
$$

and will be shown to be a constant, function of the relative angular frequency $\mathscr{T}(\omega_r)$ with $\mathscr{T}(0) = 0$.

### 3.1.2 *Dimensionless boundary value problem*

To guide the physical interpretation of the results, the following dimensionless variables and parameters of the problem are introduced

$$
\frac{r}{R_1} \to r,\ \omega_r t \to t,\ \frac{a}{\mu_0\kappa_0 R_1} \to a,\ \frac{k(T - T_a)}{\gamma\omega_r^2(\mu_0\kappa_0)^2 R_1^4} \to T,\ \frac{\boldsymbol{\sigma}}{\rho_0 R_1^2\Omega^2} \to \boldsymbol{\sigma}, \tag{3.10}
$$

together with the airgap normalized thickness parameter $\zeta \equiv \frac{R_2 - R_1}{R_1}$.

> Henceforth, for simplicity the dimensionless variables and field quantities of the problem, $r$, $t$, $a$, $T$, $\boldsymbol{\sigma}$ are denoted by the same symbol as their dimensioned counterparts.

The governing equations and associated interface and boundary conditions (in the rotor frame) are given below,[4] starting with the magnetic potential $a(r,\theta,t)$

$$\begin{aligned}
&\nabla^2 a_1 = \alpha^2 \frac{\partial a_1}{\partial t}\,, \quad \alpha^2 \equiv \mu\gamma\omega_r R_1^2\,; && 0 \leqslant r \leqslant 1\,,\\
&\nabla^2 a_2 = 0\,; && 1 \leqslant r \leqslant 1+\zeta\,,\\
&\frac{\partial a_1}{\partial r} = (1+\chi)\frac{\partial a_2}{\partial r}\,, \quad \frac{\partial a_1}{\partial \theta} = \frac{\partial a_2}{\partial \theta}\,; && r = 1\,,\\
&\frac{\partial a_2}{\partial r} = \cos(p\theta - t)\,; && r = 1+\zeta\,.
\end{aligned} \tag{3.11}$$

The governing equation and boundary condition for the rotor's temperature field $T(r,\theta,t)$ are

$$\begin{aligned}
&\mathscr{F}^{-1}\frac{\partial T}{\partial t} - \nabla^2 T = \left(\frac{\partial a_1}{\partial t}\right)^2\,, \quad \mathscr{F} \equiv \frac{k}{\rho_0 c_\epsilon \omega_r R_1^2}\,; && 0 \leqslant r \leqslant 1\,,\\
&\mathscr{B}\frac{\partial T}{\partial r} + T = 0\,, \quad \mathscr{B} \equiv \frac{k}{R_1 h_c}\,; && r = 1\,,
\end{aligned} \tag{3.12}$$

with $\mathscr{F}$ and $\mathscr{B}$ the "*F*ourier" and "*B*iot" dimensionless coefficients respectively.

Finally, the governing equations and boundary conditions for the rotor's elastic stress field $\overset{e}{\boldsymbol{\sigma}}(r,\theta,t)$ are[5]

$$\begin{aligned}
&\nabla\cdot\overset{e}{\boldsymbol{\sigma}} = \mathbf{f}\,, \quad \mathbf{f} \equiv s_j\alpha^2\frac{\partial \mathbf{a}_1}{\partial t}\times(\nabla\times\mathbf{a}_1) - s_m\nabla\left(\|\nabla\times\mathbf{a}_1\|^2\right) - r\hat{\mathbf{e}}_r\,; && 0 \leqslant r \leqslant 1\,,\\
&\overset{e}{\sigma}_{rr} = \frac{s_0}{2}\left[\left(\frac{\partial a_2}{\partial\theta}\right)^2 - \left(\frac{\partial a_2}{\partial r}\right)^2\right] - \left(\frac{s_j}{2}+s_m\right)\left(\frac{\partial a_1}{\partial\theta}\right)^2 + \left(\frac{s_j}{2}-s_m\right)\left(\frac{\partial a_1}{\partial r}\right)^2\,; && r = 1\,,\\
&\overset{e}{\sigma}_{r\theta} = -s_0\frac{\partial a_2}{\partial\theta}\frac{\partial a_2}{\partial r} + s_j\frac{\partial a_1}{\partial\theta}\frac{\partial a_1}{\partial r}\,; && r = 1\,,\\
&s_j \equiv s_0\frac{1+\Lambda}{1+\chi}\,, \quad s_m \equiv \frac{s_0}{2}\frac{\chi+\Lambda}{1+\chi}\,, \quad s_0 \equiv \frac{\mu_0\kappa_0^2}{\rho_0 R_1^2\Omega^2}\,.
\end{aligned} \tag{3.13}$$

$s_0$ is an equivalent of the "*Stuart*" number for magnetic fluids and gives the ratio of Maxwell over inertia stress magnitudes. The dimensionless coefficients $s_j$ and $s_m$ appearing in the expressions for the total stress in the rotor $\boldsymbol{\sigma}_1$ (sum of the elastic $\overset{e}{\boldsymbol{\sigma}}$ and the magnetic $\overset{m}{\boldsymbol{\sigma}}$ components respectively; see 2.26) depend on its magnetic properties while the total stress tensor in the airgap $\boldsymbol{\sigma}_2$ (Maxwell stress in vacuum; see 2.7) depends only on $s_0$. The corresponding expressions for the magnetic field and the total stress in each domain are given by

$$\begin{aligned}
&\boldsymbol{\sigma}_1 = \overset{e}{\boldsymbol{\sigma}} + \overset{m}{\boldsymbol{\sigma}}\,, \ \overset{m}{\boldsymbol{\sigma}} = s_j\mathbf{b}_1\mathbf{b}_1 + (s_m - \frac{s_j}{2})(\mathbf{b}_1\cdot\mathbf{b}_1)\mathbf{I}\,, \ \mathbf{b}_1 = \nabla\times\mathbf{a}_1\,; && 0 \leqslant r \leqslant 1\,,\\
&\boldsymbol{\sigma}_2 = \overset{m}{\boldsymbol{\sigma}} = s_0[\mathbf{b}_2\mathbf{b}_2 - \frac{1}{2}(\mathbf{b}_2\cdot\mathbf{b}_2)\mathbf{I}]\,, \ \mathbf{b}_2 = \nabla\times\mathbf{a}_2\,; && 1 \leqslant r \leqslant 1+\zeta\,.
\end{aligned}$$

4 Only the radius of each domain of validity is recorded, since in all domains the angle $\theta \in [0, 2\pi)$ and the time $t \in \mathbb{R}^+$.

5 Henceforth the rotor's body force is denoted by $\mathbf{f}$, taking the symbol used in (1.26) for the purely mechanical body force.

(3.14)

We first solve (3.11) to find the magnetic potential $a$, thus obtaining the ohmic dissipation for the heat equation (3.12), which is then used to determine the rotor's temperature field $T$. The magnetic potential gives the body forces for the linear momentum balance in (3.13), thus providing the rotor's elastic field $\overset{e}{\boldsymbol{\sigma}}$.

#### 3.1.2.1 *Magnetic Potential*

Solving the linear problem in (3.11) subject to the harmonic loading in (3.1), is more efficiently done in the complex domain, where the magnetic potential $a_k(r,\theta,t)$ takes the form

$$\begin{aligned} a_k(r,\Theta) &= \Re\{\bar{a}_k(r)\exp(-i\Theta)\} = A_k(r)\cos\Theta + B_k(r)\sin\Theta\ ,\ k=1,2\ ; \\ \Theta &\equiv p\theta - t\ , \end{aligned} \tag{3.15}$$

where $\bar{a}_k(r) = A_k(r) + iB_k(r)$ is the complex[6] magnetic potential amplitude that depends only on $r$.

In the rotor domain, (3.11) results in a Bessel differential equation for the complex amplitude $\bar{a}_1(r)$

$$\begin{aligned} r^2\frac{d^2\bar{a}_1}{dr^2} + r\frac{d\bar{a}_1}{dr} + (\bar{\alpha}^2r^2 - p^2)\bar{a}_1 = 0 \implies \bar{a}_1(r) = \bar{A}J_p(\bar{\alpha}r)\ ; \\ \bar{\alpha}^2 \equiv -i\alpha^2\ , \end{aligned} \tag{3.16}$$

where the constant $\alpha^2$ is defined in (3.11) and $J_p$ denotes a Bessel function of the first kind. The above expression for $\bar{a}_1$ accounts for the fact that there is no singularity in $r = 0$, and hence explains the absence of a Bessel function of the second kind in the general solution.

In the airgap domain, (3.11) gives a Laplace equation for the complex amplitude $\bar{a}_2(r)$

$$r^2\frac{d^2\bar{a}_2}{dr^2} + r\frac{d\bar{a}_2}{dr} - p^2\bar{a}_2 = 0 \implies \bar{a}_2(r) = \bar{B}r^p + \bar{C}r^{-p}\ . \tag{3.17}$$

The complex-valued constants $\bar{A}$, $\bar{B}$ and $\bar{C}$ appearing in (3.16) and (3.17) are determined using the interface and boundary conditions in (3.11), and are found to be

$$\begin{aligned} \bar{A} &= \frac{2\hbar}{J_p(\bar{\alpha}) + \bar{g}}\ , \\ \bar{B} &= \hbar\left[1 - \frac{2\bar{g}}{[J_p(\bar{\alpha}) + \bar{g}][1 + (1+\zeta)^{-2p}]}\right]\ , \\ \bar{C} &= \hbar\left[1 - \frac{2\bar{g}}{[J_p(\bar{\alpha}) + \bar{g}][1 + (1+\zeta)^{2p}]}\right]\ , \\ \bar{g} &\equiv \left[J_p(\bar{\alpha}) - \frac{\bar{\alpha}}{p}J_{p+1}(\bar{\alpha})\right]\left[\frac{(1+\zeta)^p + (1+\zeta)^{-p}}{(1+\zeta)^p - (1+\zeta)^{-p}}\right]\frac{1}{1+\chi}\ , \\ \hbar &\equiv \frac{(1+\zeta)}{p[(1+\zeta)^p - (1+\zeta)^{-p}]}\ . \end{aligned} \tag{3.18}$$

6 Complex quantities are henceforth denoted by an overbar ($\bar{\ }$).

Using (3.18), the sought real amplitudes $A_k(r)$ and $B_k(r)$ in (3.15) are given in terms of their complex counterparts found in (3.16) and (3.17), i.e. $A_k(r) = \Re\{\bar{a}_k(r)\}$, $B_k(r) = \Im\{\bar{a}_k(r)\}$; $k = 1, 2$.

#### 3.1.2.2 *Rotor temperature*

From the linearity of the governing equations for the temperature field in (3.12) and the magnetic potential solution in the rotor in (3.16), the forcing term in the conduction equation is found to be: $(\partial a_1/\partial t)^2 = 0.5[(B_1(r))^2 + (A_1(r))^2] + 0.5[(B_1(r))^2 - (A_1(r))^2]\cos(2\Theta) - A_1(r)B_1(r)\sin(2\Theta)$. The use of superposition and complex formulation lead to the following rotor temperature field $T(r, \theta, t)$

$$T(r, \Theta) = T_0(r) + \Re\left\{\bar{T}(r)\exp(-i2\Theta)\right\}\ ; \quad \Theta \equiv p\theta - t\ , \tag{3.19}$$

where the function $T_0(r)$ is real and $\bar{T}(r)$ is complex. The real function $T_0(r)$ is found from (3.12) to be

$$\frac{d^2T_0}{dr^2} + \frac{1}{r}\frac{dT_0}{dr} = -\frac{{B_1}^2 + {A_1}^2}{2} \implies T_0(r) = c_0 - \frac{1}{2}\int_0^r\left(\frac{1}{r}\int_0^r[B_1^2 + A_1^2]rdr\right)dr, \tag{3.20}$$

with the unknown constant $c_0$ to be determined from the boundary condition. Also recall $A_1(r)$ and $B_1(r)$ are functions of $r$.

Solving for the complex function $\bar{T}(r)$ is reduced to solving a Bessel differential equation with a forcing term through the superposition of a homogeneous and a particular solution $\bar{T}_p(r)$, as follows

$$\begin{aligned}
&r^2\frac{d^2\bar{T}}{dr^2} + r\frac{d\bar{T}}{dr} + \left(\bar{\beta}^2r^2 - (2p)^2\right)\bar{T} = r^2\frac{\bar{a}_1^2}{2} \implies \bar{T}(r) = \bar{c}J_{2p}(\bar{\beta}r) + \bar{T}_p(r);\\
&\bar{T}_p(r) = \frac{\pi}{4}\left[-J_{2p}(\bar{\beta}r)\int_0^r Y_{2p}(\bar{\beta}r)\bar{a}_1^2rdr + Y_{2p}(\bar{\beta}r)\int_0^r J_{2p}(\bar{\beta}r)\bar{a}_1^2rdr\right];\\
&\bar{\beta}^2 \equiv -\frac{2i}{\mathscr{F}};
\end{aligned} \tag{3.21}$$

where the unknown constant $\bar{c}$ in the homogeneous part of the solution will be specified from the boundary condition. In solving (3.21) we made use of the fact that the solution is bounded at $r = 0$, and hence there is no contribution from the Bessel function of the second kind $Y_{2p}$ to the homogeneous part of the solution. However, $Y_{2p}$ does enter under the integrals in the expressions for the particular solution $\bar{T}_p(r)$ as seen above. Also recall $\bar{a}_1(r)$ in the expressions is a function of $r$.

Finally, the boundary condition at $r = 1$ in (3.12) splits into two boundary conditions: one for $T_0(r)$ that gives $c_0$ and the other for $\bar{T}(r)$ that provides $\bar{c}$

$$\begin{aligned}
c_0 &= \frac{1}{2}\left[\int_0^1\frac{1}{r}\int_0^r[{B_1}^2 + {A_1}^2]rdr\,dr + \mathscr{B}\int_0^1[{B_1}^2 + {A_1}^2]rdr\right],\\
\bar{c} &= \frac{\pi}{4}\left[\int_0^1 Y_{2p}(\bar{\beta}r)\bar{a}_1^2rdr - \frac{Y_{2p}(\bar{\beta}) + \mathscr{B}\bar{\beta}Y'_{2p}(\bar{\beta})}{J_{2p}(\bar{\beta}) + \mathscr{B}\bar{\beta}J'_{2p}(\bar{\beta})}\int_0^1 J_{2p}(\bar{\beta}r)\bar{a}_1^2rdr\right],
\end{aligned} \tag{3.22}$$

where $J'_{2p}$ and $Y'_{2p}$ denote the derivatives of the first and second kind Bessel functions of order $2p$ with respect to their argument. Also recall $\bar{a}_1(r)$, $A_1(r)$, $B_1(r)$ are functions of $r$.

Having determined $T_0(r)$ and $\bar{T}(r)$, one can find from (3.19) the rotor temperature field $T(r, \Theta)$.

#### 3.1.2.3 *Rotor stresses*

The principle of superposition is used again for determining the rotor's elastic stress field $\overset{e}{\boldsymbol{\sigma}}$. Recalling the definitions for $\mathbf{f}$ in (3.13) and the solution for the magnetic potential $a_1$ in (3.15) and (3.16), the body forces can be expressed as $\mathbf{f}(r,\Theta) = \mathbf{N}(r) + \boldsymbol{\nabla} V(r,\Theta)$[7], where $\mathbf{N}(r)$ is not derivable from a potential (non-conservative part of the force field), while the remaining terms are derivable from a potential $V(r,\Theta)$.

$$
\begin{aligned}
&\mathbf{f} = \mathbf{N} + \boldsymbol{\nabla} V \,; \\
&\mathbf{N} = -\frac{s_j \alpha^2}{2}\frac{p}{r}(A_1^2 + B_1^2)\hat{\mathbf{e}}_\theta \,; \\
&V(r,\Theta) = V_0(r) + V_{cs}(r,\Theta)\,, \quad V_{cs} = V_c(r)\cos(2\Theta) + V_s(r)\sin(2\Theta)\,, \\
&V_0(r) = -\frac{r^2}{2} + \frac{s_j \alpha^2}{2}\int_0^r (A_1 B_1' - A_1' B_1)\mathrm{d}r - \frac{s_m}{2}\left(\frac{p^2}{r^2}(A_1^2 + B_1^2) + (A_1'^2 + B_1'^2)\right), \\
&V_c(r) = -\frac{s_j \alpha^2}{2} A_1 B_1 - \frac{s_m}{2}\left(\frac{p^2}{r^2}(B_1^2 - A_1^2) + (A_1'^2 - B_1'^2)\right), \\
&V_s(r) = \frac{s_j \alpha^2}{2}\frac{(A_1^2 - B_1^2)}{2} - s_m\left(\frac{p^2}{r^2} A_1 B_1 + A_1' B_1'\right).
\end{aligned}
\tag{3.23}
$$

Consequently, the rotor's elastic stress field $\overset{e}{\boldsymbol{\sigma}}$ is decomposed as follows

$$
\overset{e}{\boldsymbol{\sigma}}(r,\Theta) = \overset{e^N}{\boldsymbol{\sigma}}(r) + \overset{e^V}{\boldsymbol{\sigma}}(r,\Theta) + \overset{e^h}{\boldsymbol{\sigma}}(r,\Theta)\,, \quad
\begin{cases}
\boldsymbol{\nabla}\cdot\overset{e^N}{\boldsymbol{\sigma}} = \mathbf{N}\,, \\
\boldsymbol{\nabla}\cdot\overset{e^V}{\boldsymbol{\sigma}} = \boldsymbol{\nabla} V\,, \\
\boldsymbol{\nabla}\cdot\overset{e^h}{\boldsymbol{\sigma}} = \mathbf{0}\,,
\end{cases}
\tag{3.24}
$$

where each one of the constituent fields $\overset{e^N}{\boldsymbol{\sigma}}$, $\overset{e^V}{\boldsymbol{\sigma}}$, $\overset{e^h}{\boldsymbol{\sigma}}$ corresponds, in view of (2.25), to a compatible elastic strain field, i.e. derivable from a displacement field. By abuse of terminology we call these elastic stress fields *elastically compatible*.

Using the expression for $\mathbf{N}(r)$ from (3.23), an elastically compatible particular solution for $\overset{e^N}{\boldsymbol{\sigma}}(r)$ is found[8] by solving the tangential equilibrium ODE,

$$
\frac{\mathrm{d}\overset{e^N}{\sigma}_{r\theta}}{\mathrm{d}r} + \frac{2}{r}\overset{e^N}{\sigma}_{r\theta} = -\frac{s_j \alpha^2}{2}\frac{p}{r}(A_1^2 + B_1^2) \implies \overset{e^N}{\sigma}_{r\theta} = -\frac{s_j \alpha^2}{2}\frac{p}{r^2}\int_0^r r(A_1^2 + B_1^2)\mathrm{d}r\,. \tag{3.25}
$$

An elastically compatible particular solution for the elastic stress field $\overset{e^V}{\boldsymbol{\sigma}}$ is found using the Airy stress function method in polar coordinates (see Barber, 2010).

---

7 Given the electromagnetic part of the forcing $\overset{m}{\mathbf{f}} = -\boldsymbol{\nabla}\cdot\overset{m}{\boldsymbol{\sigma}}$ in (3.13), it is tempting to choose $\overset{e}{\boldsymbol{\sigma}} = -\overset{m}{\boldsymbol{\sigma}}$ as a particular solution to the electromagnetic forcing $\overset{m}{\mathbf{f}}$. However, this particular solution is ineligible as it does not satisfy the compatibility condition (see Barber, 2010), thus leading to the proposed approach (for additional details see Appendix B.3).

8 Because we look for a particular solution only, integration constants are discarded.

The components of $\overset{e\,V}{\boldsymbol{\sigma}}$ can be expressed in terms of a stress potential $\phi_V$ as follows

$$\begin{aligned}&\overset{e\,V}{\sigma}_{rr}=\frac{1}{r}\frac{\partial\phi_V}{\partial r}+\frac{1}{r^2}\frac{\partial^2\phi_V}{\partial\theta^2}+V\,,\ \overset{e\,V}{\sigma}_{\theta\theta}=\frac{\partial^2\phi_V}{\partial r^2}+V\,,\ \overset{e\,V}{\sigma}_{r\theta}=-\frac{\partial}{\partial r}\left(\frac{1}{r}\frac{\partial\phi_V}{\partial\theta}\right)\ ;\\&\nabla^2\phi_V=-\frac{1-2\nu}{1-\nu}V\,.\end{aligned}\tag{3.26}$$

The stress potential $\phi_V$ is found (see footnote 8), by solving the Laplacian in (3.26) with the help of (3.23)

$$\phi_V(r,\Theta)=-\frac{1-2\nu}{1-\nu}\left(\int_0^r\frac{1}{r}\int_0^r V_0 r\,dr\,dr+\frac{r^{2p}}{4p}\int_0^r V_{cs}r^{-2p+1}dr-\frac{r^{-2p}}{4p}\int_0^r V_{cs}r^{2p+1}dr\right).\tag{3.27}$$

The components of the elastically compatible homogeneous solution stress field $\overset{e\,h}{\boldsymbol{\sigma}}$ are expressed in terms of the potential $\phi_h$

$$\begin{aligned}&\overset{e\,h}{\sigma}_{rr}=\frac{1}{r}\frac{\partial\phi_h}{\partial r}+\frac{1}{r^2}\frac{\partial^2\phi_h}{\partial\theta^2}\,,\ \overset{e\,h}{\sigma}_{\theta\theta}=\frac{\partial^2\phi_h}{\partial r^2}\,,\ \overset{e\,V}{\sigma}_{r\theta}=-\frac{\partial}{\partial r}\left(\frac{1}{r}\frac{\partial\phi_V}{\partial\theta}\right)\ ;\\&\nabla^4\phi_h=0\,.\end{aligned}\tag{3.28}$$

Solving the biharmonic equation for $\phi_h$ in (3.28) we obtain[9]

$$\begin{aligned}\phi_h(r,\Theta)=\Phi_{01}\frac{r^2}{2}+\Phi_{02}\theta+\left(\Phi_{c1}r^{2p}+\Phi_{c2}r^{2p+2}\right)\cos(2\Theta)\\+\left(\Phi_{s1}r^{2p}+\Phi_{s2}r^{2p+2}\right)\sin(2\Theta)\,.\end{aligned}\tag{3.29}$$

The final expressions for $\overset{e\,h}{\boldsymbol{\sigma}},\overset{e\,V}{\boldsymbol{\sigma}}$ are obtained from (3.28) and (3.28) but are too cumbersome to be recorded here; they are given in Appendix B.4. The six constants $\Phi_{01},\Phi_{02},\Phi_{c1},\Phi_{c2},\Phi_{s1},\Phi_{s2}$ are determined by the $r=1$ boundary conditions in (3.13)

$$\begin{aligned}&\overset{e\,V}{\sigma}_{rr}(1,\Theta)+\overset{e\,h}{\sigma}_{rr}(1,\Theta)=\frac{s_0}{2}\left[\left(\frac{\partial a_2}{\partial\theta}\right)^2-\left(\frac{\partial a_2}{\partial r}\right)^2\right]-\left(\frac{s_j}{2}+s_m\right)\left(\frac{\partial a_1}{\partial\theta}\right)^2+\left(\frac{s_j}{2}-s_m\right)\left(\frac{\partial a_1}{\partial r}\right)^2,\\&\overset{e\,N}{\sigma}_{r\theta}(1,\Theta)+\overset{e\,V}{\sigma}_{r\theta}(1,\Theta)+\overset{e\,h}{\sigma}_{r\theta}(1,\Theta)=-s_0\frac{\partial a_2}{\partial\theta}\frac{\partial a_2}{\partial r}+s_j\frac{\partial a_1}{\partial\theta}\frac{\partial a_1}{\partial r}\,.\end{aligned}\tag{3.30}$$

From the decomposition in radial, cosine and sine terms (see footnote 9), result three equations for the normal and three equations for the tangential boundary conditions, thus uniquely determining the sought constants. The full expressions for the stress at the rotor (elastic and magnetic components) can be then determined from (3.14) and (3.24).

9 The solution is extracted from the general Michell, 1899 solution. Given the form of the body forces and boundary conditions, only those terms consistent with a solution of the form $\overset{e}{\boldsymbol{\sigma}}=\overset{e}{\sigma}_0(r)+\overset{e}{\sigma}_c(r)\cos(2\Theta)+\overset{e}{\sigma}_s(r)\sin(2\Theta)$ are kept. Also, all terms leading to stress singularities in $r=0$ are excluded except for the $\Phi_{02}\theta$ term required for the torque at $r=0$.

#### 3.1.2.4 *Rotor torque*

We are now in a position to give the expression for the torque/unit length $\mathcal{T}$. Recalling (3.9) and using the results for the stress field obtained above, one has

$$\mathcal{T} = 4\pi\rho_0\Omega^2 R_1^4 s_0 p \left(\frac{\hbar}{\|J_p(\bar{\alpha}) + \bar{\mathcal{G}}\|}\right)^2 \Im\left\{J_p(\bar{\alpha})\bar{\alpha}^* J_{p+1}(\bar{\alpha})^*\right\}, \tag{3.31}$$

where $(\ )^*$ denotes complex conjugation. This result gives the torque in terms of geometry, applied current (poles, amplitude and frequency), magnetic and electric properties and density of the rotor. Remarkably, $\mathcal{T}$ is independent of the mechanical properties of the rotor, i.e. its shear modulus G and Poisson ratio $\nu$.

As the torque is a function of slip velocity $\omega_r$, it is instructive to find from (3.31) the initial slope of the $\mathcal{T}(\omega_r)$ curve. Using asymptotics of the Bessel functions with respect to $\bar{\alpha}$ for $\|\bar{\alpha}\|^2 = \alpha^2 = \omega_r \mu\gamma R_1^2 \ll 1$, one obtains

$$\mathcal{T} \approx \omega_r \frac{2\pi\gamma}{p(1+p)}\left[\frac{\mu_0\kappa_0(1+\chi)(1+\zeta)R_1}{(1+\zeta)^p+(1+\zeta)^{-p}+(1+\chi)[(1+\zeta)^p-(1+\zeta)^{-p}]}\right]^2 + O(\omega_r)^2. \tag{3.32}$$

One should keep in mind that the above expression gives only the initial slope of the $\mathcal{T}(\omega_r)$ curve, but depending on the problem, the range of validity of this linear approximation can be very small.

### 3.1.3 *Results and discussion*

Although we solve an idealized motor, the results presented here correspond to materials, geometries and operating parameters found in the electrical engineering literature. The dimensionless quantities introduced in (3.10) allow a direct comparison of the results to related physically meaningful quantities.

#### 3.1.3.1 *Material, geometry and operating parameters*

The motor geometry and operating parameters used in the calculations are shown in Table 3.1. The study covers three materials typically found in electric motors: electrical steel, copper and aluminum. Despite the different motor architecture, the same values as in Lubin, Mezani, and Rezzoug, 2011a are used whenever possible. The peak value of the current sheet is presently reduced to $1.3\times10^4$ A/m – from $8\times10^4$ A/m in Lubin, Mezani, and Rezzoug, 2011a – in order to keep the maximum value of the magnetic field in the steel rotor below saturation,[10] phenomenon not accounted for here.

Unfortunately, not all needed parameters can be found for a particular electric steel, thus requiring the use of experimental data from the open literature for comparable materials. The value for the magneto-mechanical coupling coefficient $\Lambda$ is fitted from Aydin et al., 2017, for the no-prestressed case, as detailed in Appendix B.2. A typical value for the magnetic susceptibility $\chi = 4000$ for electric steel is adopted, while the elastic constants $\nu$ and E are taken from Belahcen et al., 2006.

10 The chosen current sheet amplitude results in a maximum magnetic field of about 1.3T for the base case motor (steel rotor), roughly corresponding to the onset of magnetic field saturation for typical electrical steels (e.g. M400-50A), see Rekik, Hubert, and Daniel, 2014.

| **Geometry** | | | |
|---|---|---|---|
| Rotor radius $R_1$ | 6 cm | | |
| Airgap parameter $\zeta = (R_2 - R_1)/R_1$ | 0.05 (base case) | | |
| Number of pole pairs $p$ | 2 | | |
| **Operating parameters** | | | |
| Peak value of current sheet $\kappa_0$ | $1.3\times10^4$ A/m | | |
| Angular velocity of current supply $\omega$ | $100\pi$ rad/s | | |
| Slip $s = \omega_r/\omega$ | 2% (base case) | | |
| External temperature $T_a$ | 20°C | | |
| Convection coefficient $h_c$ | 40 W/m$^2$/K | | |
| **Material properties** | **Electrical steel** | **Copper** | **Aluminum** |
| Electric conductivity $\gamma$ | $2.67\times10^6$ S/m | $5.96\times10^7$ S/m | $3.5\times10^7$ S/m |
| Magnetic susceptibility $\chi$ | 4,000 | $\approx 0$ | $\approx 0$ |
| Magneto-mechanical coupling $\Lambda$ | $-1,800$ | $\approx 0$ | $\approx 0$ |
| Mass density $\rho_0$ | 7,650 kg/m$^3$ | 8,940 kg/m$^3$ | 2,700 kg/m$^3$ |
| Young's modulus $E$ | $183\times10^9$ Pa | $117\times10^9$ Pa | $69\times10^9$ Pa |
| Poisson ratio $\nu$ | 0.34 | 0.33 | 0.32 |
| Specific heat capacity $c_\epsilon$ | 480 J/kg/K | 385 J/kg/K | 921 J/kg/K |
| Thermal conductivity $k$ | 45 W/m/K | 397 W/m/K | 225 W/m/K |

Table 3.1: Motor geometry, operating parameters and rotor material properties for the rotor boundary value problem

The rest of the material parameters – not given in Belahcen et al., 2006 and Aydin et al., 2017 – are taken from the open literature, as it is also done for the case of copper and aluminum, where we assume negligible magnetic effects ($\chi = \Lambda = 0$).

The base case motor, which serves as a benchmark, is made of electric steel, has an airgap parameter $\zeta = 0.05$ and a slip parameter $s = 0.02$. The rest of the geometric and operating parameters are kept fixed, independently of the rotor material, as shown below in Table 3.1.

As discussed in Subsection 3.1.1, the equations are solved in the rotor frame $\mathscr{R}$ and all field quantities are functions of $(r, \Theta)$, where $\Theta = p\theta - t$ and $p$ the motor pole number (here taken $p = 2$). The results here are a snapshot of these rotating fields at $t = 0$ and are presented by plotting the corresponding field quantity at $(r, \theta)$.

#### 3.1.3.2 *Magnetic field in rotor and airgap*

Magnetic field calculations for realistic geometries are routine for the electrical engineering community. The results for the current simple motor geometry are

presented here solely for the purpose of explaining the resulting force and strain fields.

The magnetic field plots in Figure 3.2 and Figure 3.3 show the contours of the dimensionless (normalized by $\mu_0\kappa_0$) magnetic field $\|\mathbf{b}\| = (b_r^2 + b_\theta^2)^{1/2}$ for three different values of the slip parameter $s = 0.02,\ 0.05,\ 0.10$ in the case of a steel rotor with an airgap parameter $\zeta = 0.05$. Notice that the magnetic field increases away from the center and peaks in a localized zone near the rotor periphery. As the slip $s$ (equivalently the relative velocity $\omega_r$) increases, the localized high magnetization zone narrows, (e.g. see Jackson, 1999 that the skin depth $\delta = (2/\gamma\omega_r\mu)^{1/2}$). The four localized magnetic field zones are a result of the number of poles ($p = 2$).

The high permeability of the rotor material ($\chi = 4000$ for electric steel) drastically increases its magnetic field, thus masking the variations of the considerably smaller – by one order of magnitude – strength of the magnetic field in the airgap in Figures 3.2. To remedy this, Figure 3.3 shows only the airgap magnetic field (hiding the rotor magnetic field) for the $s = 0.02$ slip motor of Figure 3.2(a).

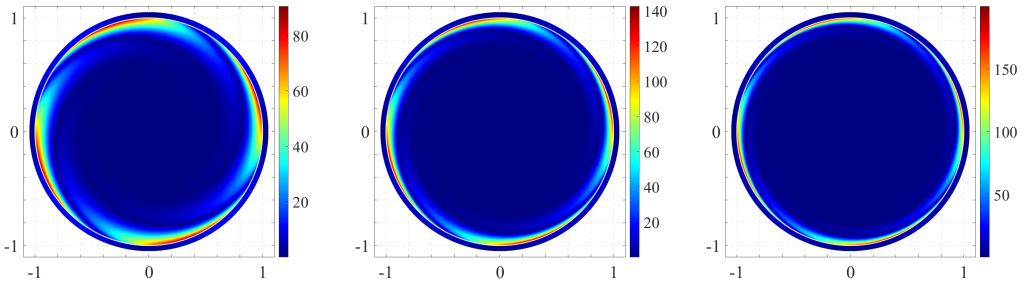


(a) $\|\mathbf{b}\|$ for $s = 0.02$ (b) $\|\mathbf{b}\|$ for $s = 0.05$ (c) $\|\mathbf{b}\|$ for $s = 0.10$

Figure 3.2: Magnetic field norm $\|\mathbf{b}\|$ for a steel rotor (normalized by $\mu_0\kappa_0$), for different values of the slip parameter $s$.

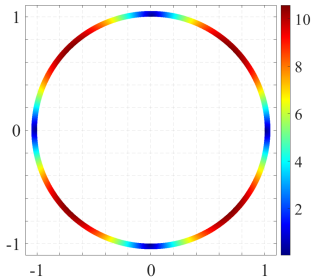


Figure 3.3: Magnetic field norm $\|\mathbf{b}\|$ in the airgap region (normalized by $\mu_0\kappa_0$) for the base case motor in Figure 3.2(a).

The influence of changing motor geometry is presented in Figure 3.4 for three different airgap parameters $\zeta = 0,02,\ 0.05,\ 0.10$ in a steel rotor and a slip value $s = 0.02$. As expected, reducing the airgap size does not affect the distribution of the magnetic field, but increases drastically the maximum strength of the field.

Comparison of the magnetic fields for different rotor materials is presented in Figure 3.5, where the results for the high magnetic susceptibility steel are con-

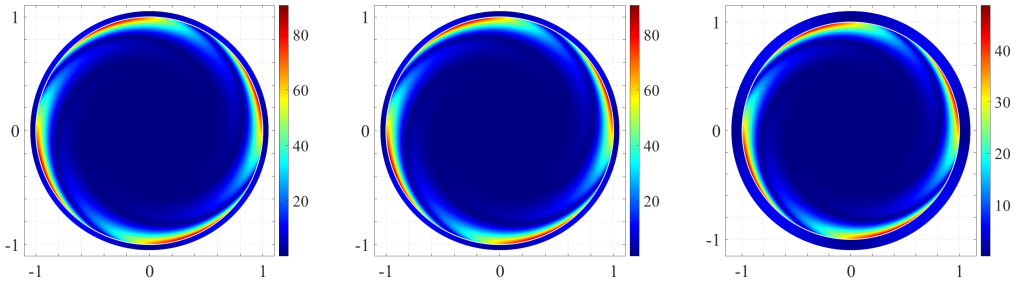

(a) $\|\mathbf{b}\|$ for $\zeta = 0.02$ (b) $\|\mathbf{b}\|$ for $\zeta = 0.05$ (c) $\|\mathbf{b}\|$ for $\zeta = 0.10$

Figure 3.4: Magnetic field norm $\|\mathbf{b}\|$ for a steel rotor (normalized by $\mu_0\kappa_0$), for different values of the airgap parameter $\zeta$.

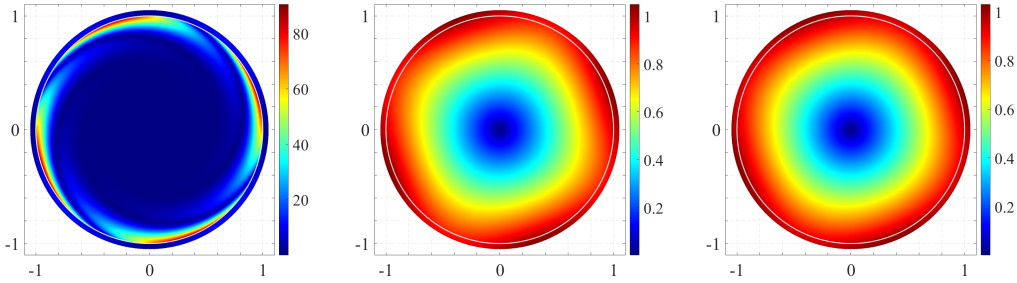

(a) $\|\mathbf{b}\|$ – steel (b) $\|\mathbf{b}\|$ – copper (c) $\|\mathbf{b}\|$ – aluminum

Figure 3.5: Magnetic field norm $\|\mathbf{b}\|$ (normalized by $\mu_0\kappa_0$), for different rotor materials in motors with $s = 0.02,\ \zeta = 0.05$.

trasted to the non-magnetic copper and aluminum rotors. The slip and airgap parameters are kept at their default value $s = 0.02$, $\zeta = 0.05$. Notice that for both the copper and aluminum rotors the maximum value of the magnetic field is two orders of magnitude less than in steel. One can also observe that the normalized magnetic field for aluminum and copper reaches its maximum value at the rotor boundary, given the absence of magnetization in these materials. The slightly larger extent for the maximum magnetic field zone for the copper rotor, is attributed to its higher electrical conductivity which results in higher induced currents than in aluminum.

#### 3.1.3.3 *Rotor temperature field*

The full-field dimensionless temperature[11] $(T - T_a)/T_a \to T(r, \Theta)$ for the base case steel rotor is presented in Figure 3.6; the normalization with respect to the reference temperature $T^a$ adopted here as a more physically meaningful choice. Since the mean field dominates, the $\Theta$-dependent variations are completely masked by the scale used to plot Figure 3.6(a). The $\Theta$-dependent variation $\Re\left\{\bar{T}(r)\exp(-i2\Theta)\right\}$, whose amplitude is four orders of magnitude lower than the mean, is plotted by itself in Figure 3.6(b). According to the values given in Table 3.1 for the thermal

11 Here T denotes absolute temperature in K and not its normalized counterpart defined in (3.10).

characteristics of the idealized motor, the almost uniform temperature increase of the rotor is a mere 0.086°C from an ambient airgap temperature of 20°C, with the maximum temperature occurring at the center.

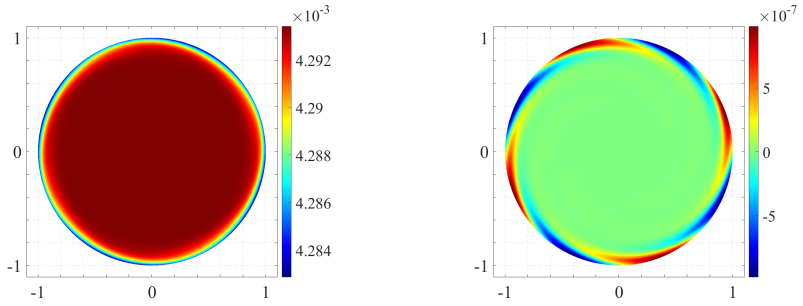


(a) Full temperature field $T(r,\Theta)$ (b) $\Theta$-variation $\Re\{\bar{T}(r)e^{-i2\Theta}\}$

Figure 3.6: Normalized temperature increase for the steel rotor (base case); (a) full field and (b) angular variation.

The influence of the rotor material on the dimensionless temperature increase $T(r,\Theta)$ in the base case motor is presented next in Figure 3.7. In comparing the results for steel in (a), copper in (b) and aluminum in (c), we notice that the temperature increase is almost uniform over the rotor, with the highest increase 0.086°C occurring in steel, 0.062°C for copper and 0.037°C for aluminum.

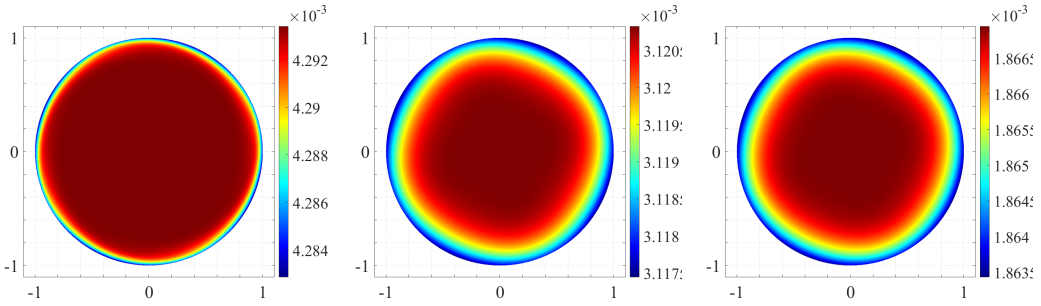


(a) $T(r,\Theta)$ – steel (b) $T(r,\Theta)$ – copper (c) $T(r,\Theta)$ – aluminum

Figure 3.7: Normalized temperature increase T for the base case motor: (a) steel, (b) copper and (c) aluminum rotors.

Ohmic dissipation is the sole dissipation mechanism considered, as discussed in the first remark of Subsection 2.2 and depends on the relative frequency $\omega_r$. The relatively low frequency used (about 1Hz, we consider $\omega_r$ at 2% slip) explains the very low temperature increase found here.

### 3.1.3.4 *Rotor current density, Lorentz and magnetic body forces*

Current density The dimensionless current density field $j = j_z = -\gamma(\partial a/\partial t)$, (normalized by $\kappa_0/R_1$) for the base case motor is presented in Figure 3.8 for steel (a), copper (b) and aluminum (c) rotors, respectively. The currents for steel are forming thin plumes near the rotor surface because of the high magnetic permeability that concentrates the magnetic field at the rotor-airgap interface – see Figure 3.5(a)

– limiting its penetration into the rotor. The current distribution for copper and aluminum rotors is very similar, given the absence of magnetization. Notice in Figure 3.8 that the maximum current values for steel are the lowest while the corresponding ones for copper are the highest, as expected by the different rotor material conductivities according to Table 3.1.

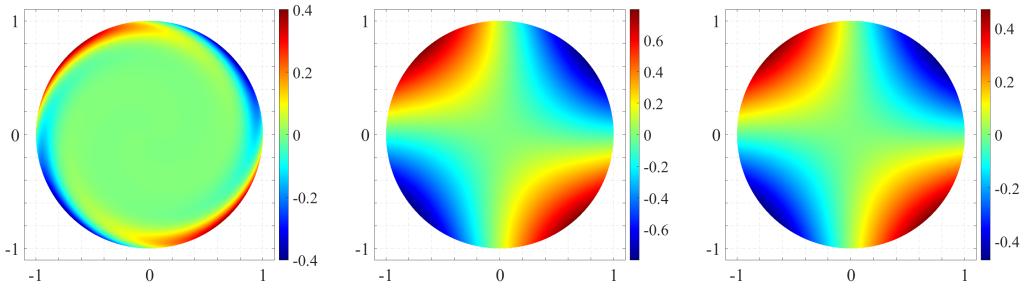

(a) $j(r,\Theta)$ - steel (b) $j(r,\Theta)$ - copper (c) $j(r,\Theta)$ - aluminum

Figure 3.8: Current density j (normalized by $\kappa_0/R_1$), for the base case motor: (a) steel, (b) copper and (c) aluminum rotors.

Lorentz, magnetization and magnetostricive body forces The different components of the magnetic body force $\overset{m}{\mathbf{f}}$, defined as the divergence of the magnetic stress $\overset{m}{\boldsymbol{\sigma}}$ in (2.25), are

$$\overset{m}{\mathbf{f}} \equiv \boldsymbol{\nabla}\cdot\overset{m}{\boldsymbol{\sigma}} = \mathbf{j}\times\mathbf{b} + \mathbf{m}\cdot(\mathbf{b}\boldsymbol{\nabla}) + \frac{\Lambda}{\mu}\mathbf{b}\cdot(\boldsymbol{\nabla}\mathbf{b})\,; \quad \mathbf{m} = \frac{\chi}{\mu}\mathbf{b}\,, \tag{3.33}$$

where $\mu = \mu_0(1+\chi)$. The three different magnetic body force components in (3.33) are: the *Lorentz body force:* $\mathbf{j}\times\mathbf{b}$, a *magnetization body force:* $\mathbf{m}\cdot(\mathbf{b}\boldsymbol{\nabla})$ and a *magnetostriction force:* $(\Lambda/\mu)\mathbf{b}\cdot(\boldsymbol{\nabla}\mathbf{b})$. The last two components are absent in non-magnetic copper and aluminum ($\chi \approx \Lambda \approx 0$).

Figure 3.9 shows the amplitude of the three different components of the electromagnetic force, (normalized by the amplitude of the centrifugal force density $\rho_0 R_1 \Omega^2$), for the base case motor with a steel rotor case. The first important observation is that the Lorentz forces are negligible, with their maximum value of the order of 1% of the inertial forces. A straightforward dimensional analysis indicates $\|\mathbf{j}\| \approx \|\mathbf{b}\|/(\mu R_1)$, giving $\|\mathbf{j}\times\mathbf{b}\| \approx \|\mathbf{b}\|^2/(\mu R_1)$ for the Lorentz component of the body force, compared to the magnetic $\chi\|\mathbf{b}\|^2/(\mu R_1)$ and magnetostrictive $\Lambda\|\mathbf{b}\|^2/(\mu R_1)$ components.

Observe that the magnetization force is larger than its inertial counterpart – up to approximately forty times at the rotor's edge due to the highest magnetic field gradients there, according to Figure 3.5(b) – pointing to the importance of accounting for magnetization body forces in electric motor models. The magnetostrictive forces are not negligible and peak at about 160% of their inertial counterpart (or about 5% of the maximum magnetization forces), a somewhat surprising result in view of the same order $\chi$ and $\Lambda$ coefficients from Table 3.1 but explained by the different expressions for the corresponding forces in (3.33).

The results in Figure 3.10 compare the magnetic body force (normalized by $\rho_0 R_1 \Omega^2$) of the base motor for the different rotor materials. Recall that the magnetic body force is just the Lorentz force for the copper and aluminum rotors, in

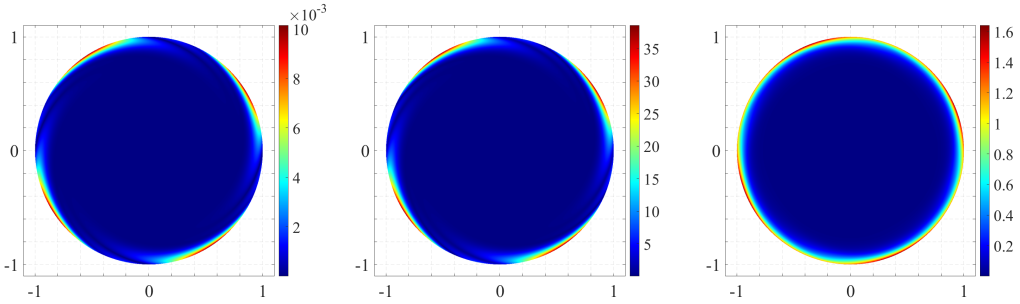

(a) Lorentz $\|\mathbf{j}\times\mathbf{b}\|$ (b) Magnetization $\|\mathbf{m}\cdot(\mathbf{b}\nabla)\|$ (c) Magnetostriction $\|(\Lambda/\mu)\mathbf{b}\cdot(\nabla\mathbf{b})\|$

Figure 3.9: Comparison of the different magnetic body forces (normalized by $\rho_0 R_1 \Omega^2$) for the base case motor with a steel rotor.

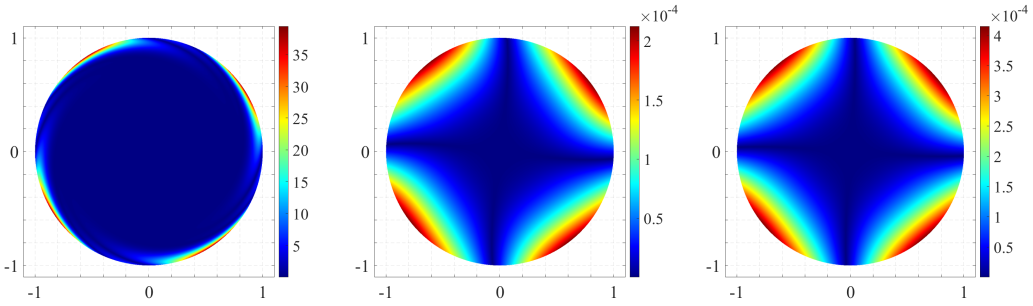

(a) $\| \overset{m}{\mathbf{f}} \|$ – steel (b) $\| \overset{m}{\mathbf{f}} \|$ – copper (c) $\| \overset{m}{\mathbf{f}} \|$ – aluminum

Figure 3.10: Comparison of the total magnetic body force $\| \overset{m}{\mathbf{f}} \|$ (normalized by $\rho_0 R_1 \Omega^2$) for the base case motor with steel, copper and aluminum rotors. Notice that the magnetic body force is the Lorentz force $\mathbf{j}\times\mathbf{b}$ for the two non-magnetic materials.

view of their negligible magnetic properties. We emphasize again the orders of magnitude difference in the magnetic body force between the magnetic (steel) and the non-magnetic (copper, aluminum) materials. The Lorentz forces for the copper and aluminum rotor cases are comparable, given their close electric conductivity (see Table Table 3.1). Notice however that although the maximum current density is higher in the better conducting copper, the corresponding maximum Lorentz force is higher for the aluminum rotor.

#### 3.1.3.5 *Total and elastic stresses*

In order to better assess the influence of the electromagnetic effects on the total $\boldsymbol{\sigma}$ and elastic $\overset{e}{\boldsymbol{\sigma}}$ stresses, we propose to compare them to the purely mechanical (only inertial body forces applied), plane strain elastic stress solution $\overset{i}{\boldsymbol{\sigma}}$ for the spinning

rotor of the base case motor under angular velocity $\Omega$, a straightforward linear elasticity calculation resulting in the following stress field[12]

$$\begin{aligned} \overset{i}{\sigma}_{rr} &= \frac{\rho_0 R_1^2 \Omega^2}{8}\left(\frac{3-2\nu}{1-\nu} - \frac{3-2\nu}{1-\nu} r^2\right), \quad \overset{i}{\sigma}_{r\theta} = 0, \\ \overset{i}{\sigma}_{\theta\theta} &= \frac{\rho_0 R_1^2 \Omega^2}{8}\left(\frac{3-2\nu}{1-\nu} - \frac{1+2\nu}{1-\nu} r^2\right). \end{aligned} \tag{3.34}$$

The maximum value for $\overset{i}{\sigma}_{rr}$ and $\overset{i}{\sigma}_{\theta\theta}$ is $[\rho_0(3-2\nu)/8(1-\nu)](R_1\Omega)^2$ and occurs at the rotor's center $r = 0$. For a more meaningful comparison to the purely mechanical stresses due to inertial effects, all future stress results are normalized by this maximum value, instead of $\rho_0(R_1\Omega)^2$ used thus far.

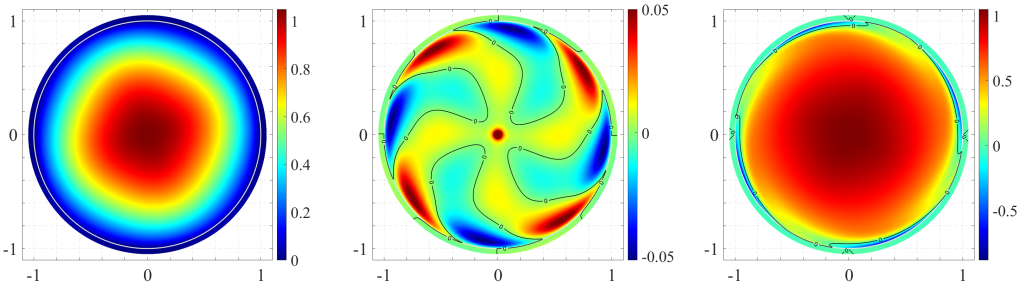

(a) $\sigma_{rr}(r,\Theta)$ (b) $\sigma_{r\theta}(r,\Theta)$ (c) $\sigma_{\theta\theta}(r,\Theta)$

Figure 3.11: Dimensionless total stresses in rotor and airgap (normalized by the maximum inertial stress): (a) normal, (b) shear and (c) hoop, for the base case steel motor.

The normalized total stress components for the base case motor with the steel rotor are presented in Figure 3.11, – with the stress fields shown both in the rotor and the airgap – where one can see the continuity of the normal $\sigma_{rr}$ and shear $\sigma_{r\theta}$ components at the rotor-airgap interface.

The total normal stress $\sigma_{rr}$ is always positive, never exceeding the maximum, purely inertial value, as seen in Figure 3.11(a). It monotonically increases away from the rotor's edge and reaches its maximum at the center, region where the electromagnetic effects are negligible, in contrast to the rotor's edge. The total shear stress $\sigma_{r\theta}$ varies symmetrically between approximately $\pm 5\%$ of the maximum (normal) inertial stress[13], following the angular pattern imposed by the $\cos(2\Theta)$ and $\sin(2\Theta)$ terms. Also notice in Figure 3.11(b) the singularity in $r = 0$ – truncated in the figure – due to the external torque applied there. The total hoop stress $\sigma_{\theta\theta}$ is positive in most of the central domain, where inertial effects dominate, with the same maximum value as for the purely inertial case. The influence of the magnetic field is however evident on the rotor's edge, where a compressive stress of the same absolute value as the maximum inertial stress does appear.

The normalized elastic stress $\overset{e}{\boldsymbol{\sigma}}$ components in the rotor are given in Figure 3.12 and differ significantly from their total stress counterparts $\boldsymbol{\sigma}$, as a simple compar-

12 Recall that $r$ denotes the radius normalized by $R_1$.

13 The rotor has no shear stresses for the purely inertial loading; plotting the shear stress over the maximum value of the inertial stress (which corresponds to the radial and hoop stresses) allows the comparison of its magnitude with respect to the normal stresses.

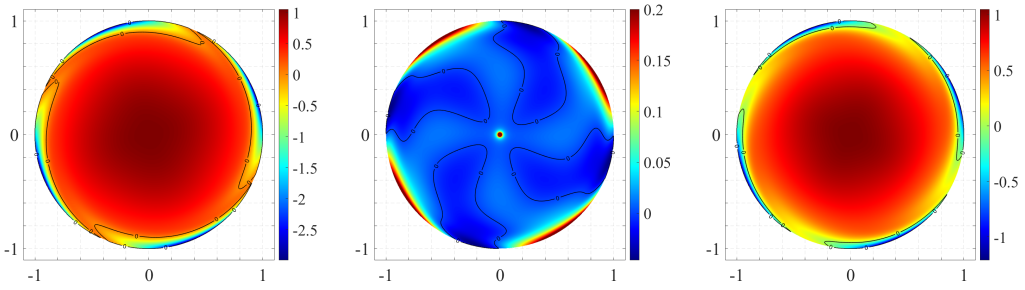

(a) $\overset{e}{\sigma}_{rr}(r,\Theta)$ (b) $\overset{e}{\sigma}_{rr}(r,\Theta)$ (c) $\overset{e}{\sigma}_{rr}(r,\Theta)$

Figure 3.12: Dimensionless elastic stresses in rotor (normalized by the maximum inertial stress): (a) normal, (b) shear and (c) hoop, for the base case steel motor.

ison between Figure 3.11 and Figure 3.12 shows. The elastic stress components are approximately their inertial counterparts $\overset{i}{\boldsymbol{\sigma}}$, given by (3.34), due to the weak magnetic fields at the center of the rotor. However, due to the strong magnetic fields at the rotor boundary, boundary layers develop near its edge resulting in strong compressive components, up to 250% times for the normal and 125% for the hoop components respectively, higher than the corresponding maximal inertial stress. For the shear stress component, a comparison between Figure 3.11(b) and Figure 3.12(b) shows larger elastic shear stresses, in particular near the rotor's edge, due to the mechanical torque produced.

#### 3.1.3.6 *Rotor torque*

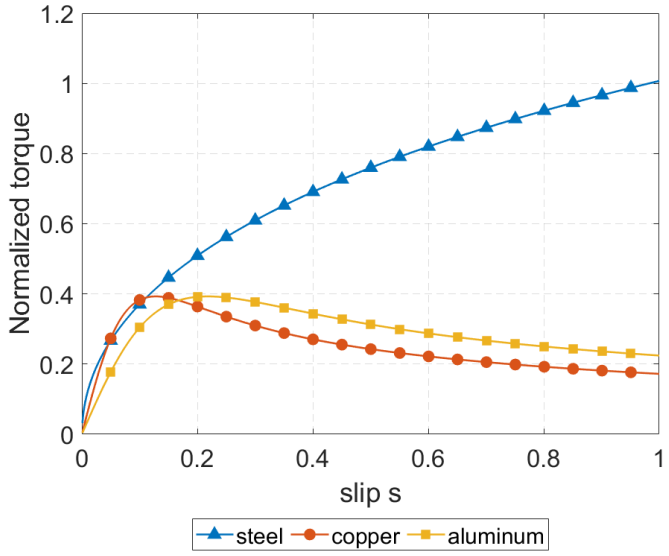


Figure 3.13: Dimensionless torque $\mathcal{T}$ (normalized by $\pi\rho_0 R_1^4\Omega^2 s_0$) vs slip coefficient $s = \omega_r/\omega$ for the base case motor with three different rotor materials.

The torque $\mathcal{T}$, normalized[14] by $\pi\rho_0 R_1^4 \Omega^2 s_0$, is plotted in Figure 3.13 as a function of the slip coefficient $s$. For low $\kappa_0$ values (where the magnetic field remains below the saturation level for steel for all slip values considered[15]) the steel rotor shows higher torque than its copper and aluminum counterparts across almost all the slip range, only slightly dominated by the copper rotor in a region around $5-10\%$ slip.

For high $\kappa_0$ values, the monotonic increase of the torque as a function of slip for steel – due to its linear magnetic response – is misleading, as saturation may occur, which is not accounted for in the model. In the base case motor, the magnetic field for the steel rotor is already close to saturation for $\kappa_0 = 1.3\times10^4, s = 2\%$ with a value of 1.3T (see Figure 3.2(a)). In this case, it is expected that due to magnetic saturation, the steel torque-slip curve above $s = 2\%$ should be reaching a maximum torque, as is the case for the copper and aluminum rotors. For $s = 5\%$ or higher, the copper motor would produce a larger torque than its steel counterpart.

### 3.1.4 *Conclusion for the rotor problem*

As a first example of application, the theory presented in Chapters 1 and 2 is employed for the analytical modeling of the rotor of an idealized asynchronous motor for which we calculate the magnetic, thermal, stress fields and torque. To better assess the influence of magnetization on stresses, three different rotor materials are examined: electric steel, copper and aluminum and different airgap and slip parameters are considered using realistic geometric and operational regime values (see Lubin, Mezani, and Rezzoug, 2011a) and material parameters (see Aydin et al., 2017). Given the linearized magnetic constitutive model adopted for the sake of an analytical solution, the applied current amplitude is chosen to produce magnetic fields below saturation levels.

Magnetic field results show, as expected, the presence of a boundary layer at the rotor's edge for the steel case and more diffuse patterns for the non-magnetic materials; about two order of magnitude difference is observed in the maximum magnetic field between the magnetic and non-magnetic materials. Comparing the Lorentz, magnetization and the magnetostrictive forces in the steel rotor case we find that the first are negligible (more than three orders of magnitude less for the first compared to the last two). Moreover, magnetostrictive body forces – resulting from the constitutive coupling between stress and magnetization effects – although smaller that their magnetic counterparts, are considerably higher than the Lorentz. This is an important finding of our calculations, since the former are usually neglected in the electric motor calculations available in the literature. As expected the magnetic body forces found in the steel rotor are concentrated along a boundary layer and significantly higher than their counterparts for the non-magnetic materials that are more diffusely distributed, thus explaining the importance of magnetic rotors for the production of a much higher torque for a given current amplitude, as long as the magnetic field remains below saturation levels.

14 The normalization quantity is the product of the rotor's area $\pi R_1^2$ by the electromagnetic stress term $\rho_0 R_1^2 \Omega^2 s_0 = \mu_0 \kappa_0^2$.

15 As shown in (3.1.3.2), the peak value of the magnetic field increases with slip.

Due to the realistic thermal parameters used in the calculations, the temperature increase in the rotor is negligible with the temperature maximum appearing in the rotor's center. Significant differences are found in the current density distribution between the magnetic and non-magnetic materials, with a boundary layer appearing in the first and diffuse patterns in the second case.

The analytical solution of the model allows the comparison of the different parts of the stress tensor (elastic and total) to the purely mechanical stresses due to inertia, revealing the significant influence of electromagnetic phenomena on the resulting stress state. Although the maximum value of total stress' normal components never exceed their purely inertial counterparts, the corresponding elastic stress components do so by developing a stress concentration boundary layer where compressive radial and hoop stresses can be up to three times higher than the maximum inertial value. Moreover, elastic shear stresses are considerably higher than the total stress and concentrated on a boundary layer about the rotor's edge.

## 3.2 STATOR BOUNDARY VALUE PROBLEM

### 3.2.1 *Problem description*

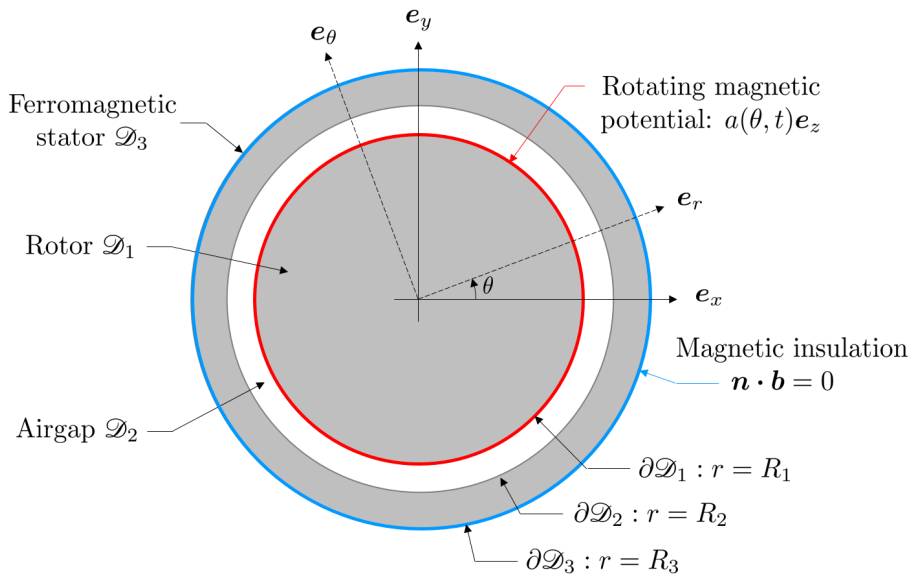


Figure 3.14: Cross-section of the simplified electric motor, indicating rotor, airgap and stator domains, together with boundary conditions for the magnetic field.

The cross-section of the simplified electric motor considered here is shown in Figure 3.14; as for the rotor problem the motor is considered infinitely long in the normal to the plane and under plane strain conditions. It is composed of a cylindrical ferromagnetic rotor (domain $\mathscr{D}_1 : 0 \leqslant r \leqslant R_1$), surrounded by a cylindrical tubular stator (domain $\mathscr{D}_3 : R_2 \leqslant r \leqslant R_3$), separated by an airgap (domain $\mathscr{D}_2 : R_1 \leqslant r \leqslant R_2$). Air surrounds the motor (domain $\mathscr{D}_4 : R_3 \leqslant r$). The interface between the different domains are denoted $\partial\mathscr{D}_1, \partial\mathscr{D}_2, \partial\mathscr{D}_3$ and shown in Figure 3.14. $\mathscr{S}(r, \theta, z)$ denotes the stator's fixed reference frame.

The motor is loaded by a known rotating magnetic potential distribution[16] at the rotor boundary $\partial\mathscr{D}_1$,

$$\partial\mathscr{D}_1 : \quad \mathbf{a}(R_1,\theta,t) = a_0\cos(p\theta-\omega t)\hat{\mathbf{e}}_z\ , \tag{3.35}$$

with $a_0$ the oscillation's amplitude in T.m. This magnetic potential supply, inspired by Pile et al., 2019b, rotates around the $z$-axis at the angular frequency $\omega/p$ and creates a rotating radial field component,

$$\partial\mathscr{D}_1 : \quad \hat{\mathbf{e}}_r\cdot\mathbf{b}(R_1,\theta,t) = -b_0\sin(p\theta-\omega t)\ ; \quad b_0 = \frac{a_0 p}{R_1} \tag{3.36}$$

It typically models the field produced by a permanent magnet rotor[17] with $p$ pairs of magnets producing a radial magnetic field and rotating at the angular frequency $\omega$.

No stator coils are considered, hence the absence of a stator current sheet in contrast to the rotor boundary value problem 3.1. Such a problem description is equivalent to an experiment where we rotate the permanent magnet rotor with the stator being unsupplied and unconnected electrically (open circuit).

In this stator boundary value problem, temperature aspects are not considered. They have already been exposed in 3.1. Some additional assumptions are necessary to solve the problem. They are:

*i) No external mechanical body forces* Gravity effects are neglected. No purely mechanical body forces, introduced in (1.26) are considered, i.e. $\mathbf{f}=\mathbf{0}$.

*ii) Negligible velocity and acceleration* We neglect the material velocity and acceleration terms.

*iii) Negligible stator currents* We assume the stator is made of ferromagnetic laminates stacked along the $z$-direction. These laminates are electrically insulated such that they prevent significant induced electric currents in the $z$-direction. This architecture is typical in electric motor to reduce Joule's losses and improve the machine's efficiency. It is a typical assumption to neglect them (e.g. see Pang et al., 2006). Maxwell-Ampère's equation at the stator in this case provides,

$$\mathscr{D}_3 : \quad \boldsymbol{\nabla}\times\mathbf{h} = \mathbf{0}\ , \tag{3.37}$$

This further translates into $\boldsymbol{\nabla}\times\mathbf{b} = \mathbf{0}$ given the linear magnetization. Another direct consequence is the Lorentz force $\mathbf{j}\times\mathbf{b}=\mathbf{0}$ and the stator is only subject to the magnetization body force $\boldsymbol{\nabla}\cdot\frac{\chi}{2\mu}(\mathbf{b}\cdot\mathbf{b})\mathbf{I} = \mathbf{m}\cdot(\mathbf{b}\boldsymbol{\nabla})$ and to the magnetostriction body force $\boldsymbol{\nabla}\cdot\frac{\Lambda}{\mu}(\mathbf{b}\mathbf{b}) = \frac{\Lambda}{\mu}\mathbf{b}\cdot(\boldsymbol{\nabla}\mathbf{b})$ (see 2.28).

*iv) Magnetic insulation at the stator external boundary* We assume that the stator magnetically shields the motor i.e. that no magnetic field flows out of the motor,

$$\partial\mathscr{D}_3 : \quad \mathbf{n}\cdot\mathbf{b} = 0 \tag{3.38}$$

16 For simplicity a single time harmonic for the magnetic potential supply is considered.

17 This model is rather crude but adopted here in the sake of simplifications

This hypothesis is common in the electric motor literature (e.g. see Gieras, 2010 §3.9.1)[18]. As a direct consequence, the Maxwell-stress *on the air side* at the outer stator surface is,

$$\partial\mathscr{D}_3: \quad \sigma_{rr} = \frac{1}{2\mu_0} b_r^2 - \frac{\mu_0}{2} h_\theta^2 = -\frac{\mu_0}{2} h_\theta^2 \,, \quad \sigma_{r\theta} = b_r h_\theta = 0 \tag{3.39}$$

where $h_\theta$ is continuous accross the interface by the interface condition on $\mathbf{h}$[19].

Henceforth all equations are written in the stator frame $\mathcal{S}$ and all field quantities are functions of $(r, \theta, t)$. These governing equations and boundary conditions for the idealized, 2D motor are summarized below.

$$\begin{aligned}
\mathscr{D}_2: &\begin{cases} \boldsymbol{\nabla}\times\mathbf{b} = 0 \,, \\ \boldsymbol{\sigma} = \overset{m}{\boldsymbol{\sigma}} = \dfrac{1}{\mu_0}\left(\mathbf{b}\mathbf{b} - \dfrac{1}{2}(\mathbf{b}\cdot\mathbf{b})\mathbf{I}\right) \,, \end{cases} \\
\mathscr{D}_3: &\begin{cases} \boldsymbol{\nabla}\times\mathbf{b} = 0, \\ \boldsymbol{\nabla}\cdot(\overset{e}{\boldsymbol{\sigma}} + \overset{m}{\boldsymbol{\sigma}}) = 0 \,, \end{cases} \\
\partial\mathscr{D}_1: &\quad \hat{\mathbf{e}}_r\cdot\mathbf{b} = -b_0 \sin(p\theta - \omega t) \,, \\
\partial\mathscr{D}_2: &\begin{cases} \hat{\mathbf{e}}_r\times[\![\mathbf{h}]\!] = 0 \,, \\ \hat{\mathbf{e}}_r\cdot[\![\mathbf{b}]\!] = 0 \,, \\ \hat{\mathbf{e}}_r\cdot(\overset{e}{\boldsymbol{\sigma}} + [\![\overset{m}{\boldsymbol{\sigma}}]\!]) = 0 \,, \end{cases} \\
\partial\mathscr{D}_3: &\begin{cases} \hat{\mathbf{e}}_r\cdot[\![\mathbf{b}]\!] = 0 \,, \\ \hat{\mathbf{e}}_r\cdot(-\overset{e}{\boldsymbol{\sigma}} + [\![\overset{m}{\boldsymbol{\sigma}}]\!]) = 0 \,, \end{cases} \\
\mathscr{D}_2\cup\mathscr{D}_3: &\quad \mathbf{a} = a(r,\theta,t)\hat{\mathbf{e}}_z \,, \ \mathbf{b} = \boldsymbol{\nabla}\times\mathbf{a} = \frac{1}{r}\frac{\partial a}{\partial\theta}\hat{\mathbf{e}}_r - \frac{\partial a}{\partial r}\hat{\mathbf{e}}_\theta \,.
\end{aligned} \tag{3.40}$$

In the interface condition for stresses on $\partial\mathscr{D}_2$ and $\partial\mathscr{D}_3$, there is no elastic stress field in the air regions $\overset{e}{\boldsymbol{\sigma}} = 0$[20], in contrast to the magnetic stress field $\overset{m}{\boldsymbol{\sigma}}$ that exists in both the stator and air regions (where it equals Maxwell-stress in vacuum). Based on the expressions for the Maxwell-stress in air (see 2.7) and the magnetic stress

18 The hypothesis of magnetic insulation on the outer stator surface is in particular used for finite element analyses as it frees from meshing and solving the magnetic field in the air regions surrounding the motor. This hypothesis may however be questionned in some cases (e.g. see Pang et al., 2006).

19 Given the continuity on $h_\theta$ no index to refer to the side of the interface at which the value is taken is required

20 The elastic stress field is only defined in the stator, the domain index notation $\overset{e}{\boldsymbol{\sigma}}_3$ is not used as unnecessary.

field $\overset{m}{\boldsymbol{\sigma}}$ at the stator (see 2.26) the expressions of the stress boundary conditions can be further expanded to provide[21],

$$\begin{aligned} \partial\mathscr{D}_2: \quad & \overset{e}{\sigma}_{rr} = -\frac{\chi^2}{2}\mu_0 h_\theta^2 - \frac{\Lambda}{\mu} b_r^2 \,; \qquad \overset{e}{\sigma}_{r\theta} = -\Lambda b_r h_\theta \\ \partial\mathscr{D}_3: \quad & \overset{e}{\sigma}_{rr} = -\frac{\chi^2}{2}\mu_0 h_\theta^2 \,; \qquad\qquad\quad \overset{e}{\sigma}_{r\theta} = 0 \end{aligned} \tag{3.41}$$

where the continuity conditions for $b_r$ and $h_\theta$ at the interfaces are accounted for together with the condition of no leak of magnetic field $b_r(R_3, \theta) = 0$.

### 3.2.2 *Dimensionless boundary value problem*

To guide the physical interpretation of the results, we define the reference magnetic[22], reference stress and reference displacement fields

$$b_{ref} \equiv \frac{p a_0}{R_2}\,, \quad \sigma_{ref} \equiv \frac{b_{ref}^2}{\mu_0}\,, \quad \epsilon_{ref} \equiv \frac{u_{ref}}{R_2} \equiv \frac{\sigma_{ref}}{2G}\,, \tag{3.42}$$

and the following dimensionless variables and parameters of the problem are introduced

$$\frac{r}{R_2} \to r, \quad r_1 \equiv \frac{R_1}{R_2}, \quad r_3 \equiv \frac{R_3}{R_2}, \quad \omega t \to t, \quad \frac{a}{a_0} \to a, \quad \frac{\boldsymbol{\sigma}}{\sigma_{ref}} \to \boldsymbol{\sigma}, \quad \frac{\mathbf{u}}{u_{ref}} \to \mathbf{u}\,. \tag{3.43}$$

> Henceforth, for simplicity the dimensionless variables and field quantities of the problem, $r$, $t$, $a$, $\boldsymbol{\sigma}$ are denoted by the same symbol as their dimensioned counterparts.

For future reference, note that given the normalization of radii by $R_2$, $r = 1$ corresponds to the domain boundary $\partial\mathscr{D}_2$ between the airgap and stator.

The governing equations and the associated interface and boundary conditions (in the stator frame) are given below,[23] starting with the magnetic potential $a$

$$\begin{aligned} & \boldsymbol{\nabla}^2 a_2 = 0\,; && r_1 \leqslant r \leqslant 1\,, \\ & \boldsymbol{\nabla}^2 a_3 = 0\,; && 1 \leqslant r \leqslant r_3\,, \\ & a_2 = \cos(p\theta - t)\,; && r = r_1, \\ & (1+\chi)\frac{\partial a_2}{\partial r} = \frac{\partial a_3}{\partial r}\,, \quad \frac{\partial a_2}{\partial \theta} = \frac{\partial a_3}{\partial \theta}\,; && r = 1\,, \\ & \frac{\partial a_3}{\partial \theta} = 0\,; && r = r_3\,. \end{aligned} \tag{3.44}$$

21 As a result of its continuity, $b_r$ – respectively $h_\theta$ – in the boundary conditions is unambiguously defined: it has the same value on each side of the interface and there is no necessity of an index referencing to the side.

22 By choosing $b_{ref} = p a_0 / R_2$ - which is close to $b_0$ in (3.36) given $R_2$ close to $R_1$ in the application later on - we meant to compare to the input rotor radial field $b_0$.

23 Only the radius of each domain of validity is recorded, since in all domains the angle $\theta \in [0, 2\pi)$ and the time $t \in \mathbb{R}^+$.

The governing equations and boundary conditions for the stator's elastic stress field $\overset{e}{\boldsymbol{\sigma}}$ are[24]

$$\begin{aligned}
&\boldsymbol{\nabla}\cdot\overset{e}{\boldsymbol{\sigma}} = \overset{m}{\mathbf{f}}\,, \quad \overset{m}{\mathbf{f}} \equiv -s_m\boldsymbol{\nabla}\left(\frac{1}{p^2}\|\boldsymbol{\nabla}\times\mathbf{a}_3\|^2\right), \quad s_m \equiv \frac{1}{2}\frac{\chi+\Lambda}{1+\chi}\,; \qquad 1\leqslant r\leqslant r_3\,,\\
&\overset{e}{\sigma}_{rr} = -\frac{\chi^2}{2(1+\chi)^2}\left(\frac{1}{p}\frac{\partial a_3}{\partial r}\right)^2 - \frac{\Lambda}{1+\chi}\left(\frac{1}{p}\frac{\partial a_3}{\partial \theta}\right)^2; \quad \overset{e}{\sigma}_{r\theta} = \frac{\Lambda}{1+\chi}\frac{1}{p^2}\frac{\partial a_3}{\partial r}\frac{\partial a_3}{\partial \theta}; \quad r = 1\,,\\
&\overset{e}{\sigma}_{rr} = -\frac{\chi^2}{2(1+\chi)^2}\left(\frac{1}{p}\frac{\partial a_3}{\partial r}\right)^2; \qquad\qquad \overset{e}{\sigma}_{r\theta} = 0\,; \qquad\qquad r = r_3\,,
\end{aligned} \tag{3.45}$$

The stress interface conditions directly derive from (3.41). The expression for the body force of electromagnetic origin arises from its definition $\overset{m}{\mathbf{f}} \equiv -\boldsymbol{\nabla}\cdot\overset{m}{\boldsymbol{\sigma}}$. Compared to the rotor stress equations (3.13), a body force term - the Lorentz force $\mathbf{j}\times\mathbf{b}$ - drops out because of the assumption of negligible stator currents. The dimensionless coefficient $s_m$ appearing in the body force expression depend on the magnetic properties $(\chi, \Lambda)$ of the stator material.

We first solve (3.44) to find the magnetic potential $a$. This magnetic potential gives the body force and interface traction for the linear momentum balance in (3.45), thus providing the stator's elastic stress field $\overset{e}{\boldsymbol{\sigma}}$.

### 3.2.2.1 *Magnetic Potential*

The solution to (3.44) subject to the harmonic loading in (3.36), takes the form[25]

$$a_k(r,\Theta) = A_k(r)\cos\Theta\,, \; k = 1,2\,; \qquad \Theta \equiv p\theta - t\,, \tag{3.46}$$

where $A_k(r)$ is the magnetic potential amplitude that depends only on $r$.

In the airgap domain, (3.44) gives a Laplace equation for the amplitude $A_2(r)$

$$r^2\frac{d^2A_2}{dr^2} + r\frac{dA_2}{dr} - p^2A_2 = 0 \implies A_2(r) = Dr^p + Er^{-p}\,. \tag{3.47}$$

In the stator domain, given the absence of electric currents (3.44) results in a Laplace equation as well for the amplitude $A_3(r)$

$$r^2\frac{d^2A_3}{dr^2} + r\frac{dA_3}{dr} - p^2A_3 = 0 \implies A_3(r) = Fr^p + Gr^{-p}\,. \tag{3.48}$$

24 Henceforth the stator's body force is denoted by $\mathbf{f}$, taking the symbol used in (1.26) for the purely mechanical body force.

25 As opposed to the rotor case calculation in Section 3.1.2.1, solving in the complex domain is not necessary because of the absence of time derivatives of $\mathbf{a}$ (associated to rotor induced currents in the rotor problem).

The constants D, E, F and G appearing in (3.47) and (3.48) are determined using the interface and boundary conditions in (3.44), and are found to be

$$\begin{aligned}
D &= \frac{\left[\chi r_3^p - (2+\chi) r_3^{-p}\right]}{\chi(r_3^p - r_3^{-p})(r_1^p + r_1^{-p}) + 2(r_3^p r_1^{-p} - r_3^{-p} r_1^p)} \,, \\
E &= \frac{\left[(2+\chi) r_3^p - \chi r_3^{-p}\right]}{\chi(r_3^p - r_3^{-p})(r_1^p + r_1^{-p}) + 2(r_3^p r_1^{-p} - r_3^{-p} r_1^p)} \,, \\
F &= \frac{-2(1+\chi) r_3^{-p}}{\chi(r_3^p - r_3^{-p})(r_1^p + r_1^{-p}) + 2(r_3^p r_1^{-p} - r_3^{-p} r_1^p)} \,, \\
G &= \frac{2(1+\chi) r_3^p}{\chi(r_3^p - r_3^{-p})(r_1^p + r_1^{-p}) + 2(r_3^p r_1^{-p} - r_3^{-p} r_1^p)} \,.
\end{aligned} \tag{3.49}$$

#### 3.2.2.2 *Stator stresses*

The principle of superposition is used again for determining the stator's elastic stress field $\overset{e}{\boldsymbol{\sigma}}$. Recalling the definitions for $\overset{m}{\mathbf{f}}$ in (3.45) and the solution for the magnetic potential $a_3$ in (3.46) and (3.48), the body forces can be entirely (as opposed to the forces of the rotor problem in Section 3.1) expressed as the gradient of a potential $V(r,\Theta)$: $\overset{m}{\mathbf{f}}(r,\Theta) = \boldsymbol{\nabla} V(r,\Theta)$[26].

$$\begin{aligned}
\overset{m}{\mathbf{f}} = \boldsymbol{\nabla} V \,; \qquad & V(r,\Theta) = V_0(r) + V_c(r)\cos(2\Theta) \,, \\
& V_0(r) = -\frac{s_m}{2}\left(\frac{p^2}{r^2} A_3^2 + A_3'^2\right) \,, \\
& V_c(r) = -\frac{s_m}{2}\left(-\frac{p^2}{r^2} A_3^2 + A_3'^2\right) \,.
\end{aligned} \tag{3.50}$$

Consequently, the stator's elastic stress field $\overset{e}{\boldsymbol{\sigma}}$ is decomposed as follows

$$\overset{e}{\boldsymbol{\sigma}}(r,\Theta) = \overset{e^h}{\boldsymbol{\sigma}}(r,\Theta) + \overset{e^V}{\boldsymbol{\sigma}}(r,\Theta) \,, \quad \begin{cases} \boldsymbol{\nabla}\cdot\overset{e^V}{\boldsymbol{\sigma}} = \boldsymbol{\nabla} V \,, \\ \boldsymbol{\nabla}\cdot\overset{e^h}{\boldsymbol{\sigma}} = 0 \,, \end{cases} \tag{3.51}$$

where $\overset{e^h}{\boldsymbol{\sigma}}$ and $\overset{e^V}{\boldsymbol{\sigma}}$ are respectively the general solution to the homogeneous stress equation and a particular solution to the stress equation. Each one of the constituent fields $\overset{e^h}{\boldsymbol{\sigma}}$, $\overset{e^V}{\boldsymbol{\sigma}}$ corresponds, in view of (2.26), to a compatible elastic strain field, i.e. derivable from a displacement field. By abuse of terminology we call these elastic stress fields *elastically compatible*.

An elastically compatible particular solution for the elastic stress field $\overset{e^V}{\boldsymbol{\sigma}}$ is found using the Airy stress function method in polar coordinates (see Barber, 2010

26 Given the electromagnetic forcing $\overset{m}{\mathbf{f}} = -\boldsymbol{\nabla}\cdot\overset{m}{\boldsymbol{\sigma}}$ in (3.45), it is tempting to choose $\overset{e}{\boldsymbol{\sigma}} = -\overset{m}{\boldsymbol{\sigma}}$ as a particular solution to the elastic stress equation. However, this particular solution is ineligible as it does not satisfy the compatibility condition (see Barber, 2010), thus leading to the proposed approach (for additional details see Appendix B.3).

and the rotor boundary value problem in section 3.1). The components of $\overset{e}{\boldsymbol{\sigma}}^{V}$ can be expressed in terms of a stress potential $\phi_V$ as follows

$$\begin{aligned} &\overset{e}{\sigma}{}^{V}_{rr} = \frac{1}{r}\frac{\partial \phi_V}{\partial r} + \frac{1}{r^2}\frac{\partial^2 \phi_V}{\partial \theta^2} + V\,,\ \overset{e}{\sigma}{}^{V}_{\theta\theta} = \frac{\partial^2 \phi_V}{\partial r^2} + V\,,\ \overset{e}{\sigma}{}^{V}_{r\theta} = -\frac{\partial}{\partial r}\left(\frac{1}{r}\frac{\partial \phi_V}{\partial \theta}\right)\,; \\ &\nabla^2 \phi_V = -\frac{1-2\nu}{1-\nu} V\,. \end{aligned} \tag{3.52}$$

The stress potential $\phi_V$ is found[27], by solving the Laplacian in (3.52) with the help of (3.50)

$$\begin{aligned} \phi_V(r,\Theta) = &-\frac{1-2\nu}{1-\nu}\left(\int_0^r \frac{1}{r}\int_0^r V_0 r\,dr\,dr \right. \\ &\left. + \left[\frac{r^{2p}}{4p}\int_0^r V_c r^{-2p+1}dr - \frac{r^{-2p}}{4p}\int_0^r V_c r^{2p+1}dr\right]\cos(2\Theta)\right)\,. \end{aligned} \tag{3.53}$$

The components of the elastically compatible homogeneous solution stress field $\overset{e}{\boldsymbol{\sigma}}^{h}$ are expressed in terms of the potential $\phi_h$

$$\begin{aligned} &\overset{e}{\sigma}{}^{h}_{rr} = \frac{1}{r}\frac{\partial \phi_h}{\partial r} + \frac{1}{r^2}\frac{\partial^2 \phi_h}{\partial \theta^2}\,,\ \overset{e}{\sigma}{}^{h}_{\theta\theta} = \frac{\partial^2 \phi_h}{\partial r^2}\,,\ \overset{e}{\sigma}{}^{h}_{r\theta} = -\frac{\partial}{\partial r}\left(\frac{1}{r}\frac{\partial \phi_h}{\partial \theta}\right)\,; \\ &\nabla^4 \phi_h = 0\,. \end{aligned} \tag{3.54}$$

Solving the biharmonic equation for $\phi_h$ in (3.54) we obtain[28]

$$\begin{aligned} \phi_h(r,\Theta) = &\Phi_{01} r^2 + \Phi_{02} r^2 \ln(r) + \Phi_{03}\ln(r) + \Phi_{04}\theta \\ &+ \left(\Phi_{c1} r^{-2p+2} + \Phi_{c2} r^{2p} + \Phi_{c3} r^{-2p} + \Phi_{c4} r^{2p+2}\right)\cos(2\Theta) \\ &+ \left(\Phi_{s1} r^{-2p+2} + \Phi_{s2} r^{2p} + \Phi_{s3} r^{-2p} + \Phi_{s4} r^{2p+2}\right)\sin(2\Theta) \end{aligned} \tag{3.55}$$

The final expressions for $\overset{e}{\boldsymbol{\sigma}}^{h}$, $\overset{e}{\boldsymbol{\sigma}}^{V}$ are obtained from (3.54) and (3.52) but are too cumbersome to be recorded here; they are given in B.5. The 12 integration constants $\Phi_{01}, \Phi_{02}, \Phi_{03}, \Phi_{04}, \Phi_{c1}, \Phi_{c2}, \Phi_{c3}, \Phi_{c4}, \Phi_{s1}, \Phi_{s2}, \Phi_{s3}, \Phi_{s4}$ are determined by the $r = 1$ and $r = r_3$ boundary conditions in (3.45). From the decomposition in radial, cosine and sine terms (see footnote 28), result three equations for the normal and three equations for the tangential boundary conditions at each radius $r = 1$ and $r = r_3$, thus uniquely determining the sought constants. The expression for the total stress at the stator (elastic and magnetic components) can then be determined from (2.26). Appendix B.5 further provides the expressions for the displacement field based on Barber, 2010.

### 3.2.3 *Results and discussion*

Although we solve an idealized motor, the results presented in this section correspond to materials, geometries and operating parameters found in the electrical engineering literature. comparison of the results to related physically meaningful quantities.

27 Because we look for a particular solution only, integration constants are discarded.

28 The solution is extracted from the general Michell, 1899 solution. Given the form of the body forces and boundary conditions, only those terms consistent with a solution of the form $\overset{e}{\boldsymbol{\sigma}} = \overset{e}{\sigma}_0(r) + \overset{e}{\sigma}_c(r)\cos(2\Theta) + \overset{e}{\sigma}_s(r)\sin(2\Theta)$ are kept. However as opposed to the calculation for the rotor problem in Section 3.1.2.3, no condition of torque or no-singularity in $r = 0$ can here be exploited to further reduce the number of integration constants.

#### 3.2.3.1 *Material, geometry and operating parameters*

The motor geometry and operating parameters used in the calculations are shown in Table 3.14. The study is based on Pile et al., 2019b: the geometric and material parameters used are values communicated by its authors and typical for electric motors. Of the parameters needed, only the magnetostriction coefficient $\Lambda$ was not provided. As for the rotor case (Section 3.1), $\Lambda$ is fitted from Aydin et al., 2017, for the no-prestressed case, as detailed in Appendix B.2. The results obtained are valid in the range of linear magnetic behavior given magnetic saturation is not accounted for here. The values for $a_0$ - corresponding to $\|\mathbf{b}\|_{max} = 1.3\text{T}$ at the stator, value considered as the onset of magnetic saturation[29] - and $\omega$ in the table are purely indicative given that they do not influence the *normalized* results provided hereafter.

| **Geometry** | |
|---|---|
| Rotor radius $R_1$ | 42.5 mm |
| Stator inner radius $R_2$ | 45 mm |
| Stator outer radius $R_3$ | 50 mm |
| Number of pole pairs $p$ | 2 |
| **Operating parameters** | |
| Peak value of the magnetic potential $a_0$ | $6.1\times10^{-3}$ T.m |
| Angular velocity of the rotor $\omega$ | $100\pi$ rad/s |
| **Material properties** | **Electrical steel** |
| Magnetic susceptibility $\chi$ | 2,500 |
| Magneto-mechanical coupling $\Lambda$ | $-1.3\times10^{3}$ |
| Mass density $\rho_0$ | 7,650 kg/m$^3$ |
| Young's modulus $E$ | $215\times10^{9}$ Pa |
| Poisson ratio $\nu$ | 0.3 |

Table 3.14: Motor geometry, operating parameters and material properties for the stator boundary value problem

As discussed in Subsection 3.2.1, the equations are solved in the stator frame $\mathcal{S}(r,\theta,t)$ and all field quantities are functions of $(r,\Theta)$, where $\Theta = p\theta - t$ and $p$ the motor pole number (here taken $p = 2$). The results here are a snapshot of these rotating fields at $t = 0$ and are presented by plotting the corresponding field quantity at $(r,\theta)$.

#### 3.2.3.2 *Magnetic field in stator and airgap*

Figure 3.15 displays the norm of the airgap and stator magnetic field, normalized by the reference magnetic field $b_{ref}$. The high magnetic stator permeability dras-

29 See for instance Rekik, Hubert, and Daniel, 2014 that reports values for the onset of magnetic field saturation for typical electrical steels (e.g. M400-50A) around 1.3T.

tically increases the magnetic field intensity to a maximum amplitude reaching more than 4.5 times the input magnetic field $b_{ref}$. The streamlines of the magnetic field are plotted in order to highlight how the magnetic field is "bent" at the airgap-stator interface by the important difference in magnetic permeabilities. This "bending" and concentration of the magnetic field explains the magnetic-shielding properties of the stator - it contains the magnetic field within - and justifies our approximation $b_r = 0$ in $r_3$.

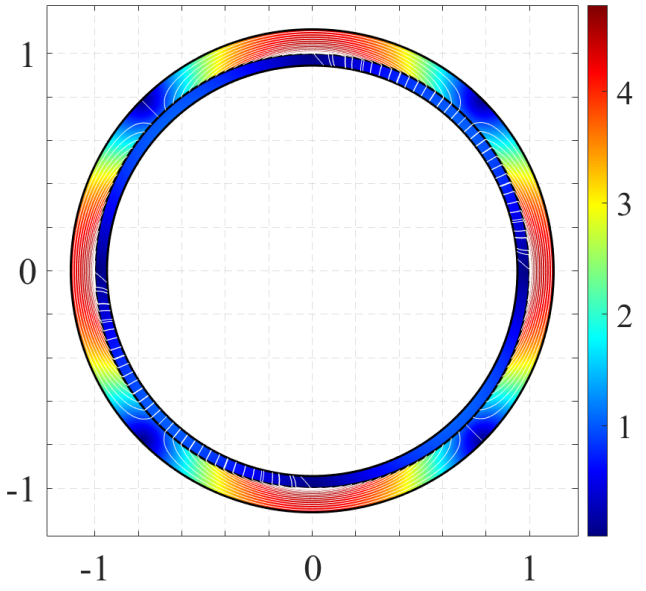


Figure 3.15: Norm of the normalized magnetic field: $\frac{||\mathbf{b}||}{b_{ref}}$ .

### 3.2.3.3 *Traction and body forces*

Figure 3.16 pictures the norm of the stator body forces of electromagnetic origin $\overset{m}{\mathbf{f}} = -\boldsymbol{\nabla}\cdot\overset{m}{\boldsymbol{\sigma}}$. The streamlines are plotted in order to visualize the direction of the local forces. Figure 3.17 provides additional information by plotting the radial and tangent force components. All forces are normalized by the reference force amplitude $f_{ref} = \frac{\sigma_{ref}}{R_2}$. The radial and tangent force components have comparable amplitudes. The radial component remains positive everywhere and pulls the stator in the $+\hat{\mathbf{e}}_r$ direction. Because evenly distributed between compression and tension along the stator in the $\hat{\mathbf{e}}_\theta$ direction, the tangent force component does not contribute to the stator's expansion and induces no torque along $\hat{\mathbf{e}}_z$ (no global pull in $\hat{\mathbf{e}}_\theta$).

Figure 3.18 pictures the distribution along $\hat{\mathbf{e}}_\theta$ of the surface traction terms that result from the jump in stresses accross the stator boundaries in $r_2$ and $r_3$. The surface traction results are normalized by the reference stress $\sigma_{ref}$. As expected from the interface conditions in (3.45) given the form of the solution for $\mathbf{a}$, the radial traction components are cosine and the tangent ones are sine. The traction on both stator boundaries are dominantly radial, and dominantly pull in the $-\hat{\mathbf{e}}_r$ direction. They seem to pull with much higher intensity than the electromagnetic

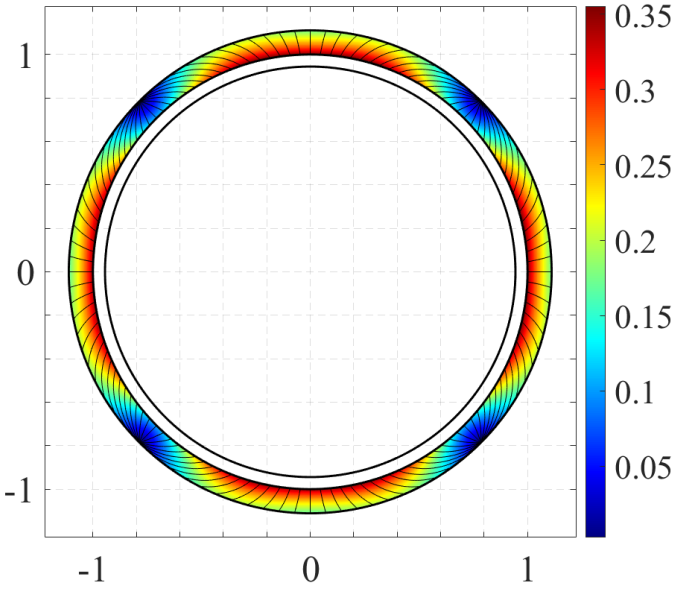


Figure 3.16: Norm of the normalized body forces of electromagnetic origin in the stator: $\frac{||\overset{m}{\mathbf{f}}||}{\sigma_{ref}/R_2}$.

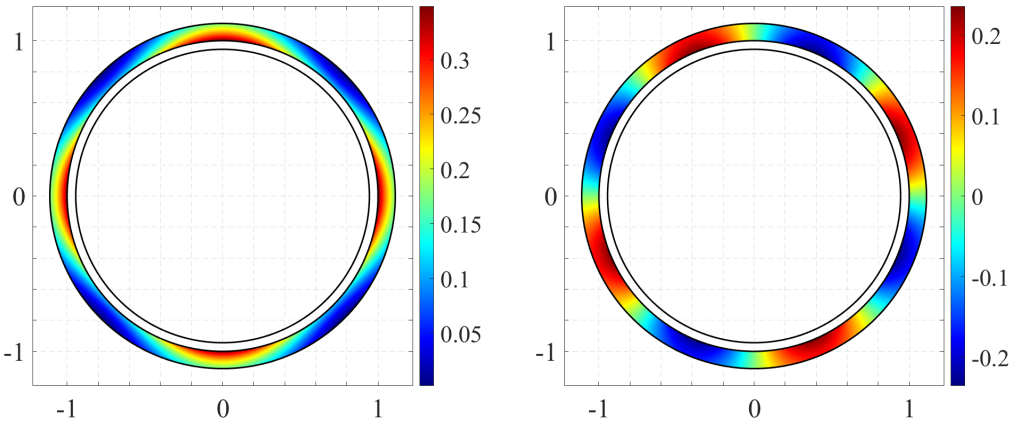


(a) $\frac{\overset{m}{\mathbf{f}}_r(r,\Theta)}{\sigma_{ref}/R_2}$ (b) $\frac{\overset{m}{\mathbf{f}}_\theta(r,\Theta)}{\sigma_{ref}/R_2}$

Figure 3.17: Components (a) radial and (b) tangent of the normalized body forces of electromagnetic origin in the stator.

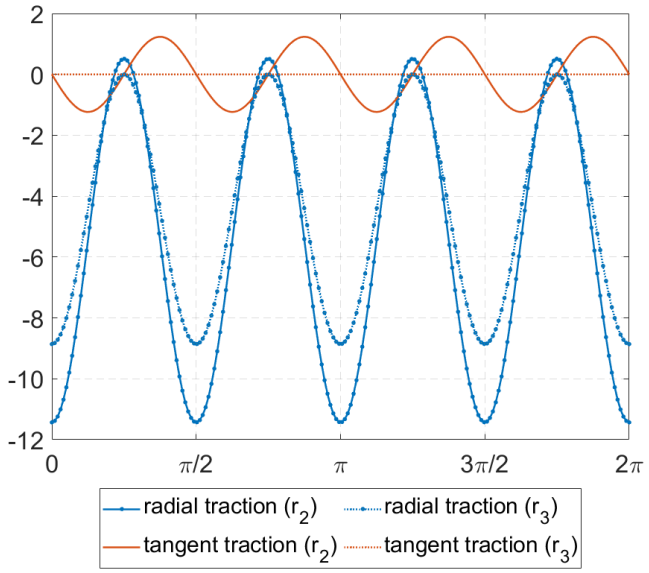


Figure 3.18: Normalized electromagnetic surface traction at interfaces $\partial\mathscr{D}_2$ and $\partial\mathscr{D}_3$: radial $\frac{\overset{e}{\sigma}_{rr}}{\sigma_{ref}}$ and tangent $\frac{\overset{e}{\sigma}_{r\theta}}{\sigma_{ref}}$.

body forces (Figure 3.17), however this is just a misleading inkling due to the normalization of the body forces by the radius $R_2$ and the fact that body forces act in volume while surface traction act on surfaces. A proper comparison involves the surface traction and $\overset{m}{\boldsymbol{\sigma}}$ the electromagnetic part of the stress (see Figure 3.19) from which the body forces derive, and shows that body forces effects are *not negligible compared to traction at the interfaces*. This concurs with the observations made on the

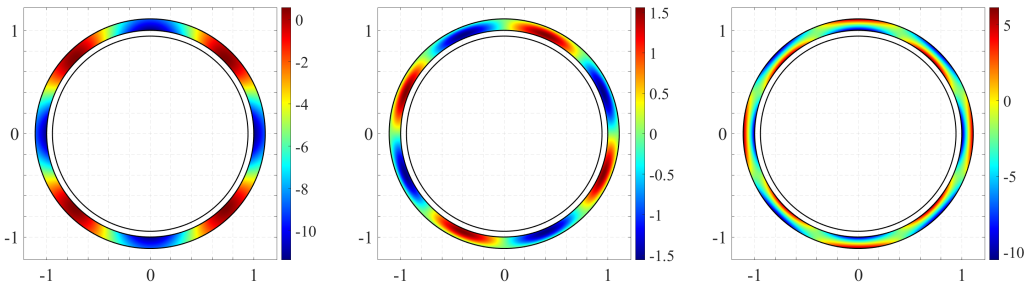

(a) $\frac{\overset{m}{\sigma}_{rr}(r,\Theta)}{\sigma_{ref}}$ (b) $\frac{\overset{m}{\sigma}_{r\theta}(r,\Theta)}{\sigma_{ref}}$ (c) $\frac{\overset{m}{\sigma}_{\theta\theta}(r,\Theta)}{\sigma_{ref}}$

Figure 3.19: Normalised magnetic part of the stresses in stator, accounting for magnetostriction ($\Lambda = -1.3\times10^3$): (a) normal, (b) shear and (c) hoop.

rotor boundary value problem (Section 3.1) that body forces are not negligible in ferromagnetic materials and that they may still be significant despite the negligible currents $\boldsymbol{\mathcal{J}} = 0$ because of force contributions other than the Lorentz force. The radial surface traction acting on the outer boundary has amplitude comparable to the radial traction on the inner stator boundary. Regarding tangent traction, as for the electromagnetic body forces θ-component (Figure 3.17) the traction terms in the

$\hat{\mathbf{e}}_\theta$ direction are purely sinusoidal in $\theta$ - no average component - and thus induce neither expansion neither pull in $\hat{\mathbf{e}}_\theta$. The fact that *neither the surface traction nor the body forces induce any resultant pull in* $\hat{\mathbf{e}}_\theta$ *- or resultant torque along* $\hat{\mathbf{e}}_z$ - explains why no boundary conditions on $\mathbf{u}$ where required in the solution process in Section 3.2. The null tangent traction force on the stator's outer boundary is explained by the boundary condition imposed on $b_r(r_3) = 0$ (hypothesis of magnetic insulation). The tangent traction on the inner boundary $r_2$ acts in opposition to the body forces in $\theta$ - positive when the body forces are negative and reciprocally.

The pics of *positive values* for the radial traction in $r = r_2$ are explained by the traction term of (3.45) that involves the magnetostriction coefficient $\Lambda$ and the radial magnetic field $b_r$. They correspond to regions where the magnetic field is dominantly radial (see Figure 3.15). In comparison, the corresponding pics for the radial traction in $r_3$ never go above zero because of the hypothesis $b_r = 0$. In these regions where the magnetic field is dominantly radial, the moderate difference between the pics of the radial traction in $r_2$ and those of the radial traction in $r_3$ highlights the moderate influence of the radial component of the magnetic field and that the *traction forces are mostly due to the tangent magnetic field component*. The tangent component of the magnetic field is indeed the "large" component on a circular stator given the jump condition $[\![h_\theta]\!] = 0$ at interfaces with air and the large difference in magnetic permeability.

The stator takes on the difference between the surface traction forces in $r_2$ and $r_3$, which is thus of more comparable amplitude with the electromagnetic body forces. Furthermore, the difference between radial surface forces in $r_2$ and $r_3$ alternates between positive and negative, which is likely to introduce bending. Similarly the net shear forces due to the interface forces alternate between positive and negative.

### 3.2.3.4 *Total and elastic stresses*

Figure 3.20 provides the normal, shear and hoop *total stress* components normalized by the reference stress $\sigma_{ref}$ that quantifies a stress input due to the input magnetic field in $r_1$. It shows a clear dominance of the hoop component with a distribution traducing bending. Here again the symmetrical amplitude on the shear stress component explains the absence of resulting torque along $\hat{\mathbf{e}}_z$ (recall (3.9)).

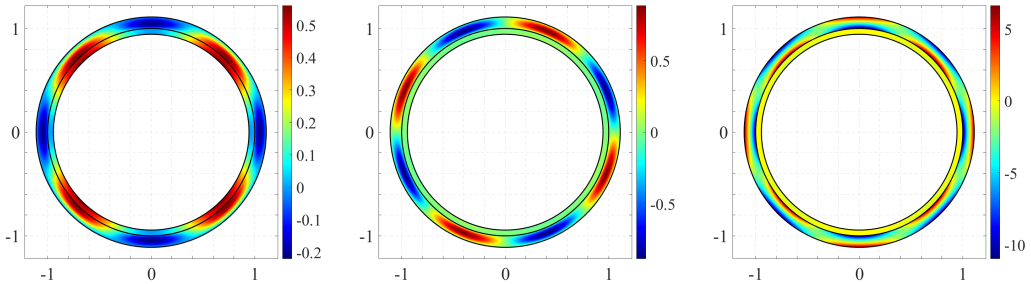


(a) $\frac{\sigma_{rr}(r,\Theta)}{\sigma_{ref}}$ (b) $\frac{\sigma_{r\theta}(r,\Theta)}{\sigma_{ref}}$ (c) $\frac{\sigma_{\theta\theta}(r,\Theta)}{\sigma_{ref}}$

Figure 3.20: Normalized total stresses in stator, accounting for magnetostriction ($\Lambda = -1.3\times10^3$): (a) normal, (b) shear and (c) hoop.

The normal stress components highlights regions of push ($\theta = 0 + k\frac{\pi}{2},\ k = 1,...4$) and pull ($\theta = \frac{\pi}{4} + k\frac{\pi}{2},\ k = 1,...4$) along the $\hat{\mathbf{e}}_r$ direction, yet of much smaller amplitude than the surface traction acting on the stator boundaries (Figure 3.18) acting along $-\hat{\mathbf{e}}_r$.

Figure 3.21 shows the distribution of the normal, shear and hoop *elastic stress* components, normalized by the reference stress $\sigma_{ref}$. The important differences between the result for the elastic stresses $\overset{e}{\boldsymbol{\sigma}}$ and the total stresses $\boldsymbol{\sigma} = \overset{e}{\boldsymbol{\sigma}} + \overset{m}{\boldsymbol{\sigma}}$ *attests of significant electromagnetic stresses* $\overset{m}{\boldsymbol{\sigma}}$ and consequently of the point previously made that the electromagnetic body forces ($\nabla\cdot\overset{m}{\boldsymbol{\sigma}}$) are not negligible. The results of Figure 3.21 show that the shear elastic stress is an order lower in magnitude when compared to the dominant radial and hoop elastic stresses. The normal elastic stress component is mostly compressive. The significant hoop stress component alternates zones of traction and compression on each side of the stator circular middle line, which indicates significant bending effects. This is highlighted by the radial displacement in Figure 3.22, which is positive in regions of negative normal elastic stress $\overset{e}{\sigma}_{rr}$ and vice-versa. This radial displacement "against" the normal stress is explained by the dominant bending along $\hat{\mathbf{e}}_z$ acting against $\overset{e}{\sigma}_{rr}$.

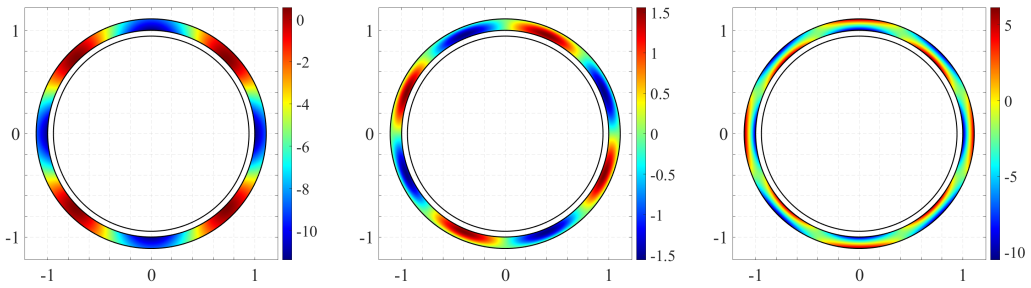

(a) $\frac{\overset{e}{\sigma}_{rr}(r,\Theta)}{\sigma_{ref}}$ (b) $\frac{\overset{e}{\sigma}_{r\theta}(r,\Theta)}{\sigma_{ref}}$ (c) $\frac{\overset{e}{\sigma}_{\theta\theta}(r,\Theta)}{\sigma_{ref}}$

Figure 3.21: Normalised elastic stresses in stator, accounting for magnetostriction ($\Lambda = -1.3\times10^3$): (a) normal, (b) shear and (c) hoop.

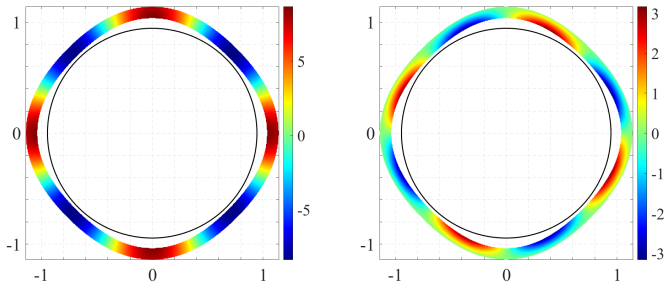

(a) $\frac{u_r(r,\Theta)}{u_{ref}}$ (b) $\frac{u_\theta(r,\Theta)}{u_{ref}}$

Figure 3.22: Normalized displacements in stator, magnified $4\times10^6$ times, accounting for magnetostriction ($\Lambda = -1.3\times10^3$): (a) radial, (b) tangent. The central circle pictures the rotor boundary $\partial\mathscr{D}_1$.

### 3.2.4 *A comparison with other models*

To gain insight on the benefits of the previous analytical developments, an interesting comparison is that of the results obtained for the previous stator boundary value problem (in the following referred to as *Model 1*) with the result one would obtain in two other cases of expressions for $\overset{m}{\boldsymbol{\sigma}}$, referred to as *Model 2* and *Model 3*. *Model 2* has the same expression as used in the previous stator stress computations, however for the particular case $\Lambda = 0$ i.e. not accounting for any magnetostriction contribution. *Model 3* is a model that has been recently proposed by (Pile et al., 2019a; Pile et al., 2019b; Pile et al., 2020) for vibroacoustic analysis of electric motors. These studies are most often performed at design or predesign stages for optimization of motor designs, and favor analytic or semi-analytic expressions of force distributions for fast analyses at reduced computational costs. In an approximation, the model proposed reduces the electromagnetic stress at the stator to

$$\overset{m}{\boldsymbol{\sigma}} = \frac{1}{\mu}\left(\mathbf{b}\mathbf{b} - \frac{1}{2}(\mathbf{b}\cdot\mathbf{b})\mathbf{I}\right) , \tag{3.56}$$

which is referred to as the "*Maxwell tensor*" for its similarity with the Maxwell stress in vacuum (same expression with $\mu = \mu_0$). As detailed in Subsection 2.2.2, this expression for $\overset{m}{\boldsymbol{\sigma}}$ accounts for the Lorentz force only and under the hypothesis of no stator currents the resulting magnetic body force $\overset{m}{\mathbf{f}} = \boldsymbol{\nabla}\cdot\overset{m}{\boldsymbol{\sigma}} = \mathbf{j}\times\mathbf{b} = 0$. The stress equation to solve on the elastic stress becomes simply

$$\mathscr{D}_3 : \quad \boldsymbol{\nabla}\cdot\overset{e}{\boldsymbol{\sigma}} = 0 . \tag{3.57}$$

At the air-stator interfaces in $r_2$ and $r_3$, the stress jump condition in terms of the continuous $b_r$ and $h_\theta$ components become,

$$\partial\mathscr{D}_2 \cup \partial\mathscr{D}_3 : \quad \begin{cases} \overset{e}{\sigma}_{rr} = \dfrac{1}{2}\dfrac{\chi}{\mu}b_r^2 + \dfrac{1}{2}\mu_0\chi h_\theta^2 \\ \overset{e}{\sigma}_{r\theta} = 0 \end{cases} . \tag{3.58}$$

Analytic calculation for this model are performed in a similar fashion as in Section 3.2.2 and on the same stator problem (same geometry, same material parameters), save for the changed stress expression. The magnetic field distribution is unaffected and remains the same. For stress calculation, because of the absence of electromagnetic body forces in this model due to the hypothesis of no stator currents, only remains the homogeneous stress field solution, with constants to be determined from application of the aforementioned stress boundary conditions (3.58) in $r_2$ and $r_3$.

Figure 3.23 provides a comparison of the radial component of interface forces in $r_2$ and $r_3$ obtained for the three models. The plot is over the range $\theta \in [0, \pi]$ for clarity of the figure, and extendable to $[0, 2\pi]$ by the $\pi/2$-periodicity of the problem (fields in $\cos(2\Theta)$ and $\sin(2\Theta)$). The radial surface forces are significantly different between Model 1, 2 and Model 3. This difference is due to the stress term $\frac{\chi}{2\mu}(\mathbf{b}\cdot\mathbf{b})\mathbf{I}$ added in our models. Between Model 1 and Model 2, one observes

a slight contribution of the magnetostrictive term $\frac{\Lambda}{\mu}\mathbf{bb}$, which as explained in Subsection 3.2.3.3 introduces some bending in Model 1, which is not occurring in Model 2. The contribution is much lower than that of magnetization forces, which concurs with observations made for the rotor case in Section 3.1. As to the tangent component of the surface forces, no comparison plot is provided given Model 2 and Model 3 both have zero tangent surface forces in $r_2$ and $r_3$. The tangent surface forces for Model 1 is given in Figure 3.18. It should finally be noted that if the interface traction on the external stator boundary for Model 3 is negligible as a result of the magnetic insulation hypothesis $b_r = 0$ - which justifies that it be neglected in the associated literature (Pile et al., 2019b; Pile et al., 2019a; Pile et al., 2020) - it is not negligible for Model 1 and Model 2 and should definitely be accounted for. Further, because of its importance, it raises the question of the impact of the negligible magnetic flux leakage hypothesis on the external stator boundary $b_r = 0$.

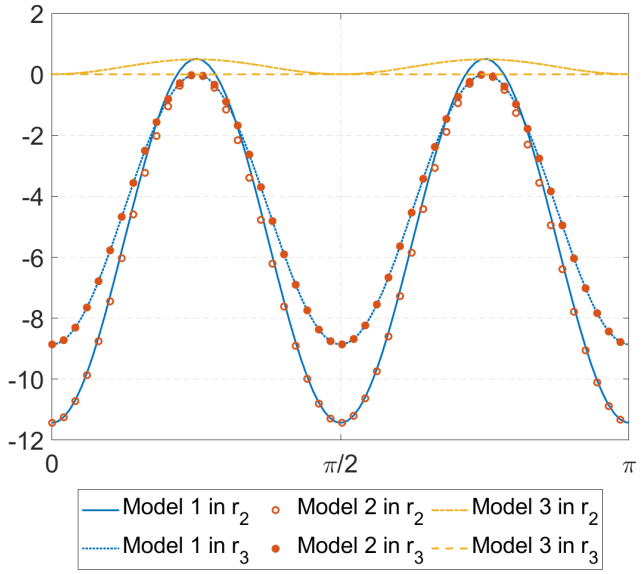


Figure 3.23: For the three models compared, radial normalized surface traction $\frac{e}{\sigma_{rr}}{\sigma_{ref}}$ at interfaces $\partial\mathscr{D}_2$ and $\partial\mathscr{D}_3$.

The general stress, elastic stress and displacement results obtained in the two configurations of Model 2 and Model 3 have distributions similar - though different - to the ones obtained in 3.2.3.4. To lighten this section, they are given in Appendix B.6. In order to highlight the differences between the three models, the following provides comparison plots for the range over which the stress, elastic stress and displacement components span for all $(r, \theta) \in \mathscr{D}_3$ (stator). For the *total stresses*, Figure 3.24 shows the same comparable results for all three models, suggesting the same total stress distribution for all three models (confirmed by looking at the additional results in Appendix B.6). Indeed, all three models solve the same equation for the total stresses $\nabla\cdot\sigma = 0$ with the same boundary conditions that $\sigma$ be equal to the Maxwell stress in air on each boundary of the stator. Because the magnetic field distribution remains unchanged from one model to another, the

Maxwell stress in air domains remains unchanged. Same equation, same boundary conditions: same results logically follow[30] for $\boldsymbol{\sigma}$. As a result of all three models hav-

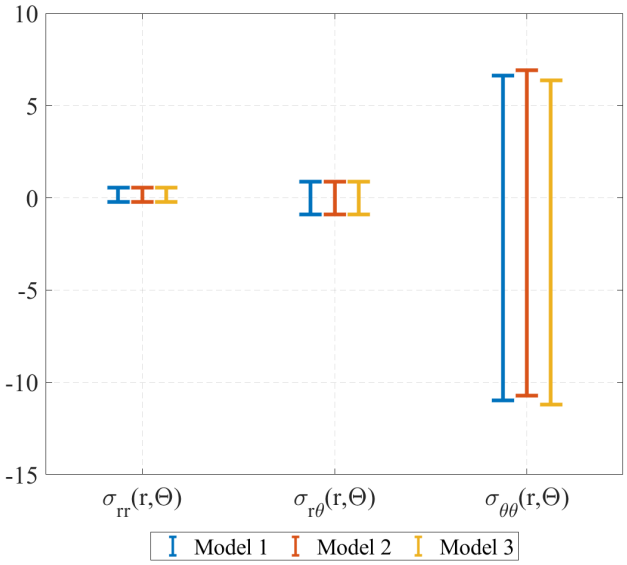


Figure 3.24: For the three models compared, range of values across all $(r,\Theta) \in \mathscr{D}_3$ for the normalized total stress $\frac{\sigma}{\sigma_{ref}}$: for the normal, shear, and hoop stress components.

ing the same total stress $\boldsymbol{\sigma}$ but different expressions for $\overset{m}{\boldsymbol{\sigma}}$, significant differences occur for $\overset{e}{\boldsymbol{\sigma}}$[31], as highlighted in Figure 3.25. One can observe from Figure 3.24 and Figure 3.25 - and additional results in Appendix B.6.2 - that Model 3 has $\overset{e}{\boldsymbol{\sigma}} = \boldsymbol{\sigma}$, following $\overset{m}{\boldsymbol{\sigma}} = 0$ as a result of the negligible currents and thus negligible body forces[32]. The differences on the elastic stresses between Model 1 and Model 3 are then mostly on the radial $\sigma_{rr}$ (roughly a factor 10), and shear $\sigma_{r\theta}$ (roughly a factor 2) stresses. The difference is much less significant on the hoop stress $\sigma_{\theta\theta}$.

Regarding the displacement field, comparison results are given in Figure 3.26 for the radial displacement $u_r(r,\Theta)$ and tangent displacement $u_\theta(r,\Theta)$. It was also judge interesting to perform the comparison on the non-harmonic "static" fraction $u_r^0$ of the radial displacement field[33]. The most striking difference between Model 1 and Model 3 is on the $u_r^0$ distribution (roughly a factor 5 on the amplitude of the spectrum of values, roughly a fator 7 on the minimum value). Further, this distribution of $u_r^0$ is centered around 0 for Model 1, while values are compressive (contraction of the stator) for Model 3. The amplitude spanned by the total radial displacement $u_r$ is roughly unchanged between Models 1 and 3 (4% shorter for Model 3). The difference is slightly higher for the tangent displacement $u_\theta$ (the amplitude is 13% higher compared to Model 1). Both model have the tangent dis-

30 The slight differences observed on the results for $\sigma_{\theta\theta}$ in Figure 3.24 are attributed to numerical errors in the numerical solution of the integration constants of the analytical stress field expressions.

31 Recall $\overset{e}{\boldsymbol{\sigma}} = \boldsymbol{\sigma} - \overset{m}{\boldsymbol{\sigma}}$.

32 Recall in the case of Model 3 $\boldsymbol{\nabla}\cdot\overset{m}{\boldsymbol{\sigma}} = \mathscr{J}\times\mathbf{b}$.

33 Recall the displacement $\mathbf{u}(r,\Theta) = \mathbf{u}^0(r) + \mathbf{u}^c(r)\cos(2\Theta) + \mathbf{u}^s(r)\sin(2\Theta)$.

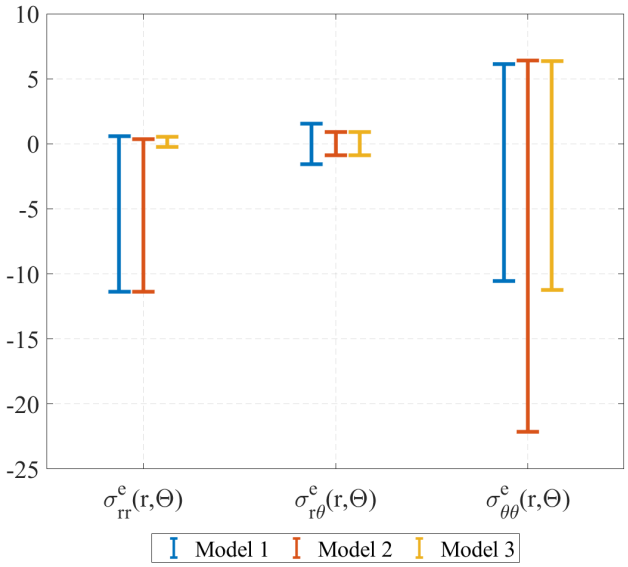


Figure 3.25: For the three models compared, range of values across all $(r,\Theta) \in \mathscr{D}_3$ for the normalized elastic stress $\frac{\overset{e}{\sigma}}{\sigma_{ref}}$: for the normal, shear, and hoop stress components.

placement $u_\theta$ centered around 0 (no rotation of the stator, as already highlighted). Overall, the differences between Model 1 and Model 3 concur with the observations made on the rotor boundary value problem in 3.1 that *in materials with strong magneto-mechanical couplings and high magnetic properties such as ferromagnetic materials, other forces than the Lorentz force appear and are significant*. The observation that the so-called "*Maxwell stress tensor*" is not enough to describe the behavior of materials that have strongly coupled magneto mechanica-behavior was already made by some authors based on theoretical grounds (e.g. see Bossavit, 2011,Bossavit, 2015). *It is here quantified on a practical example*. This point may be valuable for the improvement of the typical vibroacoustic design tools that neglect volume forces and include interface forces only (Pile et al., 2019b; Pile et al., 2019a; Pile et al., 2020). It remains interesting to see that for the present study these vibroacoustic tools, although approximate, still provide a close approximation of the amplitudes (maximum value minus minimum value) for the radial displacement $u_r$ (4% difference) and the tangent displacement $u_\theta$ (13% difference). The average stator contraction however is significantly different.

The comparison between Model 1 and Model 2[34] highlights the impact of the magnetostriction coefficient $\Lambda$. The impact on the radial elastic stress component is negligible. The difference is on the shear and hoop component of the elastic stress (roughly a factor 2 for both). As previously detailed, the magnetic field in the stator is mostly along $\hat{e}_\theta$ and stronger in that direction. Magnetostriction can be expected to act in the direction of the field mostly[35]. As a consequence, its impact on the shear and hoop components mostly seems sound. The consequences

34 Recall Model 2 is the same as Model 1 save for the magnetostriction coefficient $\Lambda = 0$.
35 Recall the magnetostrition has effect the elongation of the grains in the direction of the applied field.

on the displacement fields - going from no magnetostriction in Model 2 to magnetostriction accounted for in Model 1 - are a decreased amplitude for $u_\theta$ (roughly 30%) and an average contraction $u_r^0$ of the stator centered around 0 instead of negative everywhere in the case of Model 2. This observations seems consistent as the magnetostriction contribution added when going from Model 2 to Model 1 elongates the stator in the direction of the field - mostly in $\hat{\mathbf{e}}_\theta$ as previously mentioned -, which consequently tends to stator expansion. Save for the shift in $u_r^0$, the amplitude of the radial displacement remains unchanged (under 2% difference).

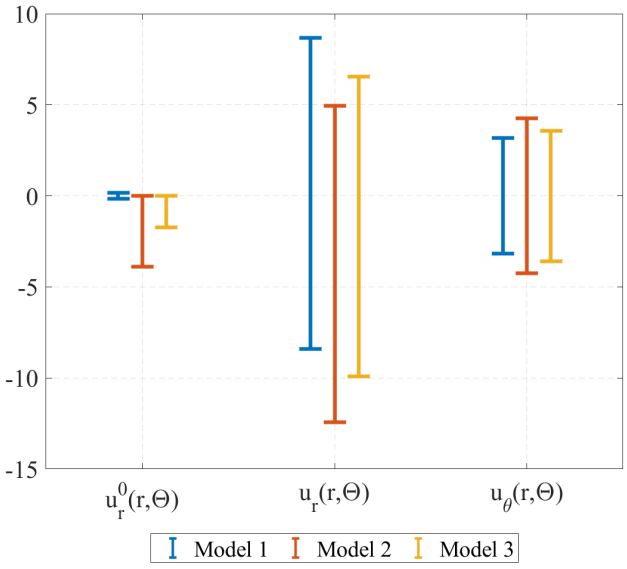


Figure 3.26: For the three models compared, range of values across all $(r,\Theta) \in \mathscr{D}_3$ for the displacement, normalized by $u_{ref}$: for the mean radial displacement $u_r^0(r)$, for the total radial displacement $u_r(r,\Theta)$ and for the total tangent displacement $u_\theta(r,\Theta)$.

### 3.2.5 *Conclusion for the stator problem*

As a second example of application, the theory presented in Chapters 1 and 2 is employed for the analytical modeling of the stator of an idealized synchronous motor for which we calculate the magnetic, stress and displacement fields. The most important results discussed for the stator analytical boundary value problem are:

MAIN RESULTS:

- We highlighted based on a practical analytical example that the magneto-mechanical couplings in the ferromagnetic materials found in electric motors are *not finely described by a material Maxwell-like stress tensor* $\overset{m}{\boldsymbol{\sigma}} = \frac{1}{\mu}(\mathbf{bb} - \frac{1}{2}(\mathbf{b}\cdot\mathbf{b})\mathbf{I})$ commonly used as an approximation in the electric motor literature (Pile et al., 2019b; Pile et al., 2019a; Pile et al., 2020). This

was already explained in for instance Bossavit, 2011; Bossavit, 2015 based on theoretical grounds. It is here quantified.

- In electric motor problems with materials that have strong magnetic properties and a strong magneto-mechanical coupled behavior, such as the ferromagnetic materials, *body forces are just as important as traction of electromagnetic origin at interfaces*, justifying the analysis and calculation of total stresses in the bulk;
- *Traction forces are mostly due to the tangent magnetic field component*, much larger than the radial component. This for instance suggests that FEM methods should focus on the precision of the tangent magnetic field;
- *Traction forces are significant on both internal and external stator surfaces*, which raises the question of computing the external magnetic field in air around the stator - instead of the magnetic insulation hypothesis $b_r = 0$ on the stator's periphery - to see if it impacts the traction boundary condition;
- The stator tends to contract in addition to ovalization, which concurs with the existing literature (e.g. see Fonteyn et al., 2010a).

# 4

# CONCLUSION OF PART I

The essential contributions of Part I are:

- Proposing a general framework, based on the direct approach of continuum mechanics using the principles of electromagnetism, mechanics and thermodynamics, suitable for the modeling of coupled thermo-magneto-mechanical problems in electric motors;
- A proper linearization of the constitutive relations in the small strains, arbitrary magnetization regime for materials with coupled magneto-mechanical behaviors;
- Examples of analytical boundary value problems for simplified electric motors to calculate temperature fields and identify different contributions of stress and body forces.

DISCUSSION Using the direct approach of continuum mechanics, based on the work of Kovetz, 2000, a general framework that couples the electromagnetic, thermal and mechanical effects is derived and subsequently applied to formulate the boundary value problem for electric motors. Particular attention is paid to the derivation of the coupled constitutive equations for isotropic materials under small strain but arbitrary magnetization, an important highlight of this work: in the field of electric motors and associated literature, the small strain expressions typically used do not comply with the angular momentum balance, an essential principle of mechanics. Due to the complex geometry of a typical electric motor (see Figure 0.1) and to the non-linear and coupled material behavior, numerical solutions of the governing equations are required. To gain insight, the theory is applied to the modeling of two idealized analytical boundary value problems.

As a first application, we calculate the magnetic, thermal, and stress fields at the rotor of an idealized asynchronous motor that has significant induced currents. Comparing the Lorentz, magnetization and the magnetostrictive forces for a rotor made of electrical steel, we find that the first are negligible and the second dominant. Magnetostrictive body forces – resulting from the constitutive coupling between stress and magnetization effects – although smaller than their magnetic counterparts, are considerably higher than the Lorentz. The comparison of the different parts of the stress tensor (elastic and total) to the purely mechanical stresses due to inertia, reveals the significant influence of electromagnetic phenomena on the resulting stress state. As a result of the significant induced currents due the skin effect, a stress concentration boundary layer develops about the rotor's edge.

A second example of application addresses the stator of an idealized permanent magnet motor for which we calculate the magnetic, stress and displacement fields. Three models are compared that include the Lorentz forces only, the Lorentz and

magnetization forces or the Lorentz, magnetization and magnetostriction forces altogether. As for the rotor case, significant differences in the elastic stress and displacement fields are observed between the models, which confirms the significant influence of the magnetization and magnetostriction forces. A comparison with existing tools and approximations of the force terms typically used for the vibroacoustic analyses of electric machines is discussed.

Both problems are solved using realistic material parameters, geometric and operational regime values and show how classical methods of elasticity can be used for the analytical solution of coupled magneto-mechanical motor problems. They both show clearly the importance of correctly accounting for the coupled magneto-mechanical effects and both interface traction and body forces of electromagnetic origin for the accurate calculation of elastic stress and displacement fields in electric motors. The proposed methodology for solving general boundary value problems is applicable to more complicated motor geometries and nonlinear constitutive responses that include moderate strains, magnetic saturation and dissipative effects. For these problems, a numerical approach based on coupled variational principles is necessary, which is the object of Part II of this thesis.

SUGGESTIONS FOR FUTURE WORK ON ANALYTICAL METHODS Despite the theory provided being general enough to account for a wide range of couplings between mechanical, magnetic and temperature fields, the analytical models provided here take assumptions on the coupling terms and the material behavior may be further refined.

For the tractability of the analytical calculation, some of the coupling terms between the magnetic field and the strains were neglected. Further investigation on the ability to account for these coupled terms - of order greater than 2 in $\mathbf{b}$ - in analytical calculation would be interesting, in particular for a better understanding of the vibroacoustics of electric motors.

The analytical method provided may possibly be extendable to the analytic modeling of more complex geometries - accounting for stator and rotor teeth and slots for instance - in the spirit of Lubin, Mezani, and Rezzoug, 2011a, Lubin, Mezani, and Rezzoug, 2011b, Lubin, Mezani, and Rezzoug, 2012.

The small strain but arbitrary magnetization expression provided, because derived from expressions that comply with thermodynamics and with the angular momentum balance, include physical restrictions that are usually not accounted for in the characterization of electrical steels. Their performance at fitting the experimental data, likely with fewer coefficients to be determined, should be investigated.

Part II

# A VARIATIONAL FORMULATION FOR FINITE ELEMENT ANALYSIS

# 5

# VARIATIONAL FORMULATION FOR ELECTRIC MOTOR PROBLEMS

In addition to the coupled magneto-mechanical behavior mentioned throughout the beginning of this work, a typical electric motor, depicted in Figure 0.1, has a complex geometry and non-linear (in particular magnetic) material behavior requiring numerical solution. This chapter pertains to the derivation of a suitable variational formulation for the subsequent numerical finite-element analysis of electric motor problems. The numerical implementation is later detailed in Chapter 6 and examples of application to electric motor problems are given in Chapter 7.

LITERATURE REVIEW The first FEM computations for stresses in electric motors used a stepwise, uncoupled, approach: electric currents and magnetic fields where calculated using a purely electromagnetic model; the electromagnetic body force vector was then introduced as the external body force in a purely mechanical model to calculate the resulting stress state (e.g. see: Reyne, Sabonnadière, and Imhoff, 1988; Javadi et al., 1995). The above-described approximate methods are inadequate to deal with the true multiphysics nature of the electric motor problem. Recognizing these issues, recent work by Fonteyn, 2010; Fonteyn et al., 2010b; Fonteyn et al., 2010a takes into account magnetoelastic coupling effects for the numerical stress calculation in electric motors. They propose a weighted residual Galerkin method based on the small strain current configuration (Eulerian) governing equations (linear momentum balance and Ampère's law), which they obtain from the direct approach. Because the numerical implementation is solved in the bulk ferromagnetic material only (for the coupled problem), it does not retrieve the Maxwell stress in the airgap region[1]. The last has a significant influence on the solution of the equation of motion. As a consequence, the formulation of Fonteyn, 2010; Fonteyn et al., 2010b artificially adds the contribution of the airgap Maxwell stress at the interface nodes between the airgap and the ferromagnetic components.

It should be mentioned here that various commercial packages exist which claim the ability to solve the magneto-mechanical problems (for instance see Ledger et al., 2016; Pile, Devillers, and Le Besnerais, 2018 for a review of various available packages). However coupled problems can take many forms depending on the semantics one uses - weak couplings, strong couplings, stepwise couplings by subsequently solving the equations of motion and the equations of electromagnetism, etc... - and it is very difficult to finely grasp in a reasonable amount of time what these codes truly solve and how. Further, these coupled modules are "rigid" in the sense that one has to comply with the possibilities that they offer and what they do not allow. As mentionned in Ledger et al., 2016, this leads to the conclusion that

1 The Maxwell stress pervades vacuum – and air regions typically assimilated to vacuum – that surrounds the motor components. This stress is responsible for surface traction that arise at the interface between air and a magnetic materials as a result of their distinct magnetic properties (see Section 2.2.3).

it is often easier to develop one's own codes. Through the possibility of defining *user elements*, the general purpose finite element code *Abaqus*, offers the possibility of defining one's own coupled FEM tools, and call to the software's solver only.

The energies of electromagnetic and coupled electro-magneto-mechanical problems are known, at least for non-dissipative problems. As such, variational formulations exists in the literature for the modeling of purely electromagnetic problems, which do not require the use of the Galerkin method. A review of variational formulations for electromagnetic problem is presented in Lazzari and Nibbi, 2000, among which is a least action principle formulation for which we also refer the reader to the work of Lax and Nelson, 1976. Other authors have suggested variational formulations for coupled-electromagnetic thermomechanical problems based on Hamilton's principle. Some of them are referred to in the introduction of Lazzari and Nibbi, 2000, among which Maugin, 1980 which proposes a variational formulation based on the Method of Virtual Powers and a series of important works around Lagrangian approaches (Trimarco, 2007; Trimarco, 2005; Trimarco, 2002; Trimarco and Maugin, 2001; Maugin, 1993) that are our interest here. This Hamilton principle based formulation has been applied to the modeling of magneto-rheological elastomers (Kankanala and Triantafyllidis, 2004) or electromagnetic forming processes (Thomas and Triantafyllidis, 2009). The formulation is Lagrangian as a requirement to retrieve the Maxwell stress contribution, and consequently it is a finite strain formulation. Despite the electric motors being typically subject to small strains, we shall propose here an extension of this variational formulation to the electric motor problem.

SUMMARY AND OUTLINE Following the approach of Thomas and Triantafyllidis, 2009, a Hamilton principle based variational formulation is considered here as a particularly efficient solution for the modeling of coupled electro-magneto-mechanical problems. For ease of derivation, it is written on the reference Lagrangian configuration and thus involves large strains although application to electric motor problem in Chapter 7 leads to small strains. We believe starting from the most general problem before restricting it for particular application ensures we remain consistent throughout the development. For that reason, in the spirit of Part I that proposes a formulation for very general coupled electromagnetic-thermomechanical problems prior to applying restrictions suitable for the modeling of electric motors, we first propose a general variational formulation for dynamic electromagneto-mechanical problems, before restricting the formulation to a more suitable form for the particular case of electric motor problems (eddy current approximation).

In the following, Section 5.1 proposes a Lagrangian for the general variational formulation of dynamic electro-magneto-mechanical problems. Applying Hamilton's principle, we show that the Lagrangian suggested complies with the theory obtained from the direct approach in Chapter 1, a non trivial result for coupled problems. In Section 5.2, we restrict the formulation in the eddy current approximation for use in electric motor problems. We show that upon applying Hamilton's principle the governing equations of the electric motor (eddy current) problem obtained from the direct approach in Chapter 2 are retrieved.

*Nota:* For simplicity and without loss of generality, the formulations provided hereafter in Sections 5.1 and 5.2 do not account for any dissipation effects, and consequently internal variables $\xi$ (see Chapter 1) are dropped. Temperature aspects are discarded as well[2]. Despite this, the theory exposed in Sections 5.1 and 5.2 remains able to encompass a wide range of non-linear coupled electro-magneto-mechanical phenomena. Also note that in this part of the thesis, we work with the form of the specific energy $\psi = \Psi(\mathbf{C}, \boldsymbol{\mathscr{E}}, \mathbf{B})$ that has the true Lagrangian magnetic field $\mathbf{B}$[3] (see Section 1.4.4).

## 5.1 A FORMULATION FOR GENERAL ELECTRO-MAGNETO-MECHANICAL PROBLEMS

Following Kankanala and Triantafyllidis, 2004; Thomas and Triantafyllidis, 2009, we write the variational formulation of the problem in the reference configuration. Doing so eases the calculation of variations: as terminals of integrals are fixed in the reference configuration, only the variations of the integrand need to be accounted for.

### 5.1.1 *A Lagrangian density for purely electromagnetic problems*

The proposed variational formulation is based on the $\phi - \mathbf{a}$ potential formulation such that conveniently two of Maxwell's law are identically satisfied by construction: Maxwell-Faraday's law and the no-magnetic monopole law (see Section 1.2.2).

From Lax and Nelson, 1976, a current configuration purely electromagnetic Lagrangian density can be defined for the study of moving and deformable bodies with no polarization nor magnetization,

$$\ell(\phi, \mathbf{a}) = \frac{\epsilon_0}{2}(\boldsymbol{e}\cdot\boldsymbol{e}) - \frac{1}{2\mu_0}(\mathbf{b}\cdot\mathbf{b}) + \mathbf{j}\cdot\mathbf{a} - q\phi \, . \tag{5.1}$$

In the above, $\boldsymbol{e}$ and $\mathbf{b}$ are functions of the potentials $\phi$ and $\mathbf{a}$ through (1.22). The potentials are taken as the Lagrangian's generalized coordinates such that when applying Hamilton's principle, the Euler-Lagrange equations for $\phi$ and $\mathbf{a}$ respectively yield Maxwell-Gauss and Maxwell-Ampère's laws for media with no polarization nor magnetization (Lax and Nelson, 1976). Note that $\mathbf{j}$ and $q$ are externally applied quantities held constant in the process of applying Hamilton's principle of variations (later in Section 5.2.2).

Passing the pure electromagnetic Lagrangian density $\ell$ (5.1) to the reference configuration provides the reference configuration Lagrangian density $\ell_0$ (Lax and Nelson, 1976),

$$\ell_0 = J\ell = \frac{\epsilon_0 J}{2}\mathbf{E}\cdot\mathbf{C}^{-1}\cdot\mathbf{E} - \frac{1}{2\mu_0 J}\mathbf{B}\cdot\mathbf{C}\cdot\mathbf{B} + \boldsymbol{\mathscr{J}}\cdot\mathbf{A} - Q\Phi \, , \tag{5.2}$$

2 We showed previouly in Part I how temperature and internal variables can be accounted for to model dissipative behaviors. These developments may help in the derivation of variational formulations that account for dissipative behaviors such as thermo-mechanical couplings, thermo-magnetic couplings and magnetic hysteresis, which are particularly relevant to the modeling of electric motors.

3 In contrast to $\psi = \hat{\psi}(\mathbf{C}, \boldsymbol{\mathscr{E}}, \tilde{\mathbf{B}})$ where $\tilde{\mathbf{B}}$ is not the true counterpart of the Eulerian magnetic field $\mathbf{b}$.

where we recall the field transformations (see equations (1.38), (1.41), (1.44), (1.50) and (1.107)),

$$\begin{aligned} &\mathbf{E} = \boldsymbol{e}\cdot\mathbf{F}\,, \qquad \boldsymbol{\mathcal{J}} = J\mathbf{F}^{-1}\cdot\boldsymbol{\jmath}\,, \quad \mathbf{A} = \boldsymbol{a}\cdot\mathbf{F}\,, \\ &\mathbf{B} = J\mathbf{F}^{-1}\cdot\mathbf{b}\,, \quad Q = Jq\,, \qquad\quad \Phi = \phi - \dot{\mathbf{u}}\cdot\boldsymbol{a}\,. \end{aligned} \tag{5.3}$$

*Notice that here and subsequently, $\dot{\mathbf{x}}$ in the expressions derived in Part I is changed for $\dot{\mathbf{u}} = \dot{\mathbf{x}}$ given $\mathbf{x} = \mathbf{X} + \mathbf{u}$ and variations will subsequently be taken with respect to $\mathbf{u}$.*

As a consequence of the transformation for $\Phi$, the reference configuration conduction current $\boldsymbol{\mathcal{J}}$ stems out in $\ell_0$ (5.2), while it was the total current $\mathbf{j} = \boldsymbol{\jmath} + q\dot{\mathbf{x}}$ that figured in $\ell$ (5.1). It should also be noted for future derivation that $\mathbf{E}$ is related to the Lagrangian electromotive intensity $\boldsymbol{\mathcal{E}}$ through,

$$\mathbf{E} = \boldsymbol{\mathcal{E}} - (\mathbf{F}^{-1}\cdot\dot{\mathbf{u}})\times\mathbf{B}\,, \tag{5.4}$$

and that the Lagrangian electromotive intensity $\boldsymbol{\mathcal{E}}$ and magnetic field $\mathbf{B}$ are related to the Lagrangian potentials $\Phi$, $\mathbf{A}$ through (1.49).

Upon applying Hamilton's principle with Lagrangian generalized coordinates $\Phi$ and $\mathbf{A}$, the Euler-Lagrange equations for $\Phi$ and $\mathbf{A}$ yield the reference configuration Maxwell-Gauss and Maxwell-Ampère's laws for media with no polarization nor magnetization (Lax and Nelson, 1976). $\boldsymbol{\mathcal{J}}$ and $Q$ are externally applied quantities, held constant when taking the variations.

### 5.1.2 *A general coupled electromagnetic-mechanical Lagrangian*

In order to account for mechanics, as well as magnetization and polarization, the pure electromagnetic Lagrangian density provided above needs to be completed with other terms. Based on Thomas and Triantafyllidis, 2009[4], the solids specific free energy $\psi$, the kinetic energy and the work of the external body forces $\mathbf{f}$ and surface tractions $\mathbf{t}_m$ are added to provide the reference configuration total Lagrangian of the system $\mathscr{L}$. For a body occupying a domain $\Omega$,

$$\mathscr{L} \equiv \int_{\mathbb{R}^3} \left( \ell_0 - \rho_0\psi + \frac{1}{2}\rho_0(\dot{\mathbf{u}}\cdot\dot{\mathbf{u}}) + \rho_0\mathbf{f}\cdot\mathbf{u} \right) dV + \int_{\partial\Omega} \mathbf{T}_m\cdot\mathbf{u} dS\,. \tag{5.5}$$

Integration over $\mathbb{R}^3$ is necessary in order to account for the electromagnetic field in both the body $\Omega$ and its surrounding space $\Omega/\mathbb{R}^3$. The density $\rho_0(\mathbf{X}) \neq 0$ for $\mathbf{X} \in \Omega$ and $\rho_0(\mathbf{X}) = 0$ for $\mathbf{X} \in \mathbb{R}^3/\Omega$. The traction $\mathbf{T}_m = \mathbf{t}_m ds/dS$ is the reference configuration counterpart of the current configuration surface traction $\mathbf{t}_m$ applied on the boundary $\partial\Omega$ of domain $\Omega$. The specific free energy $\psi$ is the same functional as that defined in Chapter 1. It makes the link between the variational and direct approaches and we have,[5]

$$\psi = \psi(\mathbf{F},\ \boldsymbol{e},\ \mathbf{b}) = \Psi(\mathbf{C},\ \boldsymbol{\mathcal{E}},\ \mathbf{B})\,. \tag{5.6}$$

4 Note that an important difference is that the specific free energy of the solid in Thomas and Triantafyllidis, 2009 is purely mechanical because of the negligible polarization and magnetization assumptions.

5 Recall that compared to Chapter 1, temperature and internal variables are not considered here.

The Lagrangian in Thomas and Triantafyllidis, 2009 is the same as (5.5) however with $\psi(\mathbf{F}, T, \xi)$ because not accounting neither for polarization nor magnetization. The fundamental difference here lays in (5.6), which enables to account for polarization and magnetization. Similar formulations are also proposed in Trimarco, 2007 and the referred literature (Trimarco, 2005; Trimarco, 2002; Trimarco and Maugin, 2001; Maugin, 1993), mostly based on a formulation with material energy depending on the polarization and magnetization $(\mathbf{p}, \boldsymbol{m})$ instead of electromotive and magnetic fields $(\boldsymbol{e}, \mathbf{b})$ – and reference configuration counterparts – and without the electric charge and current contributions.

In the Lagrangian $\mathscr{L}$ (5.5), $\boldsymbol{\mathcal{J}}$ and Q contained in $\ell_0$, together with $\mathbf{f}$ and $\mathbf{T}_m$ are externally applied quantities. They are considered fixed when applying the variational principle. The independent fields are $\Phi$, $\mathbf{A}$ and $\mathbf{u}$. In the following, we will derive the Euler–Lagrange equations of the corresponding Hamilton's variational principle and show that they do yield Gauss's law for variations with respect to $\Phi$, Ampère's law for variations with respect to $\mathbf{A}$, and the linear momentum balance for variations with respect to $\mathbf{u}$.

Note that in the spirit of Hamilton's principle, the Lagrangian is defined as

$$\mathscr{L} = \mathscr{K} - \mathscr{P} \,. \tag{5.7}$$

with $\mathscr{K}$ and $\mathscr{P}$ respectively the kinetic and potential energies. This motivates the "-" sign in front of the specific free energy contribution in (5.5) and "+" sign in front of the external work of applied loads. An interesting question – though not crucial to our problem – arises as to what is kinetic and what is potential in the pure electromagnetic Lagrangian densities (5.1) and (5.2) and in the Lagrangian of the coupled problem (5.5), as the electromagnetic fields may add contributions to the classical kinetic energy $\frac{1}{2}\rho\dot{\mathbf{x}}\cdot\dot{\mathbf{x}}$. We refer the reader to the work of Trimarco, 2005 for a discussion on that matter.

### 5.1.3 *Application of Hamilton's principle of variations*

We form the action integral $\mathscr{F}$ by integration of the Lagrangian $\mathscr{L}$ between arbitrary times $t_1$ and $t_2$,

$$\mathscr{F} \equiv \int_{t_1}^{t_2} \mathscr{L} \mathrm{d}t \,. \tag{5.8}$$

By Hamilton's principle, the action integral $\mathscr{F}$ is stationary, thus[6]

$$\delta\mathscr{F} = 0, \tag{5.9}$$

with conditions $\delta\Phi = 0$, $\delta\mathbf{A} = \mathbf{0}$ and $\delta\mathbf{u} = \mathbf{0}$ at $t = t_1$ and $t = t_2$. Given the generalized coordinates $\Phi$, $\mathbf{A}$ and $\mathbf{u}$, this reduces to

$$\mathscr{F}_{,\Phi}[\delta\Phi] = \mathscr{F}_{,\mathbf{A}}[\delta\mathbf{A}] = \mathscr{F}_{,\mathbf{u}}[\delta\mathbf{u}] = 0 \,, \tag{5.10}$$

which provides the so-called Euler-Lagrange equations, together with interface conditions, derived hereafter.

6 Here and subsequently, $\delta$ denotes the variation of a functional.

#### 5.1.3.1 *Variations with respect to* $\Phi$

For the variation with respect to $\Phi$, based on intermediate derivations provided in Appendix A.3,

$$\begin{aligned}\mathscr{F}_{,\Phi}[\delta\Phi] &= \int_{t_1}^{t_2}\int_{\mathbb{R}^3} (\ell_{0,\Phi} - \rho_0\Psi_{,\Phi})\,[\delta\Phi]\mathrm{d}V\mathrm{d}t \\ &= \int_{t_1}^{t_2}\int_{\mathbb{R}^3} \Big( (J\mathbf{C}^{-1}\cdot\epsilon_0\mathbf{E})\cdot[-\boldsymbol{\nabla}(\delta\Phi)] - Q\delta\Phi - \rho_0\frac{\partial\Psi}{\partial\mathscr{E}}\cdot[-\boldsymbol{\nabla}(\delta\Phi)]\Big)\mathrm{d}V\mathrm{d}t \\ &= \int_{t_1}^{t_2}\int_{\mathbb{R}^3} \Big( -\mathbf{D}\cdot\boldsymbol{\nabla}(\delta\Phi) - Q\delta\Phi\Big)\mathrm{d}V\mathrm{d}t\,.\end{aligned} \tag{5.11}$$

In the above, the reference configuration electric displacement $\mathbf{D}$ stems out from recognizing the transpose of the aether relation to the reference configuration in (1.110).

Now an integration by part needs to be applied. Deriving from the divergence theorem, it only applies with smooth fields. The fields considered here are reasonably assumed smooth on subdomains between surface interfaces, but piecewise smooth only over the whole space domain $\mathbb{R}^3$, that is discontinuous across interfaces. Thus the integration domain $\mathbb{R}^3$ needs to be split into the various subdomains separated by the interfaces. For simplicity, is assumed here that only two subdomains (and one interface) exist: one "motor part" (or material) domain and outside vacuum. The following can however be generalized to any number of subdomains. The material domain is $\Omega$, as already used before. Its surface boundary is $\partial\Omega$. The "vacuum" subdomain is what remains, that is $\mathbb{R}^3/\Omega$. Thus, applying the integration by part on each subdomain, with a unit normal to the interface $\mathbf{N}$, and a jump $[\![\mathbf{f}]\!] = \mathbf{f}^+ - \mathbf{f}^-$ of a field $\mathbf{f}$ across the interface oriented by the normal $\mathbf{N}$:

$$\begin{aligned}\mathscr{F}_{,\Phi}[\delta\Phi] &= \int_{t_1}^{t_2}\Big\{\int_{\Omega}(\boldsymbol{\nabla}\cdot\mathbf{D} - Q)\delta\Phi\mathrm{d}V + \int_{\mathbb{R}^3/\Omega}(\boldsymbol{\nabla}\cdot\mathbf{D} - Q)\delta\Phi\mathrm{d}V \\ &\qquad - \int_{\partial\Omega_0}\mathbf{N}\cdot[\![\mathbf{D}]\!]\,\delta\Phi\Big\}\mathrm{d}t \\ &= \int_{t_1}^{t_2}\Big\{\int_{\mathbb{R}^3}(\boldsymbol{\nabla}\cdot\mathbf{D} - Q)\delta\Phi\mathrm{d}V - \int_{\partial\Omega_0}\mathbf{N}\cdot[\![\mathbf{D}]\!]\delta\Phi\Big\}\mathrm{d}t\,.\end{aligned} \tag{5.12}$$

As a result for variations with respect to $\Phi$, one finally gets from the fundamental lemma of the calculus of variations,

$$\begin{aligned}&\mathbf{X}\in\Omega: && \boldsymbol{\nabla}\cdot\mathbf{D} = Q\,; \\ &\mathbf{X}\in\partial\Omega: && \mathbf{N}\cdot[\![\mathbf{D}]\!] = 0\,;\end{aligned} \quad \text{with:} \quad \begin{cases}\mathbf{D} = J\mathbf{F}^{-1}\cdot\mathbf{d}\,, \\ Q = Jq\,,\end{cases} \tag{5.13}$$

where one recognizes the reference configuration counterpart of Maxwell-Gauss's law derived in Section 1.3.

#### 5.1.3.2 *Variations with respect to $\boldsymbol{A}$*

For variations with respect to $\mathbf{A}$, based on intermediate derivations provided in Appendix A.3,

$$\begin{aligned}
\mathscr{F}_{,\mathbf{A}}[\delta\mathbf{A}] &= \int_{t_1}^{t_2}\int_{\mathbb{R}^3} (\ell_{0,\mathbf{A}} - \rho_0\Psi_{,\mathbf{A}})\,[\delta\mathbf{A}]\mathrm{d}V\mathrm{d}t \\
&= \int_{t_1}^{t_2}\int_{\mathbb{R}^3} \Big\{ -(J\mathbf{C}^{-1}\cdot\epsilon_0\mathbf{E})\cdot\frac{\mathrm{d}}{\mathrm{d}t}(\delta\mathbf{A}) + \boldsymbol{\mathscr{J}}\cdot\delta\mathbf{A} \\
&\qquad + \left((\mathbf{F}^{-1}\cdot\dot{\mathbf{u}})\times(J\mathbf{C}^{-1}\cdot\epsilon_0\mathbf{E})) - \frac{1}{\mu_0}\mathbf{C}\cdot\mathbf{B}\right)\cdot(\boldsymbol{\nabla}\times\delta\mathbf{A}) \\
&\qquad + \rho_0\frac{\partial\Psi}{\partial\boldsymbol{\mathscr{E}}}\cdot\frac{\mathrm{d}}{\mathrm{d}t}(\delta\mathbf{A}) - \rho_0\frac{\partial\Psi}{\partial\mathbf{B}}\cdot(\boldsymbol{\nabla}\times\delta\mathbf{A})\Big\}\mathrm{d}V\mathrm{d}t \\
&= \int_{t_1}^{t_2}\int_{\mathbb{R}^3} \Big\{ -\mathbf{D}\cdot\frac{\mathrm{d}}{\mathrm{d}t}(\delta\mathbf{A}) + \boldsymbol{\mathscr{J}}\cdot\delta\mathbf{A} - \boldsymbol{\mathscr{H}}\cdot(\boldsymbol{\nabla}\times\delta\mathbf{A})\Big\}\mathrm{d}V\mathrm{d}t\,.
\end{aligned} \tag{5.14}$$

In the above, the reference configuration electric displacement $\mathbf{D}$ and magnetomotive intensity $\boldsymbol{\mathscr{H}}$ stem out from recognizing the transpose of the aether relations to the reference configuration in (1.110) and (1.113).

As for the variations with respect to $\Phi$, integration by part, in both time and space here, needs to be applied. The same separation of space between the volume $\Omega$ occupied by the body and the surrounding space $\Omega/\mathbb{R}^3$ is considered, together with similar assumptions regarding the smoothness of the fields: smooth on subdomains between surface interfaces, but likely discontinuous across interfaces. Time and space integrals commute as the space integral is on the reference configuration. Integrating by part in time for the term in $\mathbf{D}$ accounting for $\delta\mathbf{A}(t_1) = \delta\mathbf{A}(t_2) = \mathbf{0}$, and integrating by part in space for the term in $\boldsymbol{\mathscr{H}}$ accounting for the interface discontinuities as previously exposed,

$$\mathscr{F}_{,\mathbf{A}}[\delta\mathbf{A}] = \int_{t_1}^{t_2}\Big\{\int_{\mathbb{R}^3}\Big(\dot{\mathbf{D}} + \boldsymbol{\mathscr{J}} - \boldsymbol{\nabla}\times\boldsymbol{\mathscr{H}}\Big)\cdot\delta\mathbf{A}\mathrm{d}V - \int_{\partial\Omega}(\mathbf{N}\times[\![\boldsymbol{\mathscr{H}}]\!])\cdot\delta\mathbf{A}\mathrm{d}S\Big\}\mathrm{d}t\,. \tag{5.15}$$

As a result for variations with respect to $\mathbf{A}$, one finally gets from the fundamental lemma of the calculus of variations,

$$\begin{aligned}
&\mathbf{X}\in\Omega: && \boldsymbol{\nabla}\times\boldsymbol{\mathscr{H}} = \dot{\mathbf{D}} + \boldsymbol{\mathscr{J}}\,; \\
&\mathbf{X}\in\partial\Omega: && \mathbf{N}\times[\![\boldsymbol{\mathscr{H}}]\!] = \mathbf{0}\,;
\end{aligned} \qquad \text{with:} \quad \begin{cases} \mathbf{D} = J\mathbf{F}^{-1}\cdot\mathbf{d}\,, \\ \boldsymbol{\mathscr{H}} = \boldsymbol{\hbar}\cdot\mathbf{F}\,, \\ \boldsymbol{\mathscr{J}} = J\mathbf{F}^{-1}\cdot\boldsymbol{\jmath}\,, \end{cases} \tag{5.16}$$

where one recognizes the reference configuration counterpart of Maxwell-Ampère's law derived in Section 1.3.

#### 5.1.3.3 *Variations with respect to* $\mathbf{u}$

For variations with respect to $\mathbf{u}$, based on intermediate derivations provided in Appendix A.3,

$$\begin{aligned}
\mathscr{F}_{,\mathbf{u}}[\delta\mathbf{u}] &= \int_{t_1}^{t_2}\left\{\int_{\mathbb{R}^3}\left[\left(\ell_{0,\mathbf{u}}-\rho_0\Psi_{,\mathbf{u}}\right)[\delta\mathbf{u}]+\rho_0\dot{\mathbf{u}}\cdot\frac{\mathrm{d}}{\mathrm{d}t}(\delta\mathbf{u})+\rho_0\mathbf{f}\cdot\delta\mathbf{u}\right]\mathrm{d}V\right.\\
&\qquad\left.+\int_{\partial\Omega}\mathbf{T}_m\cdot\delta\mathbf{u}\mathrm{d}S\right\}\mathrm{d}t\\
&= \int_{t_1}^{t_2}\left\{\int_{\mathbb{R}^3}\left[-J\epsilon_0\left(\left(\mathbf{C}^{-1}\cdot\mathbf{E}\right)\mathbf{E}-\frac{1}{2}(\mathbf{E}\cdot\mathbf{C}^{-1}\cdot\mathbf{E})\mathbf{I}\right)\cdot\mathbf{F}^{-1}:\boldsymbol{\nabla}\delta\mathbf{u}\right.\right.\\
&\qquad-J\epsilon_0\left((\mathbf{F}^{-1}\cdot\dot{\mathbf{u}})((\mathbf{C}^{-1}\cdot\mathbf{E})\times\mathbf{B})\cdot\mathbf{F}^{-1}\right):\boldsymbol{\nabla}\delta\mathbf{u}\\
&\qquad-\frac{1}{\mu_0 J}\left(\mathbf{B}(\mathbf{C}\cdot\mathbf{B})-\frac{1}{2}(\mathbf{B}\cdot\mathbf{C}\cdot\mathbf{B})\mathbf{I}\right)\cdot\mathbf{F}^{-1}:\boldsymbol{\nabla}\delta\mathbf{u}\\
&\qquad+\left((J\mathbf{C}^{-1}\cdot\epsilon_0\mathbf{E})\times\mathbf{B})\cdot\mathbf{F}^{-1}\right)\cdot\frac{\mathrm{d}}{\mathrm{d}t}(\delta\mathbf{u})\\
&\qquad-2\rho_0\left(\frac{\partial\Psi}{\partial\mathbf{C}}\cdot\mathbf{F}^{\mathsf{T}}\right):\boldsymbol{\nabla}\delta\mathbf{u}\\
&\qquad\left.+\rho_0\dot{\mathbf{u}}\cdot\frac{\mathrm{d}}{\mathrm{d}t}(\delta\mathbf{u})+\rho_0\mathbf{f}\cdot\delta\mathbf{u}\right]\mathrm{d}V+\int_{\partial\Omega}\mathbf{T}_m\cdot\delta\mathbf{u}\mathrm{d}S\Big\}\mathrm{d}t\\
&= \int_{t_1}^{t_2}\left\{\int_{\mathbb{R}^3}\left[-\boldsymbol{\Pi}:\boldsymbol{\nabla}\delta\mathbf{u}+\rho_0\mathbf{g}\cdot\frac{\mathrm{d}}{\mathrm{d}t}(\delta\mathbf{u})+\rho_0\mathbf{f}\cdot\delta\mathbf{u}\right]\mathrm{d}V\right.\\
&\qquad\left.+\int_{\partial\Omega}\mathbf{T}_m\cdot\delta\mathbf{u}\mathrm{d}S\right\}\mathrm{d}t\,.
\end{aligned}\tag{5.17}$$

In the above, $\boldsymbol{\Pi}$ and $\mathbf{g}$ stem out from recognizing the expressions for the reference configuration first Piola-Kirchhoff stress and momentum density respectively given in (1.106)and (1.109). Of crucial importance is to note here that the reference configuration counterpart of Maxwell's stress in vacuum (1.108) included in $\boldsymbol{\Pi}$ is retrieved thanks to the transposition of the current configuration $\ell$ to $\ell_0$ in the reference configuration. This transposition leads to $\ell_0(\Phi,\mathbf{A},\mathbf{u})$ when $\ell(\Phi,\mathbf{A})$ only, such that $\boldsymbol{\Pi}_{MW}$ results from taking the variations of $\ell_0$ with respect to $\mathbf{u}$. This favors the present choice of a Lagrangian based formulation, justifying the finite strain approach.

Then integrating by parts in space and time following the methodology previously introduced,

$$\mathscr{F}_{,\mathbf{u}}[\delta\mathbf{u}]=\int_{t_1}^{t_2}\left\{\int_{\mathbb{R}^3}\left(\boldsymbol{\nabla}\cdot\boldsymbol{\Pi}-\rho_0\dot{\mathbf{g}}+\rho_0\mathbf{f}\right)\cdot\delta\mathbf{u}\mathrm{d}V-\int_{\partial\Omega}(\mathbf{N}\cdot[\![\boldsymbol{\Pi}]\!]-\mathbf{T}_m)\cdot\delta\mathbf{u}\mathrm{d}S\right\}\mathrm{d}t\,,\tag{5.18}$$

and from the fundamental lemma of calculus of variations, one finally retrieves from variations with respect to $\mathbf{u}$,

$$\begin{aligned}
&\mathbf{X}\in\Omega: && \rho_0\dot{\mathbf{g}}=\boldsymbol{\nabla}\cdot\boldsymbol{\Pi}+\rho_0\mathbf{f}\,;\\
&\mathbf{X}\in\partial\Omega: && \mathbf{N}\cdot[\![\boldsymbol{\Pi}]\!]=\mathbf{T}_m\,,
\end{aligned}\tag{5.19}$$

where one recognizes the reference configuration counterpart of the linear momentum balance derived in Section 1.3.

Because the potentials $\Phi$ and $\mathbf{A}$ are not uniquely defined (see Section 1.3), a 3D numerical implementation of this variational principle further requires the implementation of a gauge condition for the potentials, which can be included through a penalty term in the Lagrangian $\mathscr{L}$ (e.g. see Kankanala and Triantafyllidis, 2004). In 2D, the Coulomb gauge condition is automatically enforced: a potential $\mathbf{A} = A(x, y)\hat{\mathbf{e}}_Z$ implies the Coulomb gauge $\boldsymbol{\nabla}\cdot\mathbf{A} = 0$.

## 5.2 A FORMULATION IN THE EDDY CURRENT APPROXIMATION

In the following, an eddy current approximation of the general coupled electro-magneto-mechanical formulation exposed in the previous section 5.1 is proposed. As for the most general electromagnetic-thermomechanical formulation exposed in the previous section, the proposed variational formulation is based on the $\phi - \mathbf{a}$ potential formulation (1.22).

### 5.2.1 *Lagrangian of the problem*

Neglecting the electric charge and the electric field energy (see Section 2.1), the reference configuration pure electromagnetic Lagrangian density $\ell$ (5.1) becomes in the eddy current approximation:

$$\ell(\mathbf{a}) = -\frac{1}{2\mu_0}(\mathbf{b}\cdot\mathbf{b}) + \boldsymbol{\mathcal{j}}\cdot\mathbf{a}\,. \tag{5.20}$$

As a result of neglecting electric charges $q$ in the eddy current approximation the total current $\mathbf{j}$ is reduced to the conduction current $\boldsymbol{\mathcal{j}}$ (see Section 2.1), thus $\boldsymbol{\mathcal{j}}$ now appearing in (5.20), in contrast to $\mathbf{j}$ in (5.1).

Transposition to the reference configuration provides,

$$\ell_0(\mathbf{u}, \mathbf{A}) = J\ell = -\frac{1}{2\mu_0 J}\mathbf{B}\cdot\mathbf{C}\cdot\mathbf{B} + \boldsymbol{\mathcal{J}}\cdot\mathbf{A}\,, \tag{5.21}$$

where we recall the field transformations (see equations (1.41), (1.44) and (1.50))

$$\boldsymbol{\mathcal{J}} = J\mathbf{F}^{-1}\cdot\boldsymbol{\mathcal{j}}\,, \qquad \mathbf{B} = J\mathbf{F}^{-1}\cdot\mathbf{b}\,, \qquad \mathbf{A} = \mathbf{a}\cdot\mathbf{F}\,, \tag{5.22}$$

and the Lagrangian magnetic field $\mathbf{B}$ is related to the Lagrangian potential $\mathbf{A}$ through (1.49).

Based on (5.5), the reference configuration total Lagrangian of the system becomes,

$$\mathscr{L} = \int_{\mathbb{R}^3}\left(\ell_0 - \rho_0\Psi + \frac{1}{2}\rho_0(\dot{\mathbf{u}}\cdot\dot{\mathbf{u}}) + \rho_0\mathbf{f}\cdot\mathbf{u}\right)dV + \int_{\partial\Omega}(\mathbf{T}_m\cdot\mathbf{u} + \mathbf{K}\cdot\mathbf{A})dS\,, \tag{5.23}$$

with $\mathbf{T}_m = \mathbf{t}_m ds/dS$. Here again, $\Omega$ denotes the domain occupied by the body and $\partial\Omega$ its surface. The density $\rho_0(\mathbf{X}) \neq 0$ for $\mathbf{X} \in \Omega$ and $\rho_0(\mathbf{X}) = 0$ for $\mathbf{X} \in \mathbb{R}^3/\Omega$. Integration over $\mathbb{R}^3$ is necessary in order to account for the electromagnetic field in both the body $\Omega$ and its surrounding space $\Omega/\mathbb{R}^3$. Having in mind the calculation of similar boundary value problems as in 3, the possibility of imposing a current sheet $\mathbf{K}$ on the boundary $\partial\Omega$ of the body is added in (5.23). In the eddy current

approximation the specific free energy of the medium is now $\psi = \Psi(\mathbf{C}, \mathbf{B})$ such that the dependence on the electromotive intensity $\boldsymbol{\mathscr{E}}$ is dropped (see Section 2.1). Thomas and Triantafyllidis, 2009 obtains the same Lagrangian as (5.23) in the eddy current approximation, save for a specific free energy that only depends on $\mathbf{F}$ – together with $T, \boldsymbol{\xi}$ that we dropped here – as a result of negligible magnetization in their case, and except for the current sheet term as well. The proposed Lagrangian in (5.23) adds the possibility to account for magnetization.

In the Lagrangian $\mathscr{L}$, $\boldsymbol{\mathscr{J}}$ contained in $\ell_0$ together with $\mathbf{f}$, $\mathbf{T}_m$ and $\mathbf{K}$ are externally applied quantities. They are considered fixed when applying the variational principle. As a result of the eddy current approximation, the electric potential $\Phi$ disappears from the expressions, as already discussed in Section 2.1, and the independent fields are now only $\boldsymbol{A}$ and $\mathbf{u}$. In the following, we will derive the Euler–Lagrange equations of the corresponding Hamilton's variational principle and show that they yield the corresponding eddy current approximation of Ampère's law for variations with respect to $\boldsymbol{A}$ and of the linear momentum balance for variations with respect to $\mathbf{u}$.

### 5.2.2 *Application of Hamilton's principle of variations*

The action integral $\mathscr{F}$ is formed by integration of the Lagrangian $\mathscr{L}$ between arbitrary times $t_1$ and $t_2$ and, by Hamilton's principle of variation, is stationary,[7]

$$\delta\mathscr{F} = 0\,, \qquad \mathscr{F} \equiv \int_{t_1}^{t_2} \mathscr{L}\,dt\,. \tag{5.24}$$

with conditions $\delta\boldsymbol{A} = 0$ and $\delta\mathbf{u} = 0$ at $t = t_1$ and $t = t_2$. With $\boldsymbol{A}$ and $\mathbf{u}$ the independent fields (generalized coordinates), this reduces to:

$$\mathscr{F}_{,\boldsymbol{A}}[\delta\boldsymbol{A}] = \mathscr{F}_{,\mathbf{u}}[\delta\mathbf{u}] = 0\,. \tag{5.25}$$

In the process of performing the calculus of variations hereafter, aside computations from Appendix A.3 are used, filtering out the terms that depend on $\mathbf{E}$, $\frac{\partial\Psi}{\partial\boldsymbol{\mathscr{E}}}$, $Q$, $\Phi$ as a result of the eddy current approximation.

#### 5.2.2.1 *Variations with respect to $\boldsymbol{A}$*

For variations with respect to $\boldsymbol{A}$, based on intermediate derivations provided in Appendix A.3,

$$\begin{aligned}
\mathscr{F}_{,\boldsymbol{A}}[\delta\boldsymbol{A}] &= \int_{t_1}^{t_2}\left\{\int_{\mathbb{R}^3} \left(\ell_{0,\boldsymbol{A}} - \rho_0\Psi_{,\boldsymbol{A}}\right)[\delta\boldsymbol{A}]\,dV\,dt + \int_{\partial\Omega} \mathbf{K}\cdot\delta\boldsymbol{A}\,dS\right\}dt \\
&= \int_{t_1}^{t_2}\left\{\int_{\mathbb{R}^3}\left[\boldsymbol{\mathscr{J}}\cdot\delta\boldsymbol{A} - \left(\frac{1}{\mu_0}\mathbf{B}\cdot\mathbf{C} + \rho_0\frac{\partial\Psi}{\partial\mathbf{B}}\right)\cdot(\boldsymbol{\nabla}\times\delta\boldsymbol{A})\right]dV + \int_{\partial\Omega}\mathbf{K}\cdot\delta\boldsymbol{A}\,dS\right\}dt \\
&= \int_{t_1}^{t_2}\left\{\int_{\mathbb{R}^3}\left[\boldsymbol{\mathscr{J}}\cdot\delta\boldsymbol{A} - \boldsymbol{\mathscr{H}}\cdot(\boldsymbol{\nabla}\times\delta\boldsymbol{A})\right]dV + \int_{\partial\Omega}\mathbf{K}\cdot\delta\boldsymbol{A}\,dS\right\}dt\,.
\end{aligned} \tag{5.26}$$

7 Recall $\delta$ denotes the variation of a functional.

In the above, the reference configuration magnetomotive intensity $\mathscr{H}$ stem out from recognizing the reference configuration expression in (2.17).

As for previous derivations, space is separated into the volume $\Omega$ occupied by the body and the surrounding space $\Omega/\mathbb{R}^3$, and similar assumptions regarding the smoothness of the fields are considered: smooth on subdomains between surface interfaces, but likely discontinuous across interfaces. Integrating by part in space the term in $\mathbf{H}$, accounting for the interface discontinuities as previously exposed,

$$\mathscr{F}_{,\mathbf{A}}[\delta\mathbf{A}] = \int_{t_1}^{t_2}\left\{\int_{\mathbb{R}^3}(\boldsymbol{\mathscr{J}} - \boldsymbol{\nabla}\times\boldsymbol{\mathscr{H}})\cdot\delta\mathbf{A}\,dV + \int_{\partial\Omega}(\mathbf{K} - \mathbf{N}\times[\![\boldsymbol{\mathscr{H}}]\!])\cdot\delta\mathbf{A}\,dS\right\}dt\,. \quad (5.27)$$

From the fundamental lemma of calculus of variations, one finally retrieves from variations with respect to $\mathbf{A}$,

$$\begin{array}{ll} \mathbf{X}\in\Omega: & \boldsymbol{\nabla}\times\boldsymbol{\mathscr{H}} = \boldsymbol{\mathscr{J}}\,; \\ \mathbf{X}\in\partial\Omega: & \mathbf{N}\times[\![\boldsymbol{\mathscr{H}}]\!] = \mathbf{K}\,; \end{array} \quad \text{with:} \quad \begin{cases} \boldsymbol{\mathscr{H}} = \boldsymbol{\hbar}\cdot\mathbf{F}\,, \\ \boldsymbol{\mathscr{J}} = J\mathbf{F}^{-1}\cdot\boldsymbol{\jmath}\,, \end{cases} \quad (5.28)$$

where one recognizes the reference configuration counterpart of Maxwell-Ampère's law in the eddy current approximation derived in Section 2.1.3.

#### 5.2.2.2 *Variations with respect to $\boldsymbol{u}$*

For variations with respect to $\mathbf{u}$, based on intermediate derivations provided in Appendix A.3,

$$\begin{aligned} \mathscr{F}_{,\mathbf{u}}[\delta\mathbf{u}] &= \int_{t_1}^{t_2}\left\{\int_{\mathbb{R}^3}\left[(\ell_{0,\mathbf{u}} - \rho_0\Psi_{,\mathbf{u}})[\delta\mathbf{u}] + \rho_0\dot{\mathbf{u}}\cdot\frac{d}{dt}(\delta\mathbf{u}) + \rho_0\mathbf{f}\cdot\delta\mathbf{u}\right]dV\right. \\ &\qquad \left. + \int_{\partial\Omega}\mathbf{T}_m\cdot\delta\mathbf{u}\,dS\right\}dt \\ &= \int_{t_1}^{t_2}\left\{\int_{\mathbb{R}^3}\left[\left(\frac{1}{\mu_0 J}\left(\frac{1}{2}(\mathbf{B}\cdot\mathbf{C}\cdot\mathbf{B})\mathbf{I} - \mathbf{B}(\mathbf{C}\cdot\mathbf{B})\right)\cdot\mathbf{F}^{-1} - 2\rho_0\frac{\partial\Psi}{\partial\mathbf{C}}\cdot\mathbf{F}^{\mathsf{T}}\right) : \boldsymbol{\nabla}\delta\mathbf{u}\right.\right. \\ &\qquad \left.\left. + \rho_0\dot{\mathbf{u}}\cdot\frac{d}{dt}(\delta\mathbf{u}) + \rho_0\mathbf{f}\cdot\delta\mathbf{u}\right]dV + \int_{\partial\Omega}\mathbf{T}_m\cdot\delta\mathbf{u}\,dS\right\}dt \\ &= \int_{t_1}^{t_2}\left\{\int_{\mathbb{R}^3}\left[-\boldsymbol{\Pi} : \boldsymbol{\nabla}\delta\mathbf{u} + \rho_0\dot{\mathbf{u}}\cdot\frac{d}{dt}(\delta\mathbf{u}) + \rho_0\mathbf{f}\cdot\delta\mathbf{u}\right]dV + \int_{\partial\Omega}\mathbf{T}_m\cdot\delta\mathbf{u}\,dS\right\}dt\,. \end{aligned} \quad (5.29)$$

In the above, $\boldsymbol{\Pi}$ stems out from recognizing the expressions for the reference configuration first Piola-Kirchhoff stress in the eddy current approximation in (2.20). As for the general formulation in Section 5.1, we emphasize that the reference configuration counterpart of Maxwell's stress in vacuum (1.108) included in $\Pi$ is retrieved thanks to the transposition of the current configuration $\ell$ to $\ell_0$ in the reference configuration. This transposition leads to $\ell_0(\mathbf{A},\mathbf{u})$ when $\ell(\mathbf{A})$ only, such that $\boldsymbol{\Pi}_{MW}$ results from taking the variations of $\ell_0$ with respect to $\mathbf{u}$. This favors the present choice of a Lagrangian based formulation, justifying the finite strain approach.

Then integrating by parts in space and time following the methodology previously introduced,

$$\mathscr{F}_{,\mathbf{u}}[\delta\mathbf{u}] = \int_{t_1}^{t_2}\left\{\int_{\mathbb{R}^3}(\boldsymbol{\nabla}\cdot\boldsymbol{\Pi} - \rho_0\ddot{\mathbf{u}} + \rho_0\mathbf{f})\cdot\delta\mathbf{u}\,dV + \int_{\partial\Omega}(\mathbf{T}_m - \mathbf{N}\cdot[\![\boldsymbol{\Pi}]\!])\cdot\delta\mathbf{u}\,dS\right\}. \quad (5.30)$$

From the fundamental lemma of calculus of variations, one finally retrieves from variations with respect to $\mathbf{u}$,

$$\begin{aligned} &\mathbf{X} \in \Omega : && \rho_0 \dot{\mathbf{g}} = \boldsymbol{\nabla}\cdot\boldsymbol{\Pi} + \rho_0 \mathbf{f} \\ &\mathbf{X} \in \partial\Omega : && \mathbf{N}\cdot[\![\boldsymbol{\Pi}]\!] = \mathbf{T}_m \end{aligned} \tag{5.31}$$

where one recognizes the reference configuration counterpart of the linear momentum balance derived in Section 2.1.

### 5.2.3 *The particular 2D, Quasi-static case*

A particular case for application of the variational formulation is that of 2D boundary value problems similar to the stator problem in Section 3.2, where induced currents and acceleration terms are neglected. Based on the previous developments in Section 5.2, the Lagrangian of the system is, when neglecting the external body force (gravity), the acceleration term and with no surface traction, no current sheet and in 2D,

$$\mathscr{L} = -\int_{\mathbb{R}^2} \left( \rho_0 \Psi + \frac{1}{2\mu_0 J} \mathbf{B}\cdot\mathbf{C}\cdot\mathbf{B} - \boldsymbol{\mathcal{J}}\cdot\mathbf{A} \right) \mathrm{d}S \tag{5.32}$$

Integration over $\mathbb{R}^2$ results of the restriction to a 2D space. As a result of neglecting the induced current and acceleration terms, this formulation includes no time derivatives and can be solved quasistaticaly. As a consequence, the variational principle is reduced to the extremization of $\mathscr{L}$, as in Kankanala and Triantafyllidis, 2004. As a result of the 2D hypothesis (in-plane magnetic field), the magnetic vector potential $\mathbf{A} = A(X_1, X_2)\hat{\mathbf{e}}_3$ (vector $\hat{\mathbf{e}}_3$ denotes the normal to the plane and $X_1, X_2$ the in-plane components of the position vector), such that the Gauge condition $\boldsymbol{\nabla}\cdot\mathbf{A}$ is automatically satisfied. As a result of Ampère's law and in plane $\mathbf{H}$ field, the externally applied currents can only be of the form $\boldsymbol{\mathcal{J}} = \mathcal{J}(X_1, X_2)\hat{\mathbf{e}}_3$, which further concurs with the charge conservation principle $\boldsymbol{\nabla}\cdot\boldsymbol{\mathcal{J}} = 0$.

# 6 NUMERICAL IMPLEMENTATION

OUTLINE In this chapter, we develop a numerical implementation of the variational formulation in Section 5.2 for application to boundary value problems similar to the stator problem in Section 3.2. These problems are 2D, have negligible induced currents, and we additionaly neglect acceleration terms. They are solved by extremization of the Lagrangian (5.32) as exposed in Section 5.2.3.

In Section 6.1 we derive the matrix form of the problem. In Section 6.2 the form of the specific free energy is discussed. In Section 6.3 a few additional implementation details are presented. The numerical implementation is later used for FEM analysis of motor problems in Chapter 7.

## 6.1 MATRIX FORM OF THE PROBLEM

### 6.1.1 *Lagrangian of the problem*

Neglecting the magnetic field energy in regions of space where the field is assumed negligible, the integral of the energy can be restricted to a 2D domain $\mathcal{S}$, which we further discretize into $N_e$ discrete finite elements $\mathcal{S} = \sum_{I=1}^{N_e} A_e^I$ such that based on (5.32) the Lagrangian ,

$$\mathscr{L} = \sum_{I=1}^{N_e} -\int_{A_e^I} \big(P(\mathbf{F},\mathbf{B}) - \boldsymbol{\mathscr{J}}\cdot\mathbf{A}\big)\mathrm{d}A_e \; ; \quad P(\mathbf{F},\mathbf{B}) \equiv \rho_0\Psi + \frac{1}{2\mu_0 J}\mathbf{B}\cdot\mathbf{C}\cdot\mathbf{B} \; , \tag{6.1}$$

where we introduce the energy P[1] in order to simplify the expressions obtained in the following.

We introduce the frame of reference $\mathscr{R} : \{\hat{\mathbf{e}}_1, \hat{\mathbf{e}}_2, \hat{\mathbf{e}}_3\}$ with $\hat{\mathbf{e}}_1$,$\hat{\mathbf{e}}_2$ in-plane and $\hat{\mathbf{e}}_3$ the normal to the plane. The position components along the directions of $\mathscr{R}$ are denoted $X_1, X_2, X_3$.

Recall that in order to find the solution of the solution we aim to extremize (6.1) with respect to the independent variables $\mathbf{u}$ and $\mathbf{A}$, and in 2D,

$$\mathbf{u} = u_1(X_1,X_2)\hat{\mathbf{e}}_1 + u_2(X_1,X_2)\hat{\mathbf{e}}_2 \; ; \qquad \mathbf{A} = A(X_1,X_2)\hat{\mathbf{e}}_3 \; . \tag{6.2}$$

By Section 5.2.3, the externally applied current density $\boldsymbol{\mathscr{J}} = \mathscr{J}\hat{\mathbf{e}}_3$ such that in (6.1) $\boldsymbol{\mathscr{J}}\cdot\mathbf{A} = \mathscr{J}A$.

### 6.1.2 *Element and vector of unknowns*

Our focus here was not on the choice of elements and constant strain triangular 2D elements - one integration point at the element centroid - where chosen as

1 Notice $P = \rho_0\varepsilon$ the total energy density in the reference configuration (see equation (2.22) with neglected kinetic and thermal contributions).

the simplest element for FEM formulations. Because $\mathbf{A}$ and $\mathbf{u}$ are the indedent variables of the problem, the vector of degrees of freedom for the element is

$$\mathbf{q}_e^T = \left\{ u_1^{(1)},\, u_2^{(1)},\, A^{(1)},\, u_1^{(2)},\, u_2^{(2)},\, A^{(2)},\, u_1^{(3)},\, u_2^{(3)},\, A^{(3)} \right\}, \tag{6.3}$$

where indices $(1), (2), (3)$ refer to the nodes of the element as depicted in Figure 6.1.

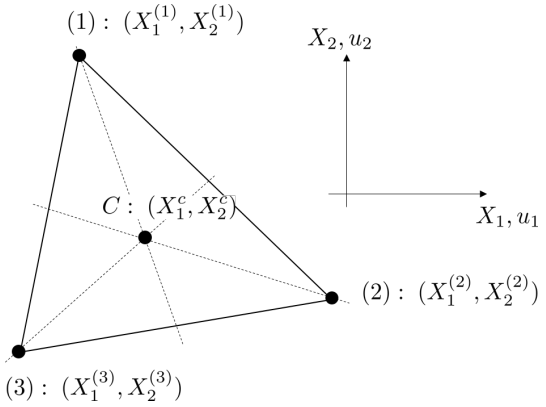


Figure 6.1: Constant strain triangular elements used for the FEM formulation.

The element vector of unknowns at the center of the element is, together with its interpolation,

$$\delta\mathbf{q} = \{\delta\mathbf{u}, \delta A\}^T = \mathbf{N}\cdot\delta\mathbf{q}_e \,. \tag{6.4}$$

The matrix $[\mathbf{N}]$ is the shape function matrix evaluated at the center of the element,

$$[\mathbf{N}] = \begin{bmatrix} N_1^c & 0 & 0 & N_2^c & 0 & 0 & N_3^c & 0 & 0 \\ 0 & N_1^c & 0 & 0 & N_2^c & 0 & 0 & N_3^c & 0 \\ 0 & 0 & N_1^c & 0 & 0 & N_2^c & 0 & 0 & N_3^c \end{bmatrix} ; \tag{6.5}$$

$$N_1^c = N_1(X_1^c, X_2^c) ; \qquad N_2^c = N_2(X_1^c, X_2^c) ; \qquad N_3^c = N_3(X_1^c, X_2^c) \,.$$

The index "c" refers to the center of the element. The three bi-linear shape functions $N_i$ are,

$$N_1(X_1, X_2) = \frac{1}{2A_e}\left[X_1^{(2)}X_2^{(3)} - X_1^{(3)}X_2^{(2)} + (X_2^{(2)} - X_2^{(3)})X_1 - (X_1^{(2)} - X_1^{(3)})X_2\right] ;$$

$$N_2(X_1, X_2) = \frac{1}{2A_e}\left[X_1^{(3)}X_2^{(1)} - X_1^{(1)}X_2^{(3)} + (X_2^{(3)} - X_2^{(1)})X_1 - (X_1^{(3)} - X_1^{(1)})X_2\right] ; \tag{6.6}$$

$$N_3(X_1, X_2) = \frac{1}{2A_e}\left[X_1^{(1)}X_2^{(2)} - X_1^{(2)}X_2^{(1)} + (X_2^{(1)} - X_2^{(2)})X_1 - (X_1^{(1)} - X_1^{(2)})X_2\right] \,.$$

Recall $A_e$ is the surface of the element. At the center of the element, the evaluation of the shape functions and their derivatives provides,

$$N_1^c(X_1^c, X_2^c) = N_2^c(X_1^c, X_2^c) = N_3^c(X_1^c, X_2^c) = \frac{1}{3} ;$$

$$\frac{\partial N_1}{\partial X_1} = \frac{X_2^{(2)} - X_2^{(3)}}{2A_e} ; \qquad \frac{\partial N_2}{\partial X_1} = \frac{X_2^{(3)} - X_2^{(1)}}{2A_e} ; \qquad \frac{\partial N_3}{\partial X_1} = \frac{X_2^{(1)} - X_2^{(2)}}{2A_e} ; \quad (6.7)$$

$$\frac{\partial N_1}{\partial X_2} = \frac{X_1^{(2)} - X_1^{(3)}}{2A_e} ; \qquad \frac{\partial N_2}{\partial X_2} = \frac{X_1^{(3)} - X_1^{(1)}}{2A_e} ; \qquad \frac{\partial N_3}{\partial X_2} = \frac{X_1^{(1)} - X_1^{(2)}}{2A_e} .$$

The index "c" refering to the center of the element is dropped in the shape function derivations given they are constant. We then finally introduce the matrix $[\mathbf{G}]$ associated with the element shape functions and their derivatives at the center of the element such that,

$$\left\{ u_1, \frac{\partial u_1}{\partial X_1}, \frac{\partial u_1}{\partial X_2}, u_2, \frac{\partial u_2}{\partial X_1}, \frac{\partial u_2}{\partial X_2}, A, B_1, B_2 \right\} = \mathbf{G} \cdot \mathbf{q}_e , \quad (6.8)$$

with

$$[\mathbf{G}] = \begin{bmatrix} N_1^c & 0 & 0 & N_2^c & 0 & 0 & N_3^c & 0 & 0 \\ \frac{\partial N_1}{\partial X} & 0 & 0 & \frac{\partial N_2}{\partial X} & 0 & 0 & \frac{\partial N_3}{\partial X} & 0 & 0 \\ \frac{\partial N_1}{\partial Y} & 0 & 0 & \frac{\partial N_2}{\partial Y} & 0 & 0 & \frac{\partial N_3}{\partial Y} & 0 & 0 \\ 0 & N_1^c & 0 & 0 & N_2^c & 0 & 0 & N_3^c & 0 \\ 0 & \frac{\partial N_1}{\partial X} & 0 & 0 & \frac{\partial N_2}{\partial X} & 0 & 0 & \frac{\partial N_3}{\partial X} & 0 \\ 0 & \frac{\partial N_1}{\partial Y} & 0 & 0 & \frac{\partial N_2}{\partial Y} & 0 & 0 & \frac{\partial N_3}{\partial Y} & 0 \\ 0 & 0 & N_1^c & 0 & 0 & N_2^c & 0 & 0 & N_3^c \\ 0 & 0 & \frac{\partial N_1}{\partial Y} & 0 & 0 & \frac{\partial N_2}{\partial Y} & 0 & 0 & \frac{\partial N_3}{\partial Y} \\ 0 & 0 & -\frac{\partial N_1}{\partial X} & 0 & 0 & -\frac{\partial N_2}{\partial X} & 0 & 0 & -\frac{\partial N_3}{\partial X} \end{bmatrix} . \quad (6.9)$$

Note that the previous accounts for $B_1 = -\frac{\partial A}{\partial X_2}$ and $B_2 = \frac{\partial A}{\partial X_1}$ as a result of $\mathbf{B} = \boldsymbol{\nabla} \times \mathbf{A}$. As a result, the matrix $[\mathbf{G}]$ conveniently enables to retrieve at the center of element the magnetic potential $A$, the magnetic field $\mathbf{B}$ and the displacement field $\mathbf{u}$ and derivatives $\mathbf{u}\boldsymbol{\nabla} = \mathbf{F} - \mathbf{I}$.

### 6.1.3 *Force vector and stiffness matrix*

In order to find the solution to our problem, we want to extremize the energy $\mathscr{L}$, which is reduced to solving the discretized problem in matrix form,

$$[\mathbf{K}][\mathbf{Q}] = [\mathbf{F}] , \quad (6.10)$$

where $[\mathbf{Q}]$ is the global vector of nodal variables of the problem, $[\mathbf{K}]$ is the global stiffness matrix and $[\mathbf{F}]$ is the global force vector. $[\mathbf{Q}]$, $[\mathbf{K}]$ and $[\mathbf{F}]$ are composed

by an assembly of respectively the element vector of degrees of freedom $\mathbf{q}_e$, the individual element stiffness matrices $[\mathbf{K}_e]$ and the element force vector $[\mathbf{F}_e]$.

The load vector for the element is obtained by the first variation of $\mathscr{L}$,

$$\mathbf{F}_e \cdot \delta\mathbf{q}_e = \int_{A_e} \left[ \frac{\partial P}{\partial F_{\alpha\beta}} \delta F_{\alpha\beta} + \frac{\partial P}{\partial B_\epsilon} \delta B_\epsilon - \mathscr{J} \delta A \right] dA_e \,, \tag{6.11}$$

where the partial derivatives of $\mathbf{P}$ with respect to $\mathbf{F}$ need to be understood as derivatives holding $\mathbf{B}$ to be consistent with variations taken with respect to variables $\mathbf{u}$ and $A$. Defining the intermediate load vector $\mathbf{F}_e^{FE}$ and integrating over the element,

$$\begin{aligned} [\mathbf{F}_e] &= A_e [\mathbf{F}_e^{FE}][\mathbf{G}] \,; \\ [\mathbf{F}_e^{FE}] &\equiv \left\{ 0,\ \frac{\partial P}{\partial F_{11}},\ \frac{\partial P}{\partial F_{12}},\ 0,\ \frac{\partial P}{\partial F_{21}},\ \frac{\partial P}{\partial F_{22}},\ -\mathscr{J},\ \frac{\partial P}{\partial B_1},\ \frac{\partial P}{\partial B_2} \right\} . \end{aligned} \tag{6.12}$$

The stiffness (tangent) matrix for the element is obtained by the second variation of $\mathscr{L}$,

$$\begin{aligned} \Delta\mathbf{q}_e \cdot \mathbf{K}_e \cdot \delta\mathbf{q}_e = \int_{A_e} \Bigg[ & \frac{\partial^2 P}{\partial F_{\alpha\beta} \partial F_{\delta\gamma}} \delta F_{\alpha\beta} \Delta F_{\delta\gamma} + \frac{\partial^2 P}{\partial B_\epsilon \partial F_{\delta\gamma}} \delta B_\epsilon \Delta F_{\delta\gamma} \\ & + \frac{\partial^2 P}{\partial F_{\alpha\beta} \partial B_\zeta} \delta F_{\alpha\beta} \Delta B_\zeta + \frac{\partial^2 P}{\partial B_\epsilon \partial B_\zeta} \delta B_\epsilon \Delta B_\zeta \Bigg] dA_e \,. \end{aligned} \tag{6.13}$$

Defining the intermediate stiffness matrix $\mathbf{K}_e^{FE}$ and integrating over the element,

$$[\mathbf{K}_e] = A_e [\mathbf{G}][\mathbf{K}_e^{FE}][\mathbf{G}] \,;$$

$$[\mathbf{K}_e^{FE}] \equiv \begin{bmatrix} 0 & 0 & 0 & 0 & 0 & 0 & 0 & 0 & 0 \\ 0 & \frac{\partial^2 P}{\partial F_{11} \partial F_{11}} & \frac{\partial^2 P}{\partial F_{11} \partial F_{12}} & 0 & \frac{\partial^2 P}{\partial F_{11} \partial F_{21}} & \frac{\partial^2 P}{\partial F_{11} \partial F_{22}} & 0 & \frac{\partial^2 P}{\partial F_{11} \partial B_1} & \frac{\partial^2 P}{\partial F_{11} \partial B_2} \\ 0 & \frac{\partial^2 P}{\partial F_{12} \partial F_{11}} & \frac{\partial^2 P}{\partial F_{12} \partial F_{12}} & 0 & \frac{\partial^2 P}{\partial F_{12} \partial F_{21}} & \frac{\partial^2 P}{\partial F_{12} \partial F_{22}} & 0 & \frac{\partial^2 P}{\partial F_{12} \partial B_1} & \frac{\partial^2 P}{\partial F_{12} \partial B_2} \\ 0 & 0 & 0 & 0 & 0 & 0 & 0 & 0 & 0 \\ 0 & \frac{\partial^2 P}{\partial F_{21} \partial F_{11}} & \frac{\partial^2 P}{\partial F_{21} \partial F_{12}} & 0 & \frac{\partial^2 P}{\partial F_{21} \partial F_{21}} & \frac{\partial^2 P}{\partial F_{21} \partial F_{22}} & 0 & \frac{\partial^2 P}{\partial F_{21} \partial B_1} & \frac{\partial^2 P}{\partial F_{21} \partial B_2} \\ 0 & \frac{\partial^2 P}{\partial F_{22} \partial F_{11}} & \frac{\partial^2 P}{\partial F_{22} \partial F_{12}} & 0 & \frac{\partial^2 P}{\partial F_{22} \partial F_{21}} & \frac{\partial^2 P}{\partial F_{22} \partial F_{22}} & 0 & \frac{\partial^2 P}{\partial F_{22} \partial B_1} & \frac{\partial^2 P}{\partial F_{22} \partial B_2} \\ 0 & 0 & 0 & 0 & 0 & 0 & 0 & 0 & 0 \\ 0 & \frac{\partial^2 P}{\partial B_1 \partial F_{11}} & \frac{\partial^2 P}{\partial B_1 \partial F_{12}} & 0 & \frac{\partial^2 P}{\partial B_1 \partial F_{21}} & \frac{\partial^2 P}{\partial B_1 \partial F_{22}} & 0 & \frac{\partial^2 P}{\partial B_1 \partial B_1} & \frac{\partial^2 P}{\partial B_1 \partial B_2} \\ 0 & \frac{\partial^2 P}{\partial B_2 \partial F_{11}} & \frac{\partial^2 P}{\partial B_2 \partial F_{12}} & 0 & \frac{\partial^2 P}{\partial B_2 \partial F_{21}} & \frac{\partial^2 P}{\partial B_2 \partial F_{22}} & 0 & \frac{\partial^2 P}{\partial B_2 \partial B_1} & \frac{\partial^2 P}{\partial B_2 \partial B_2} \end{bmatrix} . \tag{6.14}$$

The numerical implementation is performed in Abaqus via a user element, which we provide with the element stiffness matrix $[\mathbf{K}_e]$ and the element force vector $[\mathbf{F}_e]$. The algorithm solves the extremization problem using a Newton-Raphson scheme. For the definition of $[\mathbf{K}]$ and $[\mathbf{F}]$, the first and second order derivatives of $P$ with

respect to $\mathbf{F}$ and $\mathbf{B}$ need to be provided, which requires the definition of the specific free-energy $\psi$, provided in Section 6.2.

As a final note, one can realize based on the developments in Section 5.2 and 2.1 that,

$$\boldsymbol{\Pi} = \left(\frac{\partial P}{\partial \mathbf{F}}\right)^{T} \; ; \qquad \mathbf{H} = \frac{\partial P}{\partial \mathbf{B}} \; , \tag{6.15}$$

such that the components of $\boldsymbol{\Pi}$ and $\mathbf{H}$ at the center of the element are conveniently given by the components of the load vector $[\mathbf{F}]$.

## 6.2 CHOICE OF A SPECIFIC FREE ENERGY

A single user element type is defined for the modeling of the various motor domains that can include air and ferromagnetic domains made of electrical steel. As a consequence, the specific free energy we define is to be suited to the modeling of all two material types: air and electrical steel, both assumed isotropic.

For isotropic materials in 2D, the specific free energy can be expressed as a function of only 4 invariants $I_1, I_2, J_1$ and $J_2$ out of the 6 invariants for a 3D isotropic description,

$$\begin{aligned} &\Psi(\mathbf{C}, \mathbf{B}) = \psi(I_1, I_2, J_1, J_2) \; ; \\ &I_1 = \mathrm{tr}(\mathbf{C}) \; ; \qquad I_2 = \det(\mathbf{C}) = J^2 \; ; \qquad J_1 = \mathbf{B}\cdot\mathbf{B} \; ; \qquad J_2 = \mathbf{B}\cdot\mathbf{C}\cdot\mathbf{B} \; . \end{aligned} \tag{6.16}$$

The specific free energy is decomposed into a purely mechanical part and a magneto-mechanical part,

$$\rho_0 \Psi(\mathbf{C}, \mathbf{B}) = \rho_0 \psi_{mech}(\mathbf{C}) + \rho_0 \psi_{mag}(\mathbf{C}, \mathbf{B}) \; . \tag{6.17}$$

MECHANICAL ENERGY For the mechanical specific free energy $\psi_{mech}(\mathbf{C})$ a neo-hookean behavior is chosen,

$$\begin{aligned} \rho_0 \psi_{mech}(I_1, I_2) &= \frac{\lambda}{2}(J-1)^2 + \frac{G}{2}(I_1 - 3 - 2\ln J) \\ &= \frac{\lambda}{2}(I_2 - 2\sqrt{I_2} + 1) + \frac{G}{2}(I_1 - 3 - \ln I_2) \\ &= W_{mech}(I_1, I_2) \; , \end{aligned} \tag{6.18}$$

where $\lambda$ is the first Lamé coefficient and $G$ the shear coefficient. More appropriate and refined choices may be relevant for modeling metals (e.g. see Thomas and Triantafyllidis, 2009) but a neo-hookean suits our purpose well here given only small strains are expected at first. In the small strain regime, this neo-hookean energy provides the elastic stress-strain relation $\overset{\epsilon}{\boldsymbol{\sigma}} = \lambda \mathrm{tr}(\boldsymbol{\epsilon}) + 2G\boldsymbol{\epsilon}$, with $\boldsymbol{\epsilon}$ the small strain tensor previously introduced (see Chapter 2). For the modeling of air domains, the Lamé coefficients $\lambda$ and $G$ will be reduced to a negligible fraction of the Lamé coefficients of the other materials in presence so that the parasitic elastic stresses induced by the domain deformation are insignificant (in the finite-element analyses performed in Chapter 7 we use a Young modulus for air $10^{-5}$ that of the steel components).

MAGNETIC ENERGY Air has no magnetic properties (no magnetization) and as such in air domains $\psi_{mag}$ will be taken to zero. As a consequence, the chosen form for the magnetic specific free energy $\psi_{mag}$ is tailored to the modeling of ferromagnetic domains only. In the following, we focus on the modeling of an anhysteretic magnetic behavior of these ferromagnetic domains.

In the choice of a magnetic specific free energy, we are guided by the developments of Chapter 2 such that we expect to get back the expressions for stresses and strains obtained in Section 2.2 in the small strain regime. For simplicity, the magnetostriction stress contribution in $\frac{\Lambda}{\mu}\mathbf{b}\mathbf{b}$ is however here neglected.

For the choice of the magnetic part of the specific free-energy $\psi_{mag}(\mathbf{C},\mathbf{B})$, a Langevin-type model that accounts for saturation of the magnetic field is used, taking inspiration in Danas, 2017,

$$\begin{aligned}\rho_0\psi_{mag}(I_2,J_2) &= \frac{\alpha_s^2 m_s}{A}\left[\ln\left(\frac{A}{\alpha_s}\sqrt{\frac{J_2}{I_2}}\right)-\ln\sinh\left(\frac{A}{\alpha_s}\sqrt{\frac{J_2}{I_2}}\right)\right] \;;\quad A\equiv\frac{3\chi}{m_s\mu}\,, \\ &= W_{mag}(I_2,J_2)\end{aligned} \tag{6.19}$$

where $m_s$ is the value of magnetization at saturation, and $\alpha_s$ is a correction coefficient we introduce to obtain a better fit to experimental data on typical electrical steels. The reader is referred to Appendix C.1 for additional details on the derivation of this expression and the inclusion of the correction coefficient $\alpha_s$, and for the verification that the specific free energy suggested complies with the constitutive laws used in Chapter 2. Note that we matched here the constitutive behavior in small strains, small magnetization (linear regime) to the expressions from Section 2.2 - not accounting for magnetostriction - and to experimental data for magnetic saturation at zero stresses (Appendix C.1) to the best. However, for more accurate material behavior, the magneto-mechanical couplings in the model, i.e. influence of stresses on magnetization or magnetostriction, should be further investigated and compared to experimental data (e.g. see Aydin et al., 2017).

> *Nota:* This material behavior has been further improved in the later manuscript submitted for publication Hanappier, Charkaluk, and Triantafyllidis, 2021c.

Based on the definition of the specific free energy, the first and second order derivatives of P required for the stiffness matrix and load vector can be derived. The expressions are provided in Appendix C.3. Their derivation requires the derivatives of $\rho_0\psi_{mech}$ and $\rho_0\psi_{mag}$ with respect to the invariants, which are provided in Appendix C.2.

## 6.3 OTHER IMPLEMENTATION DETAILS

### 6.3.1 *Abaqus variables used*

We use the variables 1,2, 11 in Abaqus. Variables 1 and 2 are the nodal displacements U, respectively along directions X and Y of the reference configuration given the FEM code is writen in cartesian coordinates. Variables 11 of abaqus is used as A, the component along Z of the magnetic vector potential.

### 6.3.2 *Treating infinite magnetic field values in o*

To avoid infinite values in the limit $\|\mathbf{b}\| \to 0$, the first and second order derivatives are given their asymptotic expressions for $\|\mathbf{b}\| \in [0, \zeta]$ where $\zeta$ is a small parameter. We set[2] $\zeta = \sqrt{2}\ 10^{-7}$. The asymptotic expressions are provided in Appendix C.2.

### 6.3.3 *Treating air and copper domains*

For air domains, the magnetic susceptibility $\chi$ is set to zero in the input file, and the first and second Lamé coefficient are set to $10^{-5}$ that of the material. Through a `IF` statement in the user element definition, a magnetic susceptibility $\chi = 0$ sets the material volume energy $W = 0$, such that only remains for the total energy in air,

$$P(\mathbf{F}, \mathbf{B}) = \frac{1}{2\mu_0 J}\mathbf{B}\cdot\mathbf{C}\cdot\mathbf{B}\ , \tag{6.20}$$

which yields Maxwell's stress in vacuum and the aether relation $\mathbf{h} = \frac{1}{\mu_0}\mathbf{b}$ (see Section 5.2).

### 6.3.4 *Boundary conditions*

The default boundary condition setups in Abaqus enable to prescribe $U_X$, $U_Y$ and $A$. An additional DISP subroutine is used to apply complex boundary conditions, such as $A = A_0 \cos(p\theta)$ for the magnetic potential (in the spirit of Section 3.2 and further detailed in Chapter 7).

### 6.3.5 *Load definitions*

Should it be necessary, the FEM code developed enables the application of traction boundary conditions at the nodes. These condition are not passed on to the UEL. They are directly accounted for by Abaqus in the final assembly of the matrix of the whole problem.

2 There is no particular reason for the $\sqrt{(}2)$. In the code the inequality is set on the invariant $J_1 = \mathbf{B}\cdot\mathbf{B}$ and $2\ 10^{-7}$ just worked well.

# 7

# SIMULATION OF ELECTRIC MOTOR PROBLEMS

OUTLINE This section provides results obtained for the modeling of stator geometries using the numerical finite-element implementation previously presented in Chapter 6. These examples of application are meant to highlight the possibilities offered by the variational formulation presented and the FEM code developed.

In Section 7.1, the very same idealized stator problem as in Section 3.2 is solved using the FEM code. At small values of the magnetic field (range of linear magnetic behavior), the FEM results are compared to the analytical results from Section 3.2 for validation of the code. Results at larger magnetic field values (range of non linear magnetic behavior) are then given. In Section 7.2, the FEM code is used to obtain results for the magnetic field, stresses and strains on a more realistic stator geometry taken from Devillers et al., 2018 that includes teeth and slots, and at large magnetic field values.

## 7.1 FEM SIMULATION OF THE IDEALIZED STATOR PROBLEM

*Nota: In the following, "analytical results" or "analytical computations" refer to the analytical results for the idealized stator problem in Section 3.2.*

### 7.1.1 *Problem description*

GEOMETRY In this first example of application, we reproduce the boundary value problem of Section 3.2. The motor geometry is recalled in Figure 7.1 and its dimensions in Table 7.1. Because of the symmetries of the geometry - and of the loading later defined - computations are performed on a quarter motor only, hence the quarter motor geometry pictured. The naming of the lateral boundaries in the cut regions (surfaces of symmetries) in $\partial\mathscr{D}_l^1 : \theta = 0$ and $\partial\mathscr{D}_l^2 : \theta = \frac{\pi}{2}$ is introduced for future reference.

MATERIALS Table 7.1 recalls the material parameters of the problem. Compared to the analytical boundary value problem of section 3.2, the FEM implementation adds the non linear magnetic behavior based on the specific free energy definition (6.19). It requires two additional material parameters: the magnetization at saturation $m_s$, and the correction coefficient $\alpha_s$. A typical value of $m_s = 1.25\times10^6$ is found in Aydin et al., 2017 (Material 1 - M330-50A non-oriented Si-Fe electrical steel) and adopted here. From the developments in Appendix C, we take $\alpha_s = 35$.
*Nota: In the following, the loads and boundary conditions of the problem are set to match the conditions described in the analytical stator problem in Section 3.2. We work with fields of the reference configuration because the variational principle is written in the reference configuration. We introduce the stator frame of reference in the reference configuration* $\mathcal{S}(R, \theta)$.

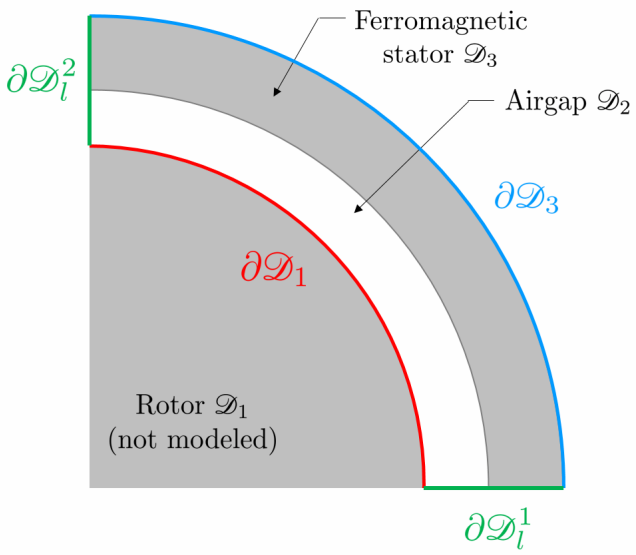


Figure 7.1: Cross-section of the quarter idealized electric motor, indicating rotor, airgap and stator domains and associated boundaries.

| | | |
|---|---|---|
| **Geometry** | | |
| Rotor bore radius | $R_1$ | 42.5 mm |
| Stator yoke bore radius | $R_2$ | 45 mm |
| Stator outer radius | $R_3$ | 50 mm |
| Number of pole pairs | $p$ | 2 |
| **Operating parameters** | | |
| Peak value of the magnetic potential | $a_0$ | $1.4\times10^{-1}$ T/m |
| Angular velocity of current supply | $\omega$ | $100\pi$ rad/s |
| **Material properties** | | **Si-Fe NO Electrical steel** |
| Initial magnetic susceptibility | $\chi$ | 2,500 |
| Magnetization at saturation | $m_s$ | $1.25\times10^{6}$ A/m |
| Correction coefficient | $\alpha_s$ | 35 |
| Mass density | $\rho_0$ | 7,650 kg/m$^3$ |
| Young's modulus | $E$ | $215\times10^{9}$ Pa |
| Poisson ratio | $\nu$ | 0.3 |

Table 7.1: For FEM: motor geometry, operating parameters and material properties for the stator idealized boundary value problem.

LOADING As in Section 3.2 the rotor comprises p-pairs ($p = 2$ here) of permanent magnets that produce a rotating radial magnetic field $B_R = -B_0 \sin(p\theta - p\Omega t)$ at the rotor boundary, with $B_0$ the amplitude of the field and $\Omega$ the rotation velocity of the rotor. This condition is enforced by setting the Dirichlet boundary condition,

$$\partial\mathscr{D}_1 : \qquad A = \frac{R_1 B_0}{p} \cos(p\theta) \, . \tag{7.1}$$

The FEM results will corresponds to a snapshot of the solution to the problem at time $t = 0$ and the solution at any time $t$ is obtained by a rotation of angle $\Omega t$. As described later on, the displacements will be prescribed on $\partial\mathscr{D}_1$ such that the boundary condition (7.1) for $\mathbf{A}$ (Lagrangian) is equivalent to the boundary condition on $\mathbf{a}$ (Eulerian) in Section 3.2.

MAGNETIC BOUNDARY CONDITIONS On the outer stator boundary magnetic insulation is enforced setting,

$$\partial\mathscr{D}_3 : \qquad A = 0 \quad \Longrightarrow \quad \mathbf{N}\cdot\mathbf{B} = 0 \, . \tag{7.2}$$

Given the small strains involved (as per later results or the analytical solution), this corresponds to the boundary condition set for the Eulerian $\mathbf{b}$ in Section 3.2.

By the magnetic field-magnetic potential relation $\mathbf{B} = \boldsymbol{\nabla}\times\mathbf{A}$, any radial plane of symmetry for $A$ is a plane of anti-symmetry for $B_r$ and consequently $B_r = 0$ throughout that plane. As a consequence, we let the boundary condition on $\partial\mathscr{D}_l^1$ and $\partial\mathscr{D}_l^2$ - which are surfaces of symmetry for both the geometry and $\mathbf{A}$ - free such that the natural Neumann boundary condition is enforced

$$\partial\mathscr{D}_l^1, \partial\mathscr{D}_l^2 : \qquad \hat{\mathbf{e}}_\theta \times \mathbf{H} = 0 \quad \Longrightarrow \quad B_r = 0 \, . \tag{7.3}$$

MECHANICAL BOUNDARY CONDITIONS The displacements are constrained on $\partial\mathscr{D}_1$. Given the symmetries, we allow radial displacements on $\partial\mathscr{D}_l^1$ and $\partial\mathscr{D}_l^2$ but prescribe tangent displacements. On $\partial\mathscr{D}_3$ the displacements are let free. As a result, we set

$$\begin{aligned} &\partial\mathscr{D}_1 : && u_r = u_\theta = 0 \, ; \\ &\partial\mathscr{D}_l^1, \partial\mathscr{D}_l^2 : && u_\theta = 0 \, . \end{aligned} \tag{7.4}$$

As a result of the free radial displacements on $\partial\mathscr{D}_l^1$ and $\partial\mathscr{D}_l^2$, and of the free radial and tangent displacements on $\partial\mathscr{D}_3$, the natural Neumann boundary conditions provide,

$$\begin{aligned} &\partial\mathscr{D}_l^1, \partial\mathscr{D}_l^2 : && \Pi_{r\theta} = 0 \, ; \\ &\partial\mathscr{D}_3 : && \Pi_{rr} = \Pi_{r\theta} = 0 \, , \end{aligned} \tag{7.5}$$

which sets equivalent constraints on the Eulerian stress field $\boldsymbol{\sigma}$ given the small strains involved (as per later results or the analytical solution).

NORMALIZATION In order to evaluate saturation levels in the machine, the following results are normalized with respect to reference values at magnetic saturation,

$$\begin{aligned} a_{ref} &= R_2 \mu_0 m_s \,, \quad b_{ref} = \mu_0 m_s \,, \quad h_{ref} = m_{ref} = m_s \,, \\ \sigma_{ref} &= \mu_0 m_s^2 \,, \quad u_{ref} = \frac{R_2 \mu_0 m_s^2}{2G} \,. \end{aligned} \tag{7.6}$$

MESH CONVERGENCE The FEM results will be compared to analytical results and the comparison replaces the need for mesh convergence studies.

### 7.1.2 *Results at small magnetic field values*

For the calculations, we use a fine unstructured mesh that includes a total of 27,783 elements, with a characteristic size of $2\times10^{-4}$m throughout all domains, refined at $1.2\times10^{-4}$m at the rotor ($\partial\mathscr{D}_1$), inner stator ($\partial\mathscr{D}_2$) and lateral symmetry boundaries ($\partial\mathscr{D}_l^1, \partial\mathscr{D}_l^2$). The magnetic field input at the rotor boundary $\partial\mathscr{D}_1$ is given an amplitude of $1\% b_{ref} = 1\% \mu_0 m_s$. In the following, averaging across neighboring elements is used for display, with the Abaqus default threshold of 75%[1]. Two separate averaging regions are defined for the airgap and stator domains such that the interface is not included - fields not averaged across the interface - so that the discontinuities are clearly visible.

Figure 7.2 presents the FEM results for the norm of the magnetic field normalized by the reference magnetic field at saturation $b_{ref} = \mu_0 m_s$. It shows that the stator magnetic field amounts to roughly 5 times the input magnetic field and 5% of the reference saturation value - roughly $7\times10^{-2}$T in true value -. At such low values, the magnetic field falls in the linear range of the b-h curve. The results for

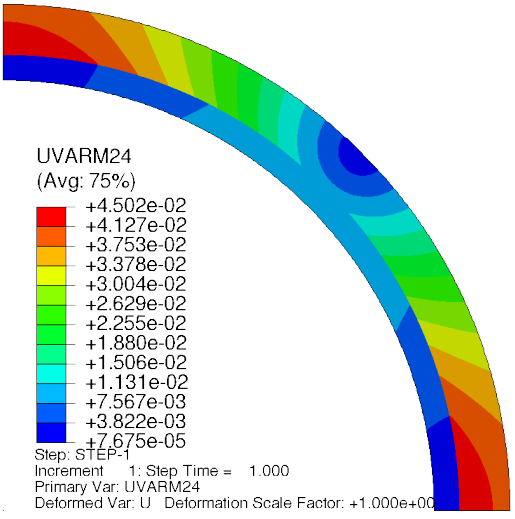


Figure 7.2: FEM results for the idealized stator at small $\mathbf{b}$: norm of the normalized magnetic field: $\frac{||\mathbf{b}||}{\mu_0 m_s}$ .

1 If two neighboring elements have values that differ by more than 75%, no averaging is performed.

the true displacements' tangent and radial components are given in Figures 7.4(a) and 7.5(a). The displacements, magnified $10^7$ times, are of order $10^{-10}$m and fall in the small strain linear range. The linearity of the problem, both in $\mathbf{b}$ and strains, is further confirmed by the computation converging in a single iteration, and justifies comparison with the analytical results from Section 3.2 for validation of the code (recall the analytical problem has linear magnetization).

VALIDATION OF THE RESULTS FOR NODAL VARIABLES Figures 7.3(a),7.4(a) and 7.5(a) provide the FEM results obtained for the nodal variables of the problem, namely the true magnetic potential $A$[2] and the true radial and tangent displacement components $u_r$ and $u_\theta$. By "true" we mean "not noramlized". The magnified deformation shows the same pattern as obtained in 3.2. To further confirm the accuracy of the FEM results, we plot in Figures 7.3(b),7.4(b) and 7.5(b) the values for the normalized nodal variables along a radial path at different cross sections $\theta = \{0, \frac{\pi}{8}, \frac{\pi}{4}\}$, and superimpose them with analytical results. The graphs show a very good accuracy for the magnetic potential $A$[3] and the tangent displacement $u_\theta$. The results very slightly deviate for $u_r$ close to the stator external edge in $r_3$, with a maximum error of 6%. Note that in the graph 7.5(b) for $u_\theta$ the curves at $\theta = 0$ and $\theta = \frac{\pi}{4}$ superimpose such that one appears missing but is not. Further, for obvious reasons of sense, we suppressed the airgap region is the graphs of $u_r$ and $u_\theta$.

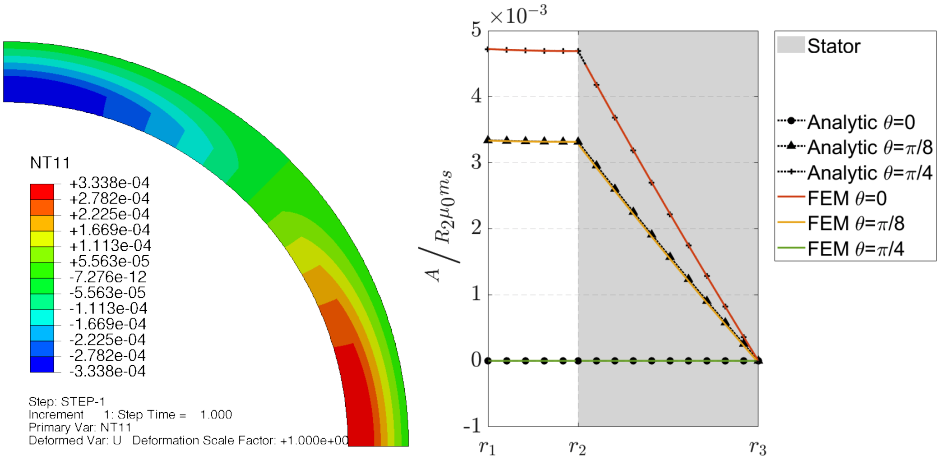


(a) $A$: FEM (b) $\frac{A}{R_2 \mu_0 m_s}$: FEM vs. analytical

Figure 7.3: FEM results for the idealized stator at small $\mathbf{b}$, for the magnetic potential: (a) FEM results for the true field, (b) FEM vs. analytical results for the normalized field.

2 Recall the vector potential $\mathbf{a}$ has a single component $a$ along $z$.

3 Note that given we are in small strain, the FEM code's nodal Lagrangian variable $A$ equals the eulerian $a$.

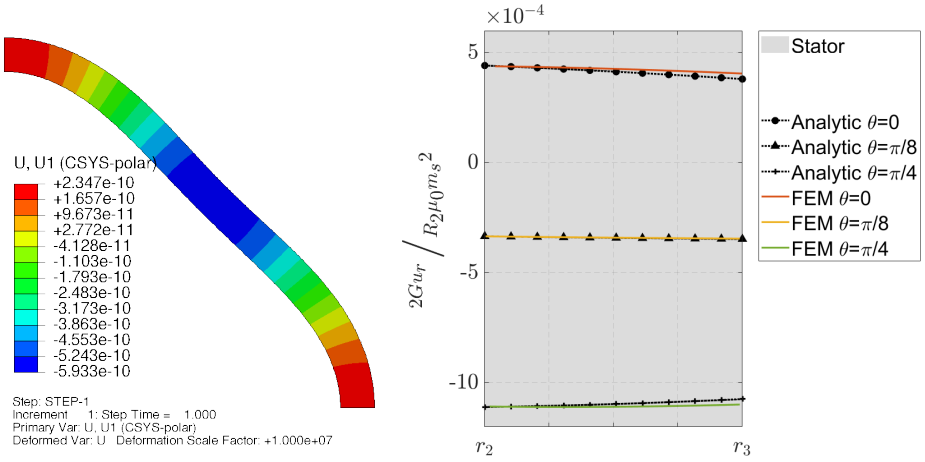


(a) $u_r$: FEM (b) $\frac{2Gu_r}{R_2\mu_0 m_s^2}$: FEM vs. analytical

Figure 7.4: FEM results for the idealized stator at small $\mathbf{b}$, for the radial displacement: (a) FEM results for the true field, (b) FEM vs. analytical results for the normalized field. Overall true deformation is magnified $10^7$ times.

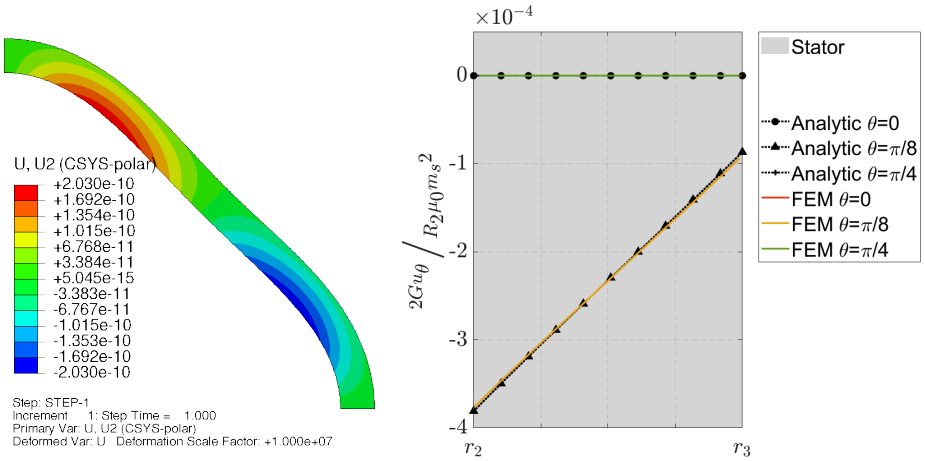


(a) $u_\theta$: FEM (b) $\frac{2Gu_\theta}{R_2\mu_0 m_s^2}$: FEM vs. analytical

Figure 7.5: FEM results for the idealized stator at small $\mathbf{b}$, for the tangent displacement: (a) FEM results for the true field, (b) FEM vs. analytical results for the normalized field. Overall true deformation is magnified $10^7$ times.

VALIDATION OF THE RESULTS FOR DERIVED VARIABLES The magnetic fields $\mathbf{B}$ and $\mathbf{H}$ and the stress field $\boldsymbol{\Pi}$ - equivalently their Eulerian counterpart $\mathbf{b}, \mathbf{h}, \boldsymbol{\sigma}$ given the small strains - derive from the nodal variables $A$ and $\mathbf{u}$ and involve the derivatives of these nodal variables. Verifying their accuracy is important as well, especially given we use constant strain - and constant b-field - triangular elements and given the importance to our problem of the interface conditions that involve those fields.

Following the approach adopted for the nodal variables, we show the FEM results for the radial magnetic field (Figure 7.6), the tangent h-field (Figure 7.7), and

the radial, shear and hoop stress components (Figures 7.8, 7.9, 7.10) and compare them with analytical results. The focus is placed on the components $b_r$ and $h_\theta$ solely here - not $h_r$ and $b_\theta$ - given they are the quantities involved in the interface conditions for $\mathbf{b}$ and $\mathbf{h}$. The comparison with the analytical data shows a very good accuracy for the magnetic components $b_r$ and $h_\theta$. The small jump that is visible at the airgap-stator interface for $b_r$ is explained by the sharp gradients and the fact that the variable is element based and computed at the element centroids, slightly off the interface on each sides of it. The same goes for the small jumps in $h_\theta$ near the airgap-stator interface and the rotor boundary.

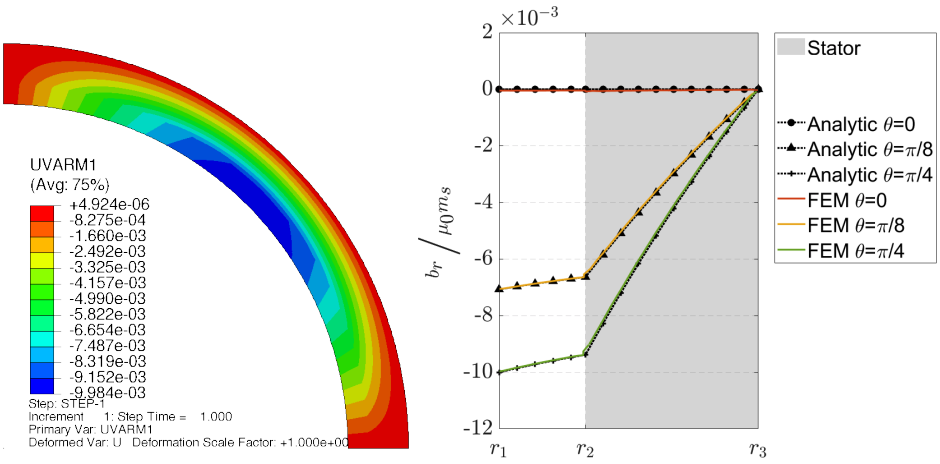


(a) FEM (b) FEM vs. analytical

Figure 7.6: FEM results for the idealized stator at small $\mathbf{b}$, for the normalized radial magnetic field $\frac{b_r}{\mu_0 m_s}$: (a) FEM, (b) FEM vs. analytical results.

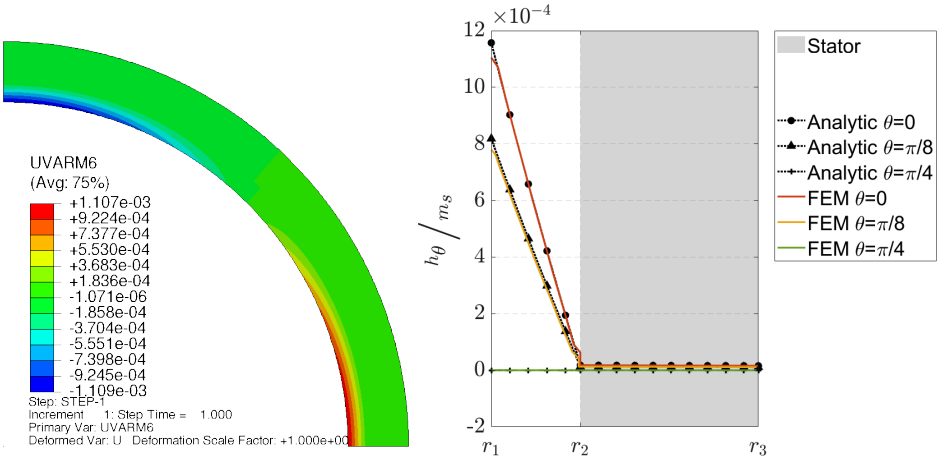


(a) FEM (b) FEM vs. analytical

Figure 7.7: FEM results for the idealized stator at small $\mathbf{b}$, for the normalized tangent h-field $\frac{h_\theta}{m_s}$: (a) FEM, (b) FEM vs. analytical results.

The stress results (Figures 7.8, 7.9 and 7.10) also show a good accuracy in the airgap and stator regions. For $\sigma_{rr}$ and $\sigma_{r\theta}$ the small jumps at the airgap-stator

interface, where the fields should be continuous, are slightly more pronounced than for $b_r$ and $h_\theta$. We explain this by the computation of $\boldsymbol{\sigma}$ at the element centroid together with the fact that $\boldsymbol{\sigma}$ depends on $\mathbf{b}^2$, such that the small uncertainties observed on $b_r$ and $h_\theta$ multiply and further impact stresses. Throughout the stator domain the stress curves are slightly noisier than for $b_r$ and $h_\theta$, which may similarly be due to the dependence of stresses on the squared magnetic field that multiplies the errors on $\mathbf{b}$, when $\mathbf{b}$ spatial derivative of the nodal variable $A$ already suffers an accuracy one order lower than $A$. In $\theta = 0$, the results for $\sigma_{rr}$ is off, which we explain by a spurious stress mode that develops from the corner in $r_3$, where $\sigma_{r\theta}$ is off by roughly the same magnitude. Although it needs to be carefully monitored, the previous developments show that this error, which seems in

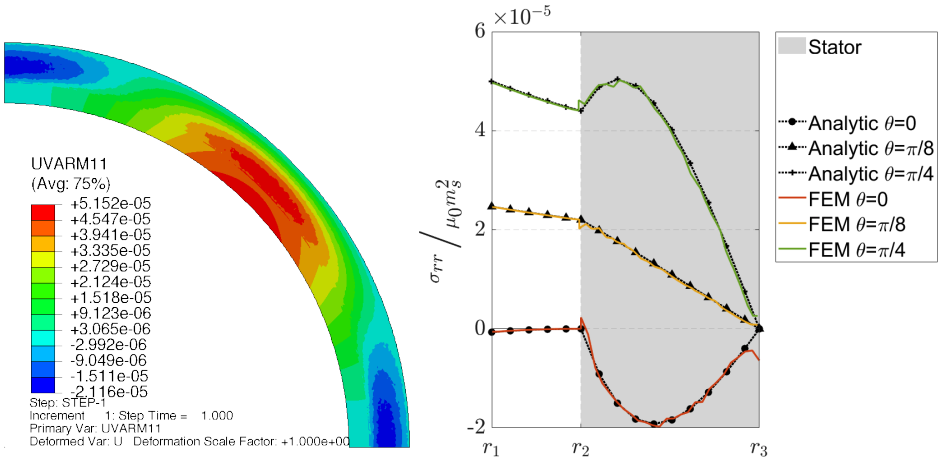


(a) FEM (b) FEM vs. analytical

Figure 7.8: FEM results for the idealized stator at small $\mathbf{b}$, for the normalized radial stress component $\frac{\sigma_{rr}}{\mu_0 m_s^2}$: (a) FEM, (b) FEM vs. analytical results.

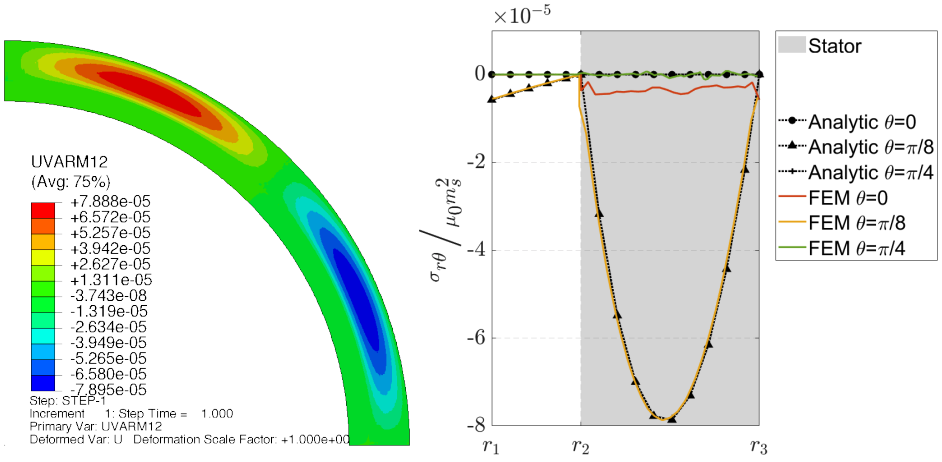


(a) FEM (b) FEM vs. analytical

Figure 7.9: FEM results for the idealized stator at small $\mathbf{b}$, for the normalized shear stress component $\frac{\sigma_{r\theta}}{\mu_0 m_s^2}$: (a) FEM, (b) FEM vs. analytical results.

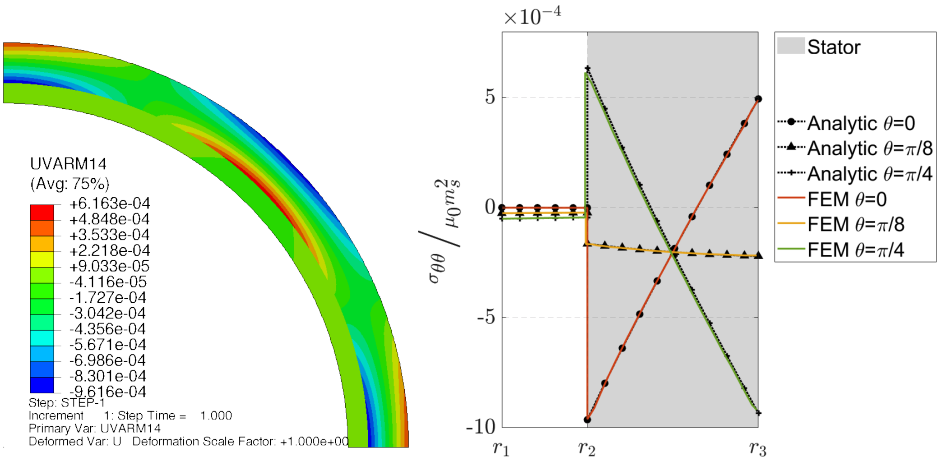


(a) FEM (b) FEM vs. analytical

Figure 7.10: FEM results for the idealized stator at small $\mathbf{b}$, for the normalized hoop stress component $\frac{\sigma_{\theta\theta}}{\mu_0 m_s^2}$: (a) FEM, (b) FEM vs. analytical results.

the end due to the modeling of a quarter motor only, does not significantly impact the solution away from the boundary (as shown by the consistency of all other results with anaytical results).

CONCLUDING REMARKS As a result, we show by comparison with analytical results that for fields falling in the linear range of the problem, the FEM code developed provide accurate results throughout the airgap and stator domains, as well as at interfaces and boundaries. Only for $u_r$ do the FEM results show a slightly high error (6%). This may be explained by the spurious traction stress solution that develops in $\theta = 0$ and - by symmetry - in $\theta = \frac{\pi}{2}$, which is consistent with an overestimation of $u_r(r_3, \theta = 0) > 0$.

The comparison with the analytical results also ensure the validity of the mesh. Despite the very fine mesh, the computation ran in under 5 seconds on a standard computer. Given the fast computation time, there was no motivation for further mesh convergence studies to investigate if the mesh can be coarsened.

We further verified from the FEM results, that given the small strain regime, the Lagrangian and Eulerian fields coincide, and that the Jacobian of the deformation $J = 1$. In addition the stress and deformation gradient results are symmetrical.

### 7.1.3 *Results at large magnetic field values*

In this section, before refining the stator geometry (the object of the later Section 7.2), we investigate the effect of magnetic saturation at higher values of the magnetic field. However, the model described in (6.19), with its correction coefficient $\alpha_s = 35$, has a major drawback : if it fits correctly to typical values from the literature at reasonable magnetic fields - fields below 1T, see Appendix C -, it multiplies by $\alpha_s$ the magnetization limit at saturation $m_s$. As a result, it starts being com-

pletely off realistic material behavior above 1T, and one has to go to unrealisticly high values of the magnetic field (> 10T) - and consequently of the stresses and strains that follow - in order to start seeing the effect of saturation. For that reason, we decided here to revert back to the initial uncorrected Langevin model ($\alpha_s = 1$). This enables to get an idea of the effect of magnetic saturation at realistic values of the magnetic field, even though the reader should bear in mind that saturation occurs too soon and too gradually when compared to typical electrical steel behavior (see Figure C.1 in Appendix subsection C.1.3).

In the following calculation, we increased the input magnetic field at the rotor boundary 20 folds compared to the previous calculation (Subsection 7.1.2) so that it now equals $20\%\mu_0 m_s$. The mesh remains unchanged. The computation now takes four iterations to converge, suggesting non-linearities as expected. The computation ran in under 10 seconds on a standard computer.

As shown by Figure 7.11, the magnetic field at the stator reaches 77% of the reference saturation value - roughly 1.2T in true value - and the effect of magnetic saturation are clearly visible by the "squared" patern around the low magnetic field regions as opposed to the circular pattern in Figure 7.2. These patterns are explained by the fact that as the magnetic field saturates in the regions of high magnetic field, the regions expand over the low magnetic field regions.

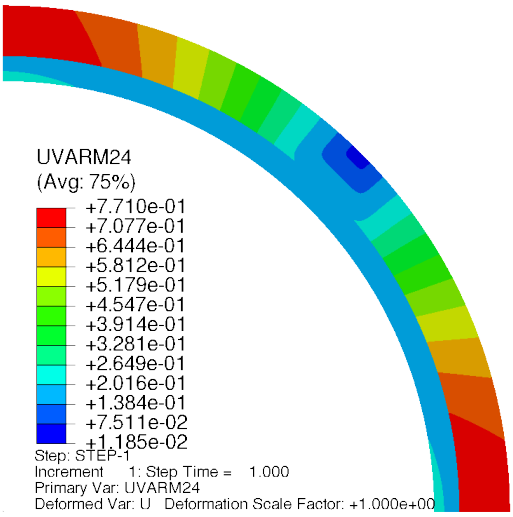


Figure 7.11: FEM results for the idealized stator at large $\mathbf{b}$: norm of the normalized magnetic field: $\frac{||\mathbf{b}||}{\mu_0 m_s}$ .

The results for the true displacements' tangent and radial components are given in Figures 7.13(a) and 7.14(a). The displacements, magnified $2\times10^4$ times, are of order 0.2µm and therefor still fall in the small strain linear range for the elastic stress-strain relation.

*Nota: Prior to the following developments, we stress out that analytical computations from Section 3.2 have linear magnetic behavior, while the FEM computations performed at large* $\mathbf{b}$ *in the present section has non-linear magnetic behavior. Still, comparison with analytical results is provided in the following in order to highlight the influence of magnetic*

*saturation. The computation results are given, but not thoroughly discussed (only a few comments of verification order are made).*

RESULTS FOR NODAL VARIABLES Figures 7.12(a),7.13(a) and 7.14(a) provide the results obtained for the nodal variables of the problem $A$, $u_r$ and $u_\theta$ and a comparison with the analytical results obtained in Section 3.2 in the case of linear magnetization. Here again, the FEM colormap shows the true values of the fields while the comparison plots are normalized. The graphs show a clearly distinct behavior due to the magnetic saturation that modifies the magnetic potential distribution.

VERIFICATION OF THE BOUNDARY AND INTERFACE CONDITIONS As a first check, we verify that the boundary conditions of the problem are correctly fulfilled ($A(r_3,\theta)=0$, $A(r_1,\theta)=A_0\cos(p\theta)$, $u_\theta(r,\theta=0)=u_\theta(r,\theta=\frac{\pi}{2})=0$). Further, the continuity condition for $A$ at the airgap-stator interface is verified as well, which implies the continuity condition for $b_r$ observed in Figure 7.15. The discontinuity of the r-derivative of $A$ at the airgap-stator interface satisfies the interface condition on $h_\theta$ as observed in Figure 7.16. Finaly for stresses, the continuity conditions on $\sigma_{rr}$ and $\sigma_{r\theta}$ at the airgap-stator interface are verified. The slight jumps of the fields at the interface remain controlled. Recall that theses were already observed in the linear magnetization regime (Section 7.1.2), with similar relative amplitude. They are attributed to an offset triggered by the evaluation of the element based variables at the mesh elements' centroids - which does not exactly coincide with the interface - together with amplification of the errors on the magnetic fields as the stresses depend on the square of the magnetic field components. Finally, the boundary condition $\sigma_{rr}(r_3,\theta)=\sigma_{r\theta}(r_3,\theta)=0$ is fulfilled, except for the slight spurious stress solution in $\theta=0$ already observed in Section 7.1.2

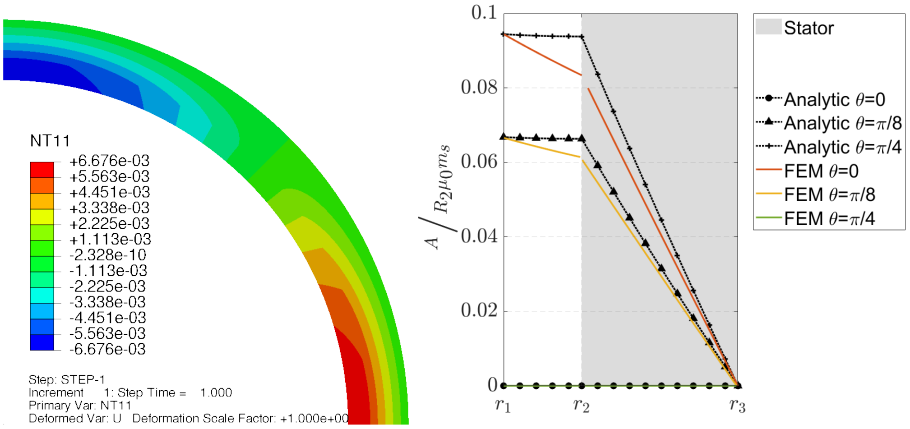


(a) $A$: FEM (b) $\frac{A}{R_2\mu_0 m_s}$: FEM vs. analytical

Figure 7.12: FEM results for the idealized stator at large $\mathbf{b}$, for the magnetic potential: (a) FEM results for the true field, (b) FEM vs. analytical results for the normalized field.

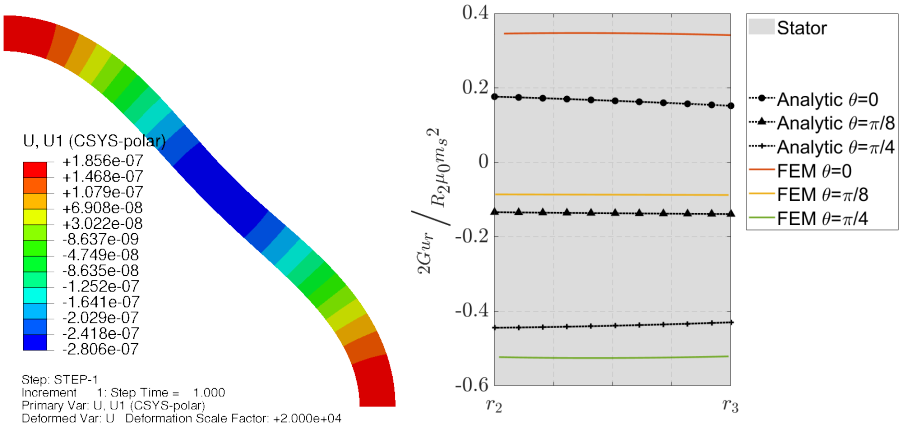


(a) $u_r$: FEM (b) $\frac{2Gu_r}{R_2\mu_0 m_s^2}$: FEM vs. analytical

Figure 7.13: FEM results for the idealized stator at large **b**, for the radial displacement: (a) FEM results for the true field, (b) FEM vs. analytical results for the normalized field. Overall true deformation is magnified $10^7$ times.

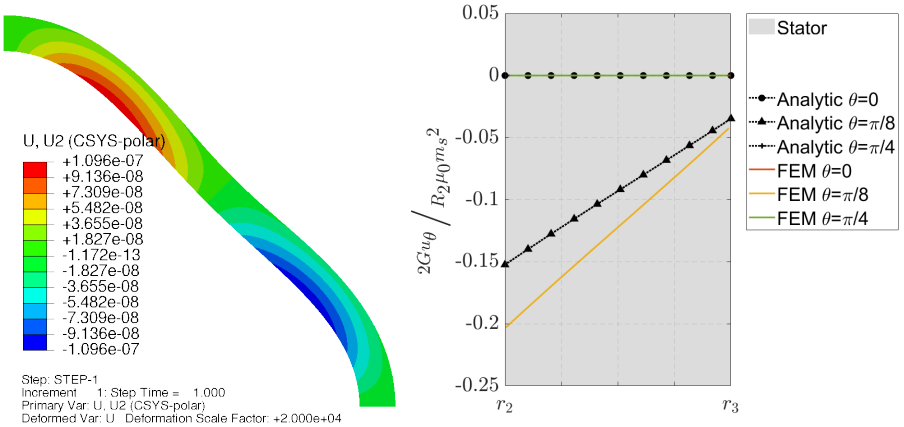


(a) $u_\theta$: FEM (b) $\frac{2Gu_\theta}{R_2\mu_0 m_s^2}$: FEM vs. analytical

Figure 7.14: FEM results for the idealized stator at large **b**, for the tangent displacement: (a) FEM results for the true field, (b) FEM vs. analytical results for the normalized field. Overall true deformation is magnified $10^7$ times.

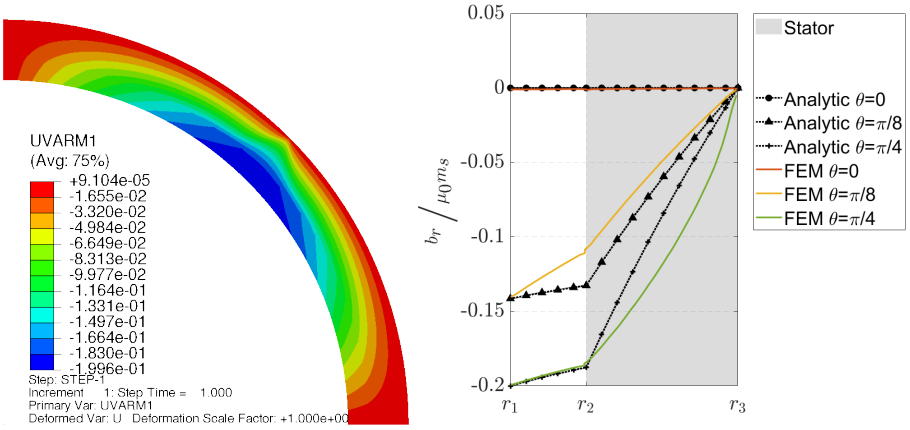


(a) FEM (b) FEM vs. analytical

Figure 7.15: FEM results for the idealized stator at large $\mathbf{b}$, for the normalized radial magnetic field $\frac{b_r}{\mu_0 m_s}$: (a) FEM, (b) FEM vs. analytical results.

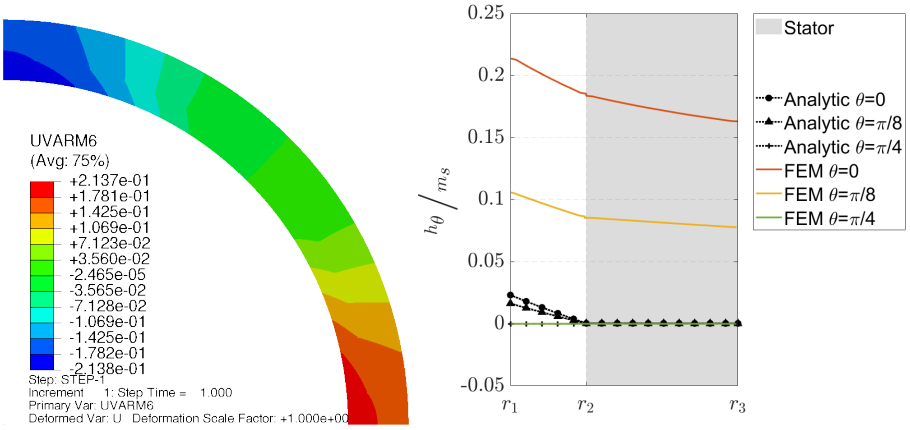


(a) FEM (b) FEM vs. analytical

Figure 7.16: FEM results for the idealized stator at large $\mathbf{b}$, for the normalized tangent h-field $\frac{h_\theta}{m_s}$: (a) FEM, (b) FEM vs. analytical results.

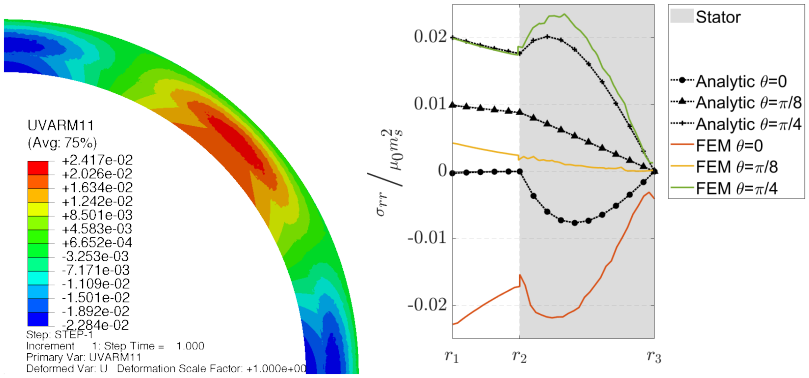


(a) FEM (b) FEM vs. analytical

Figure 7.17: FEM results for the idealized stator at large $\mathbf{b}$, for the normalized radial stress component $\frac{\sigma_{rr}}{\mu_0 m_s^2}$: (a) FEM, (b) FEM vs. analytical results.

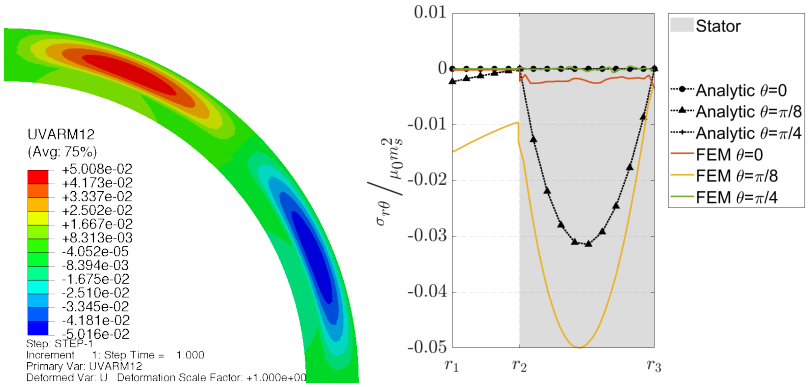


(a) FEM (b) FEM vs. analytical

Figure 7.18: FEM results for the idealized stator at large $\mathbf{b}$, for the normalized shear stress component $\frac{\sigma_{r\theta}}{\mu_0 m_s^2}$: (a) FEM, (b) FEM vs. analytical results.

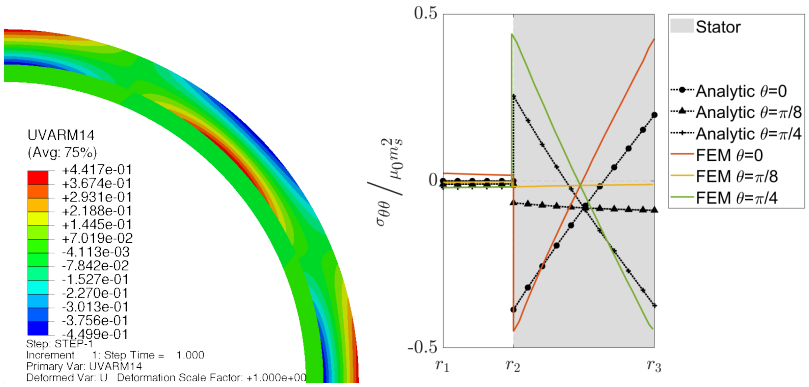


(a) FEM (b) FEM vs. analytical

Figure 7.19: FEM results for the idealized stator at large $\mathbf{b}$, for the normalized hoop stress component $\frac{\sigma_{\theta\theta}}{\mu_0 m_s^2}$: (a) FEM, (b) FEM vs. analytical results.

## 7.2 FEM SIMULATION OF A REFINED STATOR GEOMETRY

### 7.2.1 *Problem setup*

GEOMETRY FEM simulations are further performed on a slotted stator geometry to highlight the capacities of the code. The stator geometry is inspired by the benchmark machine of Devillers et al., 2018. Figure 7.20 shows the stator geometry, with the stator domain $\mathscr{D}_3$ in grey and the airgap domain $\mathscr{D}_2$ in green[4]. The mesh is displayed. Table 7.20 provides the values for the geometrical parameters. Because of the symmetries of the geometry - and of the loading later defined - computations are performed on a quarter motor only. $\partial\mathscr{D}_1$ denotes the boundary with the rotor, $\partial\mathscr{D}_3$ denotes the stator external boundary. $\partial\mathscr{D}_l^1$ and $\partial\mathscr{D}_l^2$ denotes the lateral surfaces of symmetries in $\theta = 0$ and $\theta = \frac{\pi}{2}$ respectively. The stator teeth are labeled 1 to 4 for future reference.

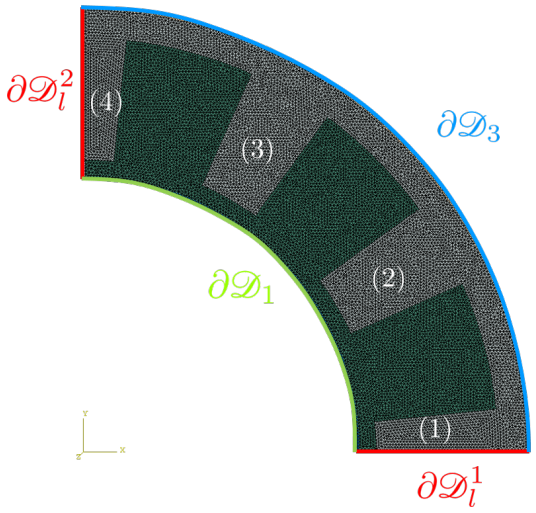


Figure 7.20: Refined stator: geometry and mesh. In grey the stator, in green the airgap.

| | | |
|---|---|---|
| Rotor bore radius | $R_1$ | 45 mm |
| Stator bore radius | $R_2$ | 48 mm |
| Stator tooth length | $H_{tooth}$ | 20 mm |
| Stator outer radius | $R_3$ | 73 mm |
| Stator slot width | $W_s$ | 18° |
| Number of stator teeth | $Z_s$ | 12 |
| Number of pole pairs | p | 2 |

Table 7.20: For FEM: motor geometry for the refined stator boundary value problem.

MATERIALS Regarding the material behavior, we use the same material parameters as previously in Section 7.1.2, given in Table 7.1. The model used for the

4 $\mathscr{D}_1$ is reserved to the rotor domain (not shown in Figure 7.20).

specific free-energy is the uncorrected model ($\alpha_s = 1$), for the reasons previously exposed in 7.1.3.

LOADING *In the following we work with fields of the reference configuration because the variational principle is written in the reference configuration. We introduce the stator frame of reference in the reference configuration $\mathcal{S}(R, \theta)$.*

As in the stator problem of Section 3.2 or the experimental setup in Devillers et al., 2018, we assume the rotor comprises p-pairs of permanent magnets that produce a rotating radial magnetic field of amplitude $B_0$ at the rotor boundary,

$$\partial\mathscr{D}_1 : \qquad \mathbf{N}\cdot\mathbf{B} = -B_0 \sin(p\theta - p\Omega t) \,, \tag{7.7}$$

where $\Omega$ is the clockwise rotation velocity of the rotor. In the present study we set $p = 2$.

For solving on a quarter motor only, the loading needs to fulfill some symmetry conditions that match with the symmetry conditions on the geometry. Namely, the problem can only be solved if the magnetic field input is symmetric or anti-symmetric across the lateral faces $\mathscr{D}_l^1$ and $\mathscr{D}_l^2$. This restricts the modeling possibilities to the discrete times $t = \frac{n\pi}{2p\Omega}$, $n \in \mathbb{N}^+$. The following computations are performed setting,

$$\partial\mathscr{D}_1 : \qquad A = \frac{R_1 B_0}{p} \cos(p\theta) \,, \tag{7.8}$$

such that it corresponds to a snapshot of the solution to the problem with loading (7.7) at any time $t = \frac{n2\pi}{p\Omega}$, $n \in \mathbb{N}^+$, for which the magnetic potential $A$ is symmetrical in $\theta = 0$ and $\theta = \frac{\pi}{2}$.

A typical motor would include copper winding in the inter-teeth slots, supplied by alternating currents to produce the excitation stator magnetic field. These are not considered here. Neither are they on the test bench that inspired the motor's geometry in Devillers et al., 2018.

MAGNETIC BOUNDARY CONDITIONS On the outer stator boundary, we assume magnetic insulation, such that we set,

$$\partial\mathscr{D}_3 : \qquad A = 0 \quad \Longrightarrow \quad \mathbf{N}\cdot\mathbf{B} = 0 \,. \tag{7.9}$$

By the magnetic field-magnetic potential relation $\mathbf{B} = \boldsymbol{\nabla}\times\mathbf{A}$, any radial plane of symmetry for $A$ is a plane of anti-symmetry for $B_r$ and consequently $B_r = 0$ throughout the plane. As a consequence, we let the boundary condition on $\partial\mathscr{D}_l^1$ and $\partial\mathscr{D}_l^2$ free such that the natural Neumann boundary condition is enforced

$$\partial\mathscr{D}_l^1, \partial\mathscr{D}_l^2 : \qquad \hat{\mathbf{e}}_\theta \times \mathbf{H} = 0 \quad \Longrightarrow \quad B_r = 0 \,. \tag{7.10}$$

Note that had we set $A$ to be anti-symmetric across the boundaries $\partial\mathscr{D}_l^1$ and $\partial\mathscr{D}_l^2$- such that occurs at times $t = \frac{pi}{p\Omega} + \frac{n\pi}{p\Omega}$, $n \in \mathbb{N}^+$ -, $B_\theta$ would be anti-symmetric across the boundaries, and consequently $B_\theta = 0$. This would then have required to set a Dirichlet boundary condition $A = \mathtt{constant}$[5], compliant with the loading and boundary conditions on $\partial\mathscr{D}_1$ and $\partial\mathscr{D}_3$.

5 For the reason that $B_\theta = -\frac{\partial A}{\partial r}$.

MECHANICAL BOUNDARY CONDITIONS The displacements are constrained on $\partial\mathscr{D}_1$. Given the symmetries, we allow radial displacements on $\partial\mathscr{D}_l^1$ and $\partial\mathscr{D}_l^2$ but prescribe tangent displacements. On $\partial\mathscr{D}_3$ the displacements are let free. As a result, we set

$$\begin{aligned} &\partial\mathscr{D}_1 : && u_r = u_\theta = 0 \, ; \\ &\partial\mathscr{D}_l^1, \partial\mathscr{D}_l^2 : && u_\theta = 0 \, . \end{aligned} \tag{7.11}$$

As a result of the free radial displacements on $\partial\mathscr{D}_l^1$ and $\partial\mathscr{D}_l^2$, and of the free radial and tangent displacements on $\partial\mathscr{D}_3$, the natural Neumann boundary conditions provide,

$$\begin{aligned} &\partial\mathscr{D}_l^1, \partial\mathscr{D}_l^2 : && \Pi_{r\theta} = 0 \, ; \\ &\partial\mathscr{D}_3 : && \Pi_{rr} = \Pi_{r\theta} = 0 \, . \end{aligned} \tag{7.12}$$

MESH CONVERGENCE Mesh convergence is studied in Appendix C.4. Three mesh configurations: coarse, fine and extrafine, are studied. The fine mesh - displayed in Figure 7.20 - is judged accurate enough and retained for the computations. It consists of 22,182 elements of approximate global size 0.5mm (recall the typical length scales from Table 7.20). The computations run in roughly 8s CPU time on a standard computer.

### 7.2.2 *Results at large magnetic field values*

Simulations were performed with an input magnetic field $B_0 = 80\%\mu_0 m_s \approx 1.26T$[6] which corresponds to the strength of typical neodymium permanent magnets used in electric motors (e.g. see Devillers et al., 2018). Figure 7.21 shows the norm of the magnetization at the stator reaching roughly 72% of the saturation magnetization $m_s$, at which the effect of the non-linear magnetization are significant (recall the uncorrected model - $\alpha_s = 1$ - used in the calculation has saturation effects occurring very early, as per Figure C.1 in Appendix C.1.3). Here again the computations show that the stator experiences only small strains, as per the displacement values reported in Figures 7.22. The results for the tangent and radial displacements are given in Figure 7.22. The displacements, magnified 3,000 times, are of order 2µm at most. They still fall in the small strain linear range for the elastic stress-strain relation. One can observe the similarity of the deformation pattern - ovalization - with that of the idealized stator in Sections 3.2 and 7.1. Given the small strains, the current configuration and reference configuration variables are equivalent[7] and the results hereafter are presented for the current configuration variables, which appears as a more natural choice.

*Nota: In the following, we denote by "stator casing" - or "stator crown" in some figures -, the tubular part of the stator, as opposed to the complementary "teeth part". In all the graphs that show curves for the field values along radial paths, the "stator teeth" domain is highlighted, but note that not all paths go through a tooth.*

6 To reach similar values of the stator magnetic field=, the increase in input magnetic field is much more significant here than for the idealized stator in Subsection 7.1.3 because the airgap is now much bigger as a result of the stator slots.

7 This point was further verified as both Eulerian and Lagrangian fields are outputs of the FEM code.

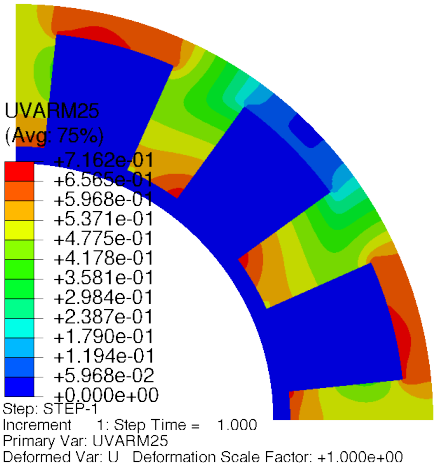


Figure 7.21: FEM results for the refined stator, for the normalized norm of the magnetization: $\frac{||\mathbf{m}||}{m_s}$ .

VERIFICATION OF THE BOUNDARY CONDITIONS As a first check, we verify that the boundary conditions of the problem are correctly fulfilled. Starting with the Dirichlet boundary conditions (7.8), (7.9) and (7.11), Figure 7.22 shows the boundary condition $u_\theta = 0$ is correctly satisfied on $\partial\mathscr{D}_l^1$ and $\partial\mathscr{D}_l^2$. The airgap mesh displacements are not pictured in Figure 7.22 but the prescribed displacement condition on the rotor boundary $\partial\mathscr{D}_1$ is fulfilled as well. Figure 7.23[8] shows the proper implementation of the loading condition on $\partial\mathscr{D}_1$ and $A = 0$ on $\partial\mathscr{D}_3$. Figure 7.24 shows the consistency with the boundary conditions on $B_r$.

For the Neumann boundary conditions, Figure 7.24 shows the proper implementation of (7.10) on the boundary $\partial\mathscr{D}_l^1$. The fact that $B_r$ is not exactly zero on the boundary is attributed to the fact that $\mathbf{B}$ is evaluated at the elements centroid. Regarding (7.12), Figure 7.27 shows the proper implementation of the boundary condition on the boundary $\partial\mathscr{D}_l^1$ and $\partial\mathscr{D}_3$. Similarly, the slight deviation from $\Pi_{r\theta} = 0$ on $\partial\mathscr{D}_l^1$ is attributed to the evaluation of the field at the elements centroid and not directly on the boundary. It is all the same for the condition $\Pi_{r\theta} = 0$ on $\partial\mathscr{D}^3$, especially for the cut in $\theta = \frac{\pi}{12}$ where the gradients in $\sigma_{r\theta}$ are very steep. Verification with the extrafine mesh showed the $\sigma_{r\theta}$ distribution is correct and does tend to zero at the boundary.

VERIFICATION OF THE INTERFACE CONDITIONS Further, the continuity condition for $A$ at the airgap-stator interfaces is verified (Figure 7.23), which implies the continuity for $b_r$ along the $\theta$-cuts as observed in Figure 7.24. The jumps on $b_\theta$ observed at airgap-stator interfaces along the $\theta$-cuts (Figure 7.25) are due to the continuity condition on $h_\theta$ and the difference in magnetic permeability of the two mediums. It should be noted that the jump are likely much underestimated

8 The author apologies to the reader for he did not find the command that allows plotting simultaneously the airgap and stator domain together with the delimitation between the two, and hence the unclear figures when the fields are continuous across interfaces like is the case for $\mathbf{A}$, although at least it makes the case of continuity.

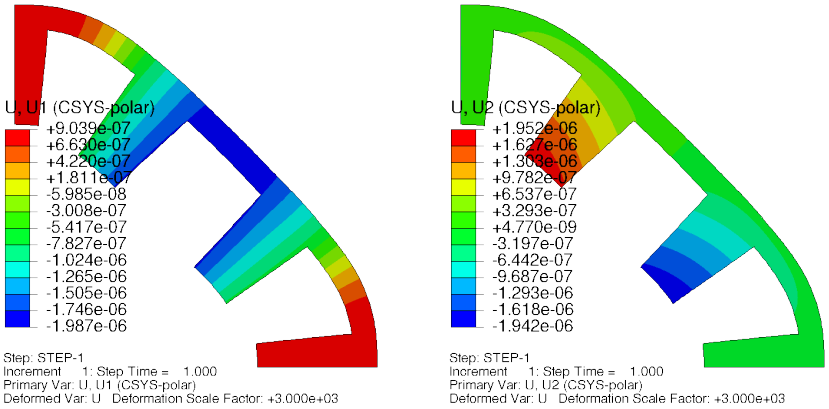


(a) $u_r$ (b) $u_\theta$

Figure 7.22: FEM results for the refined stator: (a) radial displacement, in [m] (b) tangent displacement, in [m]. Overall true deformation is magnified 3,000 times.

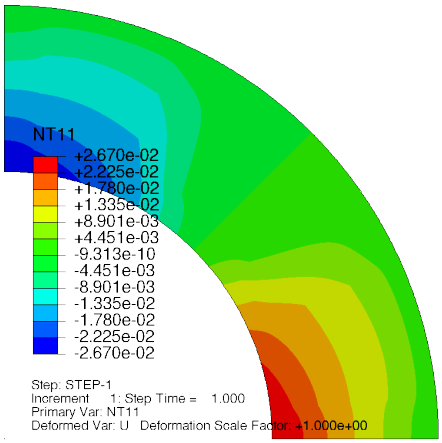


Figure 7.23: FEM results for the refined stator, for the magnetic potential A [T/m].

as a result of the inaccurate b-h curve due to the uncorrected model for $\psi$ used ($\alpha_s = 1$) (see Appendix C.1). Finally for stresses, the continuity conditions on $\sigma_{rr}$ and $\sigma_{r\theta}$ at the airgap-stator interface are verified along the $\theta$-cuts (see Figures 7.26 and 7.27). The slight jumps of the fields at the interface are attributed to the evaluation of the fields at the elements centroids and not directly at the interfaces. It was also verified aside the results plotted here that the continuity conditions for $\sigma_{r\theta}$ and $\sigma_{\theta\theta}$ across the lateral faces of the teeth were satisfied, except maybe near the base corner of the teeth where sharp stress concentrations arise. The teeth tips seems to be preserved from the problem. This issue may benefit from further investigation not undertaken here[9]. It could also be due once again to the evaluation of the fields at the elements centroids. Regarding the magnetic fields, continuity of $b_\theta$ and $h_r$ across the lateral faces of the teeth was verified as well. As opposed to stress results, no continuity issues were observed near the teeth base corners

9 The corner of the teeth could be rounded for instance like in yet even more realistic stator geometries (Fonteyn, 2010)

and teeth tips. Given the variations of the fields are much smoother than for the stress field, this goes in the sense of explaining the apparent discontinuities for the stress fields in corner regions by the offset due to the evaluation of the fields at the elements' centroids.

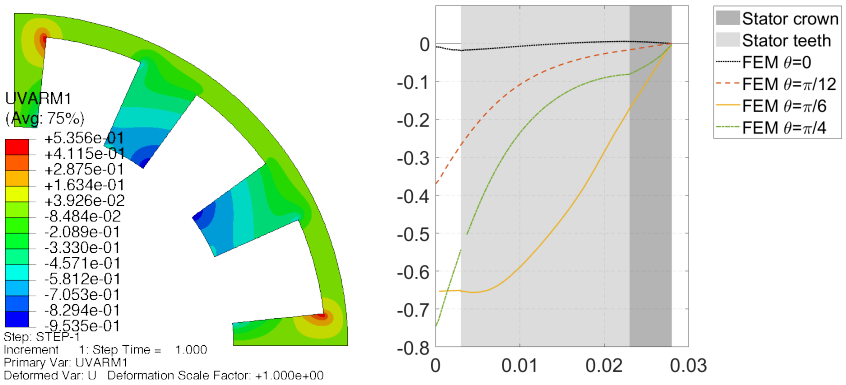


(a) Stator only (b) Cuts at $\theta = \{0°, 15°, 30°, 45°\}$

Figure 7.24: FEM results for the refined stator, for the normalized radial magnetic field $\frac{b_r}{\mu_0 m_s}$: (a) at the stator only, (b) over the whole domain for different θ-cuts.

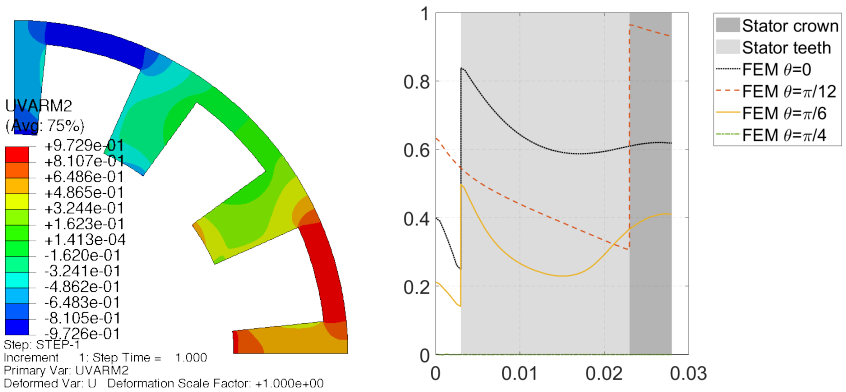


(a) Stator only (b) Cuts at $\theta = \{0°, 15°, 30°, 45°\}$

Figure 7.25: FEM results for the refined stator, for the normalized tangent magnetic field $\frac{b_\theta}{\mu_0 m_s}$: (a) at the stator only, (b) over the whole domain for different θ-cuts.

OTHER OBSERVATIONS The two middle stator teeth (2) and (3) are pushed apart as the stator casing is being bent.

Figures 7.24 and 7.25 show that the magnetic field concentrates around edges and in particular at the teeth tips where the airgap thickness that separates from the input magnetic field is reduced. Radial field is as expected more intense in the teeth (Figure 7.24), which channel the magnetic field to the stator casing were the field lines are then bent to align along the θ-direction and thus $b_\theta$ dominates in the casing (Figure 7.25).

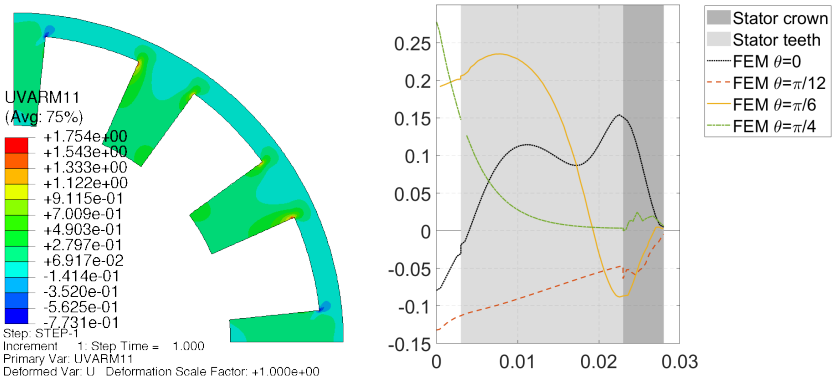


(a) Stator only (b) Cuts at $\theta = \{0°, 15°, 30°, 45°\}$

Figure 7.26: FEM results for the refined stator, for the normalized radial stress component $\frac{\sigma_{rr}}{\mu_0 m_s^2}$: (a) at the stator only, (b) over the whole domain for different θ-cuts.

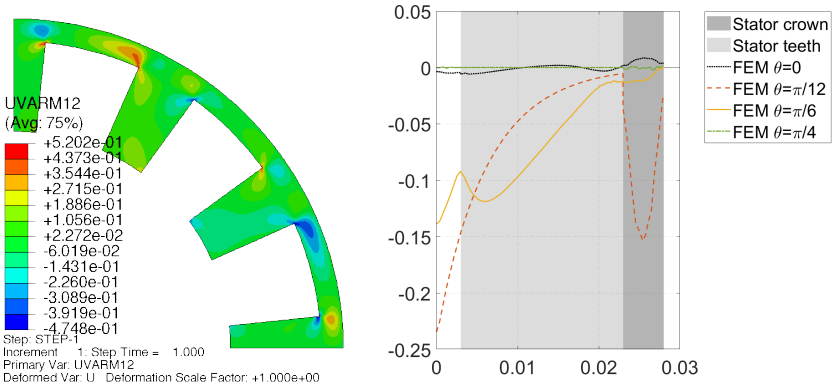


(a) Stator only (b) Cuts at $\theta = \{0°, 15°, 30°, 45°\}$

Figure 7.27: FEM results for the refined stator, for the normalized shear stress component $\frac{\sigma_{r\theta}}{\mu_0 m_s^2}$: (a) at the stator only, (b) over the whole domains for different θ-cuts.

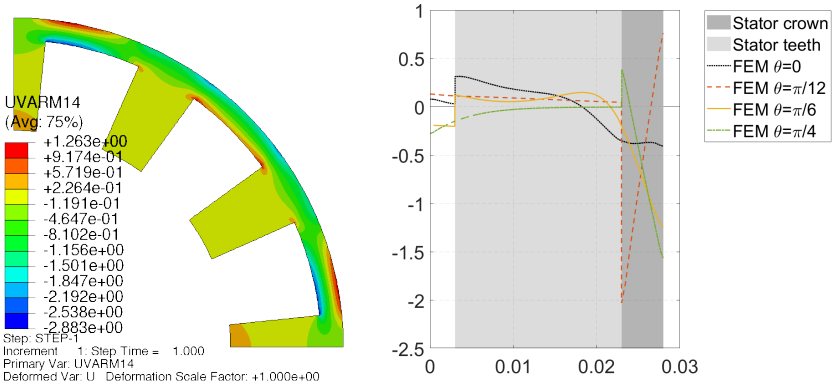


(a) Stator only (b) Cuts at $\theta = \{0°, 15°, 30°, 45°\}$

Figure 7.28: FEM results for the refined stator, for the normalized hoop stress component $\frac{\sigma_{\theta\theta}}{\mu_0 m_s^2}$: (a) at the stator only, (b) over the whole domains for different θ-cuts.

Figure 7.25 shows the tangent field gradually decays with distance to the source, except at tangent airgap-stator interfaces where it surges as a result of the difference in magnetic permeability. Despite the rather high magnetic field values at the stator near its external radius, the external field is much lower as a consequence of the ratio of magnetic permeability between the stator and ambient air, and the modeling assumption of negligible external field holds. One may still object that given the very gradual decrease of $b_\theta$ along a radius, the external field component is not much lower than in the airgap in the regions of high $b_\theta$ at the stator.

Given $\mu_0 m_s$ is of order 1T, the magnetic field in the stator reaches values of order 1T (Figure 7.24 and 7.25). Given the model retained for the material behavior has saturation effects occurring too soon compared to typical experiments on electrical steel sheets (see Appendix C.1), it can be expected that a simulation with more accurate material behavior would lead to higher magnetic field values, however more localized as saturation effects tend to extend the regions of highest magnetic fields.

The reference stress $\mu_0 m_s^2$ is of order $10^6$ Pa, such that stresses are of order 1MPa (Figures 7.26, 7.27 and 7.28). Stresses consequently falls in the range of reported magneto-mechanical couplings in electrical steels (magnetostriction and most importantly inverse magneto-striction, i.e. influence of the stress state on the magnetic permeability of the material), e.g. see Aydin et al., 2017. These high stresses with impact on the magnetic properties of the machine further occur in the stator casing, a region particularly important to the operation of the electric motor as it is meant to bend the magnetic field lines to keep the field within the machine and offer the least resistance to its flux. As we mentioned that the peaks of magnetic field tend to be lowered by our imperfect magnetization model, so is true of the peaks of stresses that should reach higher values with a more accurate model for the material behavior and hence have an even more important impact on the magnetic permeability of the material. Further, in a more realistic motor, coils or windings supplied with high currents are held between the stator teeth and may further greatly alter the stress state of the stator as they are subjected to the Lorentz forces.

The stress figures 7.26, 7.27 and 7.28 show that the stresses in the teeth, in particular for $\sigma_{rr}$ and $\sigma_{r\theta}$, are not negligible compared to stresses in the stator casing. Hence the teeth are likely to contribute significantly to the stator forces, stresses and displacement fields. Note that for $\sigma_{rr}$ in the stator casing region, some irregularities seem to occur along the paths $\theta = \frac{\pi}{12}$ and $\theta = \frac{\pi}{4}$ (Figure 7.26). These are attributed to the mesh as computations performed on the extrafine mesh showed smoother curves.

From Figure 7.27 we see that apart from fairly localized regions, $\sigma_{r\theta}$ is mostly negative, i.e. compressive, throughout the stator, highlighting a global tendency of the stator to shrink under the application of the magnetic field further highlighted by the mostly negative values for $u_r$ in Figure 7.22. This tendency was already reported in Section 3.2 on the idealized stator geometry.

In Figure 7.28 we recognize in the stator casing region the same hoop stress distribution $\sigma_{\theta\theta}$, characteristic of bending, as already observed in Section 3.2.

MAIN ELEMENTS Based on the previous discussion, the following main points are made:

1. the variational formulation and numerical implementation work well, with a non linear coupled material behavior, and a complex geometry.

2. stresses of the order of the MPa can be reached, especially in $\theta\theta$. These stresses are of a magnitude that is likely to affect the magnetic properties of the machine (see for instance Aydin et al., 2017, Daniel, Bernard, and Hubert, 2020).

3. Displacement are of the order $1\mu m$, comparable to reported magnetostriction in typical electrical steels (see for instance Aydin et al., 2017).

Points 2. and 3. highlight and justify the necessity for accurate evaluation of stresses and strains in electric motors and the development of the present code. These first results are obtained with a material behavior that would still benefit from further refinement - as highlighted in the discussion and in Section 6.2 - in order to confirm the previous results but the capacities of this numerical implementation is demonstrated.

# 8

# CONCLUSION OF PART II

The essential contributions of Part II are:

- Proposing a general variational formulation for the study of coupled magneto-mechanical problems in electric motors, under finite strain and arbitrary magnetic fields and showing its consistency with the direct approach of continuum mechanics in Part I (a non-trivial result for coupled problems);
- A numerical implementation of the variational formulation for finite element analysis of electric motor problems and verification of the code by comparison with the analytical results of Part I;
- Numerical calculation of stresses, strains and magnetic fields in a realistic stator under large magnetic fields accounting for magneto-mechanical couplings.

DISCUSSION In Part II, a general variational formulation for fully coupled-magneto-mechanical problems in electric motors is proposed and a numerical implementation is subsequently applied to the finite element analysis of a practical motor problem. The variational formulation is based on Hamilton's principle of variations.

As part of an effort to start from the most general framework before a careful application of the suitable approximations for electric motor problems, a Lagrangian for general electro-magneto-mechanical dynamic problems is first presented. An eddy current approximation version of the Lagrangian is then proposed for the modeling of electric motor problems. For both the general and approximated Lagrangian expressions, an explicit derivation of the application of Hamilton's principle is performed. Particular attention is paid to the clarity of the derivation and we show that the corresponding Euler-Lagrange equations consistently reduce to the governing equations *and* interface conditions obtained from the direct approach in Part I, a non-trivial result for coupled problems. Despite its use for electric motor problems that are usually small strains, the formulation proposed is based on a reference configuration (Lagrangian) approach, which enables to properly retrieve the Maxwell-stress contribution in the linear momentum balance.

The variational formulation is then implemented in a general purpose finite element code (Abaqus), via the definition of a user element. It is applied to a practical quasi-static stator boundary value problem neglecting induced currents and acceleration terms. A constitutive law for the specific free energy is suggested which accounts for magnetic saturation. The airgap is modeled (meshed) in order to account for the Maxwell-stress in the airgap and at interfaces. In the small magnetic field regime, the numerical implementation is validated by the finite element anal-

ysis of the stator problem of Part I and comparison with the analytical results obtained. Comparison shows a good match of the numerical and analytical results. Calculations are then performed on a more complex stator configuration that includes teeth and slots, and at large magnetic field. Despite some inaccuracies in the material behavior, this last example of application puts forward the capacities of the proposed formulation. It shows results for realistic engineering applications and the peak values obtained for the stresses - of order 1 MPa - fall in the range of non-negligible magneto-mechanical couplings.

*Additional element: In the first section of Part II, the general variational formulation for electro-magneto-mechanical dynamic problems presented goes beyond the scope of electric motors and may benefit other applications. To the best of the authors knowledge, the link between this variational formulation and the direct approach of continuum mechanics through the derivation of the Euler Lagrange equations does not exist in such clear and simple terms in the literature and is believed to be a useful contribution of the present work.*

SUGGESTIONS FOR FUTURE WORKS Our focus in this work was on the theory for the variational formulation and its implementation. The FEM model accounts for hypotheses on the material behavior, clearly mentioned throughout the thesis, that may be further investigated and improved. In particular, the modeling of the coupled magneto-mechanical behavior of electrical steels could be better fitted to experimental data (Aydin et al., 2017) using the small strain linearization from Part I. A Langevin model for magnetization written in terms of $\mathbf{h}$, instead of $\mathbf{b}$ here, would also seem to be a better model of the behavior of electrical steels. The implementation of such a model requires non-trivial manipulations involving a Legendre transform and the inversion of the Langevin function.

The variational formulation may be enriched to account for more physics such as the temperature and couplings between temperature and magnetization or temperature and stresses (thermal expansion) for instance. The framework exposed in this thesis is general enough to enable the inclusion of these physics.

Induced currents and acceleration terms were neglected. A further investigation on how they could be implemented would be beneficial, especially for induced currents that play a significant role in electric machines. The problem would then become dynamic and likely much more computational intensive. The rotor was not accounted for as well. Should it be, the question of accounting for moving meshes and parts arises.

The FEM code developed is based on constant strain triangular elements for simplicity, and because no problems of computational time or precision challenged this choice. It is likely however that different element types may be better suited given the distribution of the fields encountered in the analytic calculation. This would be even more true for dynamic computations if induced currents are included (Ledger et al., 2016).

Finally, all the previous work would greatly benefit from comparison with experimentation, the only guide that may accurately judge on the accuracy of the physics and of the material behaviors considered and remove uncertainties.

# Part III

# APPENDICES

# A

# CALCULUS DETAILS

## A.1 DERIVATION OF THE REFERENCE CONFIGURATION ELECTRIC AND MAGNETIC POTENTIALS

We have,

$$\begin{aligned} \boldsymbol{e} &\equiv -\boldsymbol{\nabla}\phi - \frac{\partial \boldsymbol{a}}{\partial t} \qquad \text{and} \qquad & \boldsymbol{\mathscr{E}} &= \boldsymbol{e}\cdot\mathbf{F} \\ \boldsymbol{b} &\equiv \boldsymbol{\nabla}\times\boldsymbol{a} & \mathbf{B} &= J\mathbf{F}^{-1}\cdot\boldsymbol{b} \end{aligned} \tag{A.1}$$

Thus, given the transformations $\boldsymbol{\mathscr{E}} = \boldsymbol{e}\cdot\mathbf{F}$ and $\mathbf{B} = J\mathbf{F}^{-1}\cdot\boldsymbol{b}$,

$$\begin{aligned} \boldsymbol{\mathscr{E}} &= -(\boldsymbol{\nabla}\phi)\cdot\mathbf{F} - \frac{\partial \boldsymbol{a}}{\partial t}\cdot\mathbf{F} + \left(\dot{\boldsymbol{u}}\times(\boldsymbol{\nabla}\times\boldsymbol{a})\right)\cdot\mathbf{F} \\ &= -\boldsymbol{\nabla}\phi - \left(\frac{\partial \boldsymbol{a}}{\partial t} - \left[\dot{\boldsymbol{u}}\cdot(\boldsymbol{a}\boldsymbol{\nabla}) - \dot{\boldsymbol{u}}\cdot(\boldsymbol{\nabla}\boldsymbol{a})\right]\right)\cdot\mathbf{F} \\ &= -\boldsymbol{\nabla}\phi - \left(\dot{\boldsymbol{a}} - (\dot{\boldsymbol{u}}\cdot\boldsymbol{a})\boldsymbol{\nabla} + \boldsymbol{a}\cdot(\dot{\boldsymbol{u}}\boldsymbol{\nabla})\right)\cdot\mathbf{F} \\ &= -\boldsymbol{\nabla}\phi - \dot{\boldsymbol{a}}\cdot\mathbf{F} - (\dot{\boldsymbol{u}}\cdot\boldsymbol{a})\boldsymbol{\nabla} + \boldsymbol{a}\cdot(\dot{\boldsymbol{u}}\boldsymbol{\nabla}) \\ &= -\boldsymbol{\nabla}(\phi - \dot{\boldsymbol{u}}\cdot\boldsymbol{a}) - \frac{d}{dt}(\boldsymbol{a}\cdot\mathbf{F}) \end{aligned} \tag{A.2}$$

$$\begin{aligned} \mathbf{B} &= J\mathbf{F}^{-1}\cdot(\boldsymbol{\nabla}\times\boldsymbol{a}) \\ &= JF^{-1}_{Ii}\epsilon^{ijk}\partial_j(a_k)\hat{\boldsymbol{e}}_I \\ &= JF^{-1}_{Ii}\epsilon^{ijk}\partial_J(a_k)F^{-1}_{Jj}\hat{\boldsymbol{e}}_I \\ &= \epsilon^{IJK}F_{kK}\partial_J(a_k)\hat{\boldsymbol{e}}_I \\ &= \epsilon^{IJK}\Big(\partial_J(a_kF_{kK}) - a_k\partial_J(F_{kK})\Big)\hat{\boldsymbol{e}}_I \\ &= \boldsymbol{\nabla}\times(\boldsymbol{a}\cdot\mathbf{F}) \end{aligned} \tag{A.3}$$

Note that the above uses the fact that $\mathbf{F}\cdot\mathbf{F}^{-1} = \mathbf{F}^{-1}\cdot\mathbf{F} = \mathbf{I}$ such that as solutions to these two equations, $\mathbf{F}$ and $\mathbf{F}^{-1}$ are:

$$\begin{aligned} F_{kK} &= \frac{\text{cofactor}(F^{-1}_{Kk})}{\det(()\mathbf{F}^{-1})} = \frac{J}{2}\epsilon^{ijk}\epsilon^{IJK}F^{-1}_{Ii}F^{-1}_{Jj} \\ F^{-1}_{Kk} &= \frac{\text{cofactor}(F_{kK})}{\det(()\mathbf{F})} = \frac{1}{2J}\epsilon^{ijk}\epsilon^{IJK}F_{iI}F_{jJ} \end{aligned} \tag{A.4}$$

As a result,

$$\begin{aligned} J\epsilon^{ijk}F^{-1}_{Ii}F^{-1}_{Jj} &= \epsilon^{ijk}\frac{1}{2}\epsilon^{ilm}\epsilon^{ILM}F_{lL}F_{mM}F^{-1}_{Jj} \\ &= (\delta_{jl}\delta_{km}-\delta_{jm}\delta_{kl})\frac{1}{2}\epsilon^{ILM}F_{lL}F_{mM}F^{-1}_{Jj} \\ &= \frac{1}{2}\epsilon^{ILM}(F_{jL}F_{kM}-F_{kL}F_{jM})F^{-1}_{Jj} \\ &= \frac{1}{2}(\epsilon^{IJM}F_{kM}-\epsilon^{ILJ}F_{kL}) \\ &= \epsilon^{IJK}F_{kK} \end{aligned} \tag{A.5}$$

## A.2 OTHER IDENTITY

Another direct consequence of (A.5), is the following identity: for two arbitrary fields $\mathbf{a}$ and $\mathbf{b}$ of the current configuration,

$$\mathbf{a}\times\mathbf{b} = J\left[(\mathbf{F}^{-1}\cdot\mathbf{a})\times(\mathbf{F}^{-1}\cdot\mathbf{b})\right]\cdot\mathbf{F}^{-1} \tag{A.6}$$

Note that despite a same symbol "$\times$", the cross product acting on the fields of the current configuration is not the same as the cross product acting on the fields of the reference configuration given the distinct sets of basis vectors.

## A.3 INTERMEDIATE VARIATIONS CALCULUS FOR APPLICATION OF HAMILTON'S PRINCIPLE

Intermediate computations of the variations of the different terms of the Lagrangian are performed here to help in the application of Hamilton's principle in 5. The independent fields (generalized coordinates) of the variational principle are $\Phi$, $\mathbf{A}$ and $\mathbf{u}$. Consequently for any scalar or tensor field $\mathbf{f}$, $\delta\mathbf{f}$ should be expressed as a function of $\delta\Phi$, $\delta\mathbf{A}$, $\delta\mathbf{u}$ and derivatives.

As a first step, one can derive the variations $\delta\mathscr{E}, \delta\mathbf{B}, \delta\mathbf{F}, \delta\mathbf{F}^{-1}$ and $\delta J$,

$$\begin{aligned} &\delta\mathscr{E} = -\boldsymbol{\nabla}(\delta\Phi) - \frac{d}{dt}(\delta\mathbf{A}) \\ &\delta\mathbf{B} = \boldsymbol{\nabla}\times(\delta\mathbf{A}) \\ &\delta\mathbf{F} = (\delta\mathbf{u})\boldsymbol{\nabla} \\ &\delta\mathbf{F}^{-1} = \frac{\partial F^{-1}_{Ii}}{\partial F_{jJ}}\delta F_{jJ}\hat{\mathbf{e}}_I\hat{\mathbf{e}}_i = -F^{-1}_{Ij}F^{-1}_{Ji}\delta F_{jJ}\hat{\mathbf{e}}_I\hat{\mathbf{e}}_i = -\mathbf{F}^{-1}\cdot((\delta\mathbf{u})\boldsymbol{\nabla})\cdot\mathbf{F}^{-1} \\ &\delta J = \frac{\partial J}{\partial\mathbf{F}} : \delta\mathbf{F} = J\mathbf{F}^{-T} : (\delta\mathbf{u})\boldsymbol{\nabla} = (J\mathbf{F}^{-1}) : \boldsymbol{\nabla}\delta\mathbf{u} \end{aligned} \tag{A.7}$$

For variations of the right Cauchy-Green tensor $\mathbf{C}$, starting with its definition $\mathbf{C} \equiv \mathbf{F}^T\cdot\mathbf{F}$,

$$\begin{aligned} &\delta\mathbf{C} = (\delta\mathbf{F})^T\cdot\mathbf{F} + \mathbf{F}^T\cdot\delta\mathbf{F} \\ &\delta\mathbf{C}^{-1} = -\mathbf{F}^{-1}\cdot\delta\mathbf{F}\cdot\mathbf{C}^{-1} - \mathbf{C}^{-1}\cdot(\delta\mathbf{F})^T\cdot\mathbf{F}^{-T} \end{aligned} \tag{A.8}$$

and then for any symmetric second order tensor $\boldsymbol{\Gamma}$, accounting for the symmetries of $\mathbf{C}$ and $\mathbf{C}^{-1}$,

$$\begin{aligned}\boldsymbol{\Gamma} : \delta\mathbf{C} &= 2\boldsymbol{\Gamma} : (\mathbf{F}^{\mathsf{T}}\cdot\delta\mathbf{F}) = 2(\boldsymbol{\Gamma}\cdot\mathbf{F}^{\mathsf{T}}) : \boldsymbol{\nabla}\delta\mathbf{u}\\ \boldsymbol{\Gamma} : \delta\mathbf{C}^{-1} &= -2\boldsymbol{\Gamma} : \left(\mathbf{F}^{-1}\cdot\delta\mathbf{F}\cdot\mathbf{C}^{-1}\right) = -2\mathbf{C}^{-1}\cdot\boldsymbol{\Gamma}\cdot\mathbf{F}^{-1} : \boldsymbol{\nabla}\delta\mathbf{u}\end{aligned} \tag{A.9}$$

Finally, for any vector $\mathbf{T}$, recalling $\mathbf{E} = \boldsymbol{\mathscr{E}} - (\mathbf{F}^{-1}\cdot\dot{\mathbf{u}}\times\mathbf{B})$ (5.4), and accounting for the expression for $\delta\mathbf{F}^{-1}$ from (A.7) in the process,

$$\begin{aligned}\mathbf{T}\cdot\delta\mathbf{E} &= \mathbf{T}\cdot\delta\boldsymbol{\mathscr{E}} - \mathbf{T}\cdot\delta\Big((\mathbf{F}^{-1}\cdot\dot{\mathbf{u}})\times\mathbf{B}\Big)\\ &= \mathbf{T}\cdot\delta\boldsymbol{\mathscr{E}} + \Big((\mathbf{F}^{-1}\cdot\dot{\mathbf{u}})\times\mathbf{T}\Big)\cdot\delta\mathbf{B} + (\mathbf{T}\times\mathbf{B})\cdot\delta(\mathbf{F}^{-1}\cdot\dot{\mathbf{u}})\\ &= \mathbf{T}\cdot\delta\boldsymbol{\mathscr{E}} + \Big((\mathbf{F}^{-1}\cdot\dot{\mathbf{u}})\times\mathbf{T}\Big)\cdot\delta\mathbf{B} + (\mathbf{T}\times\mathbf{B})\cdot(\delta\mathbf{F}^{-1}\cdot\dot{\mathbf{u}} + \mathbf{F}^{-1}\cdot\delta\dot{\mathbf{u}})\\ &= \mathbf{T}\cdot\delta\boldsymbol{\mathscr{E}} + \Big((\mathbf{F}^{-1}\cdot\dot{\mathbf{u}})\times\mathbf{T}\Big)\cdot\delta\mathbf{B}\\ &\quad + (\mathbf{T}\times\mathbf{B})\cdot\left(-\mathbf{F}^{-1}\cdot((\delta\mathbf{u})\boldsymbol{\nabla})\cdot\mathbf{F}^{-1}\cdot\dot{\mathbf{u}} + \mathbf{F}^{-1}\cdot\frac{\mathrm{d}}{\mathrm{d}t}(\delta\mathbf{u})\right)\\ &= -\mathbf{T}\cdot\boldsymbol{\nabla}(\delta\Phi) - \mathbf{T}\cdot\frac{\mathrm{d}}{\mathrm{d}t}(\delta\mathbf{A}) + \Big((\mathbf{F}^{-1}\cdot\dot{\mathbf{u}})\times\mathbf{T}\Big)\cdot(\boldsymbol{\nabla}\times\delta\mathbf{A})\\ &\quad + \Big((\mathbf{T}\times\mathbf{B})\cdot\mathbf{F}^{-1}\Big)\cdot\frac{\mathrm{d}}{\mathrm{d}t}(\delta\mathbf{u}) - \Big((\mathbf{F}^{-1}\cdot\dot{\mathbf{u}})(\mathbf{T}\times\mathbf{B})\cdot\mathbf{F}^{-1}\Big) : \boldsymbol{\nabla}\delta\mathbf{u}\end{aligned} \tag{A.10}$$

From all the previous then,

$$\begin{aligned}\delta\left(\frac{\epsilon_0 J}{2}\mathbf{E}\cdot\mathbf{C}^{-1}\cdot\mathbf{E}\right) &= \left(\frac{\epsilon_0}{2}\mathbf{E}\cdot\mathbf{C}^{-1}\cdot\mathbf{E}\right)\delta J + \frac{\epsilon_0 J}{2}\mathbf{E}\mathbf{E} : \delta\mathbf{C}^{-1} + \epsilon_0 J\mathbf{E}\cdot\mathbf{C}^{-1}\cdot\delta\mathbf{E}\\ &= \left(\frac{\epsilon_0}{2}\mathbf{E}\cdot\mathbf{C}^{-1}\cdot\mathbf{E}\right)(J\mathbf{F}^{-1}) : \boldsymbol{\nabla}\delta\mathbf{u}\\ &\quad - \epsilon_0 J\Big(\mathbf{C}^{-1}\cdot\mathbf{E}\mathbf{E}\cdot\mathbf{F}^{-1}\Big) : \boldsymbol{\nabla}(\delta\mathbf{u})\\ &\quad - (\epsilon_0 J\mathbf{C}^{-1}\cdot\mathbf{E})\cdot\boldsymbol{\nabla}(\delta\Phi) - (\epsilon_0 J\mathbf{C}^{-1}\cdot\mathbf{E})\cdot\frac{\mathrm{d}}{\mathrm{d}t}(\delta\mathbf{A})\\ &\quad - \Big((\mathbf{F}^{-1}\cdot\dot{\mathbf{u}})((\epsilon_0 J\mathbf{C}^{-1}\cdot\mathbf{E})\times\mathbf{B})\cdot\mathbf{F}^{-1}\Big) : \boldsymbol{\nabla}\delta\mathbf{u}\\ &\quad + \Big((\epsilon_0 J\mathbf{C}^{-1}\cdot\mathbf{E})\times\mathbf{B})\cdot\mathbf{F}^{-1}\Big)\cdot\frac{\mathrm{d}}{\mathrm{d}t}(\delta\mathbf{u})\\ &\quad + \Big((\mathbf{F}^{-1}\cdot\dot{\mathbf{u}})\times(\epsilon_0 J\mathbf{C}^{-1}\cdot\mathbf{E})\Big)\cdot(\boldsymbol{\nabla}\times\delta\mathbf{A})\end{aligned} \tag{A.11}$$

$$\begin{aligned}\delta\left(\frac{1}{2\mu_0 J}\mathbf{B}\cdot\mathbf{C}\cdot\mathbf{B}\right) &= -\left(\frac{1}{2\mu_0 J^2}\mathbf{B}\cdot\mathbf{C}\cdot\mathbf{B}\right)\delta J + \frac{1}{2\mu_0 J}\mathbf{B}\mathbf{B} : \delta\mathbf{C} + \frac{1}{\mu_0 J}\mathbf{B}\cdot\mathbf{C}\cdot\delta\mathbf{B}\\ &= -\left(\frac{1}{2\mu_0 J^2}\mathbf{B}\cdot\mathbf{C}\cdot\mathbf{B}\right)(J\mathbf{F}^{-1}) : \boldsymbol{\nabla}\delta\mathbf{u}\\ &\quad + \frac{1}{\mu_0 J}\Big(\mathbf{B}\mathbf{B}\cdot\mathbf{F}^{\mathsf{T}}\Big) : \boldsymbol{\nabla}\delta\mathbf{u} + \frac{1}{\mu_0 J}\mathbf{B}\cdot\mathbf{C}\cdot(\boldsymbol{\nabla}\times\mathbf{A})\end{aligned} \tag{A.12}$$

As a result, one has now for the variation of $\ell_0$ with respect to $\Phi$, $\mathbf{A}$ and $\mathbf{u}$,

$$\begin{aligned}\ell_{0,\Phi}[\delta\Phi] &= \left(\frac{\epsilon_0 J}{2}\mathbf{E}\cdot\mathbf{C}^{-1}\cdot\mathbf{E}\right)_{,\Phi}[\delta\Phi] - Q\delta\Phi\\ &= -(J\mathbf{C}^{-1}\cdot\epsilon_0\mathbf{E})\cdot\boldsymbol{\nabla}(\delta\Phi) - Q\delta\Phi\end{aligned} \tag{A.13}$$

$$\begin{aligned}\ell_{0,\mathbf{A}}[\delta\mathbf{A}] &= \left(\frac{\epsilon_0 J}{2}\mathbf{E}\cdot\mathbf{C}^{-1}\cdot\mathbf{E}\right)_{,\mathbf{A}}[\delta\mathbf{A}] - \left(\frac{1}{2\mu_0 J}\mathbf{B}\cdot\mathbf{C}\cdot\mathbf{B}\right)_{,\mathbf{A}}[\delta\mathbf{A}] + \boldsymbol{\mathscr{J}}\cdot\delta\mathbf{A}\\ &= -\Big(J\mathbf{C}^{-1}\cdot\epsilon_0\mathbf{E}\Big)\cdot\frac{d}{dt}(\delta\mathbf{A}) + \Big((\mathbf{F}^{-1}\cdot\dot{\mathbf{u}})\times(J\mathbf{C}^{-1}\cdot\epsilon_0\mathbf{E})\Big)\cdot(\boldsymbol{\nabla}\times\delta\mathbf{A})\\ &\quad - \Big(\frac{1}{\mu_0 J}\mathbf{C}\cdot\mathbf{B}\Big)\cdot(\boldsymbol{\nabla}\times\delta\mathbf{A}) + \boldsymbol{\mathscr{J}}\cdot\delta\mathbf{A}\end{aligned} \tag{A.14}$$

$$\begin{aligned}\ell_{0,\mathbf{u}}[\delta\mathbf{u}] &= \left(\frac{\epsilon_0 J}{2}\mathbf{E}\cdot\mathbf{C}^{-1}\cdot\mathbf{E}\right)_{,\mathbf{u}}[\delta\mathbf{u}] - \left(\frac{1}{2\mu_0 J}\mathbf{B}\cdot\mathbf{C}\cdot\mathbf{B}\right)_{,\mathbf{u}}[\delta\mathbf{u}]\\ &= -J\epsilon_0\left((\mathbf{C}^{-1}\cdot\mathbf{E})\mathbf{E} - \frac{1}{2}(\mathbf{E}\cdot\mathbf{C}^{-1}\cdot\mathbf{E})\mathbf{I}\right)\cdot\mathbf{F}^{-1} : \boldsymbol{\nabla}\delta\mathbf{u}\\ &\quad - J\epsilon_0\Big((\mathbf{F}^{-1}\cdot\dot{\mathbf{u}})((\mathbf{C}^{-1}\cdot\mathbf{E})\times\mathbf{B})\cdot\mathbf{F}^{-1}\Big) : \boldsymbol{\nabla}\delta\mathbf{u}\\ &\quad - \frac{1}{\mu_0 J}\left(\mathbf{B}(\mathbf{C}\cdot\mathbf{B}) - \frac{1}{2}(\mathbf{B}\cdot\mathbf{C}\cdot\mathbf{B})\mathbf{I}\right)\cdot\mathbf{F}^{-1} : \boldsymbol{\nabla}\delta\mathbf{u}\\ &\quad + \Big((J\mathbf{C}^{-1}\cdot\epsilon_0\mathbf{E})\times\mathbf{B})\cdot\mathbf{F}^{-1}\Big)\cdot\frac{d}{dt}(\delta\mathbf{u})\end{aligned} \tag{A.15}$$

Regarding the variations of the specific free energy $\rho_0\Psi$ now,

$$\rho_0\Psi_{,\Phi}[\delta\Phi] = \rho_0\left(\frac{\partial\Psi}{\partial\boldsymbol{\mathscr{E}}}\right)\cdot(-\boldsymbol{\nabla}(\delta\Phi)) \tag{A.16}$$

$$\rho_0\Psi_{,\mathbf{A}}[\delta\mathbf{A}] = \rho_0\left(\frac{\partial\Psi}{\partial\boldsymbol{\mathscr{E}}}\right)\cdot\left(-\frac{d}{dt}(\delta\mathbf{A})\right) + \rho_0\left(\frac{\partial\Psi}{\partial\mathbf{B}}\right)\cdot(\boldsymbol{\nabla}\times\delta\mathbf{A}) \tag{A.17}$$

$$\begin{aligned}\rho_0\Psi_{,\mathbf{u}}[\delta\mathbf{u}] &= \rho_0\frac{\partial\Psi}{\partial\mathbf{C}} : \delta\mathbf{C}\\ &= \left[2\rho_0\frac{\partial\Psi}{\partial\mathbf{C}}\cdot\mathbf{F}^{\mathsf{T}}\right] : (\boldsymbol{\nabla}\delta\mathbf{u}) = \left[J\mathbf{F}^{-1}\cdot\left(2\rho\mathbf{F}\cdot\frac{\partial\Psi}{\partial\mathbf{C}}\cdot\mathbf{F}^{\mathsf{T}}\right)\right] : (\boldsymbol{\nabla}\delta\mathbf{u})\end{aligned} \tag{A.18}$$

where in the above, we used the fact that, for any scalar or tensor field $\mathbf{f}(\mathbf{C},\boldsymbol{\mathscr{E}},\mathbf{B})$,

$$\left.\frac{\partial\mathbf{f}}{\partial\mathbf{C}}\right|_{(\Phi,\mathbf{A})} = \left.\frac{\partial\mathbf{f}}{\partial\mathbf{C}}\right|_{(\boldsymbol{\mathscr{E}},\mathbf{B})} \tag{A.19}$$

given fixing $(\Phi,\mathbf{A})$ fixes $(\boldsymbol{\mathscr{E}},\mathbf{B})$.

# B

# FURTHER RESULTS FOR THE ANALYTICAL BOUNDARY VALUE PROBLEMS

## B.1 ISOTROPIC, SMALL STRAIN, ARBITRARY MAGNETIZATION CONSTITUTIVE LAWS

The derivation of the constitutive laws for an isotropic magnetoelastic material for small strain $\boldsymbol{\epsilon}$, but arbitrary magnetic field $\mathbf{b}$, although straightforward requires lengthy calculations. Although such calculations have been presented in the literature a long time ago by Pao and Yeh, 1973, following the early works on magnetoelasticity by Brown, 1966, a direct comparison with our results is not possible due to the different formulations adopted (e.g. different independent variables of the free energy densities, different definitions of total stress etc.). A similar derivation can also be found in Eringen and Maugin, 1990 however for small strains $\boldsymbol{\epsilon}$ and small magnetic field $\mathbf{b}$ altogether. Such derivations are not always done consistently in the available literature; a linearized version of the invariants is often considered, thus violating the objective nature of the free energy since the small strain tensor $\boldsymbol{\epsilon}$ is not objective.

Derivations are presented here for two different scenarios: the first assumes the most general form of Helmholtz free energy $\hat{\psi}(I_k, \tilde{J}_k, T)$ and the second is based on the decoupled form $\hat{\psi} = \hat{\psi}_e(I_k) + \hat{\psi}_m(\tilde{J}_k) + \hat{\psi}_{th}(T)$ proposed in (2.23). In both cases terms in $\boldsymbol{\epsilon}$ $\mathbf{b}$ are kept, providing a more general result than the one presented in (2.25).

### B.1.1 *General form of free energy*

Recall that the current configuration expressions for the magnetization and total stress in (2.9) are found by differentiating the Helmoltz free energy $\hat{\psi}(\mathbf{C}, \tilde{\mathbf{B}}, T)$. In the case of an isotropic material $\hat{\psi}(\mathbf{C}, \tilde{\mathbf{B}}, T) = \hat{\psi}(I_1, I_2, I_3, \tilde{J}_1, \tilde{J}_2, \tilde{J}_3, T)$ whose invariants are expressed in terms of the right Cauchy-Green tensor $\mathbf{C} \equiv \mathbf{F}^T \cdot \mathbf{F}$ and $\tilde{\mathbf{B}} \equiv \mathbf{b} \cdot \mathbf{F}$ according to (2.23).

Applying the chain rule of differentiation to the expressions in (2.9), one obtains

$$
\begin{aligned}
\mathbf{m} &= -\frac{2\rho_0}{\sqrt{I_3}} \left( \frac{\partial \hat{\psi}}{\partial \tilde{J}_1} \mathbf{I} + \frac{\partial \hat{\psi}}{\partial \tilde{J}_2} \mathbf{c} + \frac{\partial \hat{\psi}}{\partial \tilde{J}_3} \mathbf{c}^2 \right) \cdot \mathbf{b} \,, \\
\boldsymbol{\sigma} &= \frac{2\rho_0}{\sqrt{I_3}} \left[ \frac{\partial \hat{\psi}}{\partial I_1} \mathbf{c} + \frac{\partial \hat{\psi}}{\partial I_2} (\mathrm{tr}(\mathbf{c})\mathbf{c} - \mathbf{c}^2) + \frac{\partial \hat{\psi}}{\partial I_3} \det(\mathbf{c}) \mathbf{I} - \frac{\partial \hat{\psi}}{\partial \tilde{J}_1} \mathbf{b}\mathbf{b} + \frac{\partial \hat{\psi}}{\partial \tilde{J}_3} (\mathbf{c}\cdot\mathbf{b})(\mathbf{c}\cdot\mathbf{b}) \right] \\
&\quad + \frac{1}{\mu_0} \left( \mathbf{b}\mathbf{b} - \frac{1}{2}(\mathbf{b}\cdot\mathbf{b})\mathbf{I} \right) - \left( \mathbf{m}\mathbf{b} + \mathbf{b}\mathbf{m} - (\mathbf{b}\cdot\mathbf{m})\mathbf{I} \right) \,,
\end{aligned}
\tag{B.1}
$$

where the left Cauchy-Green tensor $\mathbf{c} \equiv \mathbf{F}\cdot\mathbf{F}^T$ appears naturally in the constitutive relations (B.1). The subsequent algebra of small strain linearization is considerably simplified by noting that the invariants involved can be alternatively expressed in terms of $\mathbf{c}$ and $\mathbf{b}$ as follows

$$\begin{aligned} &I_1 = \mathrm{tr}(\mathbf{c}), \quad I_2 = \frac{1}{2}(\mathrm{tr}(\mathbf{c})^2 - \mathrm{tr}(\mathbf{c}\cdot\mathbf{c})), \quad I_3 = \det(\mathbf{c})\,; \quad \mathbf{c} \equiv \mathbf{F}\cdot\mathbf{F}^T\,, \\ &\tilde{J}_1 = \mathbf{b}\cdot\mathbf{b} = \|\mathbf{b}\|^2, \quad \tilde{J}_2 = \mathbf{b}\cdot\mathbf{c}\cdot\mathbf{b}, \quad \tilde{J}_3 = \mathbf{b}\cdot\mathbf{c}^2\cdot\mathbf{b}\,. \end{aligned} \tag{B.2}$$

Expanding the expressions in (B.1) about $\mathbf{c} = \mathbf{I}$ up to the first order in the small strain tensor $\boldsymbol{\epsilon} \equiv (1/2)(\boldsymbol{\nabla}\mathbf{u} + \mathbf{u}\boldsymbol{\nabla})$, for $\|\boldsymbol{\epsilon}\| \ll 1$, we obtain up to $O(\|\boldsymbol{\epsilon}\|^2)$

$$\begin{aligned} &\mathbf{m} \approx \mathbf{m}(\mathbf{c}{=}\mathbf{I}, \mathbf{b}, T) + \left.\frac{\partial \mathbf{m}}{\partial \mathbf{c}}\right|_{\mathbf{c}=\mathbf{I}} : 2\boldsymbol{\epsilon}, \quad \boldsymbol{\sigma} \approx \boldsymbol{\sigma}(\mathbf{c}{=}\mathbf{I}, \mathbf{b}, T) + \left.\frac{\partial \boldsymbol{\sigma}}{\partial \mathbf{c}}\right|_{\mathbf{c}=\mathbf{I}} : 2\boldsymbol{\epsilon}\,; \\ &\mathbf{c} - \mathbf{I} \approx 2\boldsymbol{\epsilon}\,. \end{aligned} \tag{B.3}$$

After lengthy algebraic manipulations of (B.1) and (B.3), the following expression for the magnetization $\mathbf{m}$ is found involving the scalar quantities $\zeta_i(\|\mathbf{b}\|)\,, i = 1, \cdots, 4$

$$\begin{aligned} \mathbf{m} &= \zeta_1 \mathbf{b} + \zeta_2 \mathrm{tr}(\boldsymbol{\epsilon})\mathbf{b} + \zeta_3(\mathbf{b}\cdot\boldsymbol{\epsilon}\cdot\mathbf{b})\mathbf{b} + \zeta_4 \boldsymbol{\epsilon}\cdot\mathbf{b}\,; \\ \zeta_1(\|\mathbf{b}\|) &\equiv -2\rho_0 \left[\frac{\partial \hat{\psi}}{\partial \tilde{J}_1} + \frac{\partial \hat{\psi}}{\partial \tilde{J}_2} + \frac{\partial \hat{\psi}}{\partial \tilde{J}_3}\right]_{\mathbf{c}=\mathbf{I}}\,, \\ \zeta_2(\|\mathbf{b}\|) &\equiv -\zeta_1(\|\mathbf{b}\|) - 4\rho_0 \left[\frac{\partial}{\partial I_1} + 2\frac{\partial}{\partial I_2} + \frac{\partial}{\partial I_3}\right]\left[\frac{\partial \hat{\psi}}{\partial \tilde{J}_1} + \frac{\partial \hat{\psi}}{\partial \tilde{J}_2} + \frac{\partial \hat{\psi}}{\partial \tilde{J}_3}\right]_{\mathbf{c}=\mathbf{I}}\,, \\ \zeta_3(\|\mathbf{b}\|) &\equiv -4\rho_0 \left[\frac{\partial}{\partial \tilde{J}_2} + 2\frac{\partial}{\partial \tilde{J}_3}\right]\left[\frac{\partial \hat{\psi}}{\partial \tilde{J}_1} + \frac{\partial \hat{\psi}}{\partial \tilde{J}_2} + \frac{\partial \hat{\psi}}{\partial \tilde{J}_3}\right]_{\mathbf{c}=\mathbf{I}}\,, \\ \zeta_4(\|\mathbf{b}\|) &\equiv -4\rho_0 \left[\frac{\partial \hat{\psi}}{\partial \tilde{J}_2} + 2\frac{\partial \hat{\psi}}{\partial \tilde{J}_3}\right]_{\mathbf{c}=\mathbf{I}}\,. \end{aligned} \tag{B.4}$$

A further simplification can be made for small strains in the expression of $\zeta_2$: since $|-\zeta_1 \mathrm{tr}(\boldsymbol{\epsilon})\mathbf{b}| << |-\zeta_1 \mathbf{b}|$, one has $\zeta_2 \approx -4\rho_0 \left[\frac{\partial}{\partial I_1} + 2\frac{\partial}{\partial I_2} + \frac{\partial}{\partial I_3}\right]\left[\frac{\partial \hat{\psi}}{\partial \tilde{J}_1} + \frac{\partial \hat{\psi}}{\partial \tilde{J}_2} + \frac{\partial \hat{\psi}}{\partial \tilde{J}_3}\right]_{\mathbf{c}=\mathbf{I}}$.

The corresponding small strain linearization expressions yield a total stress $\boldsymbol{\sigma}$ as the sum of an elastic $\overset{e}{\boldsymbol{\sigma}}$, a magnetic $\overset{m}{\boldsymbol{\sigma}}$ and a magnetostrictive $\overset{ms}{\boldsymbol{\sigma}}$ (involving terms of the order $\boldsymbol{\epsilon}\,\mathbf{b}$) component

$$
\begin{aligned}
\boldsymbol{\sigma} &= \overset{e}{\boldsymbol{\sigma}} + \overset{m}{\boldsymbol{\sigma}} + \overset{ms}{\boldsymbol{\sigma}} \; ; \\
\overset{e}{\boldsymbol{\sigma}} &\equiv \lambda \mathrm{tr}(\boldsymbol{\epsilon})\mathbf{I} + 2G\boldsymbol{\epsilon} \; , \\
\overset{m}{\boldsymbol{\sigma}} &\equiv \frac{1}{\mu_0}\left[\mathbf{b}\mathbf{b} - \frac{1}{2}(\mathbf{b}\cdot\mathbf{b})\mathbf{I}\right] - \zeta_1\left[\mathbf{b}\mathbf{b} - (\mathbf{b}\cdot\mathbf{b})\mathbf{I}\right] - \frac{\zeta_4}{2}\mathbf{b}\mathbf{b} \; , \\
\overset{ms}{\boldsymbol{\sigma}} &\equiv \Sigma_0\mathbf{I} + [\Sigma_1\mathbf{b}\mathbf{b} + \zeta_2(\mathbf{b}\cdot\mathbf{b})\mathbf{I}]\mathrm{tr}(\boldsymbol{\epsilon}) + [\Sigma_2\mathbf{I} + \Sigma_4\mathbf{b}\mathbf{b} + \zeta_3(\mathbf{b}\cdot\mathbf{b})\mathbf{I}](\mathbf{b}\cdot\boldsymbol{\epsilon}\cdot\mathbf{b}) \\
&\qquad + \Sigma_3[(\mathbf{b}\cdot\boldsymbol{\epsilon})\mathbf{b} + \mathbf{b}(\boldsymbol{\epsilon}\cdot\mathbf{b})] \; , \\
\lambda(\|\mathbf{b}\|) &\equiv 2\rho_0\left[\frac{\partial\hat{\psi}}{\partial I_3} - \frac{\partial\hat{\psi}}{\partial I_1}\right]_{\mathbf{c}=\mathbf{I}} + 4\rho_0\left[\left(\frac{\partial}{\partial I_1} + 2\frac{\partial}{\partial I_2} + \frac{\partial}{\partial I_3}\right)\left(\frac{\partial\hat{\psi}}{\partial I_1} + 2\frac{\partial\hat{\psi}}{\partial I_2} + \frac{\partial\hat{\psi}}{\partial I_3}\right)\right]_{\mathbf{c}=\mathbf{I}} \\
G(\|\mathbf{b}\|) &= 2\rho_0\left[\frac{\partial\hat{\psi}}{\partial I_1} + \frac{\partial\hat{\psi}}{\partial I_2}\right]_{\mathbf{c}=\mathbf{I}} \\
\Sigma_0(\|\mathbf{b}\|) &\equiv 2\rho_0\left[\frac{\partial\hat{\psi}}{\partial I_1} + 2\frac{\partial\hat{\psi}}{\partial I_2} + \frac{\partial\hat{\psi}}{\partial I_3}\right]_{\mathbf{c}=\mathbf{I}} \\
\Sigma_1(\|\mathbf{b}\|) &\equiv -\zeta_2(\|\mathbf{b}\|) - \frac{1}{2}\zeta_4(\|\mathbf{b}\|) + \Sigma_2(\|\mathbf{b}\|) \\
\Sigma_2(\|\mathbf{b}\|) &= \zeta_4(\|\mathbf{b}\|) + 4\rho_0\left[\left(\frac{\partial}{\partial\tilde{J}_2} + 2\frac{\partial}{\partial\tilde{J}_3}\right)\left(\frac{\partial\hat{\psi}}{\partial I_1} + 2\frac{\partial\hat{\psi}}{\partial I_2} + \frac{\partial\hat{\psi}}{\partial I_3}\right)\right]_{\mathbf{c}=\mathbf{I}} \\
\Sigma_3(\|\mathbf{b}\|) &\equiv -\zeta_4(\|\mathbf{b}\|) + 4\rho_0\left[\frac{\partial\hat{\psi}}{\partial\tilde{J}_3}\right]_{\mathbf{c}=\mathbf{I}} \\
\Sigma_4(\|\mathbf{b}\|) &\equiv -\zeta_3(\|\mathbf{b}\|) + 4\rho_0\left[\left(\frac{\partial}{\partial\tilde{J}_2} + 2\frac{\partial}{\partial\tilde{J}_3}\right)\left(\frac{\partial\hat{\psi}}{\partial\tilde{J}_2} + 2\frac{\partial\hat{\psi}}{\partial\tilde{J}_3}\right)\right]_{\mathbf{c}=\mathbf{I}}
\end{aligned}
\tag{B.5}
$$

and are expressed in terms of seven magnetic field-dependent coefficients: the two Lamé coefficients $\lambda(\|\mathbf{b}\|)$ and $G(\|\mathbf{b}\|)$ plus five more scalars $\Sigma_i(\|\mathbf{b}\|)$ , $i = 0, \cdots, 4$[1]. This expansion proves that in a first order approximation in $\boldsymbol{\epsilon}$, the coefficients in the expressions for $\mathfrak{m}$ and $\boldsymbol{\sigma}$ depend solely on $\|\mathbf{b}\|$. The fact that $\lambda$ and $G$ – and hence the Young's modulus $E$ – may depend on $\|\mathbf{b}\|$ is referred to as the $\Delta E$ *effect* (see e.g. Daniel and Hubert, 2009).

1 A further simplification is possible for small strains: since terms in $\zeta_1\boldsymbol{\epsilon}\mathbf{b}\mathbf{b}$ (respectively $\zeta_4\boldsymbol{\epsilon}\mathbf{b}\mathbf{b}$) are negligible in front of terms in $\zeta_1\mathbf{b}\mathbf{b}$ (respectively $\zeta_4\mathbf{b}\mathbf{b}$), one obtains $\Sigma_1 \approx -\zeta_2 + \Sigma_2$, $\Sigma_2 \approx 4\rho_0\left[\left(\frac{\partial}{\partial\tilde{J}_2} + 2\frac{\partial}{\partial\tilde{J}_3}\right)\left(\frac{\partial\hat{\psi}}{\partial I_1} + 2\frac{\partial\hat{\psi}}{\partial I_2} + \frac{\partial\hat{\psi}}{\partial I_3}\right)\right]_{\mathbf{c}=\mathbf{I}}$ and $\Sigma_3 \approx 4\rho_0\left[\frac{\partial\hat{\psi}}{\partial\tilde{J}_3}\right]_{\mathbf{c}=\mathbf{I}}$

### B.1.2 *Decoupled form of the free energy*

Under the additional hypothesis of additive decomposition for the specific free energy $\psi = \hat{\psi}_e(I_1, I_2, I_3) + \hat{\psi}_m(, \tilde{J}_1, \tilde{J}_2, \tilde{J}_3) + \hat{\psi}_{th}(T)$ in (2.23), one obtains the simplification $\zeta_2 = -\zeta_1$ yielding from (B.4) the following expression for the magnetization $\mathbf{m}$

$$\begin{aligned}
\mathbf{m} &= \zeta_1[1 - \mathrm{tr}(\boldsymbol{\epsilon})]\mathbf{b} + \zeta_3(\mathbf{b}\cdot\boldsymbol{\epsilon}\cdot\mathbf{b})\mathbf{b} + \zeta_4\boldsymbol{\epsilon}\cdot\mathbf{b}\,,\\
\zeta_1(\|\mathbf{b}\|) &= -2\rho_0\left[\frac{\partial\hat{\psi}_m}{\partial\tilde{J}_1} + \frac{\partial\hat{\psi}_m}{\partial\tilde{J}_2} + \frac{\partial\hat{\psi}_m}{\partial\tilde{J}_3}\right]_{\mathbf{c}=\mathbf{I}}\,,\\
\zeta_3(\|\mathbf{b}\|) &= -4\rho_0\left[\frac{\partial}{\partial\tilde{J}_2} + 2\frac{\partial}{\partial\tilde{J}_3}\right]\left[\frac{\partial\hat{\psi}_m}{\partial\tilde{J}_1} + \frac{\partial\hat{\psi}_m}{\partial\tilde{J}_2} + \frac{\partial\hat{\psi}_m}{\partial\tilde{J}_3}\right]_{\mathbf{c}=\mathbf{I}}\,,\\
\zeta_4(\|\mathbf{b}\|) &= -4\rho_0\left[\frac{\partial\hat{\psi}_m}{\partial\tilde{J}_2} + 2\frac{\partial\hat{\psi}_m}{\partial\tilde{J}_3}\right]_{\mathbf{c}=\mathbf{I}}\,.
\end{aligned} \tag{B.6}$$

The corresponding expressions for the elastic $\overset{e}{\boldsymbol{\sigma}}$, magnetic $\overset{m}{\boldsymbol{\sigma}}$ and magnetostrictive $\overset{ms}{\boldsymbol{\sigma}}$ components of the total stress $\boldsymbol{\sigma}$ simplify from their corresponding counterparts in (B.5) into

$$\begin{aligned}
\overset{e}{\boldsymbol{\sigma}} &= \lambda\,\mathrm{tr}(\boldsymbol{\epsilon})\mathbf{I} + 2G\boldsymbol{\epsilon}\,,\\
\overset{m}{\boldsymbol{\sigma}} &= \frac{1}{\mu_0}\left[\mathbf{b}\mathbf{b} - \frac{1}{2}(\mathbf{b}\cdot\mathbf{b})\mathbf{I}\right] - \zeta_1\left[\mathbf{b}\mathbf{b} - (\mathbf{b}\cdot\mathbf{b})\mathbf{I}\right] - \frac{\zeta_4}{2}\mathbf{b}\mathbf{b}\,,\\
\overset{ms}{\boldsymbol{\sigma}} &= \left[\Sigma_4\mathbf{b}\mathbf{b} + \zeta_3(\mathbf{b}\cdot\mathbf{b})\mathbf{I}\right](\mathbf{b}\cdot\boldsymbol{\epsilon}\cdot\mathbf{b}) + \Sigma_3\left[(\mathbf{b}\cdot\boldsymbol{\epsilon})\mathbf{b} + \mathbf{b}(\boldsymbol{\epsilon}\cdot\mathbf{b})\right]\,,
\end{aligned} \tag{B.7}$$

where the scalars $\zeta_1$, $\zeta_3$, $\zeta_4$ are given in (B.6) and $\Sigma_3$ and $\Sigma_4$ given in (B.5) but with $\hat{\psi}$ replaced by $\hat{\psi}_m$. In deriving (B.7) from (B.5) under the decoupling hypothesis, the pre-stress $\Sigma_0$ and the corresponding Lamé coefficients $\lambda, G$ are now constants independent of the magnetic field $\mathbf{b}$. It is further assumed that the elastic prestress $\Sigma_0 = 0$. Five functions of $\|\mathbf{b}\|$ are thus need to characterize the response of an isotropic, small strain, decoupled-energy, magnetoelastic material: $\zeta_1, \zeta_3, \zeta_4, \Sigma_3, \Sigma_4$.

A final remark is in order here to connect the above results to the constitutive equation in (2.25) that neglects the magnetostrictive stress component $\overset{ms}{\boldsymbol{\sigma}}$. The reason for this simplification is that for small strains ($\|\boldsymbol{\epsilon}\| \ll 1$) and assuming that the constants appearing in $\overset{m}{\boldsymbol{\sigma}}$ and $\overset{ms}{\boldsymbol{\sigma}}$ are of the same order of magnitude, one deduces that $\|\overset{ms}{\boldsymbol{\sigma}}\| \ll \|\overset{m}{\boldsymbol{\sigma}}\|$. In the field of dielectric elastomers – a completely analogous problem where $\boldsymbol{e} \to \mathbf{b}$, $\mathbf{p} \to \mathbf{m}$, $\varepsilon_0 \to \mu_0^{-1}$ – similar results that neglect the coupled terms are justified under the typical hypothesis of small strain and moderate electric field: $\boldsymbol{\epsilon} = O(\zeta)$, $\boldsymbol{e} = O(\sqrt{\zeta})$, where $\zeta$ a vanishingly small parameter (e.g. see Tian et al., 2012; Lefèvre and Lopez-Pamies, 2017). The two coefficients $\zeta_1$ and $\zeta_4$ needed for the determination of $\overset{m}{\boldsymbol{\sigma}}$ are related to the magnetic susceptibility $\chi(\|\mathbf{b}\|)$ and magnetostrictive coefficient $\Lambda(\|\mathbf{b}\|)$ by: $\zeta_1(\|\mathbf{b}\|) = \chi(\|\mathbf{b}\|)/[\mu_0(1+\chi(\|\mathbf{b}\|))]$ and $\zeta_4(\|\mathbf{b}\|) = -2\Lambda(\|\mathbf{b}\|)/[\mu_0(1+\chi(\|\mathbf{b}\|))]$.

## B.2 EXPERIMENTAL DETERMINATION OF THE MAGNETO-MECHANICAL COUPLING COEFFICIENT

Of all the material constants required for the constitutive model in (2.25) only the magneto-mechanical coupling coefficient $\Lambda$ in (2.25) is not readily available and needs to be found from experiments. Its determination is based here on results presented by Aydin et al., 2017 who provide analytical calculations as well as experimental data from Rekik, Hubert, and Daniel, 2014, for the uniaxial magnetostriction vs. the magnetic field for electrical steel samples under different levels of mechanical prestress; a schematic of the setup is depicted in Figure B.1 based on the description of the typical experimental setup from Belahcen et al., 2006.

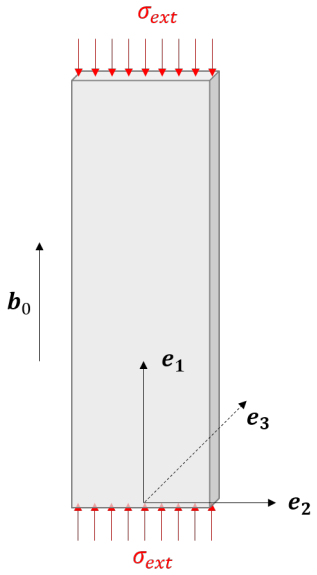


Figure B.1: Schematics of the magnetostriction setup.

A thin plate of electrical steel is subjected to an external magnetic field $b_0\hat{\mathbf{e}}_1$ along its axial direction, resulting in an axial magnetic field $b_1 = (1+\chi)b_0$ (assumed uniform) inside the specimen, where $\chi$ is the material's magnetic susceptibility[2]. The plate is also subjected to an externally applied uniaxial stress $\sigma_{ext}\hat{\mathbf{e}}_1\hat{\mathbf{e}}_1$ and hence the total stress $\boldsymbol{\sigma}$ is the sum of the applied stress and the Maxwell stress in vacuum due to the magnetic field $\mathbf{b}_0$

$$\boldsymbol{\sigma} = \overset{e}{\boldsymbol{\sigma}} + \overset{m}{\boldsymbol{\sigma}} = \sigma_{ext}\hat{\mathbf{e}}_1\hat{\mathbf{e}}_1 + \frac{1}{\mu_0}\left[\mathbf{b}_0\mathbf{b}_0 - \frac{1}{2}(\mathbf{b}_0\cdot\mathbf{b}_0)\mathbf{I}\right] \tag{B.8}$$

where the expressions for the elastic and magnetic part of the total stress are given by (2.25). The corresponding strain and the stress fields in the plate are assumed uniform with edge effects near the corners and edges of the plate neglected.

Consequently the resulting axial strain $\epsilon_{11}$ is made of an elastic component $\sigma_{ext}/E$ plus a component proportional to the square of the magnetic field strength $\zeta_m(b_1)^2$, where the curvature coefficient $\zeta_m$ depends on the magnetic constants

2 The materials used for holding the plate have no magnetic properties.

(susceptibility $\chi$ and magneto-mechanical coupling $\Lambda$). A straightforward calculation from (B.8) and (2.25), considering that the specimen's lateral strain is $\epsilon_{22} = \epsilon_{33}$, gives two independent equations

$$\begin{cases} (\lambda + 2G)\epsilon_{11} + 2\lambda\epsilon_{22} = \sigma_{ext} + \dfrac{(b_0)^2}{2\mu_0}\left[1 - (1+\chi)^2 - 2\Lambda(1+\chi)\right] , \\ \lambda\epsilon_{11} + 2(\lambda + G)\epsilon_{22} = -\dfrac{(b_0\chi)^2}{2\mu_0} , \end{cases} \tag{B.9}$$

where the Lamé constants are given in terms of Young's modulus $E$ and Poisson ratio $\nu$ by $G = E/2(1+\nu)$ and $\lambda = \nu E/(1+\nu)(1-2\nu)$. From (B.9) one obtains the sought relation between the axial strain, the external stress and the magnetic field as well as the expression for the curvature coefficient $\zeta_m$

$$\begin{aligned} &\epsilon_{11} = \frac{\sigma_{ext}}{E} + \zeta_m (b_1)^2 \, ; \\ &\zeta_m = \zeta_{m\chi} + \zeta_{m\Lambda} \, , \quad \zeta_{m\chi} \equiv -\frac{(\frac{1}{2} - \nu)\chi^2 + \chi}{E\mu_0(1+\chi)^2} \, , \; \zeta_{m\Lambda} \equiv \frac{-\Lambda}{E\mu_0(1+\chi)} \, . \end{aligned} \tag{B.10}$$

In decomposing the curvature $\zeta_m$ into a magnetic susceptibility $\zeta_{m\chi}$ and a magneto-mechanical $\zeta_{m\Lambda}$ component we follow the approach of Daniel et al., 2003[3] , where the coefficients $\zeta_{m\chi}$ and $\zeta_{m\Lambda}$ correspond respectively to the magnetic susceptibility $\chi$ and the magneto-mechanical coupling $\Lambda$ parts of the magnetic stress $\overset{m}{\boldsymbol{\sigma}}$ defined in (2.25).

For the no external stress case ($\sigma_{ext} = 0$) the data from Aydin et al., 2017, which are based on the approach adopted in Daniel et al., 2003, provide the same magneto-mechanical coupling curvature $\zeta_{m\Lambda} = 2\times10^{-6}$ T$^{-2}$ for the two materials analyzed. Unfortunately, the values for $\nu$ associated to these materials are not reported there. We assume typical values for steel: in the rotor problem (section 3.1) we consider $\nu = 0.34$, $E = 183$GPa and a magnetic susceptibility $\chi = 4\times10^3$, resulting in $\Lambda \approx -1.8\times10^3$ which is used in our calculations, as seen in Table 3.1. For the stator problem (section 3.2) we consider $\nu = 0.3$, $E = 215$GPa and a magnetic susceptibility $\chi = 2.5\times10^3$, resulting in $\Lambda \approx -1.3\times10^3$ which is used in our calculations, as seen in Table 3.14.

## B.3 THE COMPATIBILITY EQUATION AND ITS IMPLICATIONS FOR THE ROTOR AND STATOR BOUNDARY VALUE PROBLEMS

The strain-displacement relations for 2D problems in polar coordinates are,

$$\epsilon_{rr} = \frac{\partial u_r}{\partial r} \, ; \quad \epsilon_{\theta\theta} = \frac{1}{r}\left(\frac{\partial u_\theta}{\partial \theta} + u_r\right) \, ; \quad \epsilon_{r\theta} = \frac{1}{2}\left(\frac{1}{r}\frac{\partial u_r}{\partial \theta} + \frac{\partial u_\theta}{\partial r} - \frac{u_\theta}{r}\right) \, , \tag{B.11}$$

from which results the compatibility equation that strains need to verify[4]:

3 In Daniel et al., 2003 and subsequent work by this research group by "*pure magnetostrictive*" strains they refer to the strains due to the magneto-mechanical coupling $\Lambda$.

4 The reader is referred to Barber, 2010 §2.2 for additional information on the compatibility equation.

$$\frac{1}{r^2}\frac{\partial^2 \epsilon_{rr}}{\partial \theta^2} + \frac{\partial^2 \epsilon_{\theta\theta}}{\partial r^2} - \frac{2}{r}\frac{\partial^2 \epsilon_{r\theta}}{\partial r \partial \theta} - \frac{1}{r}\frac{\partial \epsilon_{rr}}{\partial r} + \frac{2}{r}\frac{\partial \epsilon_{\theta\theta}}{\partial r} - \frac{2}{r^2}\frac{\partial^2 \epsilon_{r\theta}}{\partial \theta} = 0\,. \tag{B.12}$$

In the rotor and stator problems, we look for a solution elastic stress field in the form,

$$\overset{e}{\boldsymbol{\sigma}} = \overset{e\,h}{\boldsymbol{\sigma}} + \overset{e\,p}{\boldsymbol{\sigma}}\,, \tag{B.13}$$

where $\overset{e\,h}{\boldsymbol{\sigma}}$ is the solution to the homogeneous stress equation $\boldsymbol{\nabla}\cdot\overset{e}{\boldsymbol{\sigma}} = 0$ and $\overset{e\,p}{\boldsymbol{\sigma}}$ is a particular solution to the complete stress equations (3.13) – rotor problem – and (3.45) – stator problem –.

Similarly the strain is decomposed into $\boldsymbol{\epsilon} = \boldsymbol{\epsilon}^h + \boldsymbol{\epsilon}^p$ where $\boldsymbol{\epsilon}$, $\boldsymbol{\epsilon}^h$ and $\boldsymbol{\epsilon}^p$ are linked to $\overset{e}{\boldsymbol{\sigma}}$, $\overset{e\,h}{\boldsymbol{\sigma}}$ and $\overset{e\,p}{\boldsymbol{\sigma}}$ via the stress-strain relationship. In 2D plane strains[5],

$$\begin{cases} \epsilon_{rr} = \dfrac{1+\nu}{E}\left((1-\nu)\sigma_{rr} - \nu\sigma_{\theta\theta}\right) \\ \epsilon_{\theta\theta} = \dfrac{1+\nu}{E}\left((1-\nu)\sigma_{\theta\theta} - \nu\sigma_{rr}\right) \\ \epsilon_{r\theta} = \dfrac{1+\nu}{E}\sigma_{r\theta} \end{cases} \tag{B.14}$$

The homogeneous solution elastic stress field $\overset{e\,h}{\boldsymbol{\sigma}}$ is found using the Airy stress function method. This method relies on the solution of the equations in (3.28) - rotor problem - and (3.54) - stator problem - on $\phi^h$. Because these equations derive from the compatibility equation for strains (see Barber, 2010 §4.4.1), the resulting strain field $\boldsymbol{\epsilon}^h$ associated to $\overset{e\,h}{\boldsymbol{\sigma}}$ is *compatible*[6]. Because the total strain $\boldsymbol{\epsilon}$ is required to be compatible, and $\boldsymbol{\epsilon}^h$ is compatible, then by transitivity the particular solution $\overset{e\,p}{\boldsymbol{\sigma}}$ should be such that the resulting strains $\boldsymbol{\epsilon}^p$ be *compatible* as well.

Given the stress equations in (3.13) - rotor problem - and (3.45) - stator problem - , it would be tempting to choose $\overset{e\,p}{\boldsymbol{\sigma}} = -\overset{m}{\boldsymbol{\sigma}}$ as a particular solution for the elastic stress field[7]. However, we verified[8] in both the rotor and stator problems that this solution leads to a *non-compatible* particular solution strain field $\boldsymbol{\epsilon}^p$. As such, the particular solution $\overset{e\,p}{\boldsymbol{\sigma}} = -\overset{m}{\boldsymbol{\sigma}}$ - to the electromagnetic part of the forcing - is not compatible with finding the homogeneous solution stress field from the Airy stress function method. Hence the methodology used in the rotor and stator problems of Section 3.1 and Section 3.2, which expresses the body force term $\overset{m}{\mathbf{f}} = -\boldsymbol{\nabla}\cdot\overset{m}{\boldsymbol{\sigma}}$ as the gradient of a potential $V$ - added to a directly integrable force term $\mathbf{N}$ in the case of the rotor problem -.

5 Here we provide the relations linking the true non-normalized stress and strain fields.
6 *Compatible* is to be understood as "fulfills the compatibility equation (B.12)"
7 All particular solution to the centrifugal forces set aside in the case of the rotor problem.
8 We computed the left hand side of (B.12), which would not equal 0 throughout the whole stator domain.

## B.4 STRESS AND DISPLACEMENT FIELDS FOR THE ROTOR BOUNDARY VALUE PROBLEM

The expressions for the stress and displacement fields solution to the rotor boundary value problem in Section 3.1 are detailed below.

### B.4.1 *Particular and homogeneous solution stress fields*

From (3.26) and (3.27), the particular solution stress field $\overset{e\,v}{\boldsymbol{\sigma}}$ components are

$$\begin{aligned}
\overset{e\,v}{\sigma}_{rr} &= V - \frac{1}{2}\frac{1-2\nu}{1-\nu}\left(\frac{2}{r^2}\int_0^r rV_0 dr - (2p-1)r^{2p-2}\int_0^r \frac{V_{cs}}{r^{2p-1}}dr + \frac{2p+1}{r^{2p+2}}\int_0^r r^{2p+1}V_{cs}dr\right)\\
\overset{e\,v}{\sigma}_{\theta\theta} &= \frac{\nu V}{1-\nu} + \frac{1}{2}\frac{1-2\nu}{1-\nu}\left(\frac{2}{r^2}\int_0^r rV_0 dr - (2p-1)r^{2p-2}\int_0^r \frac{V_{cs}}{r^{2p-1}}dr + \frac{2p+1}{r^{2p+2}}\int_0^r r^{2p+1}V_{cs}dr\right)\\
\overset{e\,v}{\sigma}_{r\theta} &= \frac{1}{2}\frac{1-2\nu}{1-\nu}\left((2p-1)r^{2p-2}\int_0^r \frac{V^*_{cs}}{r^{2p-1}}dr + \frac{2p+1}{r^{2p+2}}\int_0^r r^{2p+1}V^*_{cs}dr\right)
\end{aligned} \tag{B.15}$$

where $V^*_{cs} \equiv V_s\cos(2\Theta) - V_c\sin(2\Theta)$ and the $V$ potential components are given by (3.23).

From (3.28) and (3.29), the homogeneous solution stress field $\overset{e\,h}{\boldsymbol{\sigma}}$ components are (see Barber, 2010 Table 8.1)

$$\begin{aligned}
\overset{e\,h}{\sigma}_{rr} &= \Phi_{01} + \left((2p-4p^2)\Phi_{c1}r^{2p-2} + (2p+2-4p^2)\Phi_{c2}r^{2p}\right)\cos(2\Theta)\\
&\quad + \left((2p-4p^2)\Phi_{s1}r^{2p-2} + (2p+2-4p^2)\Phi_{s2}r^{2p}\right)\sin(2\Theta)\\
\overset{e\,h}{\sigma}_{\theta\theta} &= \Phi_{01} + \left(2p(2p-1)\Phi_{c1}r^{2p-2} + (2p+2)(2p+1)\Phi_{c2}r^{2p}\right)\cos(2\Theta)\\
&\quad + \left(2p(2p-1)\Phi_{s1}r^{2p-2} + (2p+2)(2p+1)\Phi_{s2}r^{2p}\right)\sin(2\Theta)\\
\overset{e\,h}{\sigma}_{r\theta} &= \frac{\Phi_{02}}{r^2} - \left(2p(2p-1)\Phi_{s1}r^{2p-2} + 2p(2p+1)\Phi_{s2}r^{2p}\right)\cos(2\Theta)\\
&\quad + \left(2p(2p-1)\Phi_{c1}r^{2p-2} + 2p(2p+1)\Phi_{c2}r^{2p}\right)\sin(2\Theta)
\end{aligned} \tag{B.16}$$

Application of the stress boundary condition in (3.30) provides the six $\Phi$ constants of integration in (B.16).

## B.5 STRESS AND DISPLACEMENT FIELDS FOR THE STATOR BOUNDARY VALUE PROBLEM

The expressions for the stress and displacement fields solution to the stator boundary value problem in Section 3.2 are detailed below.

### B.5.1 *Particular and homogeneous solution stress fields*

From (3.52) and (3.53), the particular solution stress field $\overset{e\,v}{\sigma}$ components are

$$\begin{aligned}
\overset{e\,v}{\sigma}_{rr} &= V - \frac{1}{2}\frac{1-2\nu}{1-\nu}\left(\frac{2}{r^2}\int_{r_2}^{r} rV_0 dr\right.\\
&\quad \left. - \left[(2p-1)r^{2p-2}\int_{r_2}^{r}\frac{V_c}{r^{2p-1}}dr - \frac{2p+1}{r^{2p+2}}\int_{r_2}^{r} r^{2p+1}V_c dr\right]\cos(2\Theta)\right)\\
\overset{e\,v}{\sigma}_{\theta\theta} &= \frac{\nu}{1-\nu}V + \frac{1}{2}\frac{1-2\nu}{1-\nu}\left(\frac{2}{r^2}\int_{r_2}^{r} rV_0 dr\right.\\
&\quad \left. - \left[(2p-1)r^{2p-2}\int_{r_2}^{r}\frac{V_c}{r^{2p-1}}dr - \frac{2p+1}{r^{2p+2}}\int_{r_2}^{r} r^{2p+1}V_c dr\right]\cos(2\Theta)\right)\\
\overset{e\,v}{\sigma}_{r\theta} &= -\frac{1}{2}\frac{1-2\nu}{1-\nu}\left[(2p-1)r^{2p-2}\int_{r_2}^{r}\frac{V_c}{r^{2p-1}}dr\right.\\
&\quad \left. + \frac{2p+1}{r^{2p+2}}\int_{r_2}^{r} r^{2p+1}V_c dr\right]\sin(2\Theta)
\end{aligned} \tag{B.17}$$

From (3.28) and (3.29), the homogeneous solution stress field $\overset{e\,h}{\sigma}$ components are (see Barber, 2010 Table 8.1)

$$\begin{aligned}
\overset{e\,h}{\sigma}_{rr} &= 2\Phi_{01} + \Phi_{02} + 2\Phi_{02}\ln(r) + \frac{\Phi_{03}}{r^2}\\
&\quad + \left[(-4p^2-2p+2)\Phi_{c1}r^{-2p} + (2p-4p^2)\Phi_{c2}r^{2p-2}\right.\\
&\quad \left. - (2p+4p^2)\Phi_{c3}r^{-2p-2} + (-4p^2+2p+2)\Phi_{c4}r^{2p}\right]\cos(2\Theta)\\
&\quad + \left[(-4p^2-2p+2)\Phi_{s1}r^{-2p} + (2p-4p^2)\Phi_{s2}r^{2p-2}\right.\\
&\quad \left. - (2p+4p^2)\Phi_{s3}r^{-2p-2} + (-4p^2+2p+2)\Phi_{s4}r^{2p}\right]\sin(2\Theta)
\end{aligned} \tag{B.18}$$

$$\begin{aligned}
\overset{e\,h}{\sigma}_{r\theta} &= \frac{\Phi_{04}}{r^2} - 2p\left[(-2p+1)\Phi_{s1}r^{-2p} + (2p-1)\Phi_{s2}r^{2p-2}\right.\\
&\quad \left. - (2p+1)\Phi_{s3}r^{-2p-2} + (2p+1)\Phi_{s4}r^{2p}\right]\cos(2\Theta)\\
&\quad + 2p\left[(-2p+1)\Phi_{c1}r^{-2p} + (2p-1)\Phi_{c2}r^{2p-2}\right.\\
&\quad \left. - (2p+1)\Phi_{c3}r^{-2p-2} + (2p+1)\Phi_{c4}r^{2p}\right]\sin(2\Theta)
\end{aligned} \tag{B.19}$$

$$\begin{aligned}
\overset{e\,h}{\sigma}_{\theta\theta} &= 2\Phi_{01} + 3\Phi_{02} + 2\Phi_{02}\ln(r) - \frac{\Phi_{03}}{r^2}\\
&\quad + \left[(-2p+2)(-2p+1)\Phi_{c1}r^{-2p} + 2p(2p-1)\Phi_{c2}r^{2p-2}\right.\\
&\quad + \left. 2p(2p+1)\Phi_{c3}r^{-2p-2} + (2p+2)(2p+1)\Phi_{c4}r^{2p}\right]\cos(2\Theta)\\
&\quad + \left[(-2p+2)(-2p+1)\Phi_{s1}r^{-2p} + 2p(2p-1)\Phi_{s2}r^{2p-2}\right.\\
&\quad + \left. 2p(2p+1)\Phi_{s3}r^{-2p-2} + (2p+2)(2p+1)\Phi_{s4}r^{2p}\right]\sin(2\Theta)
\end{aligned} \tag{B.20}$$

It is noticeable in these equations that the purely radius-dependent part of the stress component $\overset{e}{\sigma}_{rr}$ involves three constants: $\Phi_{01}, \Phi_{02}, \Phi_{03}$. The boundary conditions in (3.45) provides only 2 equations: one in $r = 1$, another in $r = r_3$. To solve for the integration constants, an additional equation is required. It is brought by the requirement that the tangent displacement $u_\theta$ be single valued in $\theta$, which imposes $\Phi_{02} = 0$ (see (B.23) and discussion below).

On the contrary, the stress boundary condition on $\overset{e}{\sigma}_{r\theta}$ in $r = 1$ and $r = r_3$ provide for the r-dependent part of the stress component two equation for one unknown $\Phi_{04}$. This is not inconsistent but due to a link between the boundary condition in $r = 1$ and $r = r_3$ through the magnetic field equations.

### B.5.2 *Displacement field*

In plane strain, the stress-strain relationship $\overset{e}{\boldsymbol{\sigma}} = \lambda \mathrm{tr}(\boldsymbol{\epsilon}) + 2G\boldsymbol{\epsilon}$ provides, for the normalized fields,

$$\begin{cases} (1-\nu)\overset{e}{\sigma}_{rr} - \nu\overset{e}{\sigma}_{\theta\theta} = \dfrac{\partial u_r}{\partial r} \\ -\nu\overset{e}{\sigma}_{rr} + (1-\nu)\overset{e}{\sigma}_{\theta\theta} = \dfrac{1}{r}\left(\dfrac{\partial u_\theta}{\partial \theta} + u_r\right) \\ \overset{e}{\sigma}_{r\theta} = \dfrac{1}{2}\left(\dfrac{1}{r}\dfrac{\partial u_r}{\partial \theta} + \dfrac{\partial u_\theta}{\partial r} - \dfrac{u_\theta}{r}\right) \end{cases} \tag{B.21}$$

By superposition, the displacement $\mathbf{u} = \mathbf{u}^V + \mathbf{u}^h$ associated respectively to stresses $\overset{e}{\boldsymbol{\sigma}}^V$ and $\overset{e}{\boldsymbol{\sigma}}^h$.

HOMOGENEOUS SOLUTION DISPLACEMENT FIELD The homogeneous solution normalized displacement field $\mathbf{u}^h$ is given by (see Barber, 2010 Table 9.1 to be read with $\kappa = 3 - 4\nu$ for plane strain),

$$\begin{aligned} u_r^h = {} & 2\Phi_{01}(1-2\nu)r + \Phi_{02}\left[2(1-2\nu)r\ln(r) - r\right] - \frac{\Phi_{03}}{r} \\ & + 2\Big[(1-2\nu+p)\Phi_{c1}r^{-2p+1} - p\Phi_{c2}r^{2p-1} \\ & + p\Phi_{c3}r^{-2p-1} + \Phi_{c4}(1-2\nu-p)r^{2p+1}\Big]\cos(2\theta) \\ & + 2\Big[(1-2\nu+p)\Phi_{s1}r^{-2p+1} - p\Phi_{s2}r^{2p-1} \\ & + p\Phi_{s3}r^{-2p-1} + \Phi_{s4}(1-2\nu-p)r^{2p+1}\Big]\sin(2\theta) \end{aligned} \tag{B.22}$$

$$
\begin{aligned}
u_\theta^h &= 2\Phi_{02}(2-2\nu)r\theta - \frac{\Phi_{04}}{r} \\
&+ 2\Big[(2-2\nu-p)\Phi_{s1}r^{-2p+1} - p\Phi_{s2}r^{2p-1} \\
&- p\Phi_{s3}r^{-2p-1} - \Phi_{s4}(2-2\nu+p)r^{2p+1}\Big]\cos(2\theta) \\
&- 2\Big[(2-2\nu-p)\Phi_{c1}r^{-2p+1} - p\Phi_{c2}r^{2p-1} \\
&- p\Phi_{c3}r^{-2p-1} - \Phi_{c4}(2-2\nu+p)r^{2p+1}\Big]\sin(2\theta)
\end{aligned}
\tag{B.23}
$$

As detailed in Barber, 2010 this solution discards rigid body motions. The requirement that $u_\theta = u_\theta^h + u_\theta^V$ ($u_\theta^V$ is given below) be single valued in $\theta$ imposes $\Phi_{02} = 0$.

PARTICULAR SOLUTION DISPLACEMENT FIELD Given the particular solution stress field (B.17) and (B.21), the sought solution $\mathbf{u}^V(r,\Theta)$ takes the form,

$$
u_r^V(r,\Theta) = u_r^{V0}(r) + u^{Vc}(r)\cos(2\Theta)\ ; \quad u_\theta^V(r,\Theta) = u_\theta^{Vs}(r)\sin(2\Theta) \tag{B.24}
$$

From $(B.21)_2$, given the form of $u_\theta$,

$$
u_r^{V0}(r) = r\left[(1-\nu)\overset{e}{\sigma}{}_{\theta\theta}^{V0} - \nu\overset{e}{\sigma}{}_{rr}^{V0}\right] = \frac{1-2\nu}{1-\nu}\frac{1}{r}\int_{r_2}^{r} rV_0 dr \tag{B.25}
$$

From $(B.21)_2$ given (B.24),

$$
u_\theta^{Vs} = \frac{1}{2p}\left[r\left((1-\nu)\overset{e}{\sigma}{}_{\theta\theta}^{c} - \nu\overset{e}{\sigma}{}_{rr}^{c}\right) - u_r^{Vc}\right] \tag{B.26}
$$

From $(B.21)_3$, given (B.26),

$$
u_r^{Vc} = \frac{1}{4p^2-1}\left[-4pr\overset{e}{\sigma}{}_{r\theta}^{Vs} + r^2\left((1-\nu)\frac{\partial\overset{e}{\sigma}{}_{\theta\theta}^{Vc}}{\partial r} - \nu\frac{\partial\overset{e}{\sigma}{}_{rr}^{Vc}}{\partial r}\right) - r\frac{\partial u_r^{Vc}}{\partial r}\right] \tag{B.27}
$$

The term $\frac{\partial u_r^{Vc}}{\partial r}$ is directly given by $(B.21)_1$, and the stress r-derivatives are computed from (B.17).

## B.6 STATOR PROBLEM: OTHER CONSTITUTIVE LAWS FOR STRESSES

### B.6.1 *Not accounting for the magnetostriction coefficent*

Additional results are presented for *Model 2* to which the results of *Model 1* is compared in Section 3.2.4. For *Model 2* we do not account for the magnetostriction term included in *Model 1* (case $\Lambda = 0$), such that the magnetic stress expression is,

$$
\overset{m}{\boldsymbol{\sigma}} = \frac{1}{\mu}\left(\mathbf{bb} - \frac{1}{2}(\mathbf{b}\cdot\mathbf{b})\mathbf{I}\right) + \frac{\chi}{\mu}(\mathbf{b}\cdot\mathbf{b})\mathbf{I} \tag{B.28}
$$

The stress boundary conditions are,

$$\partial\mathscr{D}_2 \cup \partial\mathscr{D}_3 : \quad \begin{cases} \overset{e}{\sigma}_{rr} = -\frac{1}{2}\mu_0\chi^2 h_\theta^2 \\ \overset{e}{\sigma}_{r\theta} = 0 \end{cases} \tag{B.29}$$

The stress equation we solve for stresses is (neglecting induced currents at the stator and thus the Lorentz force),

$$\mathscr{D}_3 : \quad \boldsymbol{\nabla}\cdot\overset{e}{\boldsymbol{\sigma}} = -\frac{\chi}{\mu}\mathbf{b}\cdot(\mathbf{b}\boldsymbol{\nabla}) \tag{B.30}$$

Figure B.2 pictures the total stress distribution at the stator in the same conditions and motor configuration than given in Table 3.14, save for $\Lambda = 0$ now. Figure 3.21 pictures the elastic stress field. Figure B.4 pictures the displacement field, with the deformation magnified 200 times showing the ovalization at the stator. The fields are normalized by the reference stress $\sigma_{ref}$ and reference displacement $u_{ref}$ introduced in (3.42).

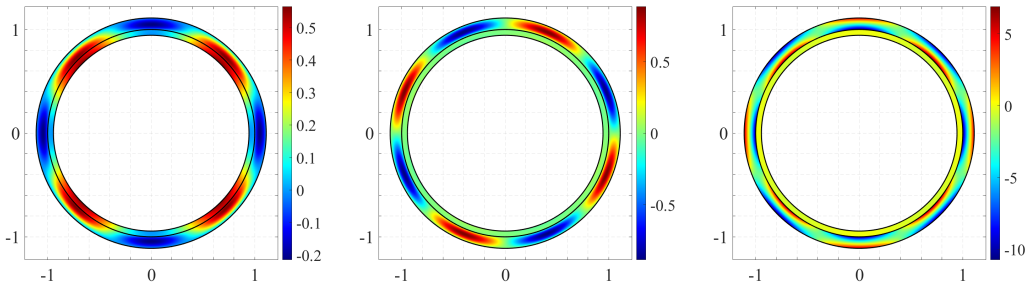

(a) $\frac{\sigma_{rr}(r,\Theta)}{\sigma_{ref}}$ (b) $\frac{\sigma_{r\theta}(r,\Theta)}{\sigma_{ref}}$ (c) $\frac{\sigma_{\theta\theta}(r,\Theta)}{\sigma_{ref}}$

Figure B.2: Normalized total stresses in stator, in the case $\Lambda = 0$ (*Model 2*): (a) normal, (b) shear and (c) hoop.

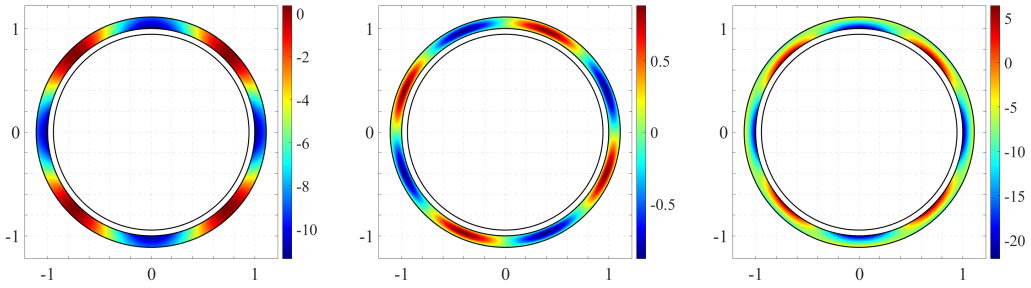

(a) $\frac{\overset{e}{\sigma}_{rr}(r,\Theta)}{\sigma_{ref}}$ (b) $\frac{\overset{e}{\sigma}_{r\theta}(r,\Theta)}{\sigma_{ref}}$ (c) $\frac{\overset{e}{\sigma}_{\theta\theta}(r,\Theta)}{\sigma_{ref}}$

Figure B.3: Normalised elastic stresses in stator, in the case $\Lambda = 0$ (*Model 2*): (a) normal, (b) shear and (c) hoop.

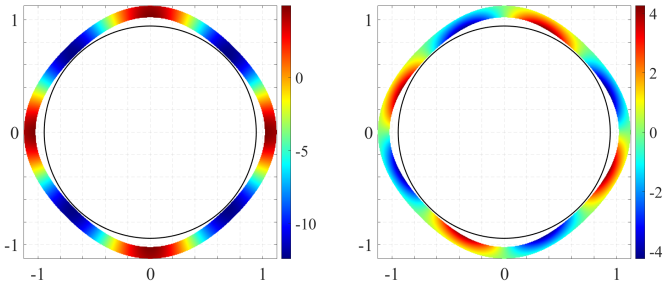


(a) $\frac{u_r(r,\Theta)}{u_{ref}}$ (b) $\frac{u_\theta(r,\Theta)}{u_{ref}}$

Figure B.4: Normalized displacements in stator, magnified 4 $10^6$ times, in the case $\Lambda = 0$ (*Model 2*): (a) radial, (b) tangent. The central circle pictures the rotor boundary $\partial\mathscr{D}_1$.

### B.6.2 *An other typical model found in the literature: the Maxwell Tensor model*

Additional results are presented for *Model 3* to which the results of our model is compared in Section 3.2.4. For this typical model found in the literature (Pile et al., 2019a; Pile et al., 2019b) and to which the results of our model is compared to in Section 3.2.4,

$$\overset{m}{\boldsymbol{\sigma}} = \frac{1}{\mu}\left(\mathbf{b}\mathbf{b} - \frac{1}{2}(\mathbf{b}\cdot\mathbf{b})\mathbf{I}\right) \tag{B.31}$$

The stress boundary conditions are,

$$\partial\mathscr{D}_2 \cup \partial\mathscr{D}_3 : \quad \begin{cases} \overset{e}{\sigma}_{rr} = \frac{1}{2}\frac{\chi}{\mu}b_r^2 + \frac{1}{2}\mu_0\chi h_\theta^2 \\ \overset{e}{\sigma}_{r\theta} = 0 \end{cases} \tag{B.32}$$

The stress equation we solve for is,

$$\mathscr{D}_3 : \quad \boldsymbol{\nabla}\cdot\overset{e}{\boldsymbol{\sigma}} = 0 \tag{B.33}$$

Figure B.5 pictures the total stress distribution at the stator in the same conditions and motor configuration than given in Table 3.14. Figure B.6 pictures the elastic stress field. Figure B.7 pictures the displacement field, with the deformation magnified 200 times showing the ovalization at the stator. The fields are normalized by the reference stress $\sigma_{ref}$ and reference displacement $u_{ref}$ introduced in (3.42). It is striking to note that the no stator current hypothesis, leading to $\boldsymbol{\nabla}\cdot\overset{m}{\boldsymbol{\sigma}} = 0$ implies $\overset{m}{\boldsymbol{\sigma}} = 0$ given the same results for $\overset{e}{\boldsymbol{\sigma}}$ and $\boldsymbol{\sigma}$ shown by Figures B.5 and B.6.

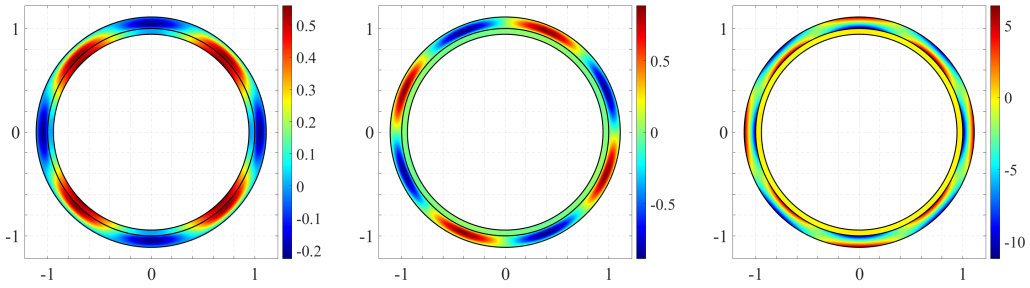

(a) $\frac{\sigma_{rr}(r,\Theta)}{\sigma_{ref}}$ (b) $\frac{\sigma_{r\theta}(r,\Theta)}{\sigma_{ref}}$ (c) $\frac{\sigma_{\theta\theta}(r,\Theta)}{\sigma_{ref}}$

Figure B.5: Normalized total stresses in stator, for the comparison model found in the literature (*Model 3*): (a) normal, (b) shear and (c) hoop.

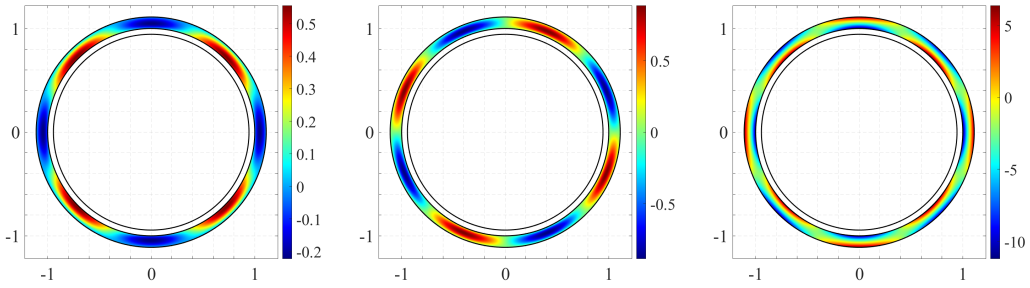

(a) $\frac{\overset{e}{\sigma}_{rr}(r,\Theta)}{\sigma_{ref}}$ (b) $\frac{\overset{e}{\sigma}_{r\theta}(r,\Theta)}{\sigma_{ref}}$ (c) $\frac{\overset{e}{\sigma}_{\theta\theta}(r,\Theta)}{\sigma_{ref}}$

Figure B.6: Normalised elastic stresses in stator, for the comparison model found in the literature (*Model 3*): (a) normal, (b) shear and (c) hoop.

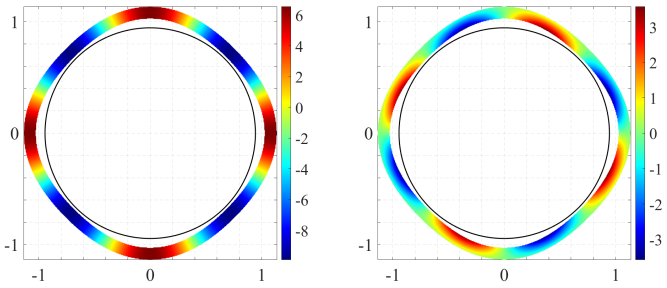

(a) $\frac{u_r(r,\Theta)}{u_{ref}}$ (b) $\frac{u_\theta(r,\Theta)}{u_{ref}}$

Figure B.7: Normalized displacements in stator, magnified 4 $10^6$ times, for the comparison model found in the literature (*Model 3*): (a) radial, (b) tangent. The central circle pictures the rotor boundary $\partial\mathscr{D}_1$.

# C

# FURTHER DETAILS REGARDING THE NUMERICAL IMPLEMENTATION

## C.1 CHOICE OF A SPECIFIC FREE ENERGY

The choice of the magnetic specific free energy $\psi_{mag}$ in Section 6.2 was arrived at after a few iterations detailed below.

At first, a specific free energy model from Danas, 2017 was taken. The constitutive equations for the magnetization and stress field in small strains and small magnetic field (linear regime) were derived and compared to the expressions in Section 2.2. Because the stress expressions did not match, a second model for $\psi_{mag}$ was derived, matching both the small strain magnetization and stress expressions in Section 2.2. The small strain and small magnetic field magnetization curve was then compared to typical values for electrical steel (Aydin et al., 2017)[1]. A mismatch was observed leading to the final model for $\psi_{mag}$ in Section 6.2 including a correction factor $\alpha_s$.

### C.1.1 *First model - the Langevin model*

One first possibility for the magneto-mechanical part of the free specific energy is to use a Langevin model, which reads with the current configuration fields (Danas, 2017)

$$\rho_0\psi_{mag}(\mathbf{F},\mathbf{b}) = \frac{m_s}{A}J\left[\ln(A\sqrt{\mathbf{b}\cdot\mathbf{b}}) - \ln(\sinh(A\sqrt{\mathbf{b}\cdot\mathbf{b}}))\right] \;;\quad A = \frac{3}{m_s}\frac{\chi}{\mu} \tag{C.1}$$

Note that this model for $\psi_{mag}$ presents a magneto-mechanical coupling through the $J = \det(\mathbf{F})$ factor.

The first order derivatives of $\psi_{mag}$ are,

$$\begin{aligned}
&\rho\frac{\partial\psi_{mag}}{\partial\mathbf{b}} = -m_s A\left[\frac{1}{A\sqrt{\mathbf{b}\cdot\mathbf{b}}} - \frac{1}{\tanh(A\sqrt{\mathbf{b}\cdot\mathbf{b}})}\right]\frac{\mathbf{b}}{\|\mathbf{b}\|}\\
&\rho\mathbf{F}\cdot\left(\frac{\partial\psi_{mag}}{\partial\mathbf{F}}\right)^{T} = m_s\left[\ln(A\sqrt{\mathbf{b}\cdot\mathbf{b}}) - \ln(\sinh(A\sqrt{\mathbf{b}\cdot\mathbf{b}}))\right]\mathbf{I}
\end{aligned} \tag{C.2}$$

The expressions for the magnetization and the magnetic part of the stress $\overset{m}{\boldsymbol{\sigma}} = \boldsymbol{\sigma} - \overset{e}{\boldsymbol{\sigma}}$ that derive from $\psi_{mag}$ are obtained using (2.9). In the small magnetic field and small strain regime, we show

$$\begin{aligned}
&\mathbf{m} = -\frac{\chi}{\mu}\mathbf{b} + O(\|\mathbf{b}\|^3)\\
&\overset{m}{\boldsymbol{\sigma}} = \frac{1}{\mu}\left(\mathbf{b}\mathbf{b} - \frac{1}{2}(\mathbf{b}\cdot\mathbf{b})\mathbf{I}\right) + O(\|\mathbf{b}\|^4)
\end{aligned} \tag{C.3}$$

1 We compare to the magnetization curves obtained in the zero pre-stress case.

Comparing with the small strain linear magnetic field expressions in (2.25), the correct expression is retrieved for $\mathbf{m}$ but the expression $\overset{m}{\boldsymbol{\sigma}}$ does not match. Working with the second tanh model provided in Danas, 2017 leads to the same small strain small magnetic field expressions (C.3). This justifies the investigation of the choice for $\psi_{mag}$ in (C.4), where the J factor is dropped compared to (C.1).

Note that in the Langevin model, given the $\overset{m}{\boldsymbol{\sigma}}$ expression (C.3) the magnetic force $\overset{m}{\mathbf{f}}$ is reduced to the Lorentz force only following 2.2.2.

### C.1.2 *Second model - modified Langevin model*

In order to retrieve both magnetization and stress expressions matching (2.25), we propose to amend the Langevin model of section (C.1.1) by taking out the J factor, leading to the modified Langevin-type formulation

$$\rho_0\psi_{mag}(\mathbf{b}) = \frac{m_s}{A}\left[\ln(A\sqrt{\mathbf{b}\cdot\mathbf{b}}) - \ln(\sinh(A\sqrt{\mathbf{b}\cdot\mathbf{b}}))\right] \;; \quad A = \frac{3}{m_s}\frac{\chi}{\mu} \tag{C.4}$$

This model for $\psi_{mag}$ no longer presents the magneto-mechanical coupling through the $J = \det(\mathbf{F})$ factor such that this formulation in terms of the Eulerian field $\mathbf{b}$ is independent of the deformation gradient $\mathbf{F}$. It is coupled in $\mathbf{C}$ and $\mathbf{B} = J\mathbf{F}^{-1}\cdot\mathbf{b}$ however when written in terms of the Lagrangian fields.

The first order derivatives of $\psi_{mag}$ are then,

$$\rho\frac{\partial\psi_{mag}}{\partial\mathbf{b}} = -m_s A\left[\frac{1}{A\sqrt{\mathbf{b}\cdot\mathbf{b}}} - \frac{1}{\tanh(A\sqrt{\mathbf{b}\cdot\mathbf{b}})}\right]\frac{\mathbf{b}}{\|\mathbf{b}\|} \;; \quad \rho\mathbf{F}\cdot\left(\frac{\partial\tilde{\psi}_{mag}}{\partial\mathbf{F}}\right)^{T} = 0 \tag{C.5}$$

such that the expressions for the magnetization and the magnetic part of the stress $\overset{m}{\boldsymbol{\sigma}} = \boldsymbol{\sigma} - \overset{e}{\boldsymbol{\sigma}}$ lead to the expected relations (2.25) in the small magnetic field and small strain regime,

$$\begin{aligned}
\mathbf{m} &= -\frac{\chi}{\mu}\mathbf{b} + O(\|\mathbf{b}\|^3)\\
\overset{m}{\boldsymbol{\sigma}} &= \frac{1}{\mu}\left(\mathbf{b}\mathbf{b} - \frac{1}{2}(\mathbf{b}\cdot\mathbf{b})\mathbf{I}\right) + \frac{\chi}{2\mu}(\mathbf{b}\cdot\mathbf{b})\mathbf{I} + O(\|\mathbf{b}\|^4)
\end{aligned} \tag{C.6}$$

One question remains: how do these expressions fit with typical experimental data in particular concerning the ferromagnetic electrical steels we hope to model. This comparison is provided in Section C.1.3.

### C.1.3 *Comparison with experimental data*

Comparison was made with the magnetization data available in Aydin et al., 2017 for typical electrical steel. It is presented in Figure C.1 where we plot the experimental b-h curve at zero pre-stress obtained for M330-50A grade electrical steel (Figure 1 of Aydin et al., 2017)[2], and the b-h curve obtained with the modified

2 The experimental b-h curve data from Aydin et al., 2017 was retrieved from the plots pictured in the article using a plot digitizer.

Langevin model (C.4). The material parameters used for the calculation, all provided in Aydin et al., 2017 are: the magnetic susceptibility $\chi = 2.15\ 10^3$, the material magnetic permeability $\mu = \mu_0(1+\chi)$, and the magnetization at saturation $m_s = 1.25\ 10^6$. The results show that the modified Langevin model does not increase rapidly enough with $\|\mathbf{h}\|$. For that reason, we introduce a correction factor $\alpha_s$ that multiplies the magnetization at saturation $m_s$ such that the specific free energy,

$$\rho_0\psi_{mag}(\mathbf{b}) = \frac{\alpha_s^2 m_s}{A}\left[\ln\left(\frac{A}{\alpha_s}\sqrt{\mathbf{b}\cdot\mathbf{b}}\right) - \ln\left(\sinh\left(\frac{A}{\alpha_s}\sqrt{\mathbf{b}\cdot\mathbf{b}}\right)\right)\right] \ ; \ A = \frac{3}{m_s}\frac{\chi}{\mu} \ . \quad \text{(C.7)}$$

This model is additionally plotted in Figure C.1. A correction factor $\alpha_s = 35$ provides a satisfying match to the M350-50A grade steel data from (Aydin et al., 2017). Note that the match is valid in the range of the experimental data provided in the article: $\|\mathbf{b}\| \in [0, 1.1\text{T}]$. At large magnetic fields however, the data may lack accuracy given the model (C.7) tends to $\alpha_s$ times the magnetization at saturation $m_s$.

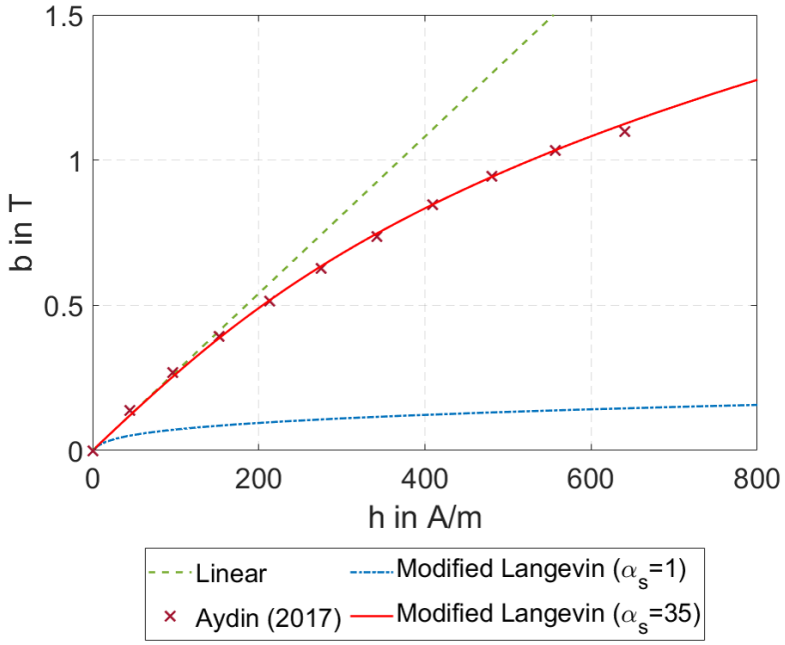


Figure C.1: Comparison of the b-h curves obtained for various models with experimental data for M350-50A grade electrical steel from Aydin et al., 2017.

### C.1.4 *Other literature references*

Various formulations are available for modeling the magnetization of anhysteretic isotropic ferromagnetic materials. Following the pioneering work of Langevin, P., 1905, these formulations do rely on Langevin functions - or associated tanh, sigmoid or double Langevin models -. However they all describe the magnetization as a function of the $\mathbf{h}$-field (Langevin, P., 1905; Steentjes et al., 2017), or even an equivalent $\mathbf{h}$-field that accounts for the coupling of domain magnetization with the bulk magnetization as in the seminal work of Jiles and Atherton, 1986. Such formulations in $\mathbf{h}$ were not straightforward to integrate in the proposed FEM code based on the Lagrangian $\mathbf{B}$ field. Other formulations are proposed in the form of

Taylor expansions with respects to the isotropic invariants however in small strains and involving a significant number of parameters (Aydin et al., 2017). These reasons motivated the choice of the simpler functional (C.7), with its correction factor to fit at best experimental magnetization curves at least on magnetic field values up to around 1T.

## C.2 FREE-ENERGY DERIVATIVES

This appendix provides the first and second order derivatives of the volume free energy $W = \rho_0 \psi$ needed in the FEM code. They are based on the specific-free-energy definition in (6.17), (6.18) and (6.19).

### C.2.1 *Derivatives for* $\psi_{mech}$

$$\begin{aligned} \frac{\partial W_{mech}}{\partial I_1} &= \frac{G}{2}\,; \qquad \frac{\partial W_{mech}}{\partial I_2} = \frac{\lambda}{2}\left(1 - \frac{1}{\sqrt{I_2}}\right) - \frac{G}{2I_2} \\ \frac{\partial^2 W_{mech}}{\partial {I_2}^2} &= -\frac{\lambda}{4I_2\sqrt{I_2}} - \frac{G}{2I_2^2} \end{aligned} \tag{C.8}$$

### C.2.2 *Derivatives for* $\psi_{mag}$

To lighten the following expressions, we define $X \equiv \frac{A}{\alpha_s}\sqrt{\frac{J_2}{I_2}}$ (recall $A \equiv \frac{3\chi}{\mu m_s}$), and we have

$$\begin{aligned} \frac{\partial W_{mag}}{\partial I_2} &= -\frac{\alpha_s^2 m_s}{A}\frac{X}{2I_2}\left[\frac{1}{X} - \frac{1}{\tanh(X)}\right] \\ \frac{\partial W_{mag}}{\partial J_2} &= \frac{m_s A}{2I_2 X}\left[\frac{1}{X} - \frac{1}{\tanh(X)}\right] \\ \frac{\partial^2 W_{mag}}{\partial I_2^2} &= \frac{\alpha_s^2 m_s}{A}\frac{1}{4I_2^2}\left[2 - 3\frac{X}{\tanh(X)} + \frac{X^2}{\tanh^2(X)} - X^2\right] \\ \frac{\partial^2 W_{mag}}{\partial J_2^2} &= -\frac{\alpha_s^2 m_s A^3}{4I_2^2 X^2}\left[\frac{2}{X^2} - \frac{1}{X\tanh(X)} - \frac{1}{\tanh^2(X)} + 1\right] \\ \frac{\partial^2 W_{mag}}{\partial J_2 \partial I_2} &= -\frac{m_s A}{4I_2^2}\left[-\frac{1}{X\tanh(X)} + \frac{1}{\tanh^2(X)} - 1\right] \end{aligned} \tag{C.9}$$

When $\mathbf{b}$ tends to zero, i.e. $J_2$ tends to zero, a Taylor expansion of the derivatives in (C.9) provides,

$$\begin{aligned}
\frac{\partial W_{mag}}{\partial I_2} &= -\frac{\alpha_s^2 m_s}{2 I_2 A}\left(-\frac{X^2}{3}+\frac{X^4}{45}\right)+O(X^6)\\
\frac{\partial W_{mag}}{\partial J_2} &= \frac{m_s A}{2 I_2}\left(-\frac{1}{3}+\frac{X^2}{45}-\frac{2X^4}{945}\right)+O(X^6)\\
\frac{\partial^2 W_{mag}}{\partial I_2^2} &= \frac{\alpha_s^2 m_s}{A}\frac{1}{4 I_2^2}\left(-\frac{4}{3}X^2\right)+O(X^4)\\
\frac{\partial^2 W_{mag}}{\partial J_2^2} &= -\frac{\alpha_s^2 m_s A^3}{4 I_2^2}\left(-\frac{2}{45}+\frac{8X^2}{945}\right)+O(X^4)\\
\frac{\partial^2 W_{mag}}{\partial J_2 \partial I_2} &= -\frac{m_s A}{4 I_2^2}\left(-\frac{2}{3}+4\frac{X^2}{45}\right)+O(X^4)
\end{aligned} \tag{C.10}$$

These expressions are used in the FEM code in the limit $\|\mathbf{b}\| < \zeta$, $\zeta$ a small parameter, as the code cannot evaluate the expressions in (C.9) for arbitrarily small values of $\mathbf{b}$ because of diverging terms. For consistency of the equations, the first order derivatives have to be Taylor expanded to one order higher in $X^2$ than the second order derivatives.

### C.2.3 *Derivatives of the invariants*

We also provide the derivatives of the invariants with respect to $(\mathbf{C}, \mathbf{B})$:

$$\begin{aligned}
&\frac{\partial I_1}{\partial \mathbf{C}} = \mathbf{I}\,; \qquad \frac{\partial I_2}{\partial \mathbf{C}} = I_2 \mathbf{C}^{-1}\,; \qquad \frac{\partial J_2}{\partial \mathbf{C}} = \mathbf{B}\mathbf{B}\,;\\
&\frac{\partial J_1}{\partial \mathbf{B}} = 2\mathbf{B}\,; \qquad \frac{\partial J_2}{\partial \mathbf{B}} = 2\mathbf{C}\cdot\mathbf{B}
\end{aligned} \tag{C.11}$$

## C.3 DERIVATIVES OF THE ENERGY P

The derivatives of P with respect to $(\mathbf{F}, \mathbf{B})$ are associated to the derivative of the energy $W$ through, for first order derivatives,

$$\begin{aligned}
\frac{\partial P}{\partial F_{kl}} &= \frac{\partial W}{\partial F_{kl}} + \frac{1}{2\mu_0 J}\left[\frac{\partial J_3}{\partial F_{kl}} - \frac{J_3}{2 I_3}\frac{\partial I_3}{\partial F_{kl}}\right]\\
\frac{\partial P}{\partial B_k} &= \frac{\partial W}{\partial B_k} + \frac{1}{2\mu_0 J}\frac{\partial J_3}{\partial B_k}
\end{aligned} \tag{C.12}$$

and for second order derivatives,

$$\begin{aligned}
\frac{\partial^2 P}{\partial F_{ij}\partial F_{kl}} &= \frac{\partial W}{\partial F_{ij}\partial F_{kl}} + \frac{1}{2\mu_0 J}\left[\frac{\partial^2 J_3}{\partial F_{ij}\partial F_{kl}} - \frac{1}{2I_3}\frac{\partial J_3}{\partial F_{ij}}\frac{\partial I_3}{\partial F_{kl}}\right. \\
&\quad + \frac{J_3}{2I_3^2}\frac{\partial I_3}{\partial F_{ij}}\frac{\partial I_3}{\partial F_{kl}} - \frac{J_3}{2I_3}\frac{\partial^2 I_3}{\partial F_{ij}\partial F_{kl}} \\
&\quad \left. - \frac{1}{2I_3}\left[\frac{\partial J_3}{\partial F_{kl}} - \frac{J_3}{2I_3}\frac{\partial I_3}{\partial F_{kl}}\right]\frac{\partial I_3}{\partial F_{ij}}\right] \\
\frac{\partial^2 P}{\partial B_i \partial B_j} &= \frac{\partial^2 W}{\partial B_i \partial B_j} + \frac{1}{2\mu_0 J}\frac{\partial^2 J_3}{\partial B_i \partial B_j} \\
\frac{\partial^2 P}{\partial F_{ij}\partial B_k} &= \frac{\partial^2 W}{\partial F_{ij}\partial B_k} + \frac{1}{2\mu_0 J}\left[\frac{\partial^2 J_3}{\partial F_{ij}\partial B_k} - \frac{1}{2I_3}\frac{\partial I_3}{\partial F_{ij}}\frac{\partial J_3}{\partial B_k}\right]
\end{aligned} \tag{C.13}$$

The derivatives of the total free energy $W$ with respect to $(\mathbf{F}, \mathbf{B})$ is linked to its derivatives with respect to the invariants through,

$$\begin{aligned}
\frac{\partial W}{\partial F_{ij}\partial F_{kl}} &= \frac{\partial^2 W}{\partial I_\alpha \partial I_\beta}\frac{\partial I_\alpha}{\partial F_{kl}}\frac{\partial I_\beta}{\partial F_{ij}} + \frac{\partial W}{\partial I_\alpha}\frac{\partial^2 I_\alpha}{\partial F_{ij}\partial F_{kl}} \\
\frac{\partial^2 W}{\partial B_i \partial B_j} &= \frac{\partial^2 W}{\partial I_\alpha \partial I_\beta}\frac{\partial I_\alpha}{\partial B_i}\frac{\partial I_\beta}{\partial B_j} + \frac{\partial W}{\partial I_\alpha}\frac{\partial^2 I_\alpha}{\partial B_i \partial B_j} \\
\frac{\partial^2 W}{\partial F_{ij}\partial B_k} &= \frac{\partial^2 W}{\partial I_\alpha \partial I_\beta}\frac{\partial I_\beta}{\partial F_{ij}}\frac{\partial I_\alpha}{\partial B_k} + \frac{\partial W}{\partial I_\alpha}\frac{\partial^2 I_\alpha}{\partial F_{ij}\partial B_k}
\end{aligned} \tag{C.14}$$

Finally, the derivatives of the invariants of the problem $I_1, I_2, J_2$ given in 6.16 with respect to $(\mathbf{F}, \mathbf{B})$ are, for first order derivatives,

$$\begin{aligned}
&\frac{\partial I_1}{\partial F_{kl}} = 2F_{kl}\,; \qquad \frac{\partial I_2}{\partial F_{kl}} = 2I_2 F^{-1}_{lk}\,; \qquad \frac{\partial J_2}{\partial F_{kl}} = 2F_{km}B_m B_l\,; \\
&\frac{\partial J_2}{\partial B_k} = 2C_{km}B_m
\end{aligned} \tag{C.15}$$

and for second order derivatives,

$$\begin{aligned}
&\frac{\partial^2 I_1}{\partial F_{ij}\partial F_{kl}} = 2\delta_{ik}\delta_{jl}\,; \qquad \frac{\partial^2 I_3}{\partial F_{ij}\partial F_{kl}} = 2I_3\left[2F^{-1}_{ji}F^{-1}_{lk} - F^{-1}_{jk}F^{-1}_{il}\right]\,; \\
&\frac{\partial^2 J_3}{\partial F_{ij}\partial F_{kl}} = 2\delta_{ik}B_j B_l\,; \qquad \frac{\partial^2 J_3}{\partial B_k \partial B_l} = 2C_{kl}\,; \\
&\frac{\partial^2 J_3}{\partial F_{ij}\partial B_k} = 2\delta_{kj}F_{im}B_m + 2F_{ik}B_j
\end{aligned} \tag{C.16}$$

## C.4 MESH CONVERGENCE STUDY FOR THE REFINED STATOR PROBLEM

Three mesh configurations were tested for mesh convergence analysis of the refined stator model from Section 7.2.

- Coarse mesh: 5,822 elements, with uniform approximate global size 1mm. Computation ran in 2.2s CPU time.
- Fine mesh: 22,182 elements, with uniform approximate global size 0.5mm. Computation ran in 8.5s CPU time.

- Extrafine mesh: 86,604 elements, with uniform approximate global size 0.25mm. Computation ran in 39s CPU time.

For size comparison, recall the airgap size a teeth tip is 3mm. The parameters, inputs and boundary conditions used for the computations are those presented in Section 7.2.

In the following, we compare the results obtained for the nodal variables $A$, $u_r$, $u_\theta$, together with the derived magnetic and stress fields $B_r$, $B_\theta$, $\Pi_{rr}$, $\Pi_{r\theta}$, $\Pi_{\theta\theta}$, for a section $\theta = 30°$, i.e. at the center line passing through the second bottom stator teeth. The path is highlighted in orange on Figure C.2. This section is presumed representative of the whole problem.

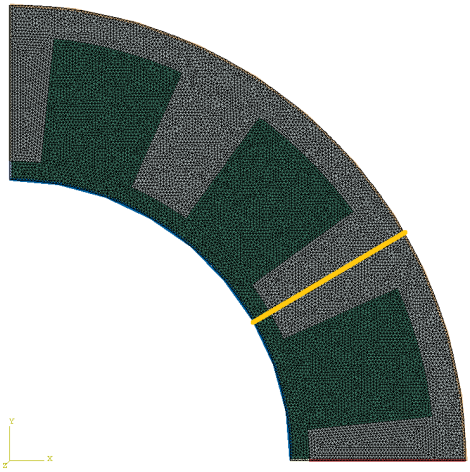

Figure C.2: In orange, path along which the fields are evaluated for mesh convergence analysis, here plotted on the fine mesh.

NODAL VARIABLES Figures C.3 compares the results obtained for the nodal variables of the problem $A$, $u_r$, $u_\theta$ (of the reference configuration) for the different mesh fineness. It shows that the magnetic potential $A$ is predicted with very good accuracy with the coarse mesh and does not require further refinement. For the displacement fields however, the coarse mesh results are slightly too inaccurate. Despite slight differences with the results obtained with the extrafine mesh, the fine mesh is a satisfying compromise.

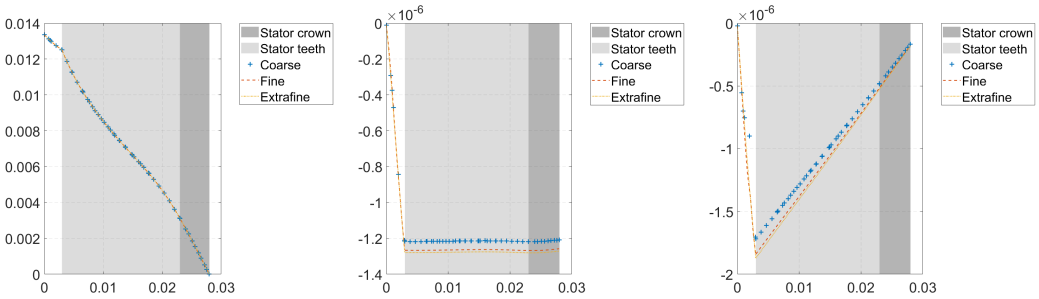


(a) Magnetic potential $A$ (b) Displacement $u_r$ (c) Displacement $u_\theta$

Figure C.3: Refined stator: FEM results for the nodal variables along the path $\theta = 30°$, for different mesh fineness. Variables are plotted against the path length from 0 at rotor radius, to 28mm at the stator external radius.

DERIVED MAGNETIC AND STRESS FIELDS Figures C.4, C.5 show the results obtained for the derived magnetic and stress fields (of the reference configuration) for the different mesh fineness. It shows that the results are much less sensitive to the mesh fineness than the results for the nodal variables. The most important differences are near the boundaries or interface of the problem or near the peak regions for the fields were the coarse mesh shows slight inaccuracies.

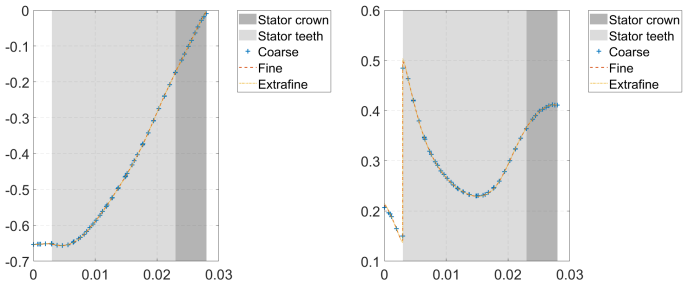


(a) Magnetic field $B_r$ (b) Magnetic field $B_\theta$

Figure C.4: Refined stator: FEM results for the magnetic field along the path $\theta = 30°$, for different mesh fineness. Variables are plotted against the path length from 0 at rotor radius, to 28mm at the stator external radius.

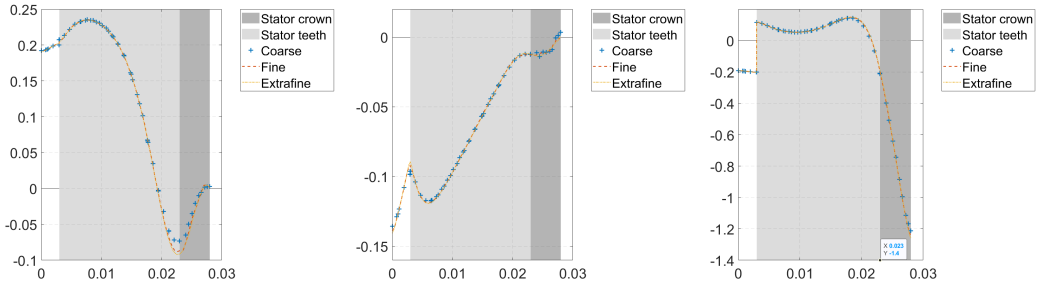


(a) $\frac{\Pi_{rr}}{\mu_0 m_s^2}$ (b) $\frac{\Pi_{r\theta}}{\mu_0 m_s^2}$ (c) $\frac{\Pi_{\theta\theta}}{\mu_0 m_s^2}$

Figure C.5: Refined stator: FEM results for the nodal variables along the path $\theta = 30°$, for different mesh fineness. Variables are plotted against the path length from 0 at rotor radius, to 28mm at the stator external radius.

CONCLUSION Overall, the coarse mesh is slightly poor. Given the result differences between the fine and extrafine mesh are very narrow, the fine mesh is judged accurate enough and used in the subsequent computations.

# BIBLIOGRAPHY


Alonso Rodriguez, A. and A. Valli (2010). *Eddy current approximation of Maxwell equations: theory, algorithms and applications*. MS & A 4. Milano: Springer-Verlag Mailand. DOI: 10.1007/978-88-470-1506-7 (cit. on pp. 35, 37).

Aydin, U., P. Rasilo, F. Martin, D. Singh, L. Daniel, A. Belahcen, M. Rekik, O. Hubert, R. Kouhia, and A. Arkkio (2017). "Magneto-mechanical modeling of electrical steel sheets." In: *Journal of Magnetism and Magnetic Materials* 439, pp. 82–90. DOI: 10.1016/j.jmmm.2017.05.008 (cit. on pp. 7, 8, 43, 44, 57, 58, 66, 74, 108, 111, 132, 133, 136, 147, 148, 157–160).

Barber, J. R. (2010). *Elasticity*. Solid Mechanics and Its Applications. Springer Netherlands. DOI: 10.1007/978-90-481-3809-8 (cit. on pp. 55, 72, 73, 148–153).

Belahcen, A., K. Fonteyn, S. Fortino, and R. Kouhia (2006). "A coupled magnetoelastic model for ferromagnetic materials." In: *Proc. of the IX Finnish Mechanics Days. von Hertzen R., Halme T.(eds.)*, pp. 673–682 (cit. on pp. 39, 44, 57, 58, 147).

Bernard, L. and L. Daniel (2015). "Effect of stress on magnetic hysteresis losses in a switched reluctance motor: Application to stator and rotor shrink fitting." In: *IEEE Transactions on Magnetics* 51.9, pp. 1–13. DOI: 10.1109/TMAG.2015.2435701 (cit. on pp. 7, 8, 42).

Bossavit, A. (2011). "Virtual Power Principle and Maxwell's tensor: Which comes first?" In: *Compel-the International Journal for Computation and Mathematics in Electrical and Electronic Engineering - COMPEL-INT J COMPUT MATH ELEC* 30, pp. 1804–1814. DOI: 10.1108/03321641111168110 (cit. on pp. 83, 85).

Bossavit, A. (2015). "Bulk forces and interface forces in assemblies of magnetized pieces of matter." In: *IEEE Transactions on Magnetics* 52.3, pp. 1–4. DOI: 10.1109/TMAG.2015.2481939 (cit. on pp. 83, 85).

Boughrara, K., T. Lubin, and R. Ibtiouen (2013). "General Subdomain Model for Predicting Magnetic Field in Internal and External Rotor Multiphase Flux-Switching Machines Topologies." In: *IEEE Transactions on Magnetics*, 18 pages. DOI: 10.1109/TMAG.2013.2260827 (cit. on p. 47).

Brown, W. F. J. (1966). *Magnetoelastic Interactions*. Springer-Verlag Berlin Heidelberg. DOI: 10.1007/978-3-642-87396-6 (cit. on pp. 35, 143).

Buffa, A., H. Ammari, and J. C. Nédélec (2000). "A Justification of Eddy Currents Model for the Maxwell Equations." In: *SIAM Journal on Applied Mathematics* 60.5, pp. 1805–1823. DOI: 10.1137/S0036139998348979 (cit. on p. 36).

Cassoret, B., S. Lopez, J.-F. Brudny, and T. Belgrand (Jan. 2014). "Non-Segmented Grain Oriented Steel in Induction Machines." In: *Progress In Electromagnetics Research C* 47, pp. 1–10. DOI: 10.2528/PIERC13112007 (cit. on p. 8).

Coleman, B. D. and W. Noll (1963). "The thermodynamics of elastic materials with heat conduction and viscosity." In: *Archive for Rational Mechanics and Analysis* 13.1, pp. 167–178. DOI: 10.1007/BF01262690 (cit. on pp. 22, 23, 25).

Cullity, B. D. and C. D. Graham (2011). *Introduction to magnetic materials*. John Wiley & Sons. DOI: 10.1002/9780470386323 (cit. on pp. 7, 42).

Daikoku, A., M. Nakano, S. Yamaguchi, Y. Tani, Y. Toide, H. Arita, T. Yoshioka, and C. Fujino (June 2005). "A high precision motor design method by finite element analysis considering stress distribution in stator core." In: *IEEE International Conference on Electric Machines and Drives, 2005*. IEEE, pp. 366–372. DOI: 10.1109/IEMDC.2005.195748 (cit. on p. 7).

Danas, K. (2017). "Effective response of classical, auxetic and chiral magnetoelastic materials by use of a new variational principle." In: *Journal of the Mechanics and Physics of Solids* 105, pp. 25–53. DOI: 10.1016/j.jmps.2017.04.016 (cit. on pp. 108, 157, 158).

Daniel, L., O. Hubert, F. Ossart, and R. Billardon (2003). "Experimental analysis and multiscale modelling of the anisotropic mechanical and magnetostrictive behaviours of electrical steels." In: *Journal de Physique IV France (Proceedings)*. Vol. 105. EDP sciences, pp. 247–254. DOI: 10.1051/jp4:20030194 (cit. on p. 148).

Daniel, L. (2018). "An analytical model for the magnetostriction strain of ferromagnetic materials subjected to multiaxial stress." In: *The European Physical Journal Applied Physics* 83.3, p. 30904. DOI: 10.1051/epjap/2018180079 (cit. on p. 8).

Daniel, L., L. Bernard, and O. Hubert (2020). "Multiscale Modeling of Magnetic Materials." In: DOI: 10.1016/B978-0-12-803581-8.12056-9 (cit. on pp. 8, 133).

Daniel, L. and O. Hubert (2009). "An analytical model for the ΔE effect in magnetic materials." In: *The European Physical Journal Applied Physics* 45.3, p. 31101. DOI: 10.1051/epjap/2009012 (cit. on p. 145).

Daniel, L., M. Rekik, and O. Hubert (2014). "A multiscale model for magnetoelastic behaviour including hysteresis effects." In: *Archive of Applied Mechanics* 84.9-11, pp. 1307–1323. DOI: 10.1007/s00419-014-0863-9 (cit. on pp. 8, 42).

Devillers, E., M. Hecquet, X. Cimetiere, J.-P. Lecointe, J. Le Besnerais, and T. Lubin (2018). "Experimental benchmark for magnetic noise and vibrations analysis in electrical machines." In: *2018 XIII International Conference on Electrical Machines (ICEM)*. IEEE, pp. 745–751. DOI: 10.1109/ICELMACH.2018.8506928 (cit. on pp. 111, 125–127).

Devillers, E., J. Le Besnerais, T. Lubin, M. Hecquet, and J.-P. Lecointe (2016). "A review of subdomain modeling techniques in electrical machines: Performances and applications." In: *2016 XXII International Conference on Electrical Machines (ICEM)*, pp. 86–92. DOI: 10.1109/ICELMACH.2016.7732510 (cit. on p. 47).

Dorfmann, A. and R. W. Ogden (2003). "Magnetoelastic modelling of elastomers." In: *European Journal of Mechanics - A/Solids* 22.4, pp. 497 –507. DOI: 10.1016/S0997-7538(03)00067-6 (cit. on pp. 8, 30, 39, 44).

Dorfmann, A. and R. W. Ogden (2004). "Nonlinear magnetoelastic deformations." In: *The Quarterly Journal of Mechanics and Applied Mathematics* 57.4, pp. 599–622. DOI: 10.1093/qjmam/57.4.599 (cit. on p. 8).

Dorfmann, A. and R. W. Ogden (2005). "Nonlinear electroelasticity." In: *Acta Mechanica* 174.3, pp. 167–183. DOI: 10.1007/s00707-004-0202-2 (cit. on p. 8).

Dorfmann, A., R. W. Ogden, and G. Saccomandi (2004). "Universal relations for non-linear magnetoelastic solids." In: *International Journal of Non-Linear Mechanics* 39.10, pp. 1699 –1708. DOI: 10.1016/j.ijnonlinmec.2004.03.002 (cit. on p. 39).

Du Trémolet De Lacheisserie, E. (1993). *Magnetostriction: theory and applications of magnetoelasticity*. CRC press, p. 430 (cit. on p. 7).

Eringen, A. C. and G. A. Maugin (1990). *Electrodynamics of continua I: foundations and solid media*. Springer-Verlag New York. DOI: 10.1007/978-1-4612-3226-1 (cit. on pp. 17, 35, 44, 143).

Fonteyn, K. (2010). "Energy-based magneto-mechanical model for electrical steel sheets." In: (cit. on pp. 7, 8, 35, 39, 43, 44, 91, 129).

Fonteyn, K., A. Belahcen, P. Rasilo, R. Kouhia, and A. Arkkio (2010a). "Contribution of Maxwell stress in air on the deformations of induction machines." In: *2010 International Conference on Electrical Machines and Systems*, pp. 1749–1753 (cit. on pp. 7, 8, 35, 39, 45, 85, 91).

Fonteyn, K., A. Belahcen, R. Kouhia, P. Rasilo, and A. Arkkio (2010b). "FEM for Directly Coupled Magneto-Mechanical Phenomena in Electrical Machines." In: *IEEE Transactions on Magnetics* 46.8, pp. 2923–2926. DOI: 10.1109/TMAG.2010.2044148 (cit. on pp. 7, 8, 35, 39, 91).

Fonteyn, K., A. Belahcen, P. Rasilo, R. Kouhia, and A. Arkkio (2010c). "Simulated results and experimental verification of a novel magneto-mechanical coupled method." In: *2010 International Conference on Electrical Machines and Systems*. IEEE, pp. 1743–1748 (cit. on pp. 39, 44).

Gieras, J. F. (2010). *Permanent Magnet Motor Technology Design and Applications, August 26*. 3rd ed. CRC Press, Taylor & Francis Group (cit. on p. 69).

Gieras, J. F. and J. Saari (2012). "Performance Calculation for a High-Speed Solid-Rotor Induction Motor." In: *IEEE Transactions on Industrial Electronics* 59.6, pp. 2689–2700. DOI: 10.1109/TIE.2011.2160516 (cit. on pp. 47, 48).

Griffiths, D. J. (2017). *Introduction to Electrodynamics*. 4th ed. Cambridge University Press. DOI: 10.1017/9781108333511 (cit. on p. 26).

Hanappier, N., E. Charkaluk, and N. Triantafyllidis (2021a). "A coupled electromagnetic–thermomechanical approach for the modeling of electric motors." In: *Journal of the Mechanics and Physics of Solids* 149, p. 104315. DOI: 10.1016/j.jmps.2021.104315 (cit. on p. 3).

Hanappier, N., E. Charkaluk, and N. Triantafyllidis (2021b). "Analytical magneto-mechanical model of the stator of an idealized electric motor." In: *submitted to IEEE Transactions on Magnetics* (cit. on p. 3).

Hanappier, N., E. Charkaluk, and N. Triantafyllidis (2021c). "Multiphysics simulation of electric motors with an application to stators." In: *submitted to International Journal of Solids and Structures* (cit. on pp. 4, 108).

Hiptmair, R. and J. Ostrowski (2005). "Coupled boundary-element scheme for eddy-current computation." In: *Journal of Engineering Mathematics* 51.3, pp. 231–250. DOI: 10.1007/s10665-004-2116-3 (cit. on pp. 35–37).

Hirsinger, L. and R. Billardon (1995). "Magneto-elastic finite element analysis including magnetic forces and magnetostriction effects." In: *IEEE Transactions on Magnetics* 31.3, pp. 1877–1880. DOI: 10.1109/20.376404 (cit. on p. 44).

Hutter, K., A. A. F. van de Ven, and A. Ursescu (2006). *Electromagnetic Field Matter Interactions in Thermoelasic Solids and Viscous Fluids*. Vol. 710. Lecture Notes in Physics. Springer-Verlag Berlin Heidelberg. DOI: 10.1007/3-540-37240-7 (cit. on pp. 8, 17, 31).

Jackson, J. D. (1999). *Classical Electrodynamics, 3rd ed.* John Wiley & Sons, Inc (cit. on p. 59).

Javadi, H., Y. Lefevre, S. Clenet, and M. L. Mazenc (1995). "Electro-magneto-mechanical characterizations of the vibration of magnetic origin of electrical machines." In: *IEEE Transactions on Magnetics* 31.3, pp. 1892–1895. DOI: 10.1109/20.376408 (cit. on p. 91).

Jiles, D. and D. Atherton (1986). "Theory of ferromagnetic hysteresis." In: *Journal of Magnetism and Magnetic Materials* 61.1, pp. 48–60. DOI: 10.1016/0304-8853(86)90066-1 (cit. on p. 159).

Joule, J. P. (1847). "XVII. On the effects of magnetism upon the dimensions of iron and steel bars." In: *The London, Edinburgh, and Dublin Philosophical Magazine and Journal of Science* 30.199, pp. 76–87. DOI: 10.1080/14786444708645656 (cit. on p. 7).

Kankanala, S. V. and N. Triantafyllidis (2004). "On finitely strained magnetorheological elastomers." In: *Journal of the Mechanics and Physics of Solids* 52.12, pp. 2869 –2908. DOI: 10.1016/j.jmps.2004.04.007 (cit. on pp. 7, 8, 17, 26, 39, 92, 93, 99, 102).

Kovetz, A. (2000). *Electromagnetic theory*. Vol. 975. Oxford University Press Oxford (cit. on pp. 8, 9, 11, 14–16, 22–25, 27–29, 31, 35, 87).

Langevin, P. (1905). "Sur la théorie du magnétisme." In: *J. Phys. Theor. Appl.* 4.1, pp. 678–693. DOI: 10.1051/jphystap:019050040067800 (cit. on p. 159).

Lax, M. and D. F. Nelson (1976). "Maxwell equations in material form." In: *Phys. Rev. B* 13 (4), pp. 1777–1784. DOI: 10.1103/PhysRevB.13.1777 (cit. on pp. 17, 92–94).

Lazzari, B. and R. Nibbi (Aug. 2000). "Variational principles in electromagnetism." In: *IMA Journal of Applied Mathematics* 65.1, pp. 45–95. DOI: 10.1093/imamat/65.1.45 (cit. on p. 92).

Ledger, P. D., A. J. Gil, R. Poya, M. Kruip, I. Wilkinson, and S. Bagwell (Feb. 2016). "Solution of an industrially relevant coupled magneto–mechanical problem set on an axisymmetric domain." en. In: *Applied Mathematical Modelling* 40.3, pp. 1959–1971. DOI: 10.1016/j.apm.2015.09.030 (cit. on pp. 35, 38, 91, 136).

Lee, E. W. (1955). "Magnetostriction and Magnetomechanical Effects." In: *Reports on Progress in Physics* 18.1, pp. 184–229. DOI: 10.1088/0034-4885/18/1/305 (cit. on p. 7).

Lefèvre, V. and O. Lopez-Pamies (2017). "Homogenization of Elastic Dielectric Composites with Rapidly Oscillating Passive and Active Source Terms." In: *SIAM Journal on Applied Mathematics* 77.6, pp. 1962–1988. DOI: 10.1137/17M1110432 (cit. on pp. 43, 44, 146).

Lopez, S., B. Cassoret, J. F. Brudny, L. Lefebvre, and J. N. Vincent (2009). "Grain Oriented Steel Assembly Characterization for the Development of High Efficiency AC Rotating Electrical Machines." In: *IEEE Transactions on Magnetics* 45.10, pp. 4161–4164. DOI: 10.1109/TMAG.2009.2023243 (cit. on p. 8).

Lubin, T., S. Mezani, and A. Rezzoug (2011a). "Analytic Calculation of Eddy Currents in the Slots of Electrical Machines: Application to Cage Rotor Induction Motors." In: *IEEE Transactions on Magnetics* 47.11, pp. 4650–4659. DOI: 10.1109/TMAG.2011.2157167 (cit. on pp. 47, 48, 57, 66, 88).

Lubin, T., S. Mezani, and A. Rezzoug (2012). "2D Analytical Calculation of Magnetic Field and electromagnetic Torque for Surface-Inset Permanent Magnet

Motors." In: *IEEE Transactions on Magnetics*, 12 pages. DOI: 10.1109/TMAG.2011.218091 (cit. on pp. 47, 88).

Lubin, T., S. Mezani, and A. Rezzoug (2011b). "2-D Exact Analytical Model for Surface-Mounted Permanent-Magnet Motors With Semi-Closed Slots." In: *IEEE Transactions on Magnetics* 47.2, pp. 479–492. DOI: 10.1109/TMAG.2010.2095874 (cit. on pp. 47, 88).

Maugin, G. A. (1980). "The method of virtual power in continuum mechanics: application to coupled fields." In: *Acta Mechanica* 35, pp. 1–70. DOI: 10.1007/BF01190057 (cit. on p. 92).

Maugin, G. A. (1993). *Material inhomogeneities in elasticity*. 1st ed. Chapman and Hall/CRC. DOI: 10.1201/9781003059882 (cit. on pp. 92, 95).

Michell, J. H. (Apr. 1899). "On the Direct Determination of Stress in an Elastic Solid, with application to the Theory of Plates." In: *Proceedings of the London Mathematical Society* s1-31.1, pp. 100–124. DOI: 10.1112/plms/s1-31.1.100 (cit. on pp. 56, 73).

Pang, Y., Z. Q. Zhu, D. Howe, S. Iwasaki, R. Deodhar, and A. Pride (2006). "Eddy Current Loss in the Frame of a Flux-Switching Permanent Magnet Machine." In: *IEEE Transactions on Magnetics* 42.10, pp. 3413–3415. DOI: 10.1109/TMAG.2006.879442 (cit. on pp. 68, 69).

Pao, Y.-H. (1978). "IV - Electromagnetic Forces in Deformable Continua." In: *Mechanics Today*. Ed. by S. NEMAT-NASSER. Pergamon, pp. 209–305. DOI: 10.1016/B978-0-08-021792-5.50012-4 (cit. on p. 44).

Pao, Y.-H. and C.-S. Yeh (1973). "A linear theory for soft ferromagnetic elastic solids." In: *International Journal of Engineering Science* 11.4, pp. 415 –436. DOI: 10.1016/0020-7225(73)90059-1 (cit. on pp. 35, 44, 143).

Pile, R., J. Le Besnerais, G. Parent, Y. Le Menach, E. Devillers, t. henneron, and J.-P. Lecointe (2019a). "Transfer Coefficients from Air-gap to Stator Bore Radius for Magnetic Force Wavenumbers -Application to Electrical Machines." Working paper or Preprint, HAL Id: hal-02168162 (cit. on pp. 47, 48, 80, 81, 83, 84, 155).

Pile, R., G. Parent, E. Devillers, t. henneron, Y. Le Menach, J. Le Besnerais, and J.-P. Lecointe (2019b). "Application Limits of the Airgap Maxwell Tensor." Working paper or Preprint, HAL Id: hal-02169268 (cit. on pp. 47, 48, 68, 74, 80, 81, 83, 84, 155).

Pile, R., E. Devillers, and J. Le Besnerais (2018). "Comparison of Main Magnetic Force Computation Methods for Noise and Vibration Assessment in Electrical Machines." In: *IEEE Transactions on Magnetics* 54.7, pp. 1–13. DOI: 10.1109/TMAG.2018.2828388 (cit. on p. 91).

Pile, R., Y. Le Menach, J. Le Besnerais, and G. Parent (2020). "Study of the Combined Effects of the Air-Gap Transfer for Maxwell Tensor and the Tooth Mechanical Modulation in Electrical Machines." In: *IEEE Transactions on Magnetics* 56.1, pp. 1–4. DOI: 10.1109/TMAG.2019.2948228 (cit. on pp. 47, 48, 80, 81, 83, 84).

Rasilo, P., D. Singh, U. Aydin, F. Martin, R. Kouhia, A. Belahcen, and A. Arkkio (2016). "Modeling of Hysteresis Losses in Ferromagnetic Laminations Under Mechanical Stress." In: *IEEE Transactions on Magnetics* 52.3, pp. 1–4. DOI: 10.1109/TMAG.2015.2468599 (cit. on pp. 8, 42).

Rekik, M., O. Hubert, and L. Daniel (2014). "Influence of a multiaxial stress on the reversible and irreversible magnetic behaviour of a 3% Si-Fe alloy." In: *International Journal of Applied Electromagnetics and Mechanics* 44.3-4, pp. 301–315. DOI: 10.3233/JAE-141793 (cit. on pp. 7, 57, 74, 147).

Reyne, G., J.-C. Sabonnadière, J. Coulomb, and P. Brissonneau (1987). "A survey of the main aspects of magnetic forces and mechanical behaviour of ferromagnetic materials under magnetisation." In: *IEEE Transactions on Magnetics* 23.5, pp. 3765–3767. DOI: 10.1109/TMAG.1987.1065518 (cit. on p. 7).

Reyne, G., J.-C. Sabonnadière, and J. F. Imhoff (1988). "Finite element modelling of electromagnetic force densities in DC machines." In: *IEEE Transactions on Magnetics* 24.6, pp. 3171–3173. DOI: 10.1109/20.92371 (cit. on pp. 7, 91).

Steentjes, S., M. Petrun, G. Glehn, D. Dolinar, and K. Hameyer (2017). "Suitability of the double Langevin function for description of anhysteretic magnetization curves in NO and GO electrical steel grades." In: *AIP Advances* 7.5, p. 056013. DOI: 10.1063/1.4975135 (cit. on p. 159).

Steigmann, D. J. (2009). "On the Formulation of Balance Laws for Electromagnetic Continua." In: *Mathematics and Mechanics of Solids* 14.4, pp. 390–402. DOI: 10.1177/1081286507080808 (cit. on pp. 8, 15, 28).

Sugawara, Y. and K. Akatsu (2013). "Characteristics of a Switched Reluctance Motor using Grain-Oriented electric steel sheet." In: *2013 IEEE ECCE Asia Downunder*, pp. 1105–1110. DOI: 10.1109/ECCE-Asia.2013.6579246 (cit. on p. 8).

Tadmor, E. B., R. E. Miller, and R. S. Elliott (2011). *Continuum Mechanics and Thermodynamics: From Fundamental Concepts to Governing Equations*. Cambridge University Press. DOI: 10.1017/CBO9781139017657 (cit. on p. 31).

Takezawa, M., K. Kitajima, Y. Morimoto, J. Yamasaki, and C. Kaido (2006). "Effect of Strain by Mechanical Punching on Nonoriented Si–Fe Electrical Sheets for a Nine-Slot Motor Core." In: *IEEE Transactions on Magnetics* 42.10, pp. 2790–2792. DOI: 10.1109/TMAG.2006.879900 (cit. on p. 7).

Thomas, J. D. and N. Triantafyllidis (2009). "On electromagnetic forming processes in finitely strained solids: Theory and examples." In: *Journal of the Mechanics and Physics of Solids* 57.8, pp. 1391 –1416. DOI: 10.1016/j.jmps.2009.04.004 (cit. on pp. 8, 17, 24, 35, 37, 38, 92–95, 100, 107).

Tian, L., L. Tevet-Deree, G. deBotton, and K. Bhattacharya (2012). "Dielectric elastomer composites." In: *Journal of the Mechanics and Physics of Solids* 60.1, pp. 181–198. DOI: 10.1016/j.jmps.2011.08.005 (cit. on pp. 43, 44, 146).

Tiersten, H. F. (1964). "Coupled Magnetomechanical Equations for Magnetically Saturated Insulators." In: *Journal of Mathematical Physics* 5.9, pp. 1298–1318. DOI: 10.1063/1.1704239 (cit. on p. 26).

Tiersten, H. F. (1990). *A development of the equations of electromagnetism in material continua*. Vol. 36. Springer Tracts in Natural Philosophy. Springer-Verlag New York. DOI: 10.1007/978-1-4613-9679-6 (cit. on p. 44).

Trimarco, C. (2002). "A Lagrangian approach to electromagnetic bodies." In: *Technische Mechanik. Scientific Journal for Fundamentals and Applications of Engineering Mechanics* 22.3, pp. 175–180. Hyperlink to article (no DOI) (cit. on pp. 92, 95).

Trimarco, C. and G. A. Maugin (2001). "Material mechanics of electromagnetic solids." In: *Configurational mechanics of materials*. Springer, Vienna, pp. 129–171. DOI: 10.1007/978-3-7091-2576-2_3 (cit. on pp. 92, 95).

Trimarco, C. (2005). "Total kinetic energy of an electromagnetic body." In: *Philosophical Magazine* 85.33-35, pp. 4277–4287. DOI: 10.1080/14786430500363817 (cit. on pp. 92, 95).

Trimarco, C. (2007). "Material electromagnetic fields and material forces." In: *Archive of Applied Mechanics* 77, pp. 177–184. DOI: 10.1007/s00419-006-0056-2 (cit. on pp. 92, 95).

ECOLE DOCTORALE

**Titre :** Modélisation électromagnétique-thermomécanique des moteurs électriques

**Mots clés :** Moteurs électriques ; Couplages multiphysiques ; Mécanique des solides ; Electromagnétisme ; Solutions analytiques ; Eléments-finis

**Résumé :** Le développement de moteurs électriques plus légers, compacts et puissants – entrainé par l'électrification rapide dans le domaine des transports en réponse aux enjeux environnementaux de notre époque – entraine une augmentation des contraintes, des courants et des champs magnétiques dans les composants des moteurs. Ces composants – notamment les composants ferromagnétiques – présentent des couplages forts de leurs propriétés magnéto-thermo-mécaniques, exacerbées dans des moteurs plus fortement sollicités. Les chargements mécaniques et thermiques de la machine influencent ses propriétés magnétiques et la conception de moteurs toujours plus performants nécessite alors d'avoir recours à des modélisations multi-physiques fiables. La compréhension et la modélisation de ces couplages est devenu un sujet de préoccupation important pour les industriels et fait l'objet de nombreux travaux de recherche. Les travaux présentés ici proposent une théorie couplée électromagnétique-thermomécanique du milieu continu et le développement d'outils analytiques et numériques pour la résolution de problèmes aux limites dans les moteurs électriques.

**Title :** Coupled electromagnetic-thermomechanical modeling of electric motors

**Keywords :** Electric motors ; Multiphysics couplings ; Continuum mechanics ; Electromagnetism ; Analytical solutions ; Finite-elements

**Abstract :** Future developments of lighter, more compact and powerful motors – driven by environmental and sustainability considerations in the transportation industry – involve higher stresses, currents and electromagnetic fields. For the components used in electric motors – especially for the ferromagnetic ones – strong couplings between mechanical, thermal and electromagnetic effects arise, which are amplified by the higher loads. They affect the machine's performance, thus requiring a consistent multiphysics modeling for the motors' design. Understanding and modeling these couplings has recently become an important subject of research. The work presented here proposes a coupled electromagnetic-thermomechanical continuum theory together with analytical and numerical (finite element) tools for the solutions of boundary value problems arising in electric motors.

**Institut Polytechnique de Paris**
91120 Palaiseau, France